

Scanning Ele

5. Scanning Electron Microscopy

Natasha Erdman, David C. Bell, Rudolf Reichelt

This chapter provides an overview of the concepts of scanning electron microscopy (SEM) from a theoretical as well as practical operational perspective. The theory section begins with the basics of image formation followed by an explanation of the interaction of the electron beam with the sample. A description of the different types of electron guns is also included. The concepts involved with image formation from a rastered (or scanned) electron beam on a surface is explained along with the mechanisms of contrast generation from sample surface topography and sample composition. The different SEM detectors are also explained including a description of the practical application of detectors under various sample conditions. Numerous diagrams and figures in this chapter illustrate imaging geometries and possible SEM system configurations. Included in the chapter is an explanation of the various instrument operation parameters for different samples as well as a discussion of the effects of electron-beam accelerating voltages on sample imaging, contrast, and resolution.

More advanced topics are also included such as the use of beam deceleration and in-lens imaging and detectors. Analytical SEM techniques are also explained with the explanation of the use of energy-dispersive x-ray detectors (EDS) used to measure sample composition as well as provide

5.1	Conventional Scanning Electron Microscopy	231
5.1.1	Electron Guns, Electron Lenses, Detectors, and Stages.....	233
5.1.2	Electron–Specimen Interaction and Signal Generation.....	245
5.1.3	Contrast Formation and Resolution.....	256
5.1.4	Specimen Preparation	264
5.1.5	Radiation Damage and Contamination .	267
5.1.6	Applications	268
5.2	Field-Emission Scanning Electron Microscopy	273
5.2.1	High-Resolution Scanning Electron Microscopy.....	273
5.2.2	Low- and Very-Low-Voltage Scanning Electron Microscopy.....	279
5.3	Scanning Electron Microscopy at Elevated Pressure	293
5.4	Microanalysis in Scanning Electron Microscopy	298
5.5	Crystal Structure Analysis by Electron Backscatter Diffraction	302
	References	305

compositional maps of a sample. Application of SEM to a variety of materials systems under varying conditions are discussed with multiple examples and illustrations given.

The earliest historical contribution to the idea of a scanning electron microscope (SEM) was probably made by *H. Stintzing* in a German patent application [5.1]. In his patent he proposed irradiating a sample with a narrowly collimated beam (light, x-ray, corpuscles) and moving the sample transversely to the beam. The magnitude of interaction between beam and sample was to be measured by a sufficiently sensitive recording device, to be amplified and then displayed on an electron tube. This idea aimed to determine the size of small particles not accessible to light microscopy. However, the method proposed was unable to generate a magnified image.

The first electron-beam scanner capable of producing an image of the surface of a bulk sample with the emitted secondary electrons (SE) was developed by *H. Knoll* [5.2]. In this instrument a focused electron beam was scanned across the sample surface by magnetic deflection line-by-line. The generated SE were converted into an electronic signal, which was amplified and then used to modulate the brightness of an electron tube. Both the electron beam of the scanner and of the display tube were scanned synchronously across the same distance by perpendicular pairs of deflection coils, thus the electron-beam scanner at that

time possessed unit magnification. The contrast in the SE image was due to the varying yield of SE caused by the different local chemical composition of the sample surface. However, submicroscopic resolution with an SEM was first obtained by *M. von Ardenne* using the transmission mode (so-called scanning transmission electron microscope (STEM)) [5.3]. The early development of electron microscopy up to 1940 has been described extensively by *E. Ruska* [5.4]. While the development of SEM in Europe was interrupted by World War II, the idea of SEM was used by *Zworykin, Hillier, and Snyder* in the United States for the construction of such an instrument [5.5]. After World War II, experiments with scanning electron microscopes started in England and France. Since 1948 *C.W. Oatley* from the Engineering Laboratory of the University of Cambridge directed intensive development in that field, which led to the first commercial scanning electron microscope available in 1965. Pioneering work in the improvement of instrumentation (e. g., electron sources, electron optics, detectors, signal processing), the investigation of electron-specimen interaction, elucidation of fundamental contrast mechanisms, and development of methods for the preparation of samples were done in the 1960s and 1970s (for books, proceedings of SEM conferences, and reviews see [5.6–16]). At the same time the SEM was applied extensively in very different fields for *imaging of surfaces*, for the local *crystallographic characterization* of polycrystalline materials by electron backscattered diffraction (EBSD), and in combination with x-ray microanalytical equipment such as an energy-dispersive spectrometer (EDX) or a wavelength-dispersive spectrometer (WDX) for the *local element analysis* of specimens (for books or proceedings of SEM conferences see [5.14, 15, 17–28]).

A significant improvement in SEM instrumentation was made by the development of the field-emission scanning electron microscope (FESEM) that became commercially available in the 1980s. In the FESEM instead of a thermionic gun a field-emission gun (FEG) is used for electron-beam generation, which allows the formation of an electron probe with a diameter of about 0.5 nm. Together with further improvements in electron optics and electron detectors on the one hand and in specimen preparation on the other hand, high-resolution imaging by FESEM became feasible. Additionally, the FESEM enables specimens to be imaged at extremely low acceleration voltages, i. e., below 1 kV, also at high resolution, without sacrificing the traditional high kV and high current (analytical) performance. The operation of the FESEM at low acceleration voltages opens new avenues for interesting applications in the characterization of surfaces (for reviews of specific aspects of the instrumentation, image formation, and application

of FESEM at conventional or low acceleration voltages, respectively, see [5.29–34]).

A very interesting step forward in the instrumentation was the development of a so-called variable pressure (VP) or environmental scanning electron microscope (ESEM) pushed in the 1980s in particular by *G.D. Danilatos*. Investigations of specimens using secondary or backscattered electrons for imaging, in SEM and FESEM restricted to high vacuum, can be performed in the VP/ESEM in a low vacuum at a pressure of about 10 up to a few thousand Pa, often assisted by introduction of water vapor into the chamber during imaging. Obviously, this is of great interest for samples that consist of materials that may contain dirt or fluids, respectively, having a partial pressure in the low vacuum range mentioned. Typical examples are water- or oil-containing natural specimens. Moreover, electric insulators can be imaged without prior conductive coating by VP/ESEM in low vacuum without significant electric charging artifacts. The VP/ESEM (ESEM was originally developed by *Electroscan*, and in later years has been used as a trade name by *FEI/Thermo*) became commercially available in 1987 (for reviews of specific aspects of the instrumentation, image formation, and application of VP/ESEM see [5.35–37]). Currently all manufacturers offer some form of variable-pressure SEM, with the ability to image with both secondary and backscatter electrons.

Modern high-resolution FESEMs have at an electron energy of 30 keV a specified resolution power in the SE mode in the range of 0.5–1 nm, which corresponds to about the size of a small molecule. It marks the smallest size of a structure accessible on one hand. Working at the lowest magnification of an SEM on the other hand allows imaging of visible structures as large as about 5 mm, i. e., high-resolution SEMs cover a wide range of six orders of magnitude for the structural characterization of surfaces. A further advantage of the SEM is the simultaneous acquisition of different signals generated by the local interaction of the beam electrons with the specimen. Each of these signals, e. g., SE and backscattered electrons (BSEs), carries different information about the sample, thus an extensive multi-dimensional data set about an area of interest can be obtained by one scan line-by-line across this area. The recording time may vary from a few seconds only to about 1 min depending on the strength of the signal and the signal-to-noise ratio (SNR) required.

Scanning electron microscopy is now a well-established method for the characterization of surfaces in ultrahigh vacuum (UHV), high vacuum (HV), and low vacuum (LV) in many different fields. Clearly, it is not possible to mention all of them, however, the main fields are certainly the materials (metals, alloys,

ceramics, glasses) and surface sciences, semiconductor research and industry, life sciences, and miscellaneous sciences such as polymer and food research, mineralogy, geology, the oil industry, and archaeology.

In addition to scanning electron microscopy some other surface-sensitive methods such as atomic force

microscopy, scanning tunneling microscopy, and photoelectron microscopy are described in this book. It is certainly of particular interest to see in detail how these surface-sensitive methods complement each other, what specific advantages they offer, and how they compare with SEM.

5.1 Conventional Scanning Electron Microscopy

The principle of a scanning electron microscope is shown schematically in Fig. 5.1. The two major parts are the microscope column and the electronics console. The microscope column consists of the electron gun (with the components cathode, Wehnelt cylinder, anode), one or two condenser lenses, two pairs of beam deflection coils (scan coils for x , y deflection), the objective lens, and some apertures. In the specimen chamber at the lower end of the microscope column are located the specimen stage and the detectors for the different signals generated by the electron-specimen interaction, though the current FESEMs often feature some form of in-lens detectors. The microscope column and the specimen chamber are evacuated using

a combination of prevacuum and high-vacuum pumps (usually turbomolecular pumps). The pressure in the specimen chamber typically amounts to about 10^{-4} Pa, allowing the beam electrons to travel from the cathode to the specimen with little interaction with the residual gas molecules. The electronics console consists of the electric power supplies for the acceleration voltage (usual range about 0.5–30 kV) as well as the condenser and objective lenses, the scan generator, and electronic amplifiers for the different signals acquired. Moreover, the console also houses one or more monitors (liquid crystal display (LCD)) for displaying the graphic user interface and live or recorded image, numerous knobs and a computer keyboard to control the elec-

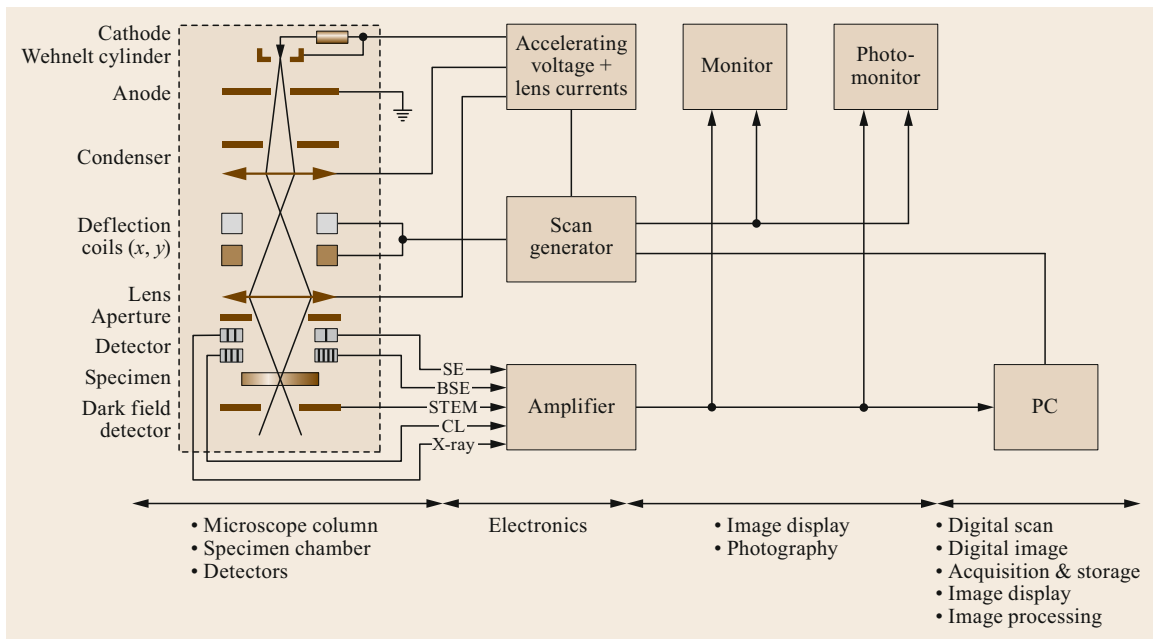


Fig. 5.1 Schematic drawing of a conventional SEM. The evacuated microscope column (inside the *dashed frame*) contains the electron gun, electromagnetic lenses, electromagnetic deflection coils, apertures, the specimen stage, and the detectors. The electronics console houses the power supplies for the acceleration voltage and the electromagnetic lenses, the scan generator, amplifiers for the signals, and monitors for display and recording of images. Modern SEMs are controlled by a PC. BSE: backscattered electrons; CL: cathodoluminescence; SE: secondary electrons; STEM: scanning transmission electron microscope signal; x-ray: x-ray signal

tron beam, the signals selected, and the image recording. More recently, some SEMs forego the numerous knobs which are replaced by a mouse-controlled interactive program running on the personal computer (PC).

How does the SEM work? The beam electrons are emitted from the cathode and accelerated by a voltage of 0.5–30 kV between the cathode and anode forming a smallest beam cross section—the crossover—near the anode with a diameter of about 10–50 μm . This spot size is too large to produce a sharp image. Therefore, the crossover is demagnified by the lens system consisting of one or two condenser lenses and one objective lens and focused on the specimen surface. Most SEMs can produce an electron beam having a smallest spot size of about 5–10 nm and an electron probe current in the range of 10^{-12} – 10^{-10} A, which is sufficient to form an image with a reasonable SNR. For higher probe currents required for some modes of operation the smallest probe spot size increases to 100 nm or more. The objective lens has a variable relatively long focal length that allows a large working distance (WD); it corresponds to the distance between the specimen and lower pole piece) in the range of about 2–50 mm. This ensures that the various signals generated by the impinging beam electrons (Fig. 5.2) in the small specimen interaction volume can be collected by detectors located lateral above the specimen with sufficient efficiency. Pairs of beam deflection coils located in front of the objective lens and controlled by a scan generator scan the electron probe line-by-line across a small area of the specimen. The detected signal is then collected

and recorded through the graphic user interface on the computer monitor screen.

The signals may vary from one location to another as the electron–specimen interaction changes because of, e. g., topography and specimen composition. The magnification of the image is given by the ratio of the length of the scan on the monitor and the corresponding length of the scan on the specimen. For example, an increase in magnification can simply be achieved by decreasing the current of the deflection coils in the microscope column (i. e., lowering the length of the scan on the specimen) and keeping the image size on the monitor constant. It should be mentioned that the magnification also depends on the WD, however, modern SEMs compensate automatically for each WD, thus keeping the displayed magnification correct. Figure 5.3 shows a series of images recorded with increasing magnifications over a range of almost three orders of magnitude.

For crystal structure analysis (Sect. 5.5) basically two strategies exist: (1) The mode of beam deflection changes from scanning line-by-line to rocking of the electron beam when the probe is at rest on a chosen location and the angle of incidence is scanned within a selectable angular range to form an electron channeling pattern. (2) The electron backscattered diffraction pattern from the point of electron-beam impact is recorded by means of a position-sensitive detector and analyzed revealing information about the local crystal structure.

One of the greatest strengths of the SEM is the tremendous depth of focus, i. e., the range of heights of the specimen being simultaneously in focus (Fig. 5.3). Because of the small objective aperture diaphragm (about 30–100 μm) and the large WD the semiangle α_p of the convergent impinging electron probe is in the order of 10 mrad only. At magnifications that are comparable to those of light microscopy (e. g., 1000 \times) the SEM has a depth of focus that is about 100 times greater than that of an optical microscope, obviously because the semiangle of convergence is much larger in the latter case.

To take full advantage of all the information that SEM can provide, an understanding of its operation modes and the influence of electron-beam parameters on the image resolution, the image contrast, the signal strength, and the SNR as well as the electron–specimen interaction is mandatory. The remarkable success of scanning electron microscopy over several decades is mainly due to the tremendous depth of focus, the brilliant image contrast, and the relatively straightforward sample preparation for imaging of surfaces, and, in combination with x-ray microanalytical equipment, its capability of local quantitative element analysis of specimens.

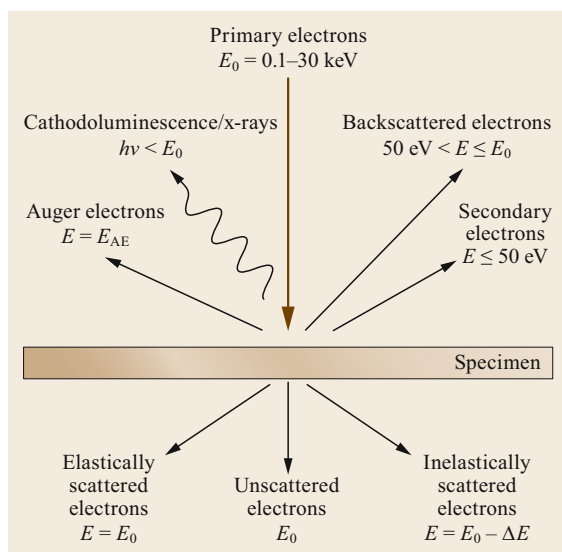


Fig. 5.2 Schematic drawing of signals for a thin sample generated by the impinging electrons

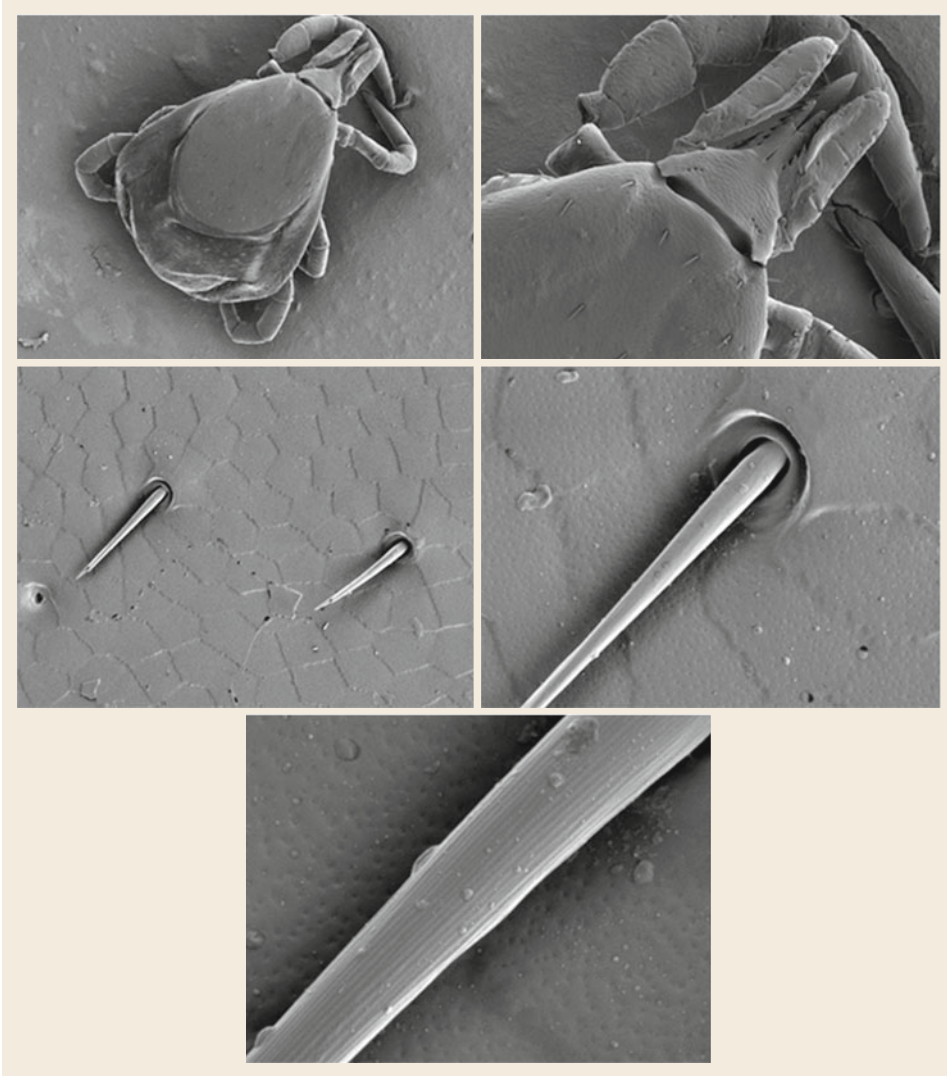


Fig. 5.3 Micrograph series of increasing magnification of a tick nymph, recorded at 2 kV (60× to 10 000×). The specimen was air dried and sputter coated with gold

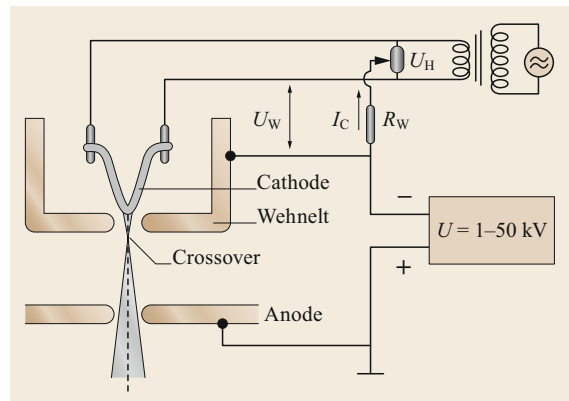
5.1.1 Electron Guns, Electron Lenses, Detectors, and Stages

Electron Guns

The electron gun provides the SEM with an electron beam of adjustable current and energy. The most classic electron gun is the triode gun based on thermionic emission from a tungsten filament heated to about $T_c = 2700\text{ K}$ (Fig. 5.4). The filament has a diameter of about 0.1 mm and is bent in the shape of a V hairpin to localize the emission area on the tip. The size of this area is

Fig. 5.4 Schematic drawing of the thermionic emission triode gun with a tungsten hairpin filament. The filament is heated by the applied voltage U_H ; R_W , variable resistor to adjust the potential U_W between the Wehnelt cylinder and cathode; U , acceleration voltage. After [5.30] ►

around $100\ \mu\text{m} \times 150\ \mu\text{m}$. By thermionic excitation the electrons overcome the work function ϕ of the tungsten



tip and a current with the density j_c is emitted according to the Richardson law

$$j_c = AT_c^2 \exp\left(-\frac{\phi}{k_B T_c}\right), \quad (5.1)$$

where A represents a constant depending on the cathode material and k_B is the Boltzmann constant; $\phi = 4.5$ eV for tungsten. The density j_c depends strongly on the temperature: j_c is about 1.8 A cm^{-2} for $T_c = 2700 \text{ K}$ and about 3 A cm^{-2} for $T_c = 2800 \text{ K}$.

The emitted electrons are accelerated from the filament at a high negative potential (e. g., -30 kV) toward the anode at ground potential (0 V). Central holes in the Wehnelt cylinder and in the anode enable a fraction of the accelerated electrons (e. g., $E_0 = 30 \text{ keV}$) to move toward the lenses in the microscope column. The emission current is typically in the order of $100 \mu\text{A}$ and can be controlled by the bias of the Wehnelt cylinder, which surrounds the filament. The negative Wehnelt bias is provided by a voltage drop caused by the emission current through the resistor R_W . The electrostatic field distribution inside the triode gun has a focusing action to the emitted electrons generating a crossover that is located between the Wehnelt cylinder and the anode. This crossover can be characterized by the diameter d_0 and the semiangle α_0 of the divergence. d_0 is usually in the order of $50 \mu\text{m}$. As we will see later the condenser and objective lenses produce a demagnified image of that crossover on the specimen surface representing the final electron probe (diameter d_p).

An important parameter of an electron gun is its axial brightness β , which is defined as the beam current per area (equal to current density) into a solid angle $\pi\alpha^2$ [5.38]

$$\beta = \frac{j}{\pi\alpha^2} = \text{const.} \quad (5.2)$$

It is important to note that the brightness remains constant for all points along the electron optical axis from the cathode through the microscope column to the

specimen. This means that the brightness of the final electron probe on the specimen surface is equal to the brightness of the gun regardless of apertures in the microscope column, i. e.,

$$\beta = \frac{4I_0}{\pi^2 d_0^2 \alpha_0^2} = \frac{4I_p}{\pi^2 d_p^2 \alpha_p^2}, \quad (5.3)$$

where I_0 is the beam current at the crossover inside the electron gun. Equation (5.3) shows that the characteristic illumination parameters I_p , d_p , and α_p cannot be changed independently. For example, an increase of β for given d_p and α_p clearly requires an increase of I_p .

The work function of tungsten is relatively high. Lanthanum hexaboride (LaB_6) has a significantly lower work function ($\phi = 2.7 \text{ eV}$) and can therefore emit greater current densities at lower temperature ($T_c = 1900 \text{ K}$). At the same time the brightness of the electron probe is also increased since the maximum brightness of an electron gun [5.38] is given as

$$\beta = \frac{j_c E_0}{\pi k T_c} \quad (5.4)$$

i. e., the brightness β is inversely proportional to the temperature of the cathode. The LaB_6 cathode consists of a small piece of an LaB_6 single crystal with a tip radius typically of about $1 \mu\text{m}$. The single crystal is supported by a nonreactive material and is resistively heated. It seems worth mentioning that (1) in the cathode chamber the operation of an LaB_6 requires a vacuum better than 10^{-4} Pa to avoid cathode contamination (tungsten cathode: about 10^{-3} Pa) and (2) its alignment is critical.

Characteristic values of the triode gun with thermionic tungsten and the LaB_6 cathode are summarized in Table 5.1.

Electron Lenses

As discussed in Sect. 5.1.1, *Electron Guns*, the electrons emerge from the electron gun as a divergent beam. Two

Table 5.1 Characteristic parameters of different electron guns

Parameters	Thermionic W-cathode ^a	LaB_6 -cathode ^{a,b}	Cold FEG ^c	Schottky emission cathode ^c
Brightness ($\text{A cm}^{-2} \text{ sr}^{-1}$)	10^5	10^6	10^7 – 10^8	10^7 – 10^8
Energy spread (eV)	1–3	0.5–2	0.2–0.3	0.5–0.6
Vacuum (Pa)	$\approx 10^{-3}$	$\approx 10^{-4}$	10^{-8} – 10^{-9}	10^{-8}
Emission current (μA)	≈ 100	$1 \rightarrow 50$	≈ 2 – 20	30–150
Life time	$\approx 80 \text{ h}$	$\approx 1000 \text{ h}$	$> 1 \text{ year}$	$> 1 \text{ year}$

^a Reimer [5.38].

^b DeVore and Berger [5.39].

^c Reimer [5.30]

or three electromagnetic lenses and apertures in the microscope column (Fig. 5.1) reconverge and focus the beam into a demagnified image of the first crossover generated by the gun. The final lens—the objective lens—focuses the beam into the smallest possible spot of 4–10 nm (thermionic source) on the sample surface, i. e., the total demagnification is about 5000×.

Rotationally symmetric electromagnetic lenses consist of a coil with NI ampere windings inside an iron pole piece. Typically, NI is in the order of 10^3 A for the condenser and objective lenses. The iron pole piece has a small gap in its axial bore. The current in the coil generates a magnetic field carried by the iron, which also appears at the gap forming a bell-shaped stray field distribution on the optical axis with a radial and axial field component. Off-axis electrons move due to the Lorentz force along screw trajectories because the radial component of the field results in a rotation around the optical axis. Electrons emerging divergently from a point in front of the lens are focused in an image point behind the lens. The lenses of SEMs can usually be considered weak lenses (because the pole piece is not saturated). In this case, the principal planes of the lens coincide with its optical center and the formulas for thin light optical lenses can be used. In close analogy to light optics the strength of an electromagnetic lens can be characterized by its focal length f . Using the thin lens formulas we can write

$$\frac{1}{f} = \frac{1}{p} + \frac{1}{q}, \quad (5.5)$$

where p is the distance from the object (= crossover) and q is the distance to the image. Both, p and q are related to the center of the lens. The magnification M is given simply by

$$M = \frac{q}{p}, \quad (5.6)$$

where $M < 1$ for $p > 2f$, i. e., a demagnified image of an object is obtained at these imaging conditions. Therefore, a strong demagnification of about 5000× of the first crossover can be obtained for $p \gg 2f$ for each of the two or three lenses by successive demagnification of each intermediate crossover. In case of two condenser lenses they usually are combined and adjusted by one control only.

The pole pieces of condenser lenses are symmetrical, i. e., the diameters of the axial bores in the upper and lower half of the pole piece are identical. In contrast to that the pole piece of the objective lens is very asymmetric (1) to limit the magnetic field at the specimen level and (2) to house the beam deflections

coils, the adjustable objective aperture, and the stigmator (not shown in Fig. 5.1). The asymmetric objective lens (called the pinhole or conical lens) adapts for the wide range of the WD of about 2–50 mm by an adjustable focal length. However, working at a large WD inevitably degrades the electron optical properties of the objective lens and enlarges the final spot size d_p . For a detailed description of the electron optical properties of electromagnetic lenses and deflection coils the reader is referred to books about electron optics [5.40–43].

All electromagnetic lenses involved in successive demagnification suffer from an imperfect rotational symmetry and aberrations, which degrade their electron optical performance. The effects of lens aberrations cannot be compensated. However, they can be minimized, which is most effective for the final—the objective—lens. Let us consider briefly the three significant effects:

1. *Spherical aberration*: The spherical aberration constant C_s causes an error disc of the diameter [5.44]

$$d_s = \frac{1}{2C_s\alpha_p^3} \quad (5.7)$$

2. *Chromatic aberration*: The chromatic aberration caused mainly by the energy spread of the electrons from the gun is characterized by the constant C_c and causes an error disc of the diameter

$$d_c = C_c \frac{\Delta E}{E_0} \alpha_p, \quad (5.8)$$

where $\Delta E/E_0$ represents the relative energy spread of the beam electrons.

3. *Diffraction*: The diffraction of electrons on the objective aperture results in a further error disc—the Airy disc—of diameter

$$d_f = \frac{0.6\lambda}{\alpha_p}, \quad (5.9)$$

where λ is the wavelength of the electrons.

In a first approximation it is possible to superpose the squared diameters of the individual discs to estimate the effective electron probe diameter

$$d_{pe}^2 = d_p^2 + d_s^2 + d_c^2 + d_f^2. \quad (5.10)$$

d_p^2 is given by (5.3) as

$$d_p^2 = \left(\frac{4I_p}{\pi^2\beta} \right) \alpha_p^{-2}.$$

More precise, but at the same time more complicated relations for the effective probe diameter were derived by *Barth and Kruit* [5.45] and *Kolarik and Lenc* [5.46].

Under the conditions normally used in conventional SEM (i. e., $E_0 = 5\text{--}30$ keV) the chromatic aberration as well as the effect of the diffraction are relatively small compared to the remaining contributions and can be neglected [5.38]. The optimum aperture α_{opt} , which allows the smallest effective electron probe diameter d_{min} , can be obtained by the first derivative $\partial d_{\text{pe}}/\partial \alpha_p = 0$ and is given as

$$\alpha_{\text{opt}} = \left(\frac{4}{3}\right)^{1/8} \left[\frac{\left(\frac{4I_p}{\pi^2\beta}\right)^{1/2}}{C_s} \right]^{1/4}. \quad (5.11)$$

By using the approach mentioned above, i. e., $d_{\text{pe}}^2 = d_p^2 + d_s^2$, and (5.3), (5.7), and (5.11), the minimum effective electron probe diameter is

$$d_{p,\text{min}} = \left(\frac{4}{3}\right)^{3/8} \left[\left(\frac{4I_p}{\pi^2\beta}\right)^{3/2} C_s \right]^{1/4}. \quad (5.12)$$

It is obvious that $d_{p,\text{min}}$ increases as I_p increases or β decreases. Both, I_p and β are parameters depending on the performance of the electron gun (5.3). C_s is a parameter characterizing the performance of the objective lens and should be as small as possible. As previously mentioned, the operation of the SEM at a large WD inevitably degrades the electron optical properties of the objective lens, i. e., C_s increases as the WD increases. Just to provide a rough idea about values for $d_{p,\text{min}}$ and α_{opt} at usual electron energies (5–30 keV), a moderate WD and a probe current I_p of about 10^{-11} A, which gives a sufficient S/N ratio, $d_{p,\text{min}}$ typically amounts to approximately 5 nm and α_{opt} to 5–10 mrad.

It is also of interest to know the maximum probe current $I_{p,\text{max}}$ under these conditions. Using (5.12) and (5.3) one obtains

$$I_{p,\text{max}} = \frac{3\pi^2}{16} \beta C_s^{-2/3} d_{p,\text{min}}^{8/3}. \quad (5.13)$$

Interestingly, it becomes obvious from (5.13) that including the effect of the spherical aberration, I_p is now proportional to $d_p^{8/3}$ instead of d_p^2 as before (5.3).

The electron probe current in an SEM equipped with a thermionic gun can be increased several orders of magnitude above 10^{-11} A as required, e. g., for microanalytical studies (Sect. 5.4). It is clear from the considerations above that an increase in the probe current inevitably increases the probe size. A rough estimate for 30-keV electrons shows that an increase of I_p

to 10^{-9} A requires a probe size of about 60 nm. However, because of the electron–specimen interaction the lateral resolution of x-ray microanalysis is limited to about 1 μm for thick samples. Therefore, a probe diameter of 100 nm or even several hundred nanometers can be tolerated without disadvantage for x-ray microanalysis in this case.

When considering the effective electron probe diameter the chromatic aberration of the objective lens could be neglected for energies > 10 keV. Because d_c is inversely proportional to E_0 (5.8) there is a significant increase for energies below 10 keV, in particular for the low-voltage range below 5 keV. For example, for 1-keV electrons the diameter of the chromatic error disc increases by a factor of 30 compared to 30 keV! When using a thermionic cathode with a tungsten filament and a probe current of about 10^{-11} A the energy spread is about 2 eV (Table 5.1) and d_c contributes dominantly to the enlargement of the probe diameter (5.10). Therefore, the thermionic source is inappropriate for imaging in the low-voltage range. As we shall see in Sect. 5.2, field-emission guns with a one order of magnitude smaller energy spread and about five orders of magnitude larger brightness are very well suited for low-voltage SEM (LVSEM).

In the context of the objective lens the existence of a stigmator was mentioned, which usually is located near the pole-piece gap. Because of imperfect rotational symmetry of the pole-piece bores, magnetic inhomogeneities of the pole piece, or some charging effects in the bore or at the objective aperture, the magnetic field in the objective lens becomes asymmetric. This causes different focal lengths in the sagittal and meridional planes, which leads to low image quality degraded by astigmatism. The astigmatism can be compensated for by adding a cylinder lens adjustable in its strength and azimuth. The effect of a cylinder lens is realized by the stigmator consisting of a pair of quadrupole lenses.

Detectors and Detection Strategies

Electron detectors specifically collect the signals emerging from the specimen as a result of electron–specimen interaction. The efficiency of the signal collection depends on the type of the detector, its performance, and its detection geometry, i. e., its position related to location of the signal emitting area. For an understanding of the recorded signals, knowledge of the influence of these parameters is critical.

Detectors. To detect electrons in SEM three different principles are commonly used. One principle is based on the conversion of signal electrons to photons by a scintillation material. Then, the photons are converted

into an electric signal by a photomultiplier, which is proportional to the number of electrons impinging on the scintillator. The second principle is based on the conversion of electrons to electron–hole pairs by a semiconductor, which can be separated before recombination causing an external charge-collection current. This current is proportional to the number of electrons impinging on the semiconductor. While the principle of scintillation detection is used for secondary, backscattered, and transmitted electrons (in case of thin specimens), the semiconductor detector is mostly used for backscattered electrons only. Finally, the third principle is based on the electron channel multiplier tube, which converts the signal electrons by direct impact at its input to secondary electrons and multiplies them inside the tube. The output signal is proportional to the number of impinging signal electrons.

Besides of electrons the electron–specimen interaction can also produce electromagnetic radiation, namely cathodoluminescence (CL) and x-rays (Fig. 5.2). Cathodoluminescence shows a close analogy to optical fluorescence light microscopy (FLM) where light emission is stimulated by irradiation with ultraviolet light (photoluminescence). In principle, for the detection of emitted light, which has a wavelength in the range of about 0.3–1.2 μm , a photomultiplier is very well suited (see above) and therefore most often used. However, the commonly low intensity of the CL signal requires, for a sufficient S/N ratio, a high collection efficiency of the emitted light. Table 5.2 presents the most common

detector types for SE, BSE, and CL. The detectors for x-rays will be described in Sect. 5.4 of this chapter.

Scintillation Detector. The scintillation detector for SE—the Everhart–Thornley (ET) detector [5.47]—is shown schematically in Fig. 5.5. The generated SE are collected by a positively biased collector grid, then they pass the grid and are accelerated by about 10 kV to the conductive coated scintillator. The scintillation material converts electrons to photons, which are guided by a metal-coated quartz glass to the photocathode of a photomultiplier where photoelectrons are generated and amplified by a factor of about 10^6 . Usually the electronic signal at the output of the photomultiplier is further amplified. Several scintillator materials, such as plastic scintillators, lithium-activated glass, P-47 powder, or yttrium-aluminum-garnet (YAG) and yttrium-aluminum-perovskite (YAP) single crystals, are in use, which differ in their performance (for details see [5.38, 50, 51, 56–58]).

When the collector grid of the ET detector is negatively biased by < -50 V SE are not collected. In this case only the BSE can reach the scintillator on almost straight trajectories because of their higher energies. The detected fraction of BSE is very low because of the small solid angle of collection, i. e., small angular collection efficiency (CE). However, for an efficient detection of BSE the solid angle of collection of BSE detectors is significantly larger by using a larger scintillator and at the same time a shorter distance to the

Table 5.2 Most common electron detectors for SEM

Signal	Type of detector	Principles	Specifications	References
SE	Everhart–Thornley	Scintillator–LP–PM	High CE; positively biased collector grid	<i>Everhart and Thornley</i> [5.47]; <i>Reimer</i> [5.38]
	Solid state	Electron–hole pair generation	SE are accelerated to > 10 keV before detection	<i>Crewe et al.</i> [5.48]; <i>Reimer</i> [5.38]
	MCP	Electron-multiplier tube	Positively biased from plate	<i>Postek and Keery</i> [5.49]; <i>Reimer</i> [5.38]
BSE	Everhart–Thornley	Scintillator–LP–PM	Very low CE; negatively biased collector grid	<i>Everhart and Thornley</i> [5.47]; <i>Reimer</i> [5.38]
	Autrata	Scintillator–LP–PM	High CE; $E_{\text{BSE}} \geq 0.8$ keV	<i>Autrata et al.</i> [5.50, 51]
	Robinson	Scintillator–LP–PM	High CE; $E_{\text{BSE}} \geq 0.9$ keV	<i>Robinson</i> [5.52]
	Solid state	Electron–hole pair generation	High CE; $E_{\text{BSE}} \geq 1.5$ keV; bandwidth about ≤ 2 MHz	<i>Stephen et al.</i> [5.53]
	MCP	Electron-multiplier tube	High CE; $E_{\text{BSE}} \geq 1$ keV; negatively biased front plate	<i>Postek and Keery</i> [5.49]
CL	Ellipsoidal or parabolic mirror with parallel or focused light output or coupled to an LP	Mirror–PM; mirror–spectrometer–PM; mirror–LP–PM	High CE; normally simultaneous BSE detection is not possible (for exceptions see <i>Autrata et al.</i> [5.50, 51])	<i>Autrata et al.</i> [5.50, 51]; <i>Bond et al.</i> [5.54]; <i>Rasul and Davidson</i> [5.55]; <i>Reimer</i> [5.38]

MCP: Microchannel plate; LP: light pipe; PM: photomultiplier; CE: collection efficiency; E_{BSE} : energy of backscattered electrons; SE: secondary electrons; BSE: backscattered electrons; CL: cathodoluminescence

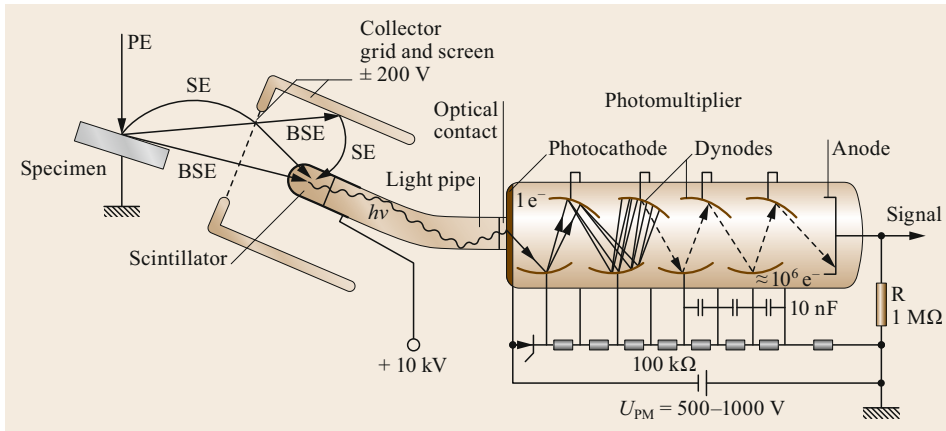


Fig. 5.5 Schematic drawing of Everhart–Thornley detector (scintillator–photomultiplier combination) for recording secondary electrons (SE). (BSE: backscattered electrons; PE: primary electrons; PM: photomultiplier; $h\nu$: energy of photons)

specimen. The BSE detector does not require the collector grid used for the SE (Fig. 5.5).

Semiconductor Detector. The semiconductor detector—often denoted as a solid-state detector—generates from an impinging electron with the energy E a mean number of electron–hole pairs given by

$$n_m = \frac{E}{E_{\text{exm}}}, \quad (5.14)$$

where $E_{\text{exm}} = 3.6 \text{ eV}$ is the mean energy per excitation in silicon [5.59]. The electron–hole pairs can be separated before recombination, in this way generating an external charge-collection current, which is proportional to the number of impinging electrons. Because of the energy dependence of n_m the BSE with higher energy contribute with a larger weight to the signal than the BSE having low energies. The semiconductor detector can be used only for the direct detection of BSE because impinging SE are absorbed in its thin electrical conductive layer. However, a special detector design for accelerating the SE to energies above 10 keV also allows for detection of SE [5.48].

Microchannel Plate Detector. A microchannel plate (MCP) consists of a large number of parallel very small electron-multiplier tubes (diameter about 10–20 μm , length of a few millimeters) covering an area of about 25 mm in diameter [5.49]. Thus this detector is thin and, when placed between objective pole piece and specimen, enlarges the work distance by only about 3.5 mm. The MCP detector system is efficient at both high and low accelerating voltages, and is capable of both secondary electron and backscattered electron detection. The MCP becomes of increasing interest for studies with low currents and in low-voltage scanning electron microscopy [5.60]. However, as yet the MCP detector

is not as common as the other detector types described above.

Cathodoluminescence Detectors. In the few cases of strongly luminescent specimens a lens or a concave mirror is sufficient for light collection [5.61]. As mentioned above, mostly the intensity of the CL signal is low, thus a high collection efficiency of the emitted light is indispensable. This requires a solid angle of collection as large as possible, an optimum transfer of the collected light to a monochromator or directly to the photomultiplier, and a photomultiplier with a high quantum efficiency in the spectral range of the CL [5.62]. Commercial CL collector and imaging systems allow for investigations with a wavelength from less than 200 to about 1800 nm in the imaging and spectroscopy mode. The following are the most commonly used collection systems:

1. *Parabolic or elliptic mirrors.* The light-emitting area of the specimen is located at the focus of the mirror and is formed into a parallel beam for a parabolic mirror [5.54] or focused to a slit of a spectrometer for an elliptic mirror [5.63]. The solid angle of collection is in the order of π sr but SE detection with an ET detector is still feasible.
2. *Rotational ellipsoidal mirror.* The light-emitting area of the specimen is located at one focus of the half of the ellipsoid of rotation [5.64]. The emitted light is focused to a light pipe or to the focal point of an optical microscope objective at the second focal point of the ellipsoid. Although the ellipsoidal mirror has the largest collection angle, the effective collection angle is limited by the acceptance angle of the light pipe or the optical microscope objective, respectively, to about 0.75π sr. The limitation by the acceptance angle can be avoided by placing a parabolic mirror below the second focal point of

the ellipsoid [5.65]. Very recently *Rau et al.* [5.66] proposed an ellipsoidal confocal system collecting the emitted light, which enables CL microtomography in SEM. In principle, the proposed system allows for CL studies at high resolution, which is well below the size of the light-emitting volume.

3. *Optical microscope objective.* The CL of an optically transparent specimen can be studied by an optical microscope objective positioned below the specimen. The collection angle of this setup amounts to about 1.4π sr [5.67].

Detection Strategies. Generally, the detectors for the various signals can be combined and each of them should have an optimum position to make the best use of the electron-specimen interaction. As a matter of fact, the space for detectors is limited in particular with a short WD or with an in-lens position of the specimen for higher resolution.

A conventional SEM commonly is equipped with an ET detector located laterally above the specimen and a BSE detector (for different types see Table 5.2) located centrally above the specimen (top position). Additional ports at the specimen chamber of the SEM enable additional detectors to be installed. Because of geometry limitations, not all of the installed detectors may be used simultaneously. However, there are retractable detectors (e. g., BSE detectors) available, which can be kept in the retracted position when not needed (providing space for another detector or allowing for a shorter WD) and can readily be moved into working position if required for signal recording. Numerous multidetector systems have been proposed for BSE and SE (for reviews see [5.38, 68]). In the top position, e. g., two semiannular semiconductor detectors [5.69, 70] allow for separation of topographic and material contrast; with a four-quadrant semiconductor detector [5.71–73] the surface profile can be reconstructed and the distinction between elements with different atomic numbers is improved. Even a six-segment semiconductor detector is of interest [5.74].

For high-resolution and LVSEM the working distance should be as short as possible (say below 5 mm) because both the focal length and the aberrations of the objective lens increase with the WD (see also Sects. 5.1.1, *Electron Lenses* and 5.2). In contrast to the asymmetric objective lens (large focal length) where the region above the specimen is a magnetic field free space, the specimen is immersed in the field of the objective lens with a short focal length. In this case the specimen is very close to the lower objective pole piece or is placed directly inside the pole-piece gap (as in a transmission electron microscope (TEM); see Chaps. 1–4). For the latter lens type—the specimen has

an *in-lens* position and is limited in size to a few millimeter only—the collection of SE takes advantage of the fact that they can spiral upward in the magnetic field of the objective lens because of their axial velocity component. The SE have to be deflected off the axis to be recorded by an ET detector located laterally above the lens (Fig. 5.6).

The separation of the downward-moving beam electrons and the upward-moving secondary electrons can be done most efficiently by an $E \times B$ system, which employs crossed electric and magnetic fields. The forces of these fields compensate each other for the beam electrons, but add for the opposite moving secondary electrons. This magnetic *through-the-lens* detection (for review see [5.75]) of SE has several advantages:

1. SE can be separated from BSE, which may not reach the detector because their higher kinetic energy causes different trajectories
2. Very high collection efficiency for real SE emerging from the specimen and a suppression of SE created on the walls of the system by BSE
3. Improved collection efficiency from inside a porous specimen (in particular cavities or holes facing the electron beam) [5.76]
4. Loss of directionality in the image because the SE are detected irrespective of the direction of emission (in contrast to the lateral position of the ET detector; Fig. 5.7a).

It seems worth mentioning that a real *through-the-lens* detection system was incorporated in one of the

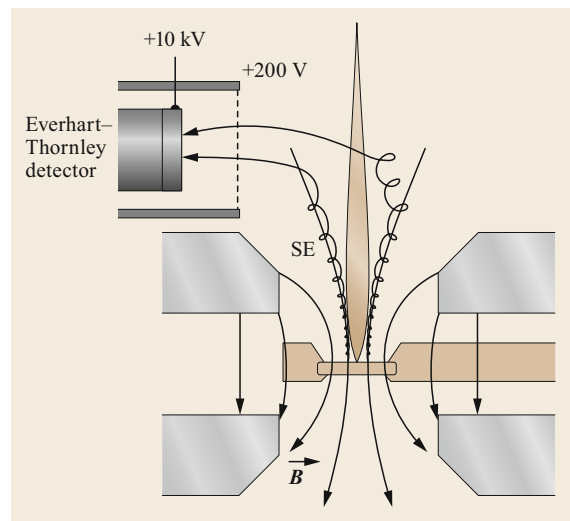


Fig. 5.6 Schematic drawing of the magnetic *through-the-lens* detection of secondary electrons (SE) for the *in-lens* position of the specimen. After [5.30]

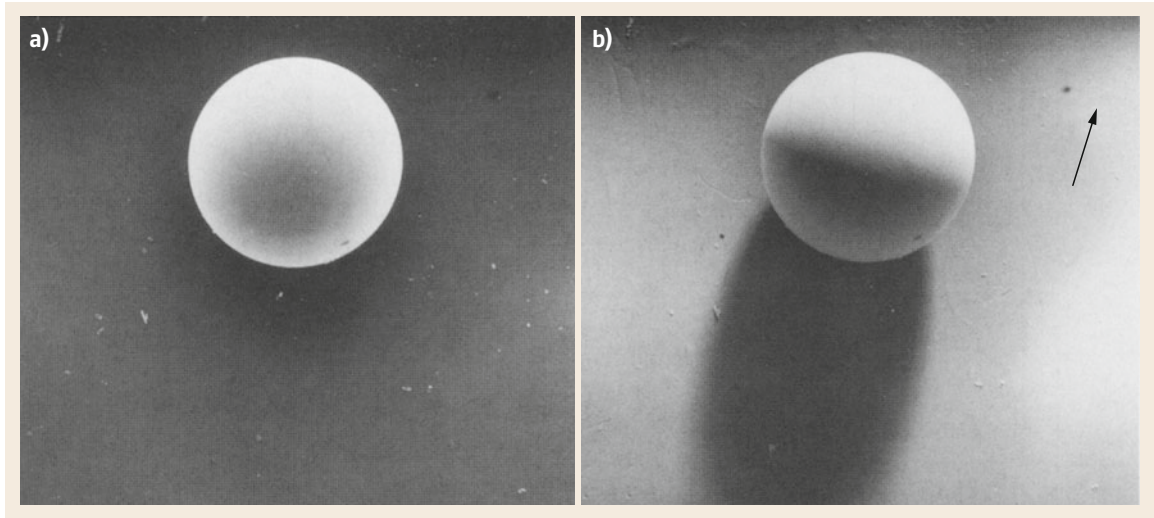


Fig. 5.7a,b Secondary (a) and backscattered electron (b) micrograph of a 1-mm steel ball. The arrow in (b) indicates the direction of the backscattered electron (negatively biased ETD) and the secondary electron detector

early SEMs [5.5]. The magnetic *through-the-lens* detection of SE was established by Koike et al. [5.77] using a TEM with scanning attachment.

Another type of *in-lens* detection of SE and BSE is used in the electrostatic detector objective lens [5.78–80]. The detector is of the annular type and possesses a high collection efficiency of SE of about 75%. Replacing the annular detector by a combination of two semiannular detectors A and B (Fig. 5.8) could be used to illustrate the topographic or material contrast, respectively [5.30]. Similarly, *in-lens* annular-type detection of SE and BSE is also used in combined or hybrid magnetic-electrostatic objective lenses [5.81]. Both types of lens are advantageous for low-voltage SEM (Sect. 5.2.2) because they provide excellent image resolution at low electron energies.

Specimen Stages and Attached Equipment

A conventional SEM is equipped with a specimen stage. The stage commonly can be loaded with the specimen via a specimen-exchange airlock chamber without breaking the high vacuum in the specimen chamber. The stage allows x, y, z movements, rotation around 360° , and tilting (the tilting range depends on the type of the stage, e.g., -15 to $+90^\circ$) of the specimen. The movements, rotation, and tilt are usually motorized in modern scanning electron microscopes. The specimen stage is eucentric if the observation point does not vary during tilting and rotation. However, some stages have this property only for tilting (semieucentric specimen stage) or do not have it (goniometric specimen stage). If the specimen stage is eucentric or semieucentric, the WD and therefore the magnification do not change dur-

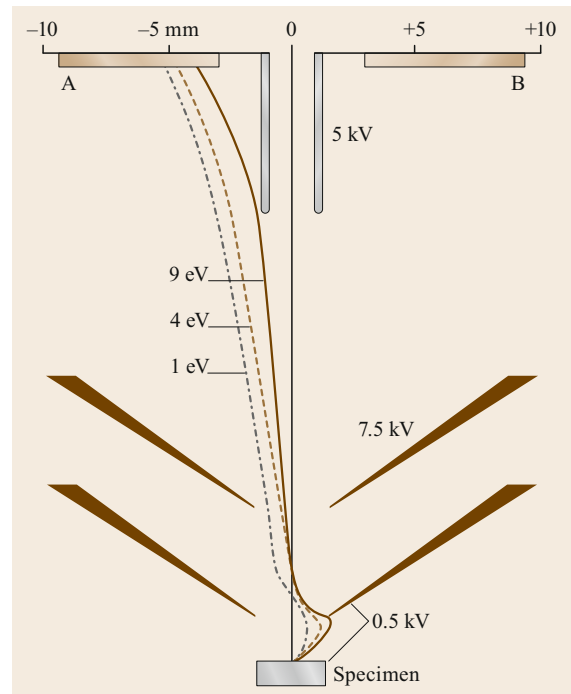


Fig. 5.8 Schematic drawing of the *in-lens* detection of secondary electrons (SE) with the electrostatic detector-objective lens

ing x, y movement or movement along the tilt axis, respectively. Usually, the specimen is at ground potential (0 V). However, the wiring allows also the recording of the specimen current or absorbed current, as well as application of specimen bias for charge neutralization

and improvement of resolution. It is obvious that the higher the electron optical performance of the SEM the better the quality of the specimen stage in terms of mechanical and thermal stability.

The manufacturers of SEMs as well as small companies supplying special attachments offer optionally specimen stages for specific investigations. For example, there are commercial hot stages available for in situ surface investigations at elevated temperatures. Depending on the type of heating device, it is possible to reach specimen temperatures up to about 1370 K with a maximum heating rate of about 200 K min^{-1} . A hot specimen stage in an environmental scanning electron microscope (Sect. 5.3) is, among other things, very useful in studying the surface modifications caused by chemical reactions due to the exposure of samples to gases. For specific in situ heating experiments, e. g., local heating with rapid thermal loads, irradiation heating by a high-power laser coupled to an SEM can be used [5.25, 82].

Mainly for investigations of organic materials and, in particular, of biological specimens, cold stages are of great interest for low-temperature studies. At low temperature the electron-beam damage of the sample due to electron-specimen interaction is smaller than at room temperature [5.83–87] and specimens can be investigated in the frozen-hydrated stage [5.88–90]. However, cold stages are also of significant interest for materials science to investigate the low-temperature behavior of materials such as changes in mechanical properties or variations in electrical conductivity. In most cases liquid nitrogen or liquid helium is used as the cooling medium. In particular the temperature range around 4 K and below down to about 1.5 K allows for the investigation of typical low-temperature phenomena such as superconductivity and low-temperature devices used in cryoelectronics. Furthermore, experiments can be performed in which the temperature range of liquid He is required by the measuring principle, e. g., the ballistic phonon signal represents an example. Here the small specimen volume locally heated by the electron beam acts as a source of phonons, which propagate ballistically (i. e., without scattering) to the opposite side of the crystal where the photon detector is located. Both, the specimen and the detector have to be kept in the temperature range of liquid He. The SEM at very low temperatures was reviewed by *Huebener* [5.91].

The Peltier cryo stage is also typically used in conjunction with VP/ESEM—the specimen needs to be cooled down below room temperature to maintain a solid(ice)/vapor (ice sublimation) environment at a reasonable pressure (for example at 0°C and $> 533 \text{ Pa}$ there is still liquid water).

Further, deformation stages are used in materials science to study static and dynamic specimen deformation-related phenomena in situ [5.25]. In more detail, different types of sample deformation such as tension and compression, unidirectional bending, bending fatigue, materials machining (e. g., study of the microscopic mechanisms of abrasive wear), and microhardness testing can be performed with a microhardness tester mounted on the stages in the SEM specimen chamber. This allows for very precise positioning of the indentations generated with a very low force and their subsequent viewing/measuring. In combination with a surface displacement transducer for the detection of acoustic emission signals, the quantitative acoustic emission due to crack coalescence can be measured [5.92]. There are also stages in different laboratories that combine, e. g., deformation and heating capabilities.

With high-precision stages based on laser interferometer technology, a new field of applications is opened up in the area of SEM/FIB-based e-beam lithography, metrology, and semiconductor failure analysis. The fine positioning of the stage is made with piezoelements, which, according to the manufacturer's specification, allow a positioning reproducibility of better than 50 nm.

To obtain ultralow-magnification SEM images an SEM equipped with a motor drive specimen stage fully controlled with a personal computer (PC) has been utilized [5.93]. This motor drive stage works as a mechanical scanning device. To produce ultralow-magnification SEM images, a combination of the mechanical scanning, electronic scanning, and digital image processing techniques is used. This is a time-saving method for ultralow magnification and wide-area observation.

The stage in the SEM specimen chamber can integrate not only tools such as a microhardness tester but also other types of high-resolution microscopes, e. g., a scanning tunneling [5.94–96], scanning force [5.97], or scanning near-field optical microscope [5.98], thus combining two different microscopic techniques with their specific advantages in one hybrid microscope.

As mentioned in the previous section, the specimen for *in-lens* SEMs must be small because it has to be placed in the gap of the objective lens. This requires specimen stages and holders almost identical to the ones used in TEM (side-entry sample exchange system). The specimen is mounted in a specimen holder, which commonly allows for tilting the specimen around one axis by $\pm 30^\circ$ or $\pm 40^\circ$. Optionally, there are, for example, double-tilt specimen holders with two tilt axes as well as hot and cold/cryoholders available. The specimen holders also normally allow the use of support grids 3 mm in diameter, which is of interest for studies in transmission mode.

Special Topics

Digital Image Recording. Modern SEMs allow recording of multichannel (e. g., SE and BSE) digital images, which are stored pixel by pixel (pixel: picture element) in a PC. Digital images usually have a square size of 512×512 , 1024×1024 pixels or larger [5.99]. However, rectangular image formats are also in use, e. g., 3000×2000 pixels. For each pixel the analog signal arriving from the detector is integrated during the pixel time. The value obtained represents the pixel intensity, which is digitized by an analog-to-digital-converter (ADC) usually into a range of 8 or 16 bit. In practice, a sufficient lateral and signal resolution can be obtained with 1024×1024 pixels and 8 bit, respectively, which requires a storage capacity over 10^7 bit, i. e., 1 MB. Twice the number of pixels in the x - and y -direction requires a 4-fold storage capacity, i. e., 4 MB. For final storage, the digital images can be transferred from the PC via fast data transfer to external mass storage devices or cloud computers.

Specimen Tilting and Stereo Imaging. Specimen stages allow the sample to be tilted, which is of interest for several special applications such as stereo imaging, reconstruction of the topography, three-dimensional (3-D) morphometry, and possibly contrast enhancement. In the case of a flat object aligned normal to the beam, i. e., the tilt angle Θ amounts to 0° , there is no distortion of the projected shape of structures. For example, circular holes in a flat specimen appear circular in the image (Fig. 5.9a). After tilting the flat object (the tilt axis has a horizontal direction in the micrograph) two effects become obvious in the image (especially visible at high tilt angles, e. g., $\Theta = 45^\circ$) (Fig. 5.9b): (1) the circular holes have an elliptic shape with an axis ratio of approximately 0.7, i. e., the shape is distorted, and (2) the upper and lower rim of the upper and lower hole appears unsharp whereas the rim of the central hole appears sharp.

The first effect is caused by the fact that because of the tilt the scanned range on the specimen surface perpendicular to the tilt axis is enlarged by a factor $1/(\cos \Theta)$ (Fig. 5.9e). That corresponds to a reduced magnification

$$M' = M \cos \Theta \quad (5.15)$$

in the direction of the short axis whereas along the tilt axis the magnification M is not affected. The effect can be fully compensated by enlarging the reduced magnification by $1/(\cos \Theta)$, which restores the magnification M (Fig. 5.9c,e). The tilt compensation can be performed directly by electronic means (hardware, the

unit is called *tilt compensation*) during scanning or posterior by digital image processing on condition that the directions of the tilt axis and the tilt angle are known.

The second effect is caused by the fact that because of the tilt the height range of the tilted specimen extends the depth of focus, thus the image is not sharp in regions outside the depth of focus. This effect can be compensated by *dynamic focusing* [5.100], i. e., by adjusting the strength of the objective lens as a function of the scan position perpendicular to the tilt axis. This adjustment brings the optimum focus position in coincidence with the surface at all working distances in the scanned range (Fig. 5.9d and e). Both effects mentioned can be compensated completely only for planar specimens and a known tilt angle.

The SEM forms in imaging mode a two-dimensional (2-D) image of a three-dimensional specimen with each of the signals generated by electron-specimen interaction (Fig. 5.2). Although these images contain a wealth of information about the specimen, there is no solid information about the third dimension, which is parallel to the optical axis. Stereo imaging is one possibility to obtain information about the third dimension. It takes advantage of the fact that depth perception is obtained when viewing an object from two separate directions. In an SEM stereo imaging is performed by taking two images—the stereo pair—at two different tilt angles of the specimen. A good stereo effect is obtained when the angles differ from each other by about 6° . A significantly larger difference in Θ overemphasizes the stereo effect whereas a smaller difference in Θ shows a softened stereo effect. Usually, a stereo pair is viewed through a stereo viewer. A simple version of a stereo viewer consists of two short focal lenses on a stand at the correct distance from the stereo pair. There are more sophisticated versions with lens-mirror combinations, which allow for a larger field of view. For each type of viewer it is mandatory to place and to align both images precisely to obtain correct depth perception. Figure 5.10 shows a stereo pair of SEM micrographs.

A further method for viewing the stereo images is the anaglyph technique [5.101], which can now readily be performed by PC (Fig. 5.56). In this technique both images are superimposed in different colors. A red-green stereo anaglyph coding can be obtained readily by freeware, e. g., ImageJ (NIH); or commercially available software, e. g., MountainMaps (Digital Surf, France). This allows for a quick and simple qualitative assessment. The mixed colored image has to be viewed by colored glasses. However, the stereo pair can also be used to calculate the height difference Δh between two image points 1 and 2 by measuring the

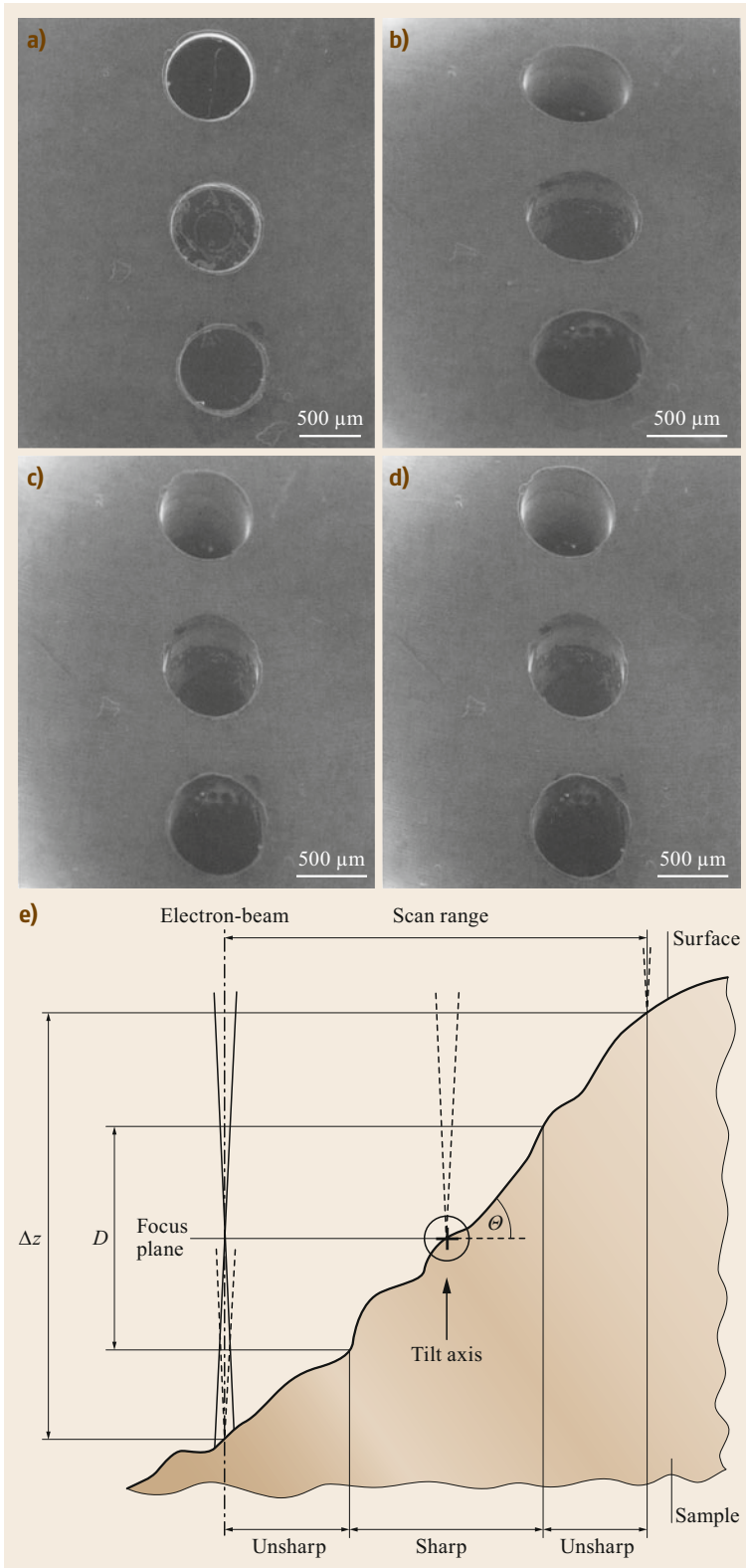


Fig. 5.9a–e Effect of tilt compensation and dynamic focusing in the SEM. Secondary electron micrographs of the holes in a flat aluminum specimen. **(a)** Tilt angle $\theta = 0^\circ$. **(b)** Tilting $\theta = 45^\circ$ around the horizontal axis (the focus of the beam is located in the center of the micrograph). **(c)** Tilt compensation is ON. **(d)** Tilt compensation and dynamic focusing are ON. The visible wall of the bore of the holes proves that the specimen is still tilted. **(e)** Schematic illustration of the effects caused by tilting the sample. The position of the optimum focus plane, the depth of focus D , and the height range Δz ($\Delta z > D$) are shown for a constant focus of the beam (solid lines). In that case, only a central region along the tilt axis is within the depth of focus (i. e., sharp image) whereas the lower and the upper range are outside D (unsharp region of the image). In the case of the dynamic focus, three positions of the beam (dashed lines) are drawn indicating that the whole scan range will be in focus, thus being imaged sharply

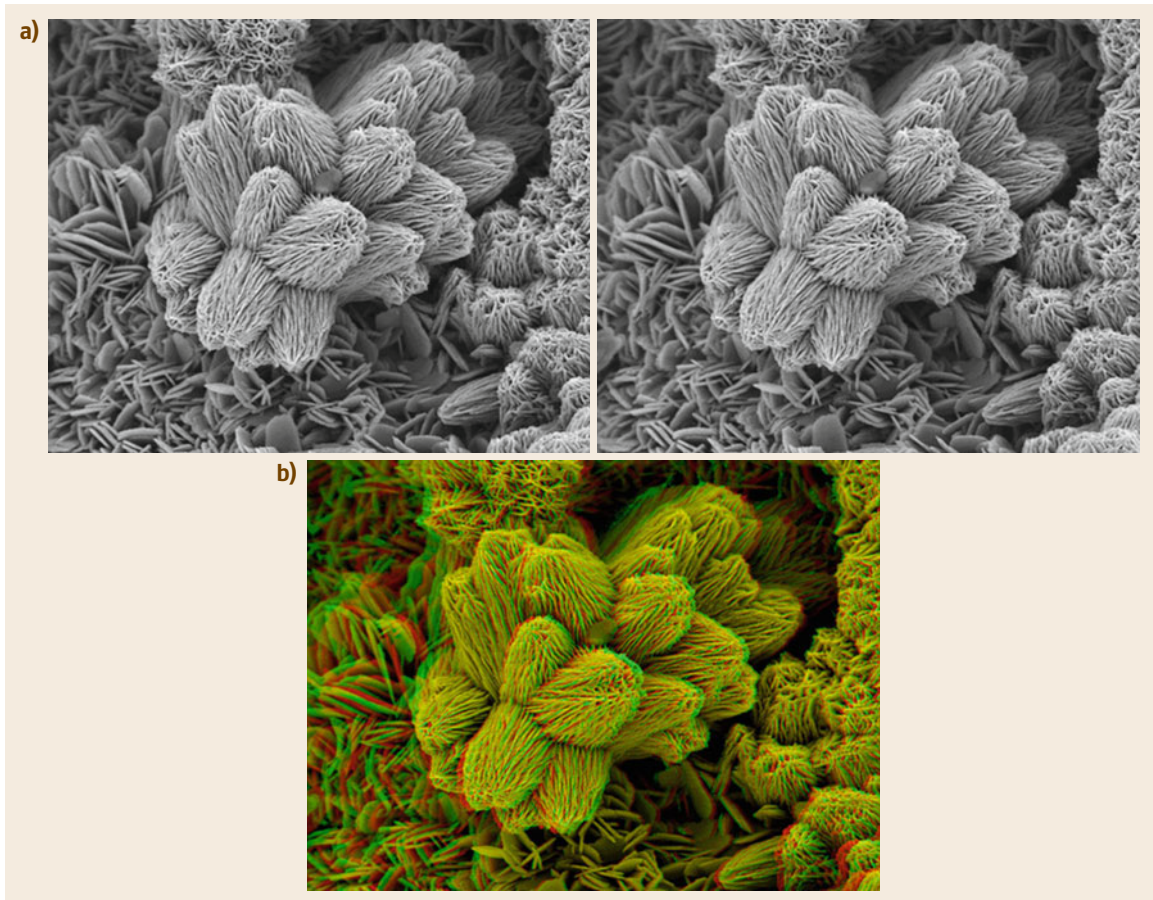


Fig. 5.10a,b Stereopair of rust (Fe_2O_3) crystals imaged at 5 kV (a) and (b) the resulting stereo (green/red) combined image. The difference in the tilt angles of the micrographs is 6°

parallax p_x given as

$$p_x = (x_2^l - x_1^l) - (x_2^r - x_1^r) \quad (5.16)$$

and

$$\Delta h = \frac{p_x}{2M \sin(\Theta_r - \Theta_l)}, \quad (5.17)$$

where $(x_2^l - x_1^l)$ corresponds to the distance between the two points in the left and $(x_2^r - x_1^r)$ to the distance between the two points in the right image. Θ_r and Θ_l correspond to the tilt angle of the specimen used for the right and left image, respectively. Equation (5.17) holds for magnifications $M > 100$, i. e., in case of parallel projection. The successful application of the latter two formulas requires (1) distinct surface structures to measure p_x with sufficient accuracy, and (2) the magnification and the tilt angle must be known exactly. On the basis of the relations (5.16) and (5.17) and data analysis

software quantitative dimensional and angular measurements, the reconstruction of the specimen topography and three-dimensional morphometry can be achieved. The latter is very useful to analyze microstructures such as blood capillaries, which have diameters in the range of a few micrometers [5.102–104]. Using the image pair imported for anaglyph generation, a point of reference has to be selected in one of the images that would also be clearly visible in the second image. The software uses this reference point to define a small region and then uses correlation to accurately align the images. Once aligned, the parallax difference allowed generation of a new 8 bit grayscale image in which depth differences are encoded as different gray values. Quantitative measurements, e. g., the volume of depressions, can be performed using the same piece of software.

Magnification Calibration. The actual magnification of the SEM is indicated numerically and by a scale bar on the monitor with a precision of about $\pm 2\%$.

However, if exact measurements have to be made (Sect. 5.1.1, *Specimen Tilting and Stereo Imaging*), the magnification should be verified using an external standard. Calibrated gratings with known spacings are commercially available from different suppliers of electron microscopy accessories (e.g., Agar Scientific, <http://www.agarscientific.com>). For a magnification range up to about $100\,000\times$ crossed gratings with spacings of 1200 and 2160 lines per mm (Fig. 5.11) are recommended.

Latex spheres of defined diameter (different diameters in the range from about 0.1 to $1\mu\text{m}$ are commercially available) can also be used. However, the size of the latex spheres varies to some extent (e.g., small diameter, $0.112\mu\text{m}$; standard deviation, $10^{-3}\mu\text{m}$; large diameter, $1.036\mu\text{m}$; standard deviation, $16.1\times 10^{-3}\mu\text{m}$). Moreover, the latex spheres are sensitive to electron radiation, thus their size may change caused by electron dose-induced damages. To calibrate the magnification range above $100\,000\times$ negatively stained catalase (periodic lattice spacings: 8.75 and 6.85 nm) can be used as standard (preferentially in the STEM mode).

5.1.2 Electron–Specimen Interaction and Signal Generation

As the beam electrons enter the specimen, they interact with the atoms of the specimen. This interaction either results in elastic or inelastic scattering of the impinging electrons.

The elastic scattering of the electron is caused by its interaction with the electrical field of the positively charged nucleus and results only in a deflection of the beam electron, i.e., after the scattering event the electron trajectory has a different direction than before scattering. There is almost no loss of kinetic energy of the electron scattered elastically. For scanning electron microscopy it is necessary to know the elastic electron scattering through large angles between 0 and 180° . The scattering can be described quantitatively by the scattering cross section σ . The exact elastic scattering cross sections for large-angle scattering are the Mott cross sections $\sigma_{\text{M,el}}$, which, in contrast to Rutherford scattering, consider the electron spin and spin-orbit coupling during scattering (for details see [5.38, 105, 106]). The easy to calculate unscreened differential Rutherford cross section $d\sigma_{\text{R,el}}/d\Omega$ are given as [5.38]

$$\frac{d\sigma_{\text{R,el}}}{d\Omega} = \frac{e^4 Z^2}{[4(4\pi\epsilon_0)^2 m^2 v^4 \sin^4(\frac{\varphi}{2})]}, \quad (5.18)$$

where $d\Omega$ is the cone of the solid angle, e is the electric charge ($e = 1.602 \times 10^{-19} \text{ C}$) and m the mass of the electron, v is the velocity of the electron, Z is the atomic number, ϵ_0 is the dielectric constant ($\epsilon_0 = 8.85 \times 10^{-12} \text{ C V}^{-1} \text{ m}^{-1}$), and φ is the scattering angle. The comparison of the differential Mott cross sections $d\sigma_{\text{M,el}}/d\Omega$ [5.107] with the unscreened differential Rutherford cross sections $d\sigma_{\text{R,el}}/d\Omega$ for electron energies between 1 and 100 keV shows that there are strong deviations of the Rutherford cross section, particularly

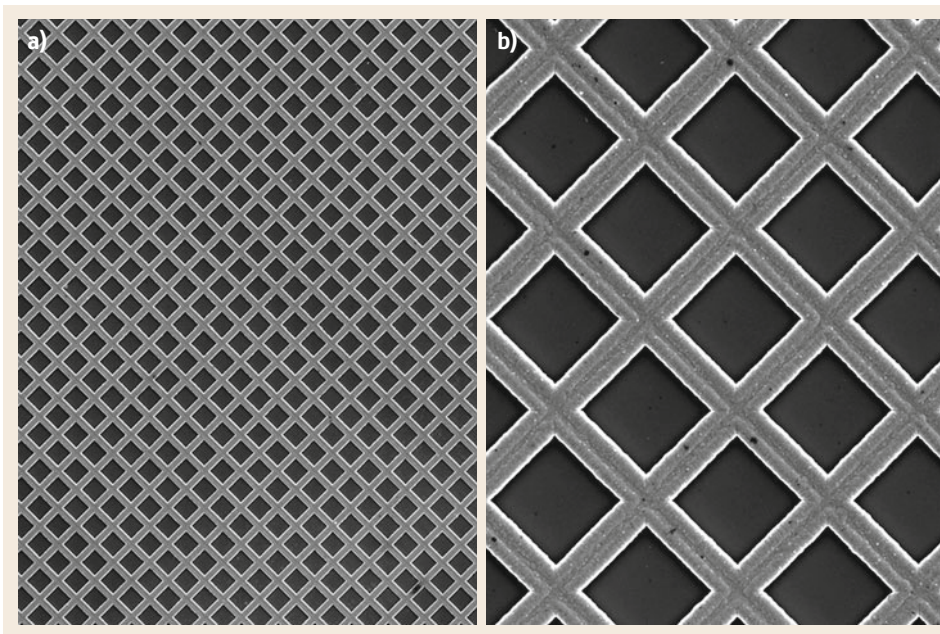


Fig. 5.11a,b SE micrograph of a standard TEM mesh grid at low (a) and medium (b) magnification at 15 kV

for high Z . Mott cross sections for electron energies below 1 keV (energy range 20 eV to 20 keV) were calculated by *Czyżewski et al.* [5.108] (see also <http://web.utk.edu/~srcutk/Mott/mott.htm>). There is very reasonable agreement between both cross sections for low atomic numbers and electron energies above 5 keV. However, for low Z and energies below 5 keV, the Rutherford cross sections are larger than the Mott cross sections for scattering angles below 70–80° and are smaller than the Mott cross sections for scattering angles above 70–80°. The probability for elastic scattering is approximately proportional to Z^2 and inversely proportional to E^2 (with $E = mv^2/2$), i. e., the scattering cross section strongly increases with the atomic number and decreases for increasing electron energy E . The total elastic scattering cross section σ_{el} can be obtained by integration

$$\sigma_{el} = 2\pi \int_0^\pi \left(\frac{d\sigma_{el}}{d\Omega} \right) \sin \varphi d\varphi. \quad (5.19)$$

σ_{el} can be used to calculate the mean free path for elastic scattering Λ_{el} , i. e., the free path between two consecutive elastic scattering events in a specimen consisting of many atoms, which is given as

$$\Lambda_{el} = \frac{1}{N\sigma_{el}}. \quad (5.20)$$

N represents the number of atoms per unit volume and can be calculated simply by

$$N = \frac{N_A \rho}{A}, \quad (5.21)$$

where ρ is the density, N_A is Avogadro's number ($N_A = 6.0221 \times 10^{23} \text{ mol}^{-1}$), and A is the atomic weight (g mol^{-1}). Much more detailed data of elastic electron-scattering cross sections were recently published [5.109].

As we shall see later, the mean free path is an important quantity for describing plural (mean number of collisions < 25) and multiple electron scattering (mean number of collisions $> 25 \pm 5$).

The inelastic scattering of the electron is caused by its interaction with the electrical field of the electrons in the solid, i. e., either with the electrons in the valence or conduction band and with atomic electrons of inner shells, respectively. After an inelastic scattering event the electron trajectory has a slightly different direction than before scattering (typically the inelastic scattering angles are of the order of a few milliradians only) and less kinetic energy. If the lost energy was transferred to electrons in the valence or conduction band

then the excitation of plasmons (a plasmon is a longitudinal charge-density wave of the valence or conduction electrons) or inter- and intraband transitions may occur. Both the energy of plasmons and the energy differences of inter- and intraband transitions are in the order of about 5–50 eV. The physics of the latter processes is reviewed by *Raether* [5.110]. If the lost energy was transferred to atomic electrons of inner shells then, for example, K-, L-, or M-shell ionization may occur. In this case the energy loss typically is higher than 50 eV. The differential inelastic electron-scattering cross section with a free electron (which is an approximation for an electron in the valence or conduction band) is given [5.38] as

$$\frac{d\sigma_{in}}{dW} = \frac{\pi e^4}{[(4\pi\epsilon_0)^2 E W^2]}, \quad (5.22)$$

where W is the energy loss. The equation shows that the differential inelastic scattering cross section is inversely proportional to electron energy E and to W^2 and that small energy losses occur with a larger probability. In a more complex approach for the differential inelastic scattering cross section the energy loss function $\Im m(-1/\epsilon)$ is used taking the dielectric properties of the material into account [5.111]. An impinging electron can be inelastically scattered passing the atom even in a distance of a few nanometers, thus the inelastic scattering is delocalized to a certain extent [5.112–116].

In the case of inner shell excitation the electron interaction is localized to an electron shell. The corresponding inelastic scattering, also called ionization cross section, is the probability of bringing a scattering atom to a given excited state through an inelastic process. The related cross sections are typically at least two orders of magnitude smaller than those for the electrons in the valence or conduction band. Calculations of the ionization cross sections of the K-, L-, and M-shell have been published [5.117–119].

The total inelastic scattering cross section σ_{in} can be obtained by integration

$$\sigma_{in} = 2\pi \int_0^\pi \left(\frac{d\sigma_{in}}{d\Omega} \right) \sin \varphi d\varphi. \quad (5.23)$$

The mean free path for inelastic scattering Λ_{in} is given analogous to (5.20) as

$$\Lambda_{in} = \frac{1}{N\sigma_{in}} \quad (5.24)$$

(for detailed data and calculation of the electron inelastic mean free path see *Powell and Jablonski* [5.120]).

The total scattering cross section then is given as

$$\sigma = \sigma_{\text{el}} + \sigma_{\text{in}}. \quad (5.25)$$

In bulk specimens multiple scattering of the impinging electrons takes place. Mainly the multiple elastic scattering causes a successive broadening of their angular distribution and can, after numerous scattering events, result in beam electrons leaving the specimen. The beam electrons, which leave the specimen, are designated as backscattered electrons and carry an important class of information about the local specimen volume through which they have been passing. Multiple inelastic scattering along the electron trajectories results in a slowing down and the beam electron can come to a standstill if it cannot leave the specimen as BSE. The majority of beam electrons are scattered both elastically as well as inelastically. Therefore, the majority of BSE have energies smaller than E_0 (Fig. 5.12). The broadening of the angular distribution can be calculated analytically using the autoconvolution of the single scattering distribution expanded in terms of Legendre polynomials [5.121].

Another method to treat multiple scattering is the simulation of the successive scattering events by Monte Carlo calculations for about 10^3 – 10^5 electron trajectories (Fig. 5.13; for Monte Carlo simulations of electron scattering see [5.105, 122–129]).

In this method, the most important scattering parameters, such as scattering angle, mean free electron path, and energy loss, are simulated for each individual scattering event along the trajectory by a computer using random numbers and probability functions of the scattering parameters. The energy loss along the trajectory (in units of eV cm^{-1}) can be described by the *Bethe* continuous-slowning-down approximation [5.130]

$$\frac{dE}{ds} = -7.8 \times 10^{10} \left(\frac{Z\rho}{AE} \right) \ln \left(1.166 \frac{E}{J} \right), \quad (5.26)$$

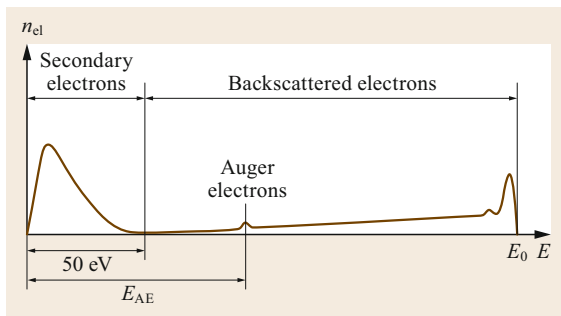


Fig. 5.12 Schematic energy distribution of electrons emitted n_{el} from a surface as a result of its bombardment with fast electrons with energy E_0

where ρ is the density (g cm^{-3}), E the electron energy (eV), and J the mean ionization potential in eV [5.131] given by

$$J = 9.76Z + 58.8Z^{-0.19}. \quad (5.27)$$

The limitations of the Bethe expression at low electron energy can be overcome by using an energy-dependent value J^* for the mean ionization potential [5.132]

$$J^* = \frac{J}{\left(\frac{1+kJ}{E} \right)} \quad (5.28)$$

where k varies between 0.77 (carbon) and 0.85 (gold). The total traveling distance of a beam electron in the specimen—the Bethe range R_B —can be obtained by integration over the energy range from E_0 to a small threshold energy and extrapolation to $E = 0$.

The practical electron range R (Fig. 5.14) obtained by fitting experimental data of specimens with different Z over a wide energy range is given by the power law

$$R = aE_0^n, \quad (5.29)$$

where n is in the range of about 1.3–1.7 and the parameter a depends on the material [5.38]. Characteristic values for R , σ_{el} , σ_{in} , Λ_{el} , and I_{in} are shown in Table 5.3. It shows that independent of the electron energy the electron range for carbon is about one order of magnitude larger than for gold. The decrease of the electron energy from 30 to 1 keV, i. e., a factor of 30, reduces the electron range by a significantly higher factor of roughly 300.

The mean free path lengths indicate after which traveling distance on average elastic and inelastic collisions will occur. For example, in a thin organic specimen having a thickness of 50–100 nm only a few collisions on average will take place with 30 keV electrons but about seven times more with 5 keV electrons. Specimens, which have thicknesses of about $t \leq 10[\Lambda_{\text{el}}\Lambda_{\text{in}}/(\Lambda_{\text{el}} + \Lambda_{\text{in}})]$ can also be imaged in the transmission mode (Figs. 5.1 and 5.2) using unscattered, elastically or inelastically scattered electrons, respectively. The angular and energy distribution of the scattered electrons can be calculated by Monte Carlo simulations if the elemental composition and the density of the specimen are known [5.133, 134].

The inelastic electron-scattering events in the specimen cause secondary electrons, Auger electrons, cathodoluminescence, and x-rays, which carry a wealth of local information about the topography, the electronic structure, and the composition of the specimen. The signals, resulting from inelastic electron scattering, can also be calculated by Monte Carlo simulations.

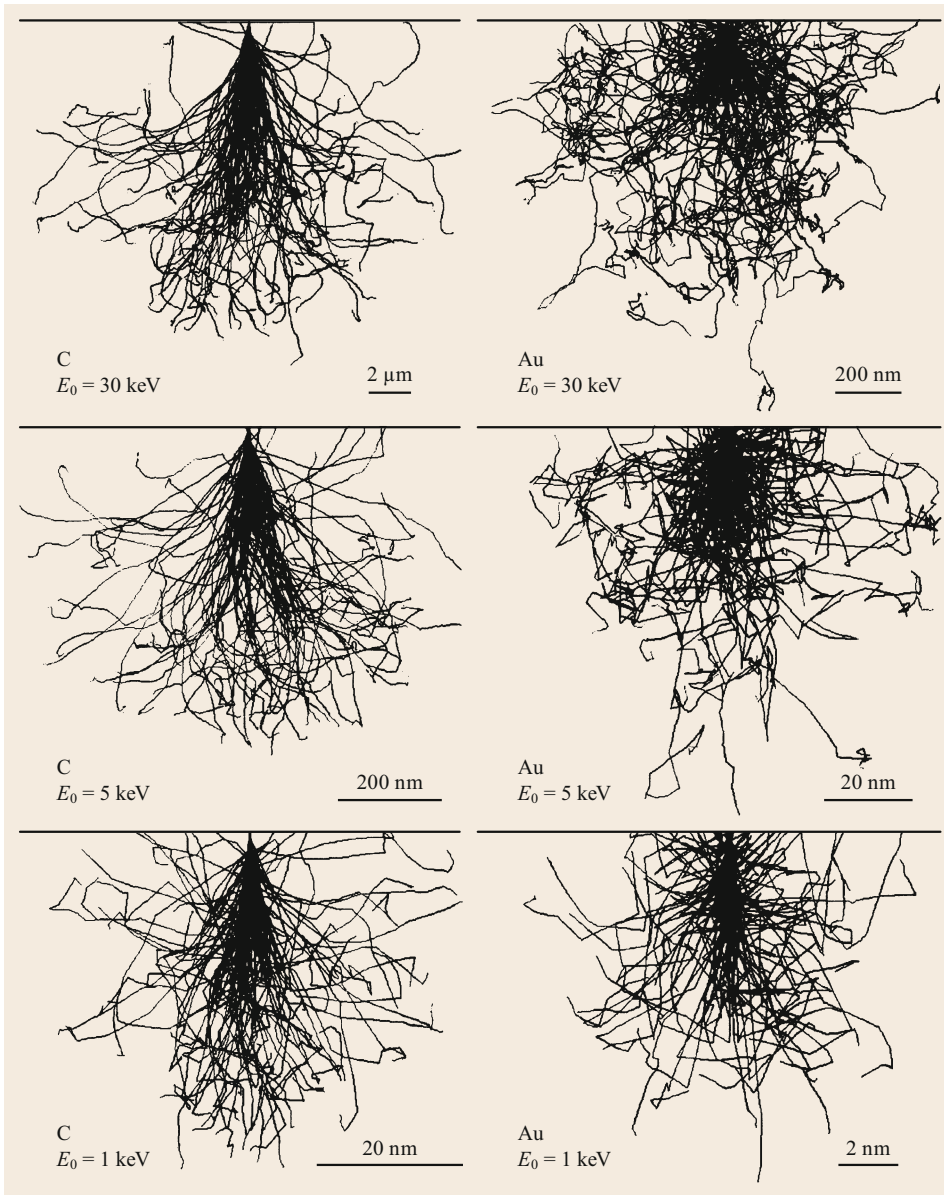


Fig. 5.13 Monte Carlo simulation of the trajectories of 100 electrons for carbon (atomic number $Z = 6$) and gold ($Z = 79$) for electron energies $E_0 = 30, 5,$ and 1 keV. For simulation of the electron trajectories the Monte Carlo program MOCASIM [5.126] was used. Note the different scales across three orders of magnitude indicated by bars and the variation of the shape of the local volume where electron scattering takes place. That local volume is usually denominated as the excitation volume

Secondary Electrons

The energy spectrum of the electrons emitted from a specimen irradiated with fast electrons consists of secondary electrons, backscattered electrons, and Auger electrons (Fig. 5.12). The SE show a peak at low energies with a most probable energy of 2–5 eV. By definition the maximum energy of SE amounts to 50 eV. Secondary electrons are generated by inelastic scattering of the beam electrons along their trajectories within the specimen (Fig. 5.14). The physics of secondary electron emission is reviewed by *Kollath* [5.135] and *Dekker* [5.136] but is beyond the scope of this chap-

ter. Because of the low energy of the SE only those SE are observable that are generated within the escape depth from the surface. The actual escape depth of SE for pure elements varies with their atomic number [5.137]. A general rule for their escape depth is $t_{SE} = 5\Lambda_{SE}$ [5.138], where Λ_{SE} is the mean free path of the SE. t_{SE} amounts to about 5 nm for metals and up to about 75 nm for insulators [5.139]. The angular distribution of SE follows Lambert's law, i. e., is a $\cos \zeta$ distribution, where ζ represents the SE emission angle relative to the surface normal [5.140, 141]. The angular distribution of the SE is not important for

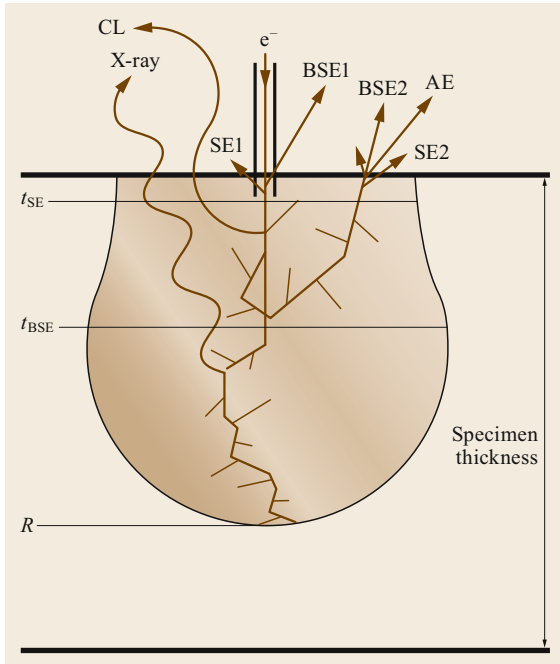


Fig. 5.14 Schematic illustration of the generation of secondary electrons SE1 and SE2, backscattered electrons BSE1 and BSE2, Auger electrons: AE, cathodoluminescence CL, and x-rays in a bulky specimen. t_{SE} and t_{BSE} indicate the escape depth for SE and BSE, respectively. R is the electron range

the image contrast in SEM because the extraction field of the ET detector normally collects the emitted SE. The situation, however, is different in case of magnetic

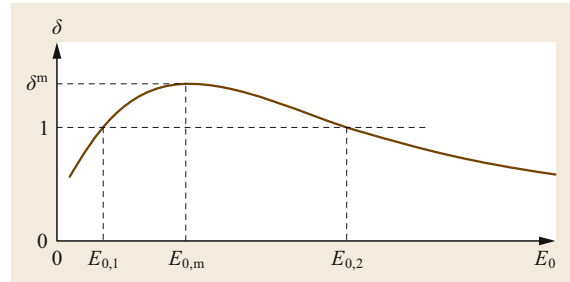


Fig. 5.15 Schematic representation of the SE yield δ versus the energy E_0 of beam electrons

through-the-lens detection where no electric extraction field is applied (Fig. 5.6).

Figure 5.15 shows schematically the SE yield δ versus the energy of the beam electrons, which is the number of SE produced by one beam electron. δ increases with E_0 , reaches its maximum δ^m at $E_{0,m}$, and then decreases with further increasing E_0 . Typical values for metals are $0.35 \leq \delta^m \leq 1.6$ and $100 \text{ eV} \leq E_{0,m} \leq 800 \text{ eV}$ and for insulators $1.0 \leq \delta^m \leq 10$ and $300 \text{ eV} \leq E_{0,m} \leq 2000 \text{ eV}$ [5.139]. For $E_0 \gg E_{0,m}$, δ is proportional to $E_0^{-0.8}$ [5.142], which indicates that δ is significantly smaller at 30 than at 5 keV. Both parameters, δ^m at $E_{0,m}$ depend on the ionization energy of the surface atoms [5.143]. Figure 5.16 shows the SE yield δ versus the energy E_0 for the element copper.

There is no monotonic relation between δ and the atomic number as shown in Fig. 5.17. However, published data of δ scatter which indicates that the specimen surface conditions and the quality of the vacuum can significantly affect the secondary yield [5.145].

Table 5.3 Characteristic values for R , σ_{el} , σ_{in} , A_{el} , and A_{in}

Element	Parameter	$E_0 = 1 \text{ keV}$	$E_0 = 5 \text{ keV}$	$E_0 = 10 \text{ keV}$	$E_0 = 30 \text{ keV}$
Carbon $Z = 6$	$\sigma_{el} (\text{nm}^2) \times 10^2$	0.65	0.11	0.055	0.018
	$\sigma_{in} (\text{nm}^2) \times 10^2$	1.95	0.33	0.165	0.054
	$A_{el} (\text{nm})$	1.5	9.0	18	55
	$A_{in} (\text{nm})$	0.5	3.0	6	18
	$R (\mu\text{m})$	0.033	0.49	1.55	9.7
	Copper $Z = 29$	$\sigma_{el} (\text{nm}^2) \times 10^2$	1.84	0.64	0.37
$\sigma_{in} (\text{nm}^2) \times 10^2$		1.10	0.38	0.22	0.09
$A_{el} (\text{nm})$		0.64	1.8	3.2	7.8
$A_{in} (\text{nm})$		1.07	3.0	5.3	13
$R (\mu\text{m})$		0.007	0.11	0.35	2.26
Gold $Z = 79$		$\sigma_{el} (\text{nm}^2) \times 10^2$	3.93	1.6	1.05
	$\sigma_{in} (\text{nm}^2) \times 10^2$	0.79	0.32	0.21	0.10
	$A_{el} (\text{nm})$	0.43	1.0	1.6	3.3
	$A_{in} (\text{nm})$	2.15	5.0	8.0	16.5
	$R (\mu\text{m})$	0.003	0.05	0.17	1.0

Values are listed for four different electron energies between 1 and 30 keV and three elements having a low (C), medium (Cu), and high atomic number (Au), respectively. For calculation, the following densities were used: C, $\rho = 2 \text{ g cm}^{-3}$; Cu, $\rho = 8.9 \text{ g cm}^{-3}$; Au, $\rho = 19.3 \text{ g cm}^{-3}$

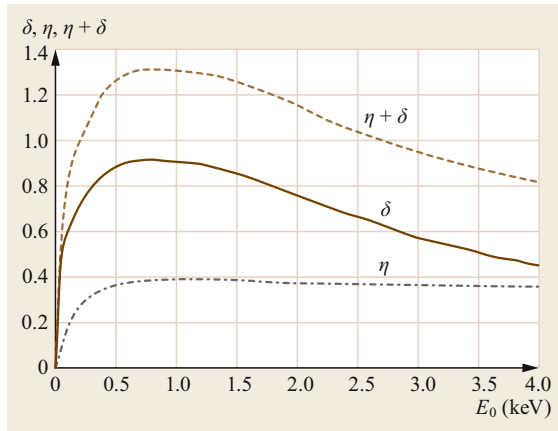


Fig. 5.16 SE yield δ , BSE yield η , and $\delta + \eta$ versus the energy E_0 for polycrystalline copper at $\theta = 0^\circ$. (Data from [5.144])

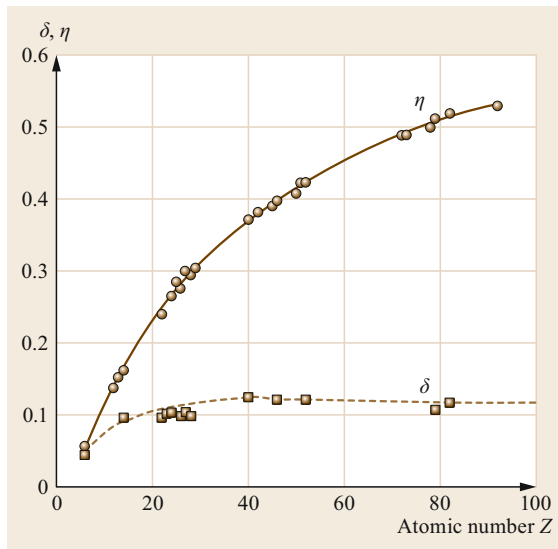


Fig. 5.17 SE yield δ and BSE yield η versus atomic number Z at $E_0 = 30$ keV and $\theta = 0^\circ$. (Data from [5.146, 147])

Secondary electrons generated by the incident beam electrons are designated SE1 [5.142]. The SE1 carry local information about the small cylindrical volume that is given approximately by the cross section of the beam $(\pi/4)d_{pe}^2$ and the escape depth t_{SE} . For a beam diameter about ≤ 1 nm the SE1 deliver high-resolution information. Those beam electrons, which are multiply scattered and emerge from the specimen as BSE, also generate secondary electrons within the escape depth. These secondary electrons are designated SE2 [5.142]. Their origin is far from the point of incidence of the beam caused by the spatial distribution of BSE. Changes of the amount of SE2 correlate with corre-

sponding changes of BSE, thus SE2 carry information about the volume from which the BSE originate. The size of the volume depends on the electron range R and is much larger than the excitation volume of the SE1 for electron energies $E_0 > 1$ keV (Fig. 5.14 and Table 5.3); thus SE2 deliver low-resolution information. The SE yield δ consists of the contributions of SE1 and SE2 given as

$$\delta = \delta_{SE1} + \eta\delta_{SE2}, \quad (5.30)$$

where η is the BSE coefficient and δ_{SE2} the SE2 yield, i. e., the number of SE2 generated per BSE. For $E_{0,m} < E_0 < 5$ keV the ratio $\delta_{SE2}/\delta_{SE1}$ amounts to about 4 and for $E_0 \geq 10$ keV about 2 [5.138]. For an increasing angle of incidence θ , this ratio decreases [5.148].

The SE yield increases with increasing angle of incidence θ according to (Fig. 5.18)

$$\delta(\theta) = \frac{\delta_0}{\cos \theta}; \quad \delta_0 = \delta(\theta = 0). \quad (5.31)$$

This relation is valid for a specimen with a mean atomic number, for $E_0 \geq 5$ keV, and θ up to a few degrees below 90° . The increase of δ with θ is greater for specimens with a low atomic number and smaller for samples with high Z [5.13]. For crystalline objects, the increase of δ with θ is superimposed by electron channeling and crystalline orientation contrast (Sect. 5.1.3). The distinct dependence of the SE yield on θ provides the basis for the topographic contrast in secondary electron micrographs.

Backscattered Electrons

The majority of BSE is due to multiple scattering of the beam electrons within the specimen (Fig. 5.14). The energy spectrum of the backscattered electrons is shown schematically in Fig. 5.12. By definition the energy of BSE is in the range $50 \text{ eV} < E_{BSE} \leq E_0$. The BSE spectrum has a small peak consisting of elastically scattered electrons at E_0 (this peak is not visible in Fig. 5.12). Toward energies lower than E_0 there is a broad peak, which covers the range down to about $0.7E_0$ for high atomic numbers and further down to about $0.4E_0$ for low atomic numbers. The majority of BSE are within this broad peak. For high atomic number elements such as gold, the maximum of the distinct peak is at about $0.9E_0$, whereas for low atomic numbers, e. g., carbon, the maximum of the less distinct peak is located at about $(0.5-0.6)E_0$. The cumulative fraction of 50% of BSE is reached for carbon at $E_{BSE}/E_0 = 0.55$ and for gold at 0.84, respectively [5.28]. It seems worth mentioning that the energy distribution of BSE is shifted toward higher energy if the angle of incident electrons is larger than 70° [5.9].

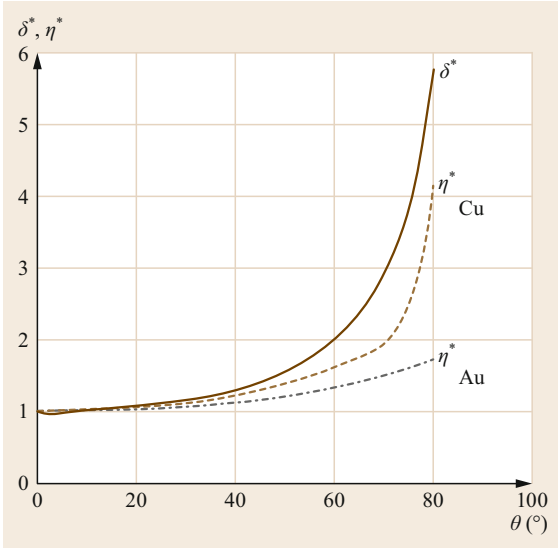


Fig. 5.18 Normalized SE yield δ^* and BSE yield η^* versus the angle of incidence θ of the electron beam. $\delta^* = \delta(\theta)/\delta_0$, $\eta^* = \eta(\theta)/\eta_0$. η was calculated for gold and copper according to (5.34)

As shown in Fig. 5.14, the BSE can originate either from the small area directly irradiated by the electron beam—they are denoted as BSE1—or after multiple elastic and inelastic scattering events from a significantly larger circular area around the beam impact point, which are designated BSE2. The lateral distribution of BSE2 has been calculated by Monte Carlo simulation for different materials [5.149, 150]. It shows that the BSE-emitting surface area increases with electron energy E_0 . For a given energy E_0 the size of the BSE-emitting area increases with descending atomic number. As with SE1, the BSE1 carry local information about the small volume and deliver high-resolution information for a beam diameter of about ≤ 1 nm. As a consequence of lateral spreading the BSE2 carry information about a much larger region, thus fine structural details on the scale of the beam diameter cannot be resolved.

Figure 5.14 also shows that the beam electrons travel in a small subsurface volume before they return to the surface to escape as BSE2. The escape depth of BSE is much larger than t_{SE} and depends on—in contrast to t_{SE} —the electron energy E_0 . Experimental data for different materials show that t_{BSE} amounts to about half of the electron range R [5.142, 151].

Knowledge of the angular distribution of BSE is of great importance for understanding and optimization of BSE detection geometry. For normal beam incidence the angular distribution can be approximated by a $\cos \zeta$ distribution [5.142], where ζ represents the BSE emis-

sion angle relative to the surface normal. Because of the fact that the emitted BSE move on nearly straight trajectories, the angular detector position has a strong influence on the collection efficiency of the detector. For non-normal beam incidence the distribution is asymmetric and a reflection-like emission maximum is observed. The angular distribution consists for large angles of incidence θ of cosine distribution approximately directed to $-\theta$ and a superimposed fraction at smaller emission angles [5.142].

The BSE coefficient η is defined by

$$\eta = \frac{n_{BSE}}{n_b}, \quad (5.32)$$

where n_{BSE} is the number of BSE and n_b is the number of incident electrons. η is approximately independent of the electron energy E_0 in the range of about 10–30 keV. For low atomic numbers and beam energies below 5 keV η increases as E_0 decreases, whereas for medium and high atomic numbers η decreases with E_0 (Fig. 5.16) [5.152]. However, at low energies η depends in a complex manner on the atomic number [5.145, 146].

The BSE coefficient monotonically increases with the atomic number as shown for 30 keV in Fig. 5.17. Because of the approximate independence of the electron energy E_0 , the graph of the BSE coefficient is valid for beam energy ranging from 30 down to about 5 keV. The graph of η versus Z can be approximated by a polynomial [5.153]

$$\eta(Z) = 0.0254 + 0.016Z - 1.86 \times 10^{-4}Z^2 + 8.31 \times 10^{-7}Z^3. \quad (5.33)$$

For energies below 5 keV the dependence of η on Z is more complicated (for details see [5.34, 154–156]). The distinct dependence of the BSE coefficient on the atomic number Z provides the basis for the atomic number contrast (Sect. 5.1.3).

Like the SE yield, the backscattering coefficient also increases monotonically with increasing angle of incidence θ according to [5.157]

$$\eta(\theta) = (1 + \cos \theta)^{-9/\sqrt{Z}}. \quad (5.34)$$

Figure 5.18 shows the graphs $\eta(\theta)$ versus θ for Cu ($Z = 29$) and Au ($Z = 79$). The graphs indicate the strong influence of the atomic number, in particular for $\theta > 50^\circ$. The monotonic increase of η with θ provides the basis for the topographic contrast in BSE micrographs. For the sake of completeness it should be mentioned that Drescher et al. [5.142] derived from experimental data at 25 keV an analytical expression for $\eta(\theta, Z)$ other than the one given by (5.34).

The backscattering coefficient of a single crystal depends sensitively on the direction of the incident electrons related to the crystal lattice [5.151, 158]. This dependence is caused by the regular three-dimensional arrangement of the atoms in the lattice, whose atomic density depends on the direction. The backscattering coefficient is lower along directions of low atomic density, which permits a fraction of the incident electrons to penetrate deeper than in amorphous material before being scattered. Those electrons have a reduced probability of returning to the specimen surface and leaving the sample as BSE. The maximum relative variation of the backscattering coefficient is in the order of 5%.

Transmitted Electrons

When the thickness of a specimen approaches the electron range R or becomes even smaller than R , an increasing fraction of beam electrons is transmitted. Specimens that are sufficiently thin (typically less than 100 nm), or particles mounted onto a thin electron-transparent film supported by a metallic mesh grid commonly used in TEM and STEM can then be imaged in transmission mode in the SEM. To improve the stability of the 5 nm-thick carbon film, the film is placed onto a holey thick carbon film supported by a mesh grid. In contrast to a solid support, a 5 nm-thick carbon film contributes only insignificantly to the SE and BSE signal, thus particles deposited onto a thin support film can be imaged in the normal manner using SE and BSE, respectively, providing complimentary information from several different detectors. An example of STEM imaging is shown in Fig. 5.19. The figure demonstrates the same specimen (zeolite decorated with nanoparticles) that was imaged using SE, BSE, and STEM modes.

As a result of electron–specimen interaction the transmitted electrons can be unscattered or elastically or inelastically scattered (Fig. 5.20). Because of their

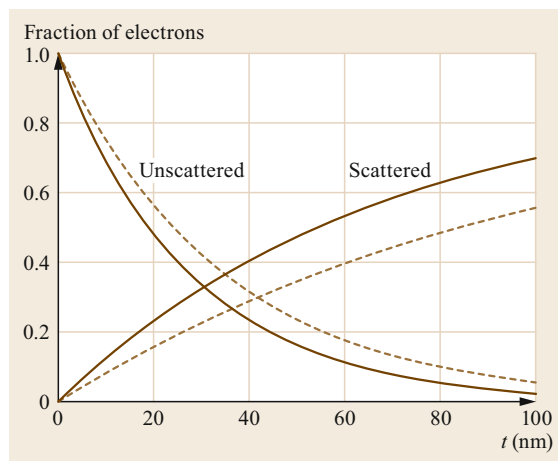


Fig. 5.20 Fraction of transmitted electrons scattered into an angular range of 25–300 mrad for carbon ($\rho = 2 \text{ g cm}^{-3}$; solid line) and protein ($\rho = 1.35 \text{ g cm}^{-3}$; dashed line). Parameters: $E_0 = 30 \text{ keV}$, $\alpha_p = 10 \text{ mrad}$. The graphs show an increasing fraction of scattered and a decreasing fraction of unscattered electrons with increasing thickness. (Calculation according to [5.134])

characteristic angular and energy distribution, the transmitted electrons can be separated by placing suitable detectors below the specimen. Frequently, a rather simple and inexpensive device for observing an STEM image [5.159]—sometimes called *poor man's STEM in SEM detector*—is used. The transmitted electrons are passing through an angle-limiting aperture, strike a tilted gold-coated surface, and thus create a high SE and BSE signal, which can then be collected by a conventional ET detector. The angle-limiting aperture cuts off the transmitted, scattered electrons. In this case the *poor man's STEM in SEM detector* acquires those electrons, which represent the bright-field signal. The *poor man's STEM in SEM detector* just cuts the transmitted

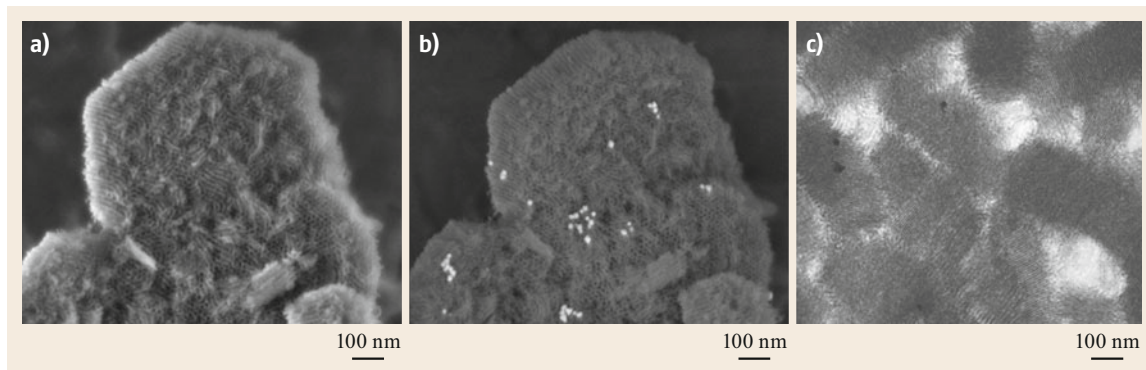


Fig. 5.19a–c Comparison of (a) SE (1 kV); (b) BSE (1 kV); and (c) STEM-in-SEM (30 kV) images of mesoporous silica loaded with Pd nanoparticles

scattered electrons without making use of their inherent information. Both the elastically and the inelastically scattered electrons are signals, which very sensitively depend on the mass thickness ρt if the specimen thickness $t \leq [\Lambda_{\text{el}} \Lambda_{\text{in}} / (\Lambda_{\text{el}} + \Lambda_{\text{in}})]$ [5.133, 160] (Fig. 5.19) can be used.

Another important application of STEM-in-SEM imaging is the measurement of the physical probe size of the SEM using a thin carbon film (thickness below 10 nm, preferably containing nanoparticles of gold or gold-palladium for better contrast). In this case, the broadening of the electron beam in the film is negligible and so the resolution of the STEM image is equal to the probe diameter. The image resolution can be determined either by analysis of the diffractogram (power spectrum) of the STEM micrograph [5.38, 161, 162] or by cross-correlation function analysis [5.163] of the phase noise in the bright-field STEM image of the carbon film. The latter directly yields the probe diameter of the SEM [5.162].

Combining the SE and BSE detectors above as well as the bright-field and dark-field detectors below the specimen, its surface as well as its internal structure can be observed simultaneously in the SEM.

Cathodoluminescence

Cathodoluminescence (CL) is the emission of light generated by the electron bombardment of semiconductors and insulators ([5.164]; Fig. 5.14). Those materials have an electronic band structure characterized by a filled valence band and an empty conduction band separated by an energy gap $\Delta E_{\text{CV}} = E_{\text{C}} - E_{\text{V}}$. Electrons from the valence band can interact inelastically with a beam electron and can be excited to an unoccupied state in the conduction band. The excess energy of the excited electron will be lost by a cascade of nonradiative phonon and electron excitations. Most of the recombination processes of excited electrons with holes in the valence band are nonradiative processes, which elevate the sample temperature. There are different radiative processes, which take place in inorganic materials, semiconductors, and organic molecules.

In inorganic materials intrinsic and extrinsic transitions can take place. The intrinsic emission is due to direct recombination of electron-hole pairs. Extrinsic emission is caused by the recombination of trapped electrons and holes at the donor and acceptor level, respectively. The trapping increases the probability of recombination. The extrinsically emitted photons have a lower energy than intrinsically emitted photons.

In semiconductors the radiative recombination can be due to the direct collision of an electron with a hole with the emission of a phonon. Depending on the nature of the band structure of the material, the recombina-

tion can be either direct or indirect. In the latter case, the recombination must occur by simultaneous emission of a photon. Indirect recombination is less likely than direct recombination. If the material contains impurities, the process of recombination via impurity level becomes important. The modification of CL efficiency as a function of the purity and the perfection of the material is the most important aspect of the use of this method in scanning electron microscopy. It is because of such modifications that a contrast is generated (for details see [5.165, 166]). It was shown in some cases that the sensitivity of CL analyses can be at least 10^4 times higher than that obtainable by x-ray microanalysis, i. e., an impurity concentration as low as 10^{14} cm^{-3} [5.167].

In organic materials the excitation is inside an individual molecule. Electrons go from a ground state to a singlet state at least two states above. Then the deexcitation to the ground state is radiationless up to the singlet state directly above the ground level and from this state the deexcitation can be either radiationless or radiative with decay times larger than 10^{-7} s (fluorescence). The CL spectra depend on the chemical structure of the molecule [5.168, 169]. Cathodoluminescence of organic matter also can be caused by selective staining with luminescent molecules (fluorochromes). Typical fluorochromes are, e. g., fluoresceine, fluoresceine isothiocyanate (FITC), and acridine orange.

Independent of the material the light generated by CL inside the specimen has to pass the surface according to the Snell law [5.170]. The critical angle θ_{t} of total internal reflection is given as

$$\sin \theta_{\text{t}} = \frac{n_1}{n}, \quad (5.35)$$

where $n_1 = 1$ (vacuum) and n is the refractive index of the specimen ($1 < n < 5$). As shown by (5.35) the fraction of emitted light is significantly reduced by total internal reflection for $n > 2$ (semiconductors).

X-Rays

The x-ray spectrum is considered to be that part of the electromagnetic spectrum that covers the wavelengths λ_{X} from approximately 0.01 to 10 nm. The energy of x-rays is given as

$$E_{\text{X}} = h\nu = \frac{hc}{\lambda_{\text{X}}}, \quad (5.36)$$

where $h = 6.6256 \times 10^{-34} \text{ J s}$ is Planck's constant, $c = 2.99793 \times 10^8 \text{ m s}^{-1}$ is the speed of light, and ν is the frequency of x-rays. The x-rays are generated by deceleration of electrons (x-ray continuum or Bremsstrahlung)

or by electron transition from a filled higher state to a vacancy in a lower electron shell (characteristic x-ray lines) (Fig. 5.21).

The x-ray continuum is made up of a continuous distribution of intensity as a function of energy whereas the characteristic spectrum represents a series of peaks of variable intensity at discrete element-specific energies. As the electron energy increases the intensity of the continuous spectrum also increases and the maximum of the distribution is shifted toward higher energies. The general appearance of the continuous spectrum is independent of the atomic number of the specimen, however, the absolute intensity values are dependent on the atomic number. The maximum possible energy E_X is given by the electron energy E_0 , which corresponds to instantaneous stopping of an electron at a single collision (Duane–Hunt limit). According to *Kramers* [5.171] the intensity of the continuous spectrum I_C emitted in an energy interval with the width dE_X is given as

$$I_C(E_X)dE_X = \frac{kZ(E_0 - E_X)}{E_X} dE_X. \quad (5.37)$$

k represents the Kramers constant, which varies slightly with the atomic number [5.38]. A detailed treatment of the continuous x-ray emission is given by *Stephenson* [5.172].

The characteristic x-ray spectrum consisting of peaks at discrete energies is superimposed on the continuous x-ray spectrum (Fig. 5.21). Their positions are independent of the energy of the incident electrons. The peaks occur only if the corresponding atomic energy level is excited. The generation of characteristic

x-rays consists of three different steps. First, a beam electron interacts with an inner shell electron of an atom and ejects this inner shell electron leaving that atom in an excited state, i.e., with a vacancy on the electron shell. Second, subsequently the excited atom relaxes to the ground state by transition of an electron from an outer to an inner shell vacancy. The energy difference ΔE_{ch} between the involved shells is characteristic for the atomic number. Third, this element-specific energy difference is expressed either by the emission of an electron of an outer shell with a characteristic energy (Auger electron) or by the emission of a characteristic x-ray with energy $E_X = \Delta E_{ch}$. The fraction of characteristic x-rays emitted when an electron transition occurs is given by the fluorescence yield ω . This quantity increases with the atomic number and depends on the inner electron shell involved (Fig. 5.22). The complement, $1 - \omega$, represents the Auger electron yield, which gives the corresponding fraction of Auger electrons produced. The fluorescence yield for the different shells and subshells can be calculated (for details see [5.173]).

Moseley studied the line spectra in detail and found that the general appearance of the x-ray spectrum is the same for all elements. The energy of a characteristic x-ray line depends on the atomic shells involved in the transition resulting in the emission of this line. The x-ray lines can be classified in series according to the shell where the ionization took place, e.g., K-, L-, M-shell, etc. The quantum energies of a series are given by Moseley's law

$$E_X = A(Z - B)^2, \quad (5.38)$$

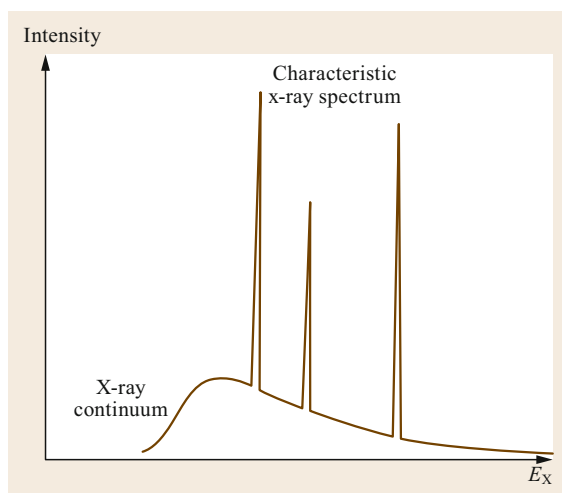


Fig. 5.21 Schematic representation of the x-ray spectrum emitted from a specimen bombarded with fast electrons

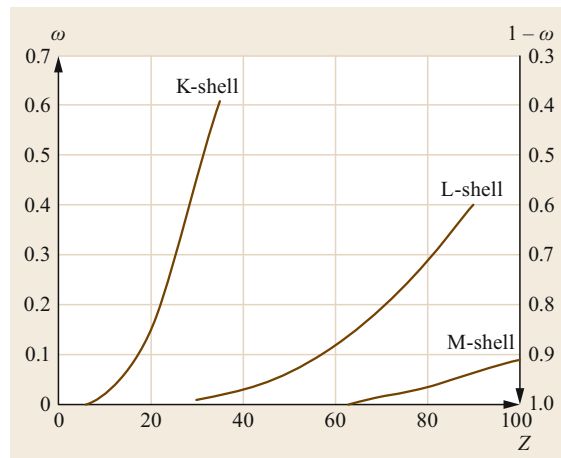


Fig. 5.22 Dependence of the x-ray fluorescence yield ω and its complement $(1 - \omega)$ of the K-, L-, and M-shell from the atomic number Z . The complement $(1 - \omega)$ corresponds to the Auger electron yield

where A and B are parameters that depend on the series to which the line belongs. The characteristic x-ray energy E_X is denoted by symbols that identify the transition that produced it. The first letter, e. g., K, L, identifies the original excited level, whereas the second letter, e. g., α , β , designates the type of transition occurring. For example, K_α denotes the excitation energy between the K- and L-shell, whereas K_β denotes the excitation energy between the K- and M-shell. Transitions between subshells are designated by a number, e. g., a transition from the subshell L_{III} to K is denoted as $K_{\alpha 1}$ and from the subshell L_{II} to K is denoted as $K_{\alpha 2}$, respectively. The transition from the subshell L_I to K is forbidden. The characteristic x-ray energies and x-ray atomic energy levels for the K-, L-, and M-shells are listed in tables [5.174, 175]. Fortunately, the atomic energy levels are not strongly influenced by the type and strength of the chemical bonds. However, chemical effects on x-ray emission are observed for transitions from the valence electron states, which are involved in chemical bonds. In such cases, the narrow lines show changes of their shape and their position (energy shift < 1 eV) as well [5.176].

Auger Electrons

As mentioned in Sect. 5.1.2, X-Rays when an excited atom relaxes to the ground state by transition of an electron from an outer to an inner shell the energy difference ΔE_{ch} between the involved shells can be expressed by the emission of an electron of an outer shell with a characteristic energy E_{AE} . The emission is due to the Auger effect [5.177, 178] and the emitted electron is designated as an Auger electron (AE). Its energy E_{AE} is given by

$$E_{AE} = \Delta E_{ch} - E_{ionr}, \quad (5.39)$$

where the term E_{ionr} contains the ionization energy of the AE-emitting outer shell and also considers relaxation effects. The shape and the position of the AE peaks are influenced by the type and strength of the chemical bonds [5.179]. The AE peaks have an energy width of a few electronvolts and are superimposed on the low-energy range of the BSE spectrum up to energies of about 2.5 keV (Fig. 5.12). The identification of the AE peaks on the BSE background [5.180] can be improved by differentiation of the electron energy spectrum.

The Auger electrons are generated within the excitation volume (Fig. 5.14). Because of their low energies only AE with a short pathway to the specimen surface can escape. However, energy losses caused by inelastic scattering on the pathway to the surface remove AE from the AE peaks. The decrease of the AE peak is pro-

portional to $\exp(-x/\Lambda_{AE})$, where x denotes the length of the path inside the specimen and Λ_{AE} the mean free path of the AE. Depending on their energy and the atomic number of the specimen the mean free path Λ_{AE} can have values in the range of about 0.4 nm to a few nanometers [5.181, 182]. If AEs are inelastically scattered on their path to the surface, then they cannot be identified as an AE in the BSE background. Therefore, only atoms within a depth of about Λ_{AE} can contribute to the AE peaks. Since Auger electrons yield information on element concentrations very near the surface, the specimen must be in an ultrahigh vacuum environment and special sample preparations are required (e. g., ion sputtering in situ, cleavage in situ) to obtain clean surfaces.

Because the AE yield of the K-shell $1 - \omega_K$ is much larger than ω_K for light elements (Fig. 5.22) AE spectroscopy is advantageous for elements with atomic number $Z = 4$ ($\omega_K = 4.5 \times 10^{-4}$) up to $Z \approx 30$ ($\omega_K = 4.8 \times 10^{-1}$) [5.183]. Similar to SE, which are also emitted only from a very thin surface layer, the AE can be generated directly by the beam electrons and by BSE within a larger circular area around the beam impact point (Fig. 5.14). Like the SE yield, which increases with increasing angle of incidence θ according to $\delta(\theta) = \delta_0 / \cos \theta$ (5.31), the integral AE peak intensity is proportional to $1 / \cos \theta$ [5.38, 184, 185].

Recent developments in scanning Auger microscopy and AE spectroscopy are described by Jacka [5.186].

Others

The incident electron beam bombards the specimen with electrons thereby introducing a negative electric charge. A certain amount of negative electric charge is leaving the specimen as secondary (I_{SE}), backscattered (I_{BSE}), and Auger electrons (I_{AE}). To avoid an accumulation of charges a specimen current I_{sp} must flow from the specimen to the ground. The conservation equation for the electric charge is

$$I_p = I_{SE} + I_{BSE} + I_{AE} + I_{sp}, \quad (5.40)$$

where I_p is the probe current. The specimen current changes the sign when $I_{SE} + I_{BSE} + I_{AE} > I_p$. Because $I_{SE} + I_{BSE} \gg I_{AE}$ this means basically that $\delta + \eta > 1$ (Fig. 5.16). I_{sp} depends on the angle of beam incidence θ and the electron energy E_0 as expected from $\delta(\theta, E_0)$ and $\eta(\theta, E_0)$ [5.38]. The resolution of specimen current images is comparable to that of BSE images. One advantage of the specimen current mode is that the contrast is independent of the detector position. A critical review of this mode was published by Newbury [5.187].

5.1.3 Contrast Formation and Resolution

Since the image formation is due to the image signal fluctuation ΔS from one point to another point, the contrast C is designated as in television to be

$$C = \frac{S - S_{av}}{S} = \frac{\Delta S}{S} \quad (5.41)$$

S_{av} is the average value of the signal and S represents the signal of the considered point ($S > S_{av}$, i. e., C is always positive). The signal fluctuation may be caused by local differences in the specimen topography, composition, lattice orientation, surface potential, magnetic or electric domains, and electrical conductivity. The minimum contrast is obtained if $S = S_{av}$, whereas the maximum contrast is obtained for $S_{sv} = 0$. This is the case, e. g., when the signal S from a feature is surrounded by a background with $S_{av} = 0$. The contrast will be visible if C exceeds the threshold value of about 5×10^{-2} .

According to the point-resolution criterion two image points separated by some horizontal distance (i. e., within the x - y plane perpendicular to the optical axis) are resolved when the minimum intensity between them is 75% or less of the maximum intensity. Because of the inherent noise of each signal of the SEM characterized by its signal-to-noise ratio (SNR) the drop to 75% of the maximum intensity will not be reliably defined at the minimum distance. Consequently, at low SNR two image points can be resolved only if their distance is larger than the minimum distance reliably defined for noiseless signals.

As opposed to the light or transmission electron microscope the resolution of the SEM cannot be defined by Rayleigh's criterion. The resolution obtained in the SEM image depends in a complex manner on the electron-beam diameter, the electron energy, the electron-specimen interaction, the selected signal, the detection, as well as the electronic amplification and electronic processing. An object *point* corresponds to the size of a small local excitation volume (Figs. 5.13 and 5.14) designated as the spatial detection limit from which a sufficient signal can be obtained. Obviously, the point resolution cannot be less than the spatial detection limit. It becomes clear from Fig. 5.14 that the spatial resolution of an SEM is different for each signal since the size of the signal-emitting volume as well as the signal intensity depends on the type of signal selected.

The important *quality parameters* such as spatial resolution, astigmatism, and SNR of SEM images, as well as drift and other instabilities that occur during imaging, can be determined most reliably and objectively by Fourier analysis of the recorded micrographs [5.38, 161]. However, such determinations

are problematic, since, unlike TEM resolution specimens, there is no single type of sample that will give completely unambiguous results, especially in the current microscope environment, where the resolution is measured in angstroms for high-end systems (typical resolution quoted for an FESEM hovers around 8–10 Å). Other measurement procedures involve measuring the separation gap between two particles or via a line profile through a defined sharp edge structure. These techniques are subjective in nature. Defining the edge of a particle will be different from one person to the next based on how that person interprets the edge of a particle. When using the line profile method, the distance for the signal transition is considered to be related to probe diameter. While the traditional convention and measurement have been done at the 84th and 16th percentile of the transition (1σ value), different SEM manufacturers have reported values at 75th/25th and 65th/35th percentile. This leads to lower reported values of resolution even from the same edge profile in an image.

Another layer of complexity is added with digital image acquisition in today's SEMs. The pixel resolution of the final image has an impact on the smallest features that can be resolved, meaning that the resolution measurement is intimately linked to the pixel size. Consider an image taken at $100\,000\times$ with a field of view of $1.28\ \mu\text{m}$. If the image pixel resolution is 1280×960 , then we have a pixel length of $1\ \text{nm}/\text{pixel}$. To distinguish a probe diameter of $3\ \text{nm}$ would require image information that could be observed across only 3 pixels. Taking the same image with an increased pixel density of 2560×1920 would mean that the same information could be observed across 6 pixels.

Clearly, resolution specifications cannot be compared easily today between different manufacturers, so far as there is no standardized methodology and specimen.

Topographic Contrast

Presumably the SEM is most frequently used to visualize the topography of three-dimensional objects. The specimen topography gives rise to a marked topographic contrast obtained in secondary and backscattered images. This contrast has a complex origin and is formed in SE images by the following mechanisms:

1. Dependence of the SE yield δ on the angle of incidence θ of the electron beam at the local surface element (5.31). The tilt angle of the local surface elements is given by the topography of the sample.
2. Dependence of the detected signal on the angular orientation of the local surface element related to

the ET detector (Sect. 5.1.1, *Detectors and Detection Strategies*). SE generated *behind* local elevations, in holes, in fissures, or in cavities reach the ET detector incomplete. This causes a more or less pronounced shadow contrast (Fig. 5.7a).

3. Increase of the SE signal when diffusely scattered electrons pass through an increased surface area. This is the case at edges or at protruding surface features, which are smaller than the excitation volume. Electron diffusion leads to overbrightening of edges and small surface protrusions in the micrograph and is known as an edge effect.
4. Charging artifacts with objects of low electric conductivity.

Contributions (1) to (3) are illustrated by SE micrographs of different specimens shown in Figs. 5.23a and 5.24a as well as schematically by profiles of the topography and the related SE signals in Fig. 5.25. In these figures the direction to the ET detector is indicated. The ball in Fig. 5.23a shows a contrast, which is mainly due to the varying angle θ of beam incidence across the ball ((1) above) and the angular orientation of the local surface elements related to the Everhart–Thornley detector ETD ((2) above). The collection efficiency of the ETD is significantly higher for surface elements facing the detector than for those on the back (shadow region). Whereas the intensity of emitted secondary electrons of the ball reveals radial symmetry, the effect of detection geometry causes the nonradial symmetric image intensity distribution of the ball (Fig. 5.25a–c). The rim of the ball is bright in the SE image because of the enhanced SE emission due to an incidence angle $\theta \approx 90^\circ$ and the effect of diffusely scattered electrons passing through an increased surface area ((3) above). The radius of the ball is larger than the electron range R (Fig. 5.14) therefore the latter effect occurs just near the rim of the ball. If the mean radius of ball-like particles becomes comparable or smaller than the electron range, diffusely scattered electrons generate more SE over the whole particle surface, thus the SE emission typically is distinctly enhanced (small particles are marked by small arrowheads in Figs. 5.23a and 5.24a). If the shadow contrast is visible in the image and the direction toward the ETD is known then elevations and depressions clearly can be readily identified (Fig. 5.23a). Another way to distinguish elevations and depressions is to record and to analyze SE stereopairs.

The SE micrograph of large crystal-like particles (Fig. 5.24a) basically shows the same contrast mechanisms as discussed above but with a more complex structured sample than the ball. The individual flat surface planes of the crystal-like particles occur with al-

most constant brightness because of the constant angle of beam incidence and the constant detection geometry (provided that there is no shadow effect from other large particles). Some surface planes possess fissures of different size, which typically appear rather dark because just a minor fraction of the generated SE can escape from inside the fissures. In such cases SE can be extracted either by a positively biased grid in front of the specimen [5.188] or by a superimposed magnetic field in which the SE follow spiral trajectories around the lines of magnetic flux until they reach the collecting field of the ETD [5.76].

It should be mentioned that the laterally located ETD also registers those BSE, which are within the small solid angle of collection defined by the scintillator area and the specimen–scintillator distance. The BSE contribute in the order of 10–20% to the SE signal [5.38] and are the same as those collected by the negatively biased ET detector. Furthermore, BSE that are not intercepted by the detector strike the pole piece of the objective lens and the walls of the specimen chamber. These stray BSE generate so-called SE3 emitted from the interior surfaces of the specimen chamber. The SE3 carry BSE information and form a significant fraction of the SE signal for specimens with an intermediate and high atomic number [5.189].

The contrast in BSE images is formed by the following mechanisms:

1. Dependence of the BSE coefficient η on the angle of incidence θ of the electron beam at the local surface element (5.34).
2. Dependence of the detected signal on the angular orientation of the local surface element related to the BSE detector (Sect. 5.1.1, *Detectors and Detection Strategies*). BSE emitted *behind* local elevations, in holes, or in cavities, which do not reach the BSE detector on nearly straight trajectories, are not acquired. This causes a pronounced shadow contrast (Fig. 5.7b).
3. Increase of the BSE signal when diffusely scattered electrons pass through an increased surface area. This is the case at edges or at protruding surface features, which are smaller than the excitation volume.

The BSE leave the specimen on almost straight trajectories and only those within the solid angle of collection of the BSE detector can be recorded. Thus, dedicated BSE detectors have a large solid angle of collection to record a significant fraction of the BSE and to generate a signal with a sufficient SNR. The larger the solid angle of collection the less pronounced the shadow effects.

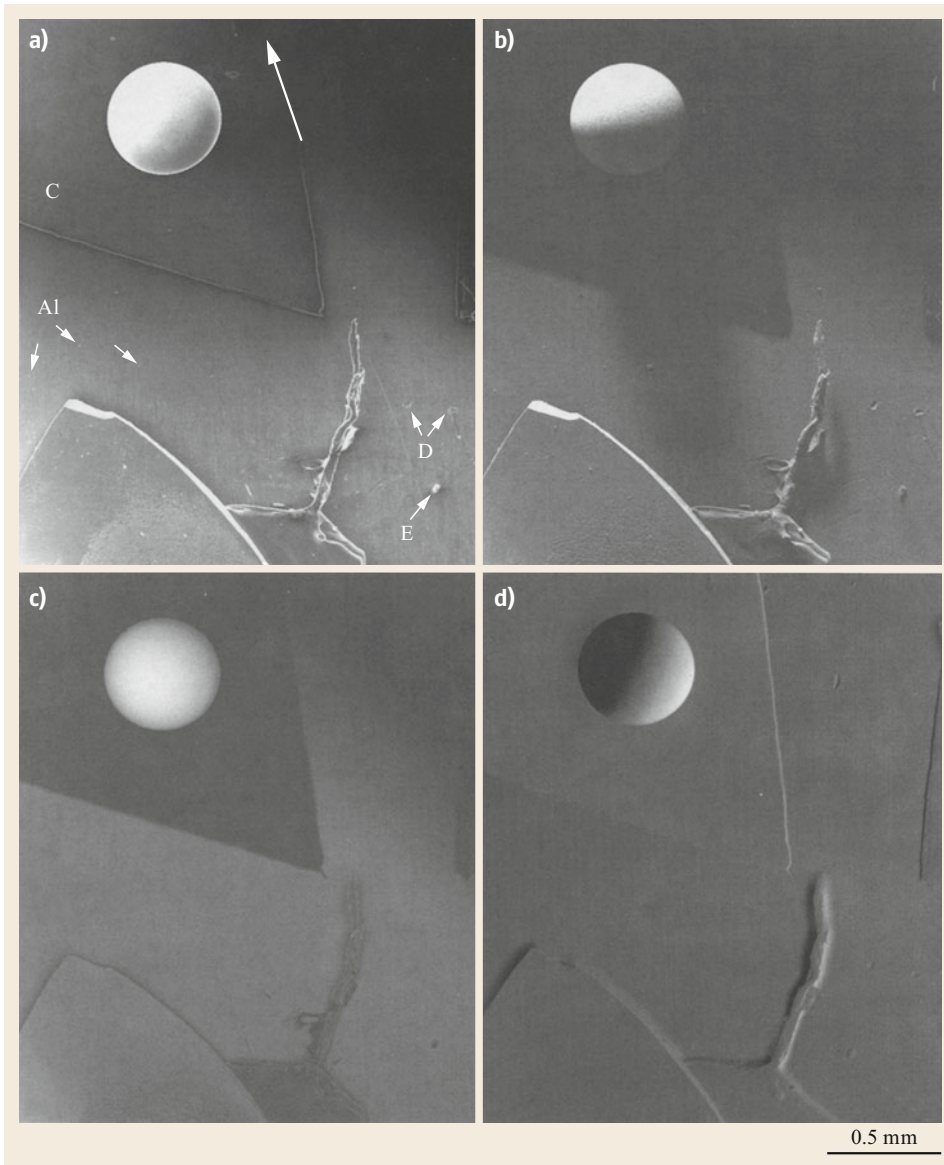


Fig. 5.23a–d Secondary (a) and backscattered electron micrographs (b–d) of a steel ball recorded at 30 kV and normal beam incidence. The arrow in (a) indicates the direction of the laterally located ET detector. The BSE micrographs shown in (c,d) were acquired using a four-quadrant semiconductor detector mounted below the objective pole piece, which records BSE over a large solid angle. The steel ball is mounted on carbon (marked by C), which is supported by aluminum (marked by Al). The small arrows in (a) indicate small particles with enhanced SE emission (bright blobs in the SE image). Elevations (E) and depressions (D) are also marked by small arrows

Contributions (1) to (3) mentioned above are illustrated by BSE micrographs from two specimens used for SE imaging and are shown in Figs. 5.23b,c and 5.24b and c as well as schematically by profiles of the topography and the related BSE signals in Fig. 5.25. Two different types of BSE images are shown: the highly directional image recorded with the negatively biased ETD (Figs. 5.23b and 5.24b) and the top-view image recorded with the four-quadrant semiconductor detector mounted below the objective pole piece (Figs. 5.23c and 5.24c). The ball in Fig. 5.23b shows a contrast, which is mainly due to the varying angle θ of beam incidence across the ball ((1)

above) and the angular position of the local surface elements related to the negatively biased ETD ((2) above). A pronounced sharp shadow occurs at the back of the ball and behind the ball (shadowed oblong area of the support). Whereas the intensity of the BSE of the ball reveals radial symmetry, the effect of detection geometry causes the nonradial symmetric image intensity distribution of the ball (Fig. 5.25a,d). The fade contour of the ball at its back is due to BSE redirected toward the negatively biased ETD by scattering on some interior surfaces of the specimen chamber. The pronounced directional shadow contrast in the image allows for unambiguous identification of eleva-

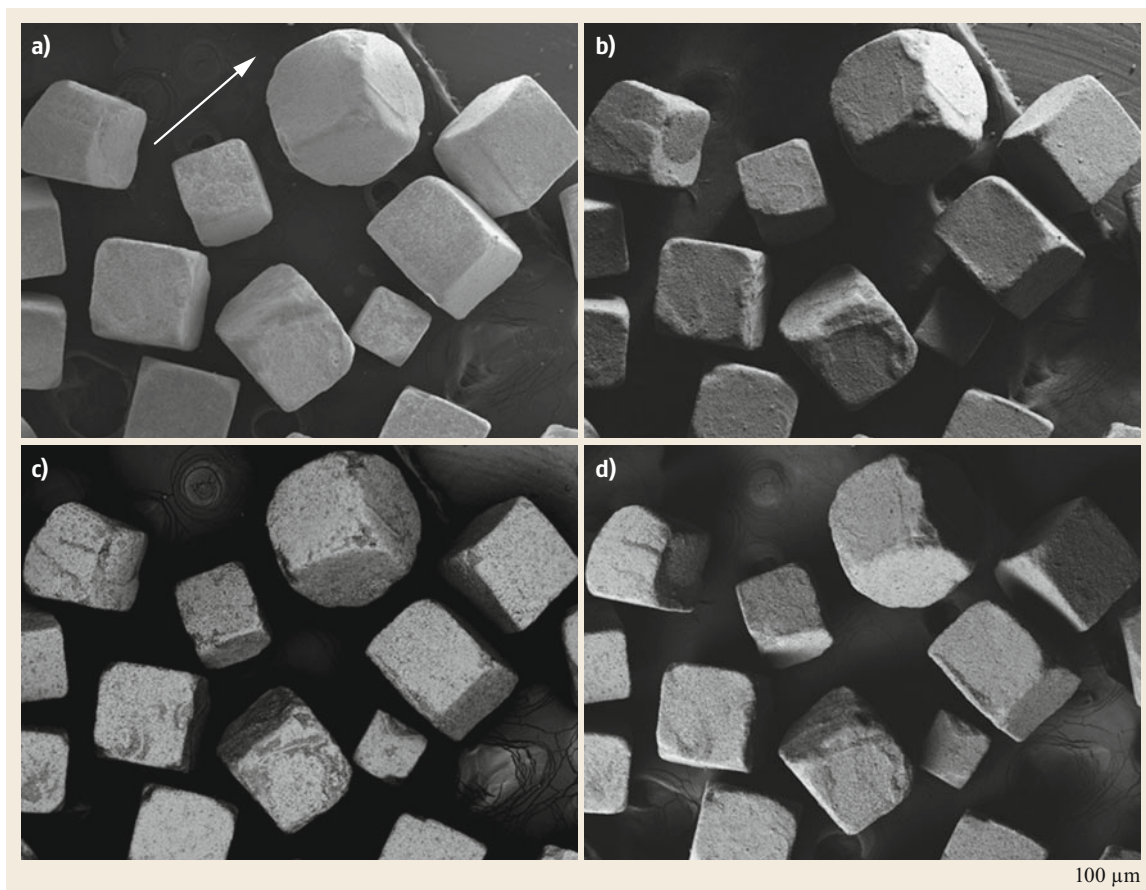


Fig. 5.24a–d Secondary (a) and backscatter (b–d) electron micrographs of table salt crystals coated with gold recorded at 10 kV. The arrow in (a) indicates the direction of the ET detector. (b) Shows an image recorded with ET detector with collector cage at -100 V; (c) is a backscatter image recorded with a 3-segment solid-state detector (A+B chips), showing mainly compositional contrast; (d) is a backscatter image recorded with a 3-segment solid-state detector (C-chip only), showing mainly topography

tions and depressions (Fig. 5.23b). Moreover, if the detection geometry of the BSE is known, the length of the shadow can be used in some cases to obtain a rough estimate of the height of elevations or depth of depressions.

The BSE micrograph of the ball recorded with the four-quadrant semiconductor detector (Fig. 5.23c) shows an almost radial symmetric image intensity distribution. It is obvious that the increase of the BSE coefficient η with the increasing angle of incidence θ (Fig. 5.18) toward the rim of the ball is superimposed by the stronger counteracting effect of the directed asymmetric distribution of BSE for non-normal beam incidence (Sect. 5.1.2, *Backscattered Electrons*). The shadow-like hem along the contour of the elevations reflects the fact that BSE emitted from the lower surrounding ar-

eas toward elevations can be absorbed or redirected; thus those BSE do not reach the BSE detector. In the case of depressions there is also a shadow-like hem but it is located inside the contour of the depression. A comparison of the different types of BSE images in Fig. 5.23b,c clearly shows that the topography of the sample is pronounced in Fig. 5.23b while—as we shall see later—the atomic number contrast is pronounced in Fig. 5.23c.

The BSE micrographs of large crystal-like particles (Fig. 5.24b,c) basically show the same contrast mechanisms as discussed previously (no orientation anisotropy of the electron backscattering and SE emission [5.158, 190] is involved). Figure 5.24b recorded with the negatively biased ETD shows large shadowed regions (containing almost no information) and some highlighted individual flat surface planes of the crystal-

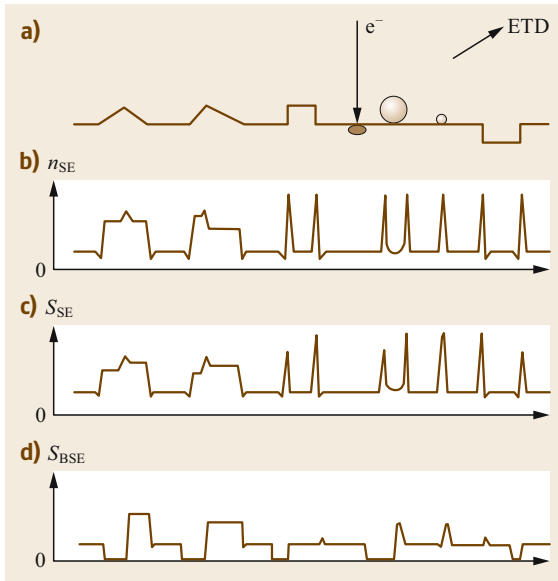


Fig. 5.25a–d Schematic specimen surface profile of an assumed topography having elementally shaped elevations and a depression (a). Those elemental shapes are present in the samples shown in Figs. 5.23 and 5.24. The size of the excitation volume of the electron beam is drawn in relation to the local topographic structures. The amount n_{SE} of locally emitted SE is shown qualitatively in (b) and the corresponding SE signal S_{SE} in (c). The BSE signal S_{BSE} collected by the negatively biased ET detector is schematically presented by the graph in (d). ETD, Everhart–Thornley detector

like particles that occur with almost constant brightness because of the constant angle of beam incidence of the constant detection geometry. Figure 5.24b demonstrates that the detection geometry used for recording was not at an optimum. The micrograph obtained with the four-quadrant semiconductor detector is shown in Fig. 5.24c, which depicts exactly the same area as Fig. 5.24b. Because of the large solid angle of collection of this BSE detector the effects mentioned above in (1) and (2) do generate just small differences in the image intensity of differently oriented surface planes of the crystal-like particles. The effect of shadowing is not substantial in that micrograph. The increase of the BSE signal at edges, at surface steps, and small protruding particles ((3) above) located on the flat surface planes due to enhanced BSE emission is significant. The fissures on some surface planes of the crystal-like particles (Fig. 5.24a) occur in the BSE micrograph also as rather dark features because just a minor fraction of the BSE can escape from inside the fissures.

The SEM micrographs are closely analogous to viewing a macroscopic specimen by eye. In the light optical analogy the specimen is illuminated with light from the side of the detector and viewed from the position of the electron beam [5.68, 191]. When a rather diffuse illumination is used then all surface elements are illuminated but those directed to the light source are highlighted. This corresponds to the situation for the positively biased ETD. The light optical analogy shows a pronounced shadow contrast if a directional light source illuminates the specimen surface from a suitable direction. This situation closely resembles BSE images recorded with a positively biased ETD. The strong light optical analogy very likely explains the fact that SEM micrographs of objects with a distinct topography can be readily interpreted even without extensive knowledge of the physics *behind* the imaging process.

As briefly mentioned in Sect. 5.1.1, *Detection Strategies*, the topographic and the material contrast can be pronounced or suppressed, respectively, by a combination of the signals of two oppositely placed detectors, *A* and *B*. Two BSE semiconductor detectors were first used by Kimoto et al. [5.69] and they showed that the sum $A + B$ results in material and the difference $A - B$ in topographic contrast. Volbert and Reimer [5.192] used a BSE/SE converter system and two opposite ET detectors for that kind of contrast separation in the SEM. The four-quadrant semiconductor detector used for recording Figs. 5.23c and 5.24c allows for signal mixing of the four signals acquired simultaneously. Figures 5.23c and 5.24c represent the sum of the four signals (S_{Q1}, \dots, S_{Q4}), thus both micrographs show a pronounced material contrast. By addition of the signals of two adjacent quadrants at a time (i. e., $S_{Q1} + S_{Q2} = A$; $S_{Q3} + S_{Q4} = B$) the effect of two semi-annular detectors *A* and *B* is obtained. The difference image $A - B$ shows a pronounced topographic contrast (Fig. 5.23d). The directionality in Fig. 5.23d can be varied readily by using a different combination of the individual signals of the quadrants, e. g., $A = S_{Q2} + S_{Q3}$ and $B = S_{Q1} + S_{Q4}$. Difference SE and BSE images recorded at exactly defined detection geometry allow for the reconstruction of the surface topography [5.68, 71–73]; see also Sect. 5.1.1, *Detection Strategies and Specimen Tilting and Stereo Imaging*. However, special care is required for the reconstruction of the surface topography using BSE images because of artifacts in the reconstructed image [5.68]. To demonstrate the effect of directionality for four different detections Fig. 5.26 shows four individual BSE micrographs each recorded with another quadrant of the semiconductor detector. The individual BSE images contain superimposed topographic and compositional contrast components.

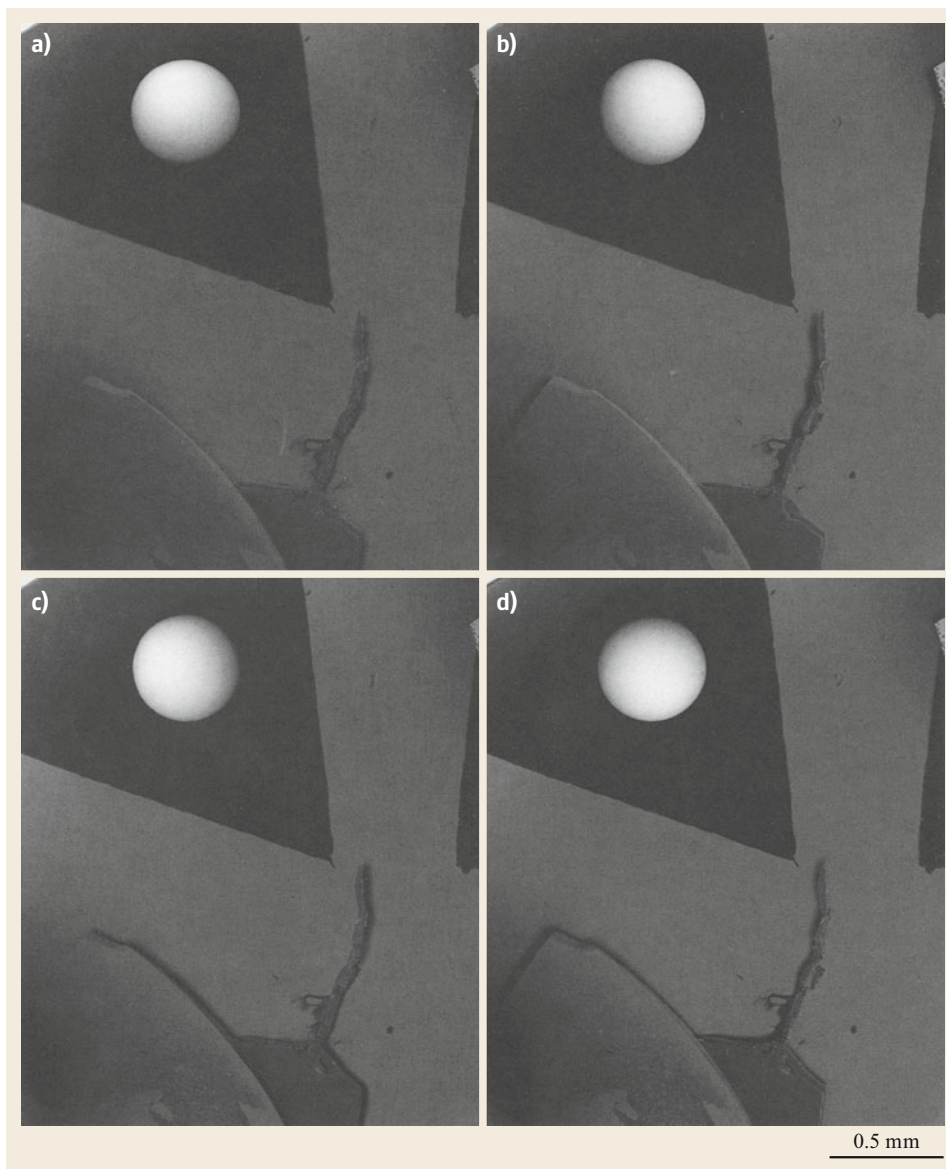


Fig. 5.26a–d BSE micrographs of a steel ball on carbon (Fig. 5.23) each recorded with another individual quadrant of the four-quadrant semiconductor detector. (a) $(-x)$ -quadrant, (b) $(+y)$ -quadrant, (c) $(-y)$ -quadrant, (d) $(+x)$ -quadrant. The micrographs were recorded at 30 kV and normal beam incidence. The angular position of the four-quadrant semiconductor detector is rotated clockwise against the x - y coordinates of the images by 34° . Shadows of the surface step of the feature at the *bottom left* of each image help to identify the position of the active quadrant visually

Material Contrast

The material or compositional contrast arises from local differences in chemical composition of the object investigated. As shown in Fig. 5.17, the SE yield δ increases weakly with increasing atomic number but the increase is significantly less than that of the BSE coefficient η . Experimental values of δ (see, e.g., the data collection by Joy [5.145]) scatter strongly around a mean curve. The increase of $\delta(Z)$ with Z is mainly due to SE (5.30) generated by emitted BSE near the specimen surface (SE2). At electron energies larger than 5 keV the SE images usually show the same compositional con-

trast as the corresponding BSE image. This situation is illustrated in Fig. 5.23a–c where at normal beam incidence carbon ($Z = 6$) is darker than aluminum ($Z = 13$) in both the SE and BSE image. Table 5.4 gives some numerical values for the compositional contrast for carbon, aluminum, and iron calculated with the related BSE coefficients for normal beam incidence, which qualitatively agrees with the contrasts obtained in Fig. 5.23c. At accelerating voltages below 5 kV, the interpretation of the observed contrast gets quite complicated, and often times there is a reversal of BSE contrast [5.34, 68].

Table 5.4 Compositional contrast calculated according to (5.33) for normal beam incidence $\theta = 0$ for the elements C, Al, and Fe

Element 1 (Z)	Element 2 (Z)	η_1	η_2	$C = \frac{(\eta_1 - \eta_2)}{\eta_2}$
Aluminum (13)	Carbon (6)	0.1530	0.0641	0.581
Iron (26)	Carbon (6)	0.2794	0.0641	0.771
Iron (26)	Aluminum (13)	0.2794	0.1530	0.452

Compare Figs. 5.23b,c and 5.26. $E_0 = 30$ keV

Other Contrasts

Voltage Contrast. The secondary electron image intensity varies if the potential of the specimen is positively or negatively biased with respect to the ground. In principle, a positively biased surface area shows decreased image intensity because low-energy SE are attracted back to the specimen by the electric field. Conversely, a negatively biased surface area shows enhanced image intensity because all SE are repulsed from the specimen. This voltage-dependent variation in contrast is designated as voltage contrast and dates back to the late 1950s [5.193–195]. Strictly speaking all emitted electrons are influenced to some extent by the potential of the sample, but only the SE and, in principle, the Auger electrons can be used for voltage contrast studies [5.196]. The use of Auger electrons is more difficult than that of SE because of the very low yield of AE and the ultrahigh vacuum requirements of AE analysis.

The voltage contrast depends on the energy of the beam electrons and on the properties of the specimen, being most pronounced in the low electron energy region where the SE yield is highest (Fig. 5.12). Biasing the specimen positively or negatively by a few volts not only affects the amount of emitted SE but also their trajectories. This is caused by the fact that the majority of the SE have energies of a few electron volts in contrast to BSE and Auger electrons. The effect of specimen voltage on the SE trajectories is rather complex because it depends on the SE detection geometry, the sample position in the specimen chamber, the properties of the sample, and the operation conditions of the SEM. However, voltage contrast is a valuable tool for the investigation of a wide range of simple faults in microelectronic devices or studies of the potential distribution at grain boundaries obtained on the cross section of varistors at applied low DV voltage and their breakdown behavior at elevated voltage [5.197]. The voltage contrast is also used to characterize the surface charge distribution of ferroelectrics [5.198–200] and piezoelectrics [5.201].

Voltage contrast measurements can also be performed in a dynamic mode on semiconductor devices by pulsing the electron beam (called electron stro-

boscopy [5.202]) synchronously with the device signal as shown by *Plows and Nixon* [5.203]. This dynamic mode allows for quantitative voltage contrast measurements on semiconductor devices at high-frequency operation conditions known as electron-beam testing widely used by the electronics industry for the development, fault diagnosis, and debugging of innovative integrated circuits. High-frequency electron stroboscopy requires high-speed electrostatic beam-blanking systems with subnanosecond time resolution. For very high-frequency electron stroboscopy in the gigahertz range a special transverse-longitudinal combination gate system [5.204] or microwave structure-based beam-blanking techniques have been employed [5.205]. A comprehensive treatment of the fundamentals of voltage contrast and stroboscopy has been published by *Davidson* [5.206] and the state of the art of voltage contrast has been reviewed by *Girard* [5.207]. Furthermore, improvements of voltage contrast detectors as well as of detection strategies are discussed in detail by *Dubbeldam* [5.208]. Voltage contrast is now of a mature age, but the extension to future microelectronics also presupposes an extension in the domain of in situ testing methods and techniques.

Electron Beam-Induced Current. The electron beam generates a variety of signals emitted from the specimen as shown in Figs. 5.2 and 5.14. In semiconductors the primary electrons generate electron-hole pairs or minority carriers within the excitation volume. The mean number of electron-hole pairs is given by E_0/E_{exm} (5.14), where E_{exm} is the mean energy per electron-hole pair-forming event. For example, E_{exm} amounts to 3.6 eV for Si and 2.84 eV for Ge, i. e., one 10 keV electron generates on average approximately 2.7×10^3 electron-hole pairs in Si and 3.5×10^3 in Ge [5.209]. The charge-collection (CC) signal is detected between two electric contacts; one of these contacts collects the electrons and the other one collects the holes. If electromotive forces caused by electron voltaic effects are generated by the beam electrons in the specimen then a charge-collection current I_{CC} designated as an electron beam-induced current (EBIC) flows through the ohmic contacts. If no electron voltaic effects occur,

the beam electrons cause local β -conductivity, where the separation of charge carriers results in an electron beam-induced voltage (EBIV). The most important type of signal of the two charge-collecting modes is EBIC. A detailed treatment of the basic physical mechanisms and applications of the charge-collection mode is given by Holt [5.210, 211], Deamy [5.212], Reimer [5.38], Shea et al. [5.213], Alexander [5.214], and Yakimov [5.215].

EBIC can be observed in SEM simply by connecting a high-gain large-bandwidth amplifier across the specimen using the amplified EBIC signal as a video signal. The input impedance of the amplifier must be very low relative to that of the specimen to measure the true EBIC. For usual electron probe currents of some nanoamperes the charge collection currents are in the order of microamperes since for many materials the mean energy per electron-hole pair is between approximately 1 and 13 eV [5.211]. In contrast to EBIC, for the measurement of the true EBIV an amplifier with a very high input resistance is necessary.

The resolution obtained in the charge-collecting modes depends on the size of the excitation volume within the specimen, which readily can be extracted from Monte Carlo simulation data (Sect. 5.1.2). For the CC mode, a depth and a lateral resolution have to be defined. The depth-dose function, which represents the energy loss per unit depth in the electron-beam direction, determines the depth resolution. The lateral-dose function, which represents the energy loss per unit distance perpendicular to the electron-beam direction, determines the lateral resolution. There are also empirical [5.216] and semiempirical expressions [5.217] as well as several analytical models [5.218, 219] for the depth-dose and for the lateral-dose function as well [5.218, 219].

Electron-beam chopping and time-resolved EBIC can enhance the accuracy of measurements in several cases, e. g., for the estimation of the depth of the p-n junction parallel to the surface [5.220] or allows for quantitative analysis of electrical properties of defects in semiconductors [5.221] and interesting applications for the failure analysis of VLSI (very-large-scale integration) circuits [5.222].

Crystal Orientation Contrast. As previously mentioned, the backscattering coefficient η of a single crystal varies with the direction of the incident beam electrons related to the crystallographic orientation (Sect. 5.1.2). This effect is caused by the variation of the atomic density, which the incident electrons encounter when penetrating into the crystal. In certain crystallographic directions the beam electrons penetrate more deeply. Those directions represent *channels*

for the incident electrons. Changing the direction of the incident electrons relative to the crystallographic orientation causes the so-called crystal orientation or channeling contrast of the BSE image, which amounts to a maximum of approximately 5%. Scanning at low magnification both moves the electron probe and changes the angle of incidence across the field, thereby generating an electron channeling pattern (ECP). At higher magnification the angle of beam incidence varies insignificantly across the small scanned field and channeling contrast is obtained in polycrystalline samples from small grains with different crystal orientations (Fig. 5.27). The information depth of the crystal orientation contrast is in the order of a few nanometers only [5.38] and therefore the contrast is very sensitive to distortions of the crystal at the surface. The channeling contrast reaches the maximum at energies between 10 and 20 keV [5.158, 223].

An orientation anisotropy also occurs for the secondary yield [5.158], which gives rise to an SE orientation contrast.

Magnetic Contrasts. Basically, two different types of magnetic contrast can arise from the interaction of the emitted electrons with the magnetic field of small domains of the specimen.

Type-1 Magnetic Contrast. Secondary electrons are deflected after emission by an external magnetic field, thus generating a magnetic contrast [5.224]. External magnetic fields can exist in natural or synthetic engineered ferromagnetic materials such as magnetic tape, magnetic cards, and computer disks. The fringe fields near the surface are highly inhomogeneous and the SE trajectories are affected by the Lorentz force, which is proportional to $\mathbf{v} \times \mathbf{B}$ where \mathbf{v} is the velocity vector of the SE and \mathbf{B} the magnetic field. The most probable velocity corresponds to the electron energy of a few electronvolts (Sect. 5.1.2, *Secondary Electrons*). The acting Lorentz force deflects the trajectories of the SE

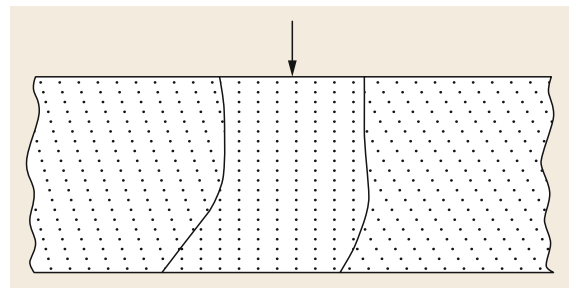


Fig. 5.27 Cross section of a polycrystalline sample having grains with different crystal lattice orientation relative to the electron beam

and the resulting effect can be approximated to a tilt of Lambert's angular SE emission characteristics of the SE (Sect. 5.1.2, *Secondary Electrons*; [5.38]). Figure 5.28 illustrates this effect for two domains in the specimen having oppositely directed external magnetic fields. To observe type-1 magnetic contrast in the case of weak magnetic fields an ETD with a high angular sensitivity, a two-detector system [5.224, 225] or digital image processing [5.226, 227] has been employed. For the type-1 magnetic contrast low beam electron energies are favorable because of the enhanced SE yield and therefore an increased signal-to-noise ratio (SNR). The actual problems related to the complicated mechanism of type-1 magnetic contrast and its relatively low resolution were discussed by *Szmaja* [5.226].

Type-2 Magnetic Contrast. This type of contrast arises from the deflection of backscattered electrons by the internal magnetic field within the specimen [5.228, 229]. Depending on the direction of the magnetic field inside the sample, the BSE are bent toward or away from the surface between consecutive scattering events, i. e., the BSE coefficient is increased in domains where trajectories are bent toward the surface and decrease when bending the BSE trajectories in an opposite direction. To observe a sufficient type-2 magnetic contrast the beam electrons need an energy of at least 30 keV and a relatively high beam current [5.230]. The BSE signal modulation due to magnetic fields inside the specimen is typically less than 1% of the collected current and unwanted topographic contrasts can be reduced

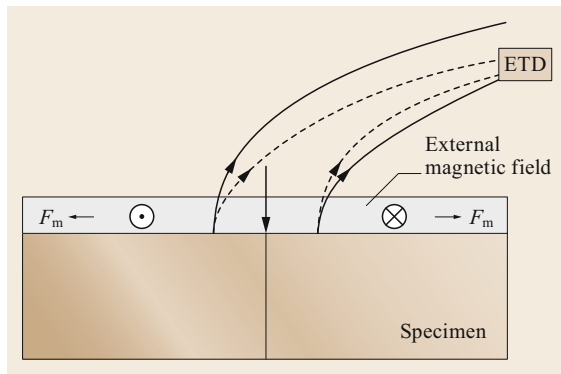


Fig. 5.28 Scheme of type-1 magnetic contrast formation between two domains having oppositely directed external magnetic fields. The dashed lines indicate the SE trajectories for the most probable SE energy to the positively biased Everhart–Thornley detector (ETD) without a magnetic field and the solid lines the trajectories with magnetic fields. The effect of the magnetic force F_m on the SE tilts the trajectories by a small angle toward or away from the ETD, respectively

in comparison with this magnetic contrast by a lock-in technique [5.230, 231].

5.1.4 Specimen Preparation

The specimen preparation procedures required for optimum results of scanning electron microscopic investigations are of crucial importance. The dedicated preparation of the specimen under study is an essential prerequisite for the reliability of the experimental data obtained and has a significance comparable to the performance of the SEM used for the investigation. Unfortunately, the importance of specimen preparation is often underestimated. In principle, the preparation required depends significantly on the properties of the specimen to be investigated as well as on the type of SEM study, i. e., whether imaging of the surface or of cross sections of the sample (Sects. 5.1.2, 5.1.3, and 5.4), crystallographic characterization by electron diffraction techniques (Sect. 5.5), or x-ray microanalytical investigations (Sect. 5.4) are considered. Bearing in mind the variety of specimens having unknown properties on the one hand and the multitude of possible investigation techniques on the other hand, it is obvious that the choice of the most promising preparation procedures can be a rather complex matter. Although the preparation techniques are described in a variety of books [5.10, 23, 232–241], collections of methods [5.242, 243] with updates, and publications, the successful preparation still also depends in many cases on experience and skillful hands.

It is beyond the scope of this chapter to discuss the wide field of preparation techniques. Therefore, a brief rather general outline of specimen preparation with reference to specific literature will be given. Figure 5.29 schematically outlines some important preparation procedures used for inorganic and organic materials. As a general rule, a successful investigation by SEM requires specimens, which have clean surfaces, sufficient electrical conductivity, are not wet or oily, and possess a certain radiation stability, to resist electron irradiation during imaging. Another critical parameter is a conductive pathway that needs to be created between the specimen and the holder, otherwise the specimen will exhibit significant instability under the electron beam (such a pathway could be achieved by using conductive paint or tape). An exception of this rule is allowed only for SEMs working at ambient pressure (say at low vacuum; Sect. 5.3), which permits direct imaging of dirty, wet, or oily samples, although radiation damage occurs with radiation-sensitive specimens. The goal of an ideal preparation consists in making specimens accessible for high-vacuum SEM studies without changing the relevant properties under investigation.

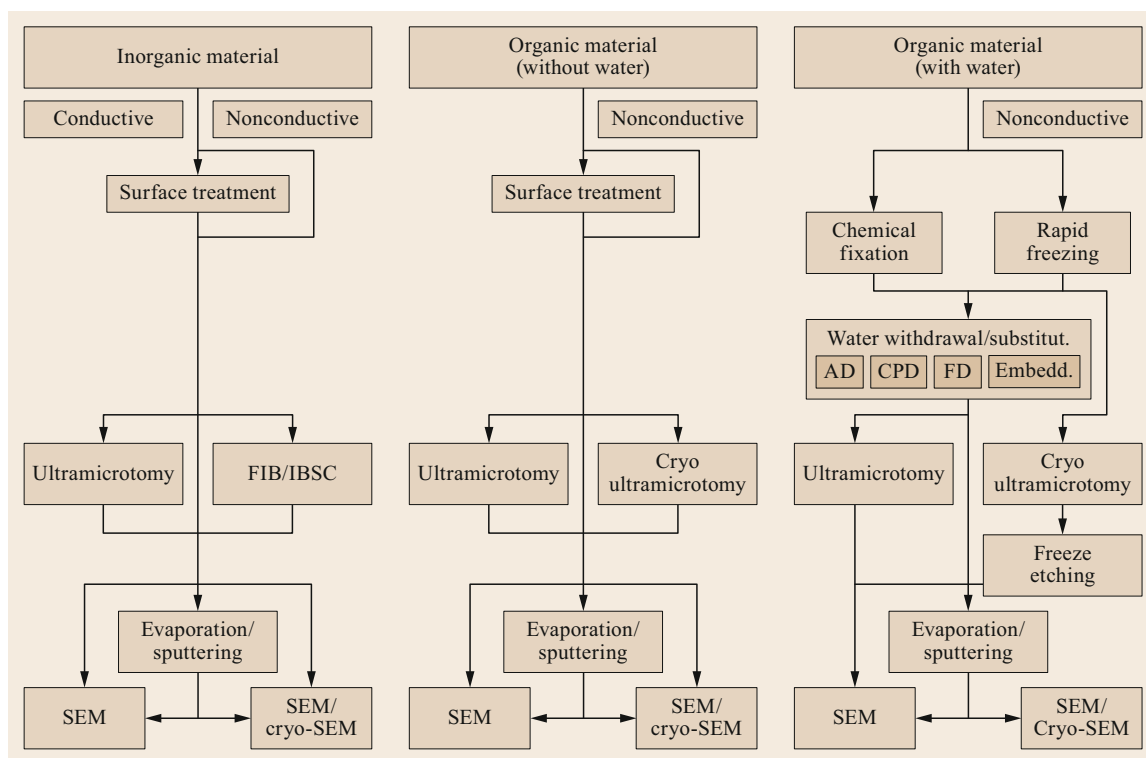


Fig. 5.29 Schematic drawing of important preparation procedures for SEM used for inorganic and organic materials with and without water. AD, air drying; CPD, critical point drying; FD, freeze drying; FIB, focused ion beam; IBSC, ion beam slope cutting

Many inorganic samples with sufficient electrical conductivity, such as metals, alloys, or semiconductors, can be imaged directly with little or no specimen preparation (Fig. 5.29). This is one very useful feature of scanning electron microscopy. In some cases a surface treatment may be required, e. g., to clean the specimen surface with an appropriate solvent, possibly in an ultrasonic cleaner, and with low-energy reactive gas plasma for the removal of hydrocarbon contamination [5.244]. The cleanings are suitable to prepare electrically conductive specimens for surface imaging in SEM. In the case of nonconductive samples, such as ceramics, minerals, or glass, a conductive coating [5.245] with a thin metal film (e. g., gold, platinum, tungsten, chromium) or a mixed conductive film (e. g., gold/palladium, platinum/carbon, platinum/iridium/carbon) is required for good-quality imaging. For x-ray microanalysis carbon coating is preferred because of its minimum effect on the x-ray spectrum. The coating can be performed by evaporation [5.232, 243, 246, 247], by diode sputtering [5.248], or by planar magnetron sputtering [5.249, 250]. High-quality conductive thin-film coating for high-resolution SEM (Sect. 5.2) can be performed in an oil-free high vacuum by both evaporation,

using e. g., tungsten, tantalum/tungsten, platinum/carbon, or platinum/iridium/carbon, and rotary shadowing methods [5.247, 251–253] as well as by ion beam and by Penning sputtering with, e. g., chromium, tantalum, and niobium [5.254].

For the study of microstructural features (Sect. 5.5) and for microanalytical investigations (Sect. 5.4) a flat surface is required, therefore rough specimen surfaces have to be flattened by careful grinding and subsequent polishing according to standard metallographic methods [5.255]. To remove mechanical deformations caused by grinding and mechanical polishing, a final treatment with electrochemical polishing or ion beam polishing may be necessary. In case of polycrystalline and heterogeneous material, selective etching by ion bombardment may be used, which generates a surface profile caused by locally different sputtering yields, thus giving rise to topographic contrast of grains and the individual materials [5.256, 257].

Often, specimens need to be characterized and analyzed both above and below the surface, e. g., if the subsurface composition of the material, process diagnosis, failure analysis, in situ testing, or three-dimensional reconstruction of the spatial microstructure is required.

Flat cross sections through the specimen can be obtained by ultramicrotomy ([5.258–260]; the block face can be used for SEM imaging), broad ion beam cutting [5.261–263], an FIB technique [5.264–268], or by a combination of an FIB system with a field-emission SEM (SEM/FIB), which allows the precise positioning of the cross section and, most importantly, realtime high-resolution SEM imaging of the cutting process, which enables, among other things, the examination of the spatial structure [5.269–274]. An example for two perpendicular vertical cross sections into an integrated circuit is shown in Fig. 5.30. The combined SEM/FIB additionally can be equipped with analytical techniques such as energy-dispersive x-ray spectroscopy and electron backscatter diffraction allowing for three-dimensional elemental and structural analysis of the interior of the specimen.

The other class of samples consists of organic material, which usually has an insufficient electrical conductivity for scanning electron microscopy. Although biological specimens contain water—the water content ranges in human tissues from approximately 4 to 99% [5.275]—many other organic materials do not, e. g., numerous polymers. The preparation strategies to be applied to specimens with and without water differ (Fig. 5.29), although there are also some similarities between them.

The surface treatment of organic specimens without water, such as cleaning, grinding, polishing, and etching by dissolution, chemical attack, or ion bombardment, has many similarities to the surface treatment of inorganic materials. A detailed discussion of and the

recipes for specific preparation procedures for polymers are given in the chapter *Specimen preparation methods* in the book by Sawyer and Grubb [5.32]. Analogous to nonconductive inorganic materials, conductive coating with a thin metal film (e. g., gold, platinum, tungsten, chromium) or a mixed conductive film (e. g., gold/palladium, platinum/carbon, platinum/iridium/carbon) is required for good-quality imaging. If the subsurface structure of the material has to be studied, flat cross sections usually are prepared by ultramicrotomy or cryo-ultramicrotomy, depending on the cutting behavior of the specimen under study. In principle, cutting with ions and imaging and analysis with electrons by using a combined FIB/SEM tool is possible also with polymers. It was recently shown that ion milling is possible, e. g., with rubber ([5.276]; also Fig. 5.31) and with polymer material (Fig. 5.32).

Most of the organic specimens that contain water are biological samples. A small fraction of water-containing specimens is nonbiological, e. g., hydrogels. The water-containing specimens cannot be investigated in the wet state in the SEM in high vacuum without some additional preparation steps. In principle, three different preparation strategies exist to make wet specimens accessible to SEM investigations:

1. Withdrawal of the water
2. Replacement of the water by some vacuum-resistant material such as resins or freeze substitution [5.277, 278] of the ice of the rapidly frozen specimen by some organic solvent
3. Rapid freezing of the water.

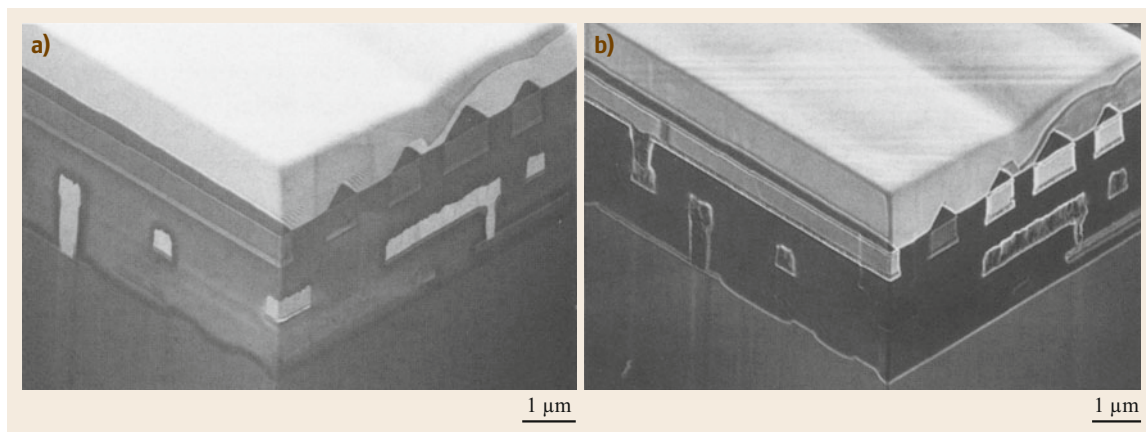


Fig. 5.30a,b Integrated circuit with two perpendicular vertical cross sections into the interior. FIB sectioning was performed with the CrossBeam[®] tool from Carl Zeiss NTS. The secondary electron images using the EDT were obtained by the field-emission SEM (a) at 3 kV and by the FIB system (b) at 5 kV. Both micrographs reveal the site-specific internal structure of the integrated circuit, although some features occur with different contrast caused by different mechanisms of SE generation by electrons (a) and ions (b). (Courtesy of Carl Zeiss NTS, Oberkochen, Germany)

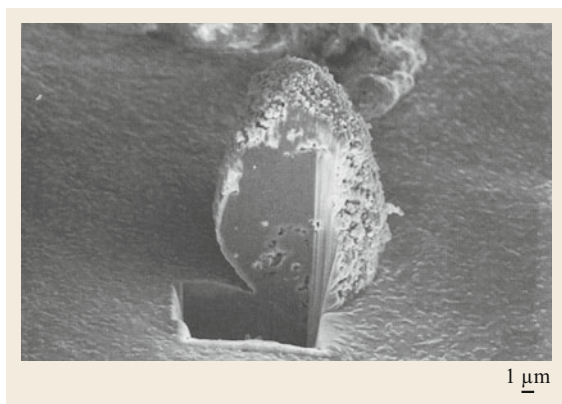


Fig. 5.31 Secondary electron micrograph (*through-the-lens* detection) of a site-specific FIB cross-sectioned abrasive wear particle of a tyre supported onto carbon. The FIB sectioning and imaging at 5 kV was performed with the CrossBeam® tool combining a focused ion beam system with a field-emission SEM [5.270]. The cross section reveals the interior features of the rubber particle. (Courtesy of Carl Zeiss NTS, Oberkochen, Germany)

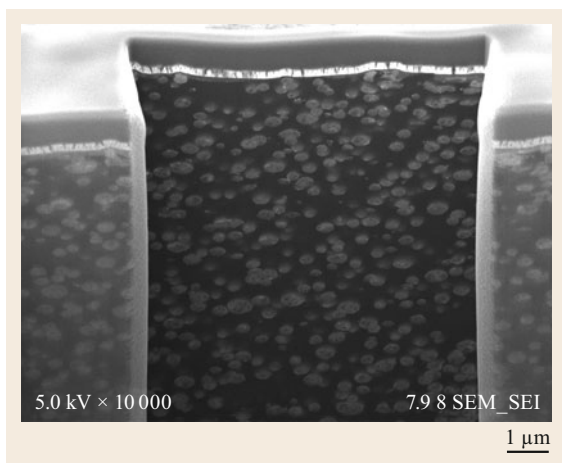


Fig. 5.32 SE micrograph showing cross section of acrylonitrile butadiene styrene (ABS) polymer produced using JEOL JIB-4600F SEM-FIB. Image is taken using 5 kV

Irrespective of the preparation strategy used the native spatial structure of the specimen should be maintained. Air drying, which is the most simple method of drying, is not suitable for drying soft specimens because the surface tension induces remarkable forces during the process of air drying, deforming the specimen irreversibly [5.279, 280]. Figure 5.29 shows different paths, which can be used, even though the degree of structural preservation depends on the preparation procedures applied. The different preparation procedures

have been described in detail [5.236, 240, 243, 279, 281–283]. Among the different preparation methods rapid freezing is the method of choice for preparing biological specimens in a defined physiological state [5.240]. In the case of chemical fixation, which may create artifacts [5.283], the water of the sample has to be withdrawn or replaced afterward. If the surface structure of the specimen has to be studied, then the specimen surface has to be coated with a thin conductive film prior to SEM investigation. If the interior of the specimen has to be studied, the sample has to be opened by sectioning with the ultramicrotome or possibly FIB and subsequently coated. In the case of physical fixation, i. e., rapid freezing, the specimen has to be opened by freeze fracturing (for a review see [5.284, 285]), cryosectioning, or now possibly by ion milling the frozen-hydrated sample (ion milling in ice is possible [5.272]). After short partial freeze drying (also called freeze etching), the fracture face or block face has to be properly coated by a conductive film and then can be directly analyzed in the cryo-SEM [5.285–288]. Another possible path is complete freeze-drying and subsequent conductive coating of the sample, which then can be analyzed at room temperature in the SEM.

5.1.5 Radiation Damage and Contamination

The inelastic electron–specimen interaction inevitably damages the irradiated specimen and can induce contamination at the specimen surface. Although radiation damage, in particular of organic specimens, has been extensively investigated for thin films in transmission electron microscopy, comparatively little has been systematically studied for irradiation-sensitive samples in SEM. This may be due to the fact that the interpretation of radiation damage in TEM is easier because of the uniform ionization density through thin specimens. In bulk specimens, however, the ionization density is a function of the depth (for a detailed treatment of the depth–dose function see [5.289]) and a layer below the surface at the maximum ionization density will be damaged faster than others within the electron range R (Figs. 5.13 and 5.14). According to the Bethe stopping power in (5.26), the damage will be proportional to $1/E \ln(1.166E/J)$. Table 5.5 gives values of the stopping power for carbon and protein for electron energies from 0.1 to 30 keV, which show the increase of the stopping power with decreasing electron energy. It is commonly assumed that the shape of the depth–dose curve is not a function of either the primary electron energy or the material when normalized to the electron range [5.289]. That means that the layer with the maximum ionization density approaches the surface as the electron energy decreases.

Table 5.5 Mean ionization potential J ((5.27) and (5.28), respectively) and the Bethe stopping power dE/ds (5.26) for carbon and protein at different electron energies

Sample	Parameter	$E = 0.1 \text{ keV}$	$E = 1.0 \text{ keV}$	$E = 5.0 \text{ keV}$	$E = 10 \text{ keV}$	$E = 30 \text{ keV}$
Carbon	J (eV)	56.5	92.8	98.5	99.2	100.4
	dE/ds (eV/cm)	-56.4	-19.7	-6.4	-3.7	-1.5
Protein	J (eV)	50.6	78.0	82.0	83.0	83.0
	dE/ds (eV/cm)	-43.8	-14.2	-4.5	-2.6	-1.1

The values listed for dE/ds have to be multiplied by 10^7 . The following values were used for the calculation [5.133]: carbon: $Z = 6$; $A = 12$; $\rho = 2 \text{ g cm}^{-3}$; protein: mean atomic number $\langle Z \rangle = 3.836$; $A = 7.7$; $\rho = 1.35 \text{ g cm}^{-3}$

In organics, the radiation breaks chemical bonds due to the transfer of typically tens of electron volts to an electron at the site of the interaction of many intra- and intermolecular bonds, which generates free radicals [5.290–292]. Many excited species will very rapidly recombine in 10^{-9} – 10^{-8} s and will reform the original chemical structure dissipating the absorbed energy as heat. Some recombinations will form new structures, breaking chemical bonds and forming others. If the material was initially crystalline, defects will form and gradually it will become amorphous. In addition to these structural changes the generated free radicals will rapidly diffuse to and across the surface or can evaporate, i. e., loss of mass and composition change will occur [5.84, 85, 160, 191, 293–296]. Bubbles may form at high dose rates when volatile products are trapped. Not only the beam electrons damage the organic sample but also fast secondary electrons ($E_{SE} > 50 \text{ eV}$) can produce damage outside the directly irradiated specimen area [5.297]. Furthermore, beam-induced electrostatic charging and heating can also damage organic samples. Conductive coating of the organic specimen, as suggested for inorganic materials by Strane et al. [5.298], can keep trapped free radicals as well as reduce beam-induced temperature rise or electrostatic charging [5.299]. Lowering of the temperature of the specimen is a further measure to reduce the sensitivity of an organic specimen to structural damage and mass loss. However, the reduction factor depends considerably on the material of the specimen.

The radiation damage mechanisms in semiconductors are different from those described above. As mentioned in Sect. 5.1.1, *Detectors* and Sect. 5.1.3, *Electron Beam-Induced Current*, the incident electrons generate electron-hole pairs, which will be trapped in the silicon oxide layer due to their decreased mobility. This can generate space charges, which in turn can affect the electronic properties of the semiconductor.

Beam-induced contamination is mass gain, which occurs when hydrocarbon molecules on the specimen surface are polymerized by the beam electrons. The polymerized molecules have a low surface mobility, i. e., the amount of polymerized molecules in-

creases in the surface region where polymerization takes place. There are two main sources for hydrocarbon contamination: (1) gaseous hydrocarbons arising from oil pumps, vacuum grease, and possibly O-rings, and (2) residual hydrocarbons on the specimen. Several countermeasures exist to reduce the contamination to a tolerable level [5.300–302]. The amount of gaseous hydrocarbons is substantially reduced when the SEM is operated with an oil-free pumping system and a so-called cold finger (liquid nitrogen cooled copper plate) located above the specimen. Further, the contamination rate falls more rapidly as the specimen temperature is lowered, and below -20°C contamination is difficult to measure [5.301]. This is caused by the reduced diffusion of hydrocarbons on the specimen. In some cases, preirradiation of a large surface area with the electron beam is helpful, which immobilizes (polymerizes) hydrocarbons around the field of view to be imaged. Finally, specimens are mostly exposed to the atmosphere before transfer into the specimen chamber. Weakly bound molecules (e. g., hydrocarbons) can be completely eliminated by gently heating the sample in the specimen exchange chamber (low vacuum) to 40 – 50°C for several minutes by a spot lamp [5.303]. A detailed topical review on the radiation damage and contamination in electron microscopy is given by Egerton et al. [5.87].

5.1.6 Applications

Scanning electron microscopy is an indispensable tool for investigations of a tremendous variety of specimens from very different fields such as materials science, mineralogy, geology, semiconductor research, microelectronics, industry, polymer research, ecology, archeology, art, and life sciences. Although the investigations are not restricted just to imaging of surface structures, the majority of SEM studies apply the imaging modes. As mentioned previously, considerable additional information about the local elemental composition, electronic and magnetic properties, crystal structure, etc. can be acquired when the SEM is combined with supplementary equipment such as electron and x-ray

spectrometers to take advantage of the energy spectra of the emitted electrons and x-rays. Table 5.6 surveys the information, which can be obtained from inorganic and organic specimens not containing water. Further, in situ scanning electron microscopy allows for different specific specimen treatments in the specimen chamber [5.25], which serves as a microlaboratory, and the simultaneous observation of the specimen response (Table 5.7).

The advancement of nanoscale science and technology demands the manipulation of nano-objects at the molecular level and ultimately the manufacture of things via a bottom-up approach. For instance, a four-nanoprobe system can be installed inside a field-

emission SEM, which may be used for gripping, moving, and manipulating nano-objects, e. g., carbon nanotubes, setting up electric contacts for electronic measurements, tailoring the structure of the nano-object by cutting, etc. and for making nanostructures [5.304]. The SEM in this setup allows for visualization of the four nanoprobe operating inside the specimen chamber as well as the process of formation of microstructures.

Less spectacular, but nevertheless important, are applications of scanning electron microscopy to image macroscopic samples in the millimeter range at very low magnification (about $10\times$ to $100\times$), which cannot be seen clearly by the eye or by the light microscope for some reasons. Two examples from very different fields

Table 5.6 SEM applications on specimens from materials science, mineralogy, geology, polymer science, semiconductors, and microelectronics (state-of-the-art preparation and image analysis techniques are required to take full advantage of the capabilities of SEM)

Specimen	Information
Metals, alloys, and intermetallics	<i>At the specimen surface:</i> Topography (three-dimensional); microroughness; cracks; fissures; fractures; grain size and shape; texture; phase identification; localization of magnetic domains; size and shape of small particles; elemental composition; elemental map; grain orientation; defects <i>Inside the specimen:</i> Grain and phase structures; three-dimensional microstructure; cracks; fissures; material inclusions; elemental composition
Ceramics, minerals, glasses	<i>At the specimen surface:</i> Topography (three-dimensional); microroughness; cracks; fissures; fractures; grain size and shape; pores; phase identification; size and shape of small particles; elemental composition <i>Inside the specimen:</i> Grain and phase structures; three-dimensional microstructure; cracks; fissures; material inclusions; pores; elemental composition
Polymers, wood	<i>At the specimen surface:</i> Morphology; topography (three-dimensional); microroughness; cracks; fissures; fractures; pores; size and shape of small fibers and particles; fiber assemblage in woven fabrics; elemental composition <i>Inside the specimen:</i> Cracks; fissures; fractures; pores; composite structure; elemental composition
Semiconductors, integrated circuits, microelectronic devices	Defect studies (with CL); metallization and passivation integrity; quality of wire bonds; electrical performance; design validation; fault diagnosis; testing

Table 5.7 In situ treatments in SEM and available information about specimens from materials science

Treatment	Information
Static and dynamic deformation, e. g., by tension, compression, bending, machining	Kinematic processes during deformation; submicrometer cracks visible only under load; localized deformation centers, e. g., slip bands, crack nucleation; deformation-induced acoustic emission
Laser irradiation, e. g., in pulse mode, Q-switch mode	Phase transformations; structural modifications; crack formation due to thermal shock; diffusion processes; laser-induced surface melting and evaporation processes; vapor deposition on substrates; cumulative effects of multiple laser pulses
Ion beam irradiation	Depth profile/cross section; grain boundaries; spatial microstructure; internal grain and phase structures
Electrical and magnetic effects	Reversible and irreversible breakdown of voltage barriers; size distribution of magnetic and ferroelectric domains; orientation distribution of magnetic and ferroelectric domains; effects accessible by EBIC, EBIV, and CL

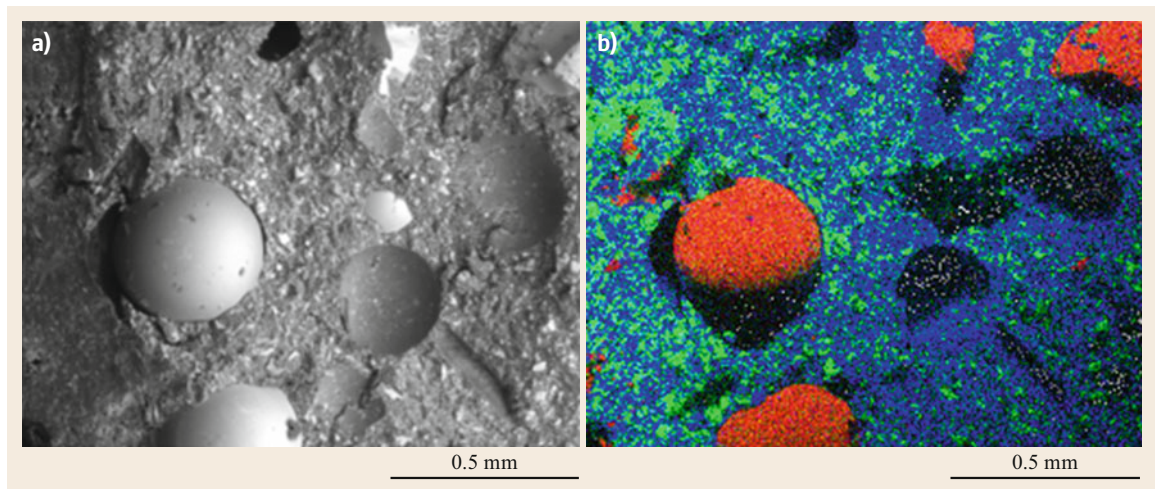


Fig. 5.33a,b BSE micrograph (a) showing the microstructure of the material used to paint the white reflecting road demarcation lines; some of the light-reflecting glass spheres are missing (depressions in the paint surface). Overlay EDS map of various constituents is shown as well (b)—Ti (blue), Ca (green), and Si (red). For safety reasons protruding sharp-edge particles are embedded in the material to generate high friction between the tires and the white lines

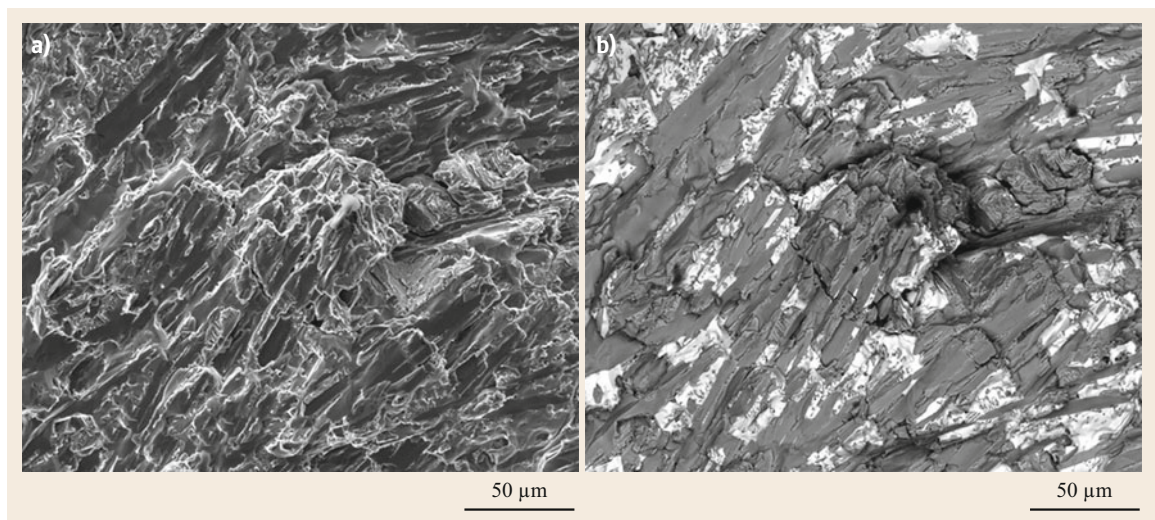


Fig. 5.34a,b Secondary (a) and backscatter (b) images of metal fracture recorded at 20 kV. The contrast in the SE image shows the overall surface morphology, whereas the BSE image highlights the location of the high Z material (white patches)

are shown in Figs. 5.33 and 5.34 taking advantage of the large depth of focus as well as distinct topographic and material contrast.

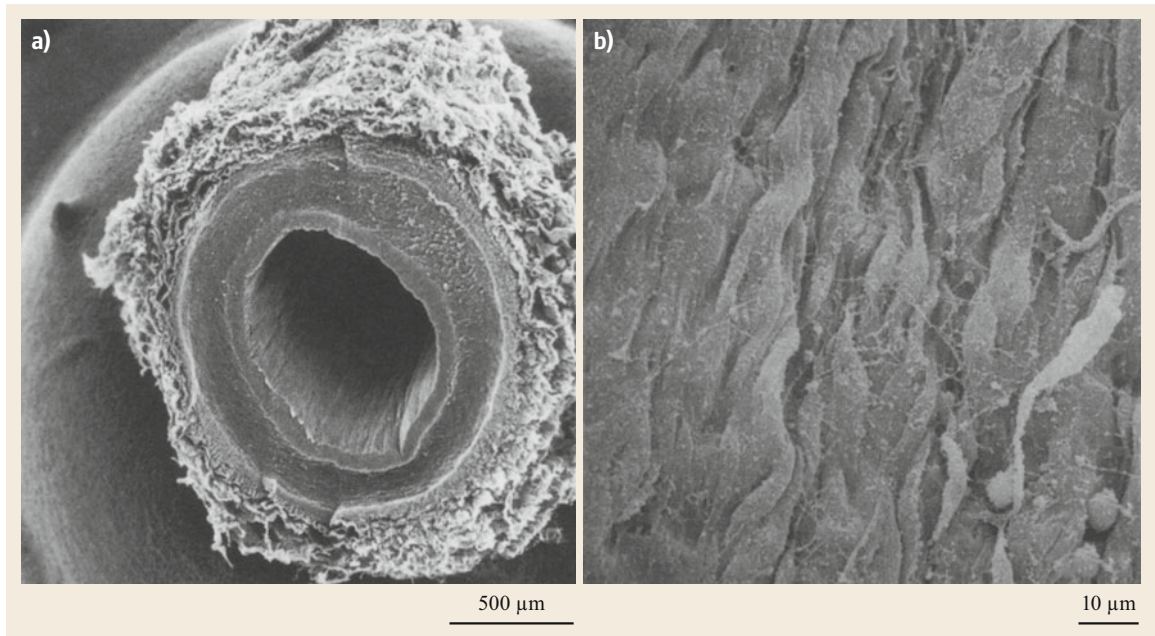
Working in the low-magnification range, the depth of focus limit in the SEM (Sect. 5.1.1, *Specimen Tilt- ing and Stereo Imaging*) can be overcome by recording stacks of through-focus images (as in conventional and confocal optical microscopy), which are digitally post-processed to generate an all-in-focus image [5.305]. The application of the technique is advantageous when BSE imaging of spongy specimens is required, as

demonstrated with examples from the study of human osteoporotic bone [5.305].

In life sciences, application of SEM mainly for morphological studies is also widespread and started when commercial SEMs became available in the late 1960s [5.306]. However, in life sciences SEM is used less than TEM. Table 5.8 provides a survey of the specimens and information that can be obtained by SEM. Engineered biomaterials and tissues are becoming increasingly important in biomedical practice and it has become clear that cellular responses to materials de-

Table 5.8 SEM applications on specimens from life sciences (state-of-the-art preparation and image analysis techniques are required to take full advantage of the capabilities of SEM)

Specimen	Information
Bones, teeth, dentin, cartilage, hairs, fingernails, toenails	<i>At the specimen surface:</i> Morphology; ultrastructure, pathological alterations of ultrastructure, microstructure, roughness; cracks; fissures; fractures; elemental composition <i>Inside the specimen:</i> Three-dimensional microstructure; cracks; fissures; elemental composition
Biomaterials, e. g., gallstone, kidney stone, tartar, calcification	<i>At the specimen surface:</i> Morphology; microstructure, cracks; fissures; fractures; grain size and shape; size and shape of small particles; elemental composition <i>Inside the specimen:</i> Grain size and shape; microstructure; cracks, fissures; material inclusions; cavities; elemental composition
Soft tissues cells, bacteria	<i>At the specimen surface:</i> Morphology; topography (three-dimensional); roughness; ultrastructure; pathological alterations of ultrastructure; size and shape of cells and bacteria; elemental composition <i>Inside the specimen:</i> Ultrastructure; pathological alterations of ultrastructure; elemental composition
Biomaterials, implants, prostheses	Morphology; biocompatibility; biostability; ultrastructure of and degradation mechanisms at the bone–implant interface; mineral apposition; cell and tissue apposition; adsorption behaviors of fibrinogen, albumin, and fresh plasma on implants for the cardiac–vascular systems; fault diagnosis of prostheses; failure analysis after loading tests in simulator; wear of prostheses; surface erosion of prostheses after use

**Fig. 5.35a,b** Secondary electron micrograph of the cross-sectioned radial artery at low magnification (a) and of the endothelial cells at medium magnification (b). The vessel was critical point dried and sputter coated with gold

pend on structural properties of the material at both the micrometer and nanometer scale. SEM is one of several methods for controlling material properties on both of these scales and thus it is increasingly used to study those materials.

Scanning electron microscopy can be used for comparative morphological studies of tissues as demonstrated by the application in cardiovascular surgery

to detect endothelial damage caused by skeletonization [5.307]. In cardiovascular surgery, the radial artery is increasingly used for myocardial revascularization because of its presumed advantageous long-term patency rates. The vessel can be harvested as a pedicle or skeletonized. The SEM reveals the endothelial morphology (Fig. 5.35), and thus allows comparison of the skeletonization technique with pedi-

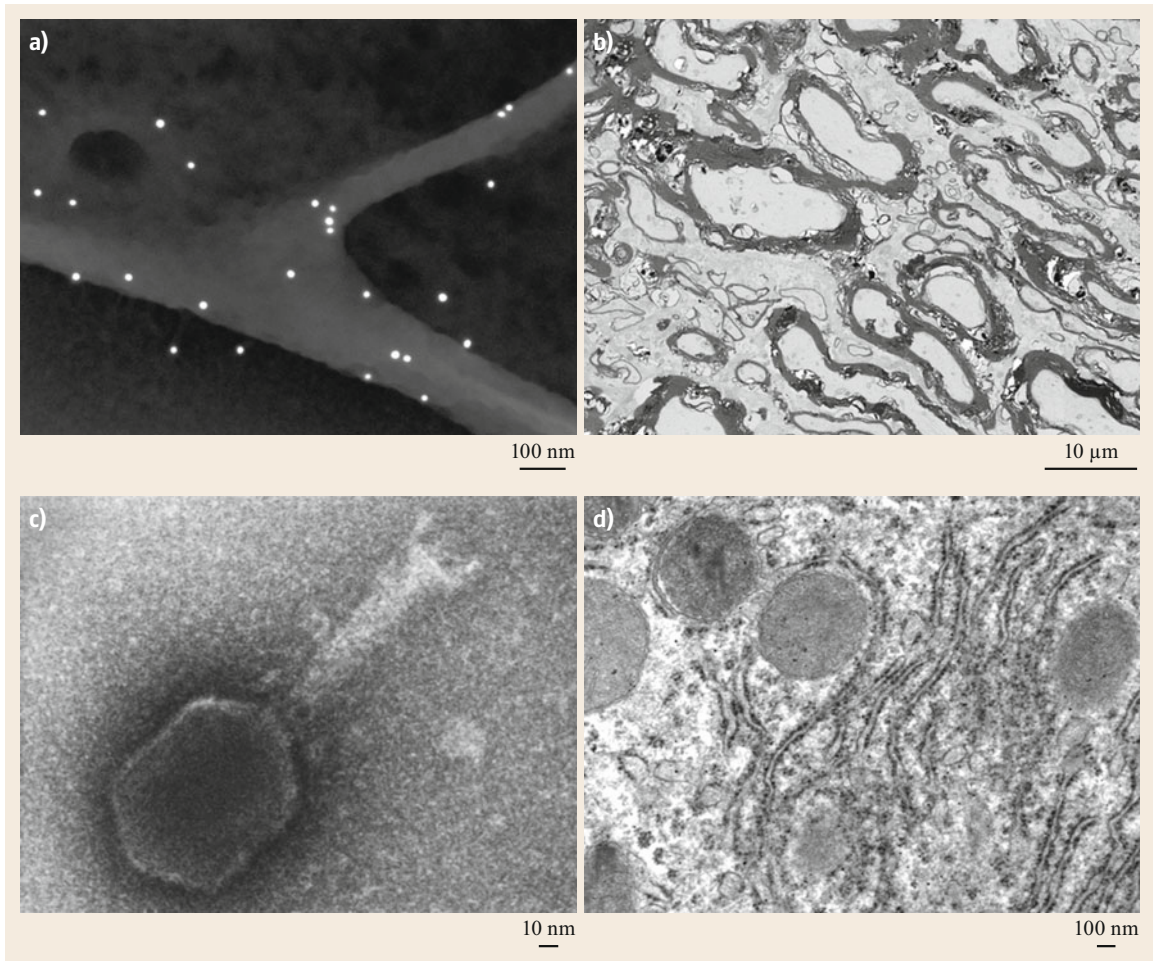


Fig. 5.36 (a) 10 nm Au-labeled cell (BSE image, 10 kV); (b) mouse brain thin section (through-the-lens BSE image at 2 kV, inverted); (c) T4 bacteriophage (STEM-in-SEM image, 30 kV); (d) kidney thin section (STEM-in-SEM image, 30 kV)

cle preparation using either an ultrasonic scalpel or scissors.

Figure 5.36 shows additional examples of SEM imaging of various biological specimens—from immune-labeled cells, to pathology of brain and kidney and even viruses.

Microtechnology and *microelectromechanical systems* (MEMS) are additional fields in which SEM is used as a tool for monitoring processes, detecting defects, or measuring sizes and distances, e. g., in micromachines and micromechanical or micromachining processes [5.308–311].

The acquisition of quantitative data about the third dimension (stereo, 3-D) of surfaces and interior specimen structures was previously mentioned (Sect. 5.1.4). In general, this requires digital image analysis, specific instrumentation for the SEM (e. g., specimen stage, detectors), and special specimen preparation (e. g., ultramicrotome, IBSC, FIB). For example, techniques such as array tomography [5.312] and serial block-face SEM [5.313] have become prominent avenues for tomographic information collection for biological specimens using SEM.

5.2 Field-Emission Scanning Electron Microscopy

The diameter of the electron beam at the specimen surface sets a fundamental lower limit to the signal localization and, therefore, also to the resolution, which can potentially be obtained. As discussed in Sect. 5.1.2 and shown in Figs. 5.13 and 5.14, the SE and BSE are emitted from a surface area, which commonly is much larger than the beam diameter at the specimen surface. The large emitting area is caused by multiple elastic and inelastic electron-scattering events within the excitation volume, whose size depends on the specimen composition and energy of the beam electrons. Only the SE1 and BSE1 generated as the beam enters the specimen carry local information, while the SE2 and BSE2 carry information about the larger region surrounding the point of beam entrance (Fig. 5.14). High-resolution information can be obtained from SE1 and BSE1 generated by an electron probe with a diameter at the specimen surface of about 1 nm or even less. A probe of that small size can be achieved by using field-emission electron sources, electromagnetic lenses with low aberration coefficients (5.7), (5.8), and (5.10), and both highly stabilized acceleration voltage (5.8) and objective lens current. High-resolution scanning electron microscopy at conventional acceleration voltages—that is 5–30 kV—will be treated in Sect. 5.2.1. Alternatively, high-resolution information, in principle, can also be achieved when the excitation volume is reduced to a size similar to the SE1 and BSE1 emitting area by using low-energy beam electrons. By definition, electrons below 5 keV are considered low-energy beam electrons and, consequently, scanning electron microscopy at low energies is called scanning low-energy electron microscopy or low (acceleration)-voltage scanning electron microscopy (LVSEM). This type of scanning electron microscopy will be treated in Sect. 5.2.2. However, the majority of commercial high-resolution SEMs are capable of operation at both conventional energies, i. e., from 5 to usually 30 keV, and at low energies, i. e., below 5 keV down to usually 0.1 keV (current models of FESEM can go down to 10 eV).

5.2.1 High-Resolution Scanning Electron Microscopy

Electron Guns

Two different types of electron guns are currently available as sources for high-resolution SEM: the cold field-emission gun (CFEG) and the so-called Schottky emission cathode (SEC). The characteristic parameters of the different electron guns are listed in Table 5.1.

Schottky emission cathodes are of the ZrO/W(100) type—also called ZrO/W(100) thermal field emitter

(TFE)—and have a tip radius of $\approx 0.1\text{--}0.5\ \mu\text{m}$ [5.314]. The work function of the TFE is lowered to about 2.8 eV. In operation the SEC is heated to about 1000–1500 K and electrons are extracted by a high electric field, which lowers the potential barrier (Schottky effect). The SEC brightness is about three orders of magnitude higher and the energy spread of the emitted electrons is about a factor of 2 lower than those for the thermionic W-cathode. Presently, the SEC in commercial high-resolution SEM is used more frequently than the CFEG.

The CFEG usually consists of a very sharp [100] or [321] oriented tungsten single crystal and two anodes in front, which extract (first anode) and accelerate or decelerate (second anode) the electrons by the electric field to a final energy $E_0 = eU$ (Fig. 5.37). Caused by the small tip radius r , which is in the range of 10 to about 50 nm, the electric field strength amounts to at least $10^8\ \text{V cm}^{-1}$ with an extraction voltage of approximately 4–5 kV applied between the first anode and the tip. Because of the high field strength at the tip the width of the potential barrier is significantly reduced and field emission takes place. The field-emission current density j_c is described by the Fowler–Nordheim equation

$$j_c = \frac{c_1 |E|^2}{\phi} \exp\left(-\frac{c_2 \phi^{3/2}}{|E|}\right), \quad (5.42)$$

where $|E| \approx U_1/r$, c_1 and c_2 depend weakly on $|E|$, and ϕ is the work function of tungsten. The density j_c depends strongly on $|E|$, and E can be varied by U_1 . The

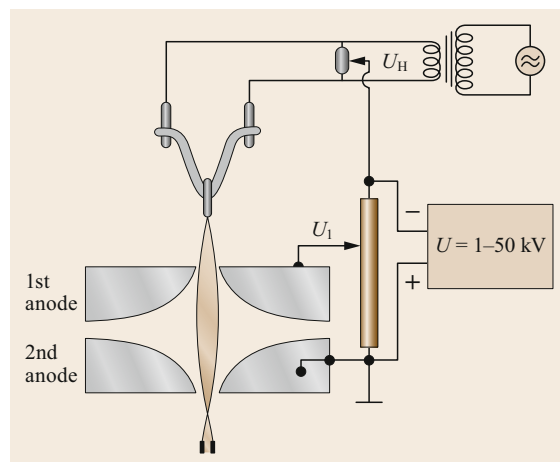


Fig. 5.37 Schematic drawing of the field-emission gun with an electrolytically polished sharp monocrystalline tungsten tip. U , acceleration voltage; U_1 , extraction voltage. (After [5.30])

cold FEG (CFEG) is operated at room temperature and generates a current density of typically $2 \times 10^5 \text{ A cm}^{-2}$. However, after several hours of work adsorbed gas layers have to be removed by short heating to about 2500 K (flashing), otherwise the emission current becomes very unstable. The distinct advantage of the cold FEG is the low-energy spread (0.2–0.3 eV).

Field-emission guns require ultrahigh vacuum in the order of 10^{-8} – 10^{-9} Pa in the gun chamber, which is generated by ion-getter pumps. This means that SEMs equipped with an FEG need a sophisticated and consequently cost-intensive vacuum system.

Electron Lenses

Electron lenses are used to demagnify the virtual source size, which amounts to 3–5 nm for the cold FEG, and about 20–30 nm for the Schottky emitter. To obtain an electron-beam diameter of about 1 nm or less a demagnification of only 10–100 \times is required in contrast to up to about 5000 \times for the thermionic emission triode gun (Sect. 5.1.2, *Electron Lenses*). To achieve the smallest effective electron probe diameter, the spherical and the chromatic aberration constants have to be as small as possible ((5.7), (5.8), and (5.10)). In the conventional SEM usually large working distances ranging from about 10 to 40 mm are used. Typical values of the spherical aberration constant C_s are 10–20 mm. Since C_s increases strongly with increasing WD ($C_s \approx \text{WD}^3$) sufficiently small values of $C_s \approx 1$ –2 mm can be achieved only with very short WD, i. e., the focus of the electron beam has to be inside (so-called *in-lens* type) or very close to the objective lens (frequently called *semi-in-lens* with a snorkel-type conical objective lens [5.315]). The chromatic aberration constant C_c corresponds approximately to the focal length of the objective lens for large WD, i. e., also the chromatic aberration is strongly lowered at a very short WD. The shortest WD of the *in-lens*-type SEM is about 2.5 mm in order to secure a specimen traverse in the x - and y -direction perpendicular to the optical axis as well as specimen tilt angles up to a maximum of $|\pm 15^\circ|$. Larger tilt angles obviously require a larger work distance. To obtain the minimum effective electron probe diameter under these conditions, the optimum aperture α_{opt} has to be used (5.11). Presently, the highest resolution obtained with the *in-lens*-type FESEM at 30 keV using a test sample amounts to 0.4 nm [5.316].

In addition, hybrid lens design SEM columns have become quite popular in recent years. Such column design typically features some form of a combination electrostatic-electromagnetic objective lens to provide the user with utmost versatility in terms of the types of samples that can be imaged and analyzed. For fur-

ther review of these designs, please see *Bell and Erdman* [5.34].

Detectors and Detection Geometries

The detectors used in field-emission scanning electron microscopes (FESEM) have been described in Sect. 5.1.1, *Detectors*. The detection geometry depends on the particular type of FESEM. The instruments using the conventional specimen position outside the objective lens (*out-lens*), i. e., the WD is in the range of about 5–30 mm, are commonly equipped with an ET detector located laterally above the specimen and a BSE detector located centrally above the specimen. The *semi-in-lens* or electrostatic/electromagnetic combination lens instruments, where the specimen is outside but immersed in the field of the objective lens, usually have both the detector arrangement of the *out-lens*-type SEM and the *through-the-lens* detection, thus combining the advantages of both detection geometries. The *in-lens*-type SEM is restricted to *through-the-lens* detection (Sect. 5.1.1, *Detection Strategies*).

Specimen Stages

The purpose of the specimen stage in high-resolution scanning electron microscopes is of course the same as in conventional SEM, i. e., the stage has to allow for precise backlash-free movement, tilting, and possibly rotation of the sample during the investigation. As for conventional SEM, there are optionally special specimen stages available that allow investigations of the specimen at elevated temperature, during different types of mechanical deformation, at positive or negative bias, and last at low temperature. Independent of the special type of specimen stage, a higher stability in terms of mechanical vibrations as well as mechanical or thermal drift is required to avoid any deterioration of the performance of the high-resolution SEM. The *in-lens*-type SEMs use side-entry specimen holders, which are almost identical to the ones used in TEMs (Sect. 5.1.1, *Specimen Stages and Attached Equipment*). However, the limited space available in this type of SEM places some restrictions on the specimen stage for the ultimate resolution of *in-lens*-type FESEM.

Contrast Formation and Resolution

At high beam energy, e. g., 30 keV, the lateral extension of the excitation volume in the specimen is for carbon approximately 10 μm and for a high atomic number element such as gold about 1 μm (Fig. 5.13). Secondary and backscattered electrons are emitted from a surface area of the specimen, which corresponds in size to about the lateral extension of the excitation volume (Fig. 5.14). As discussed in Sect. 5.1.2, *Secondary Electrons* and *Backscattered Electrons* the SE2

and BSE2 represent the majority of the SE and BSE, respectively, whereas the SE1 and BSE1, both carrying high-resolution information, represent the minority. Assuming for simplicity an electron-beam diameter of 1 nm, the ratio of the lateral size of the excitation volume and the beam diameter amounts to approximately 10^4 for carbon and 10^3 for gold. By choosing the magnification such that the field of view at the specimen surface approaches the lateral size of the excitation volume, i.e., related to a 100-nm image size about $10000\times$ for carbon and $100000\times$ for gold, both the SE2 and the BSE2 contributions will change in response to the features of the field of view on the size scale of the excitation volume. In contrast to this the SE1 and BSE1 contributions will change in response to the features of the field of view approximately on a size scale of the electron-beam diameter. That means that in the course of scanning the electron beam across the field of view, the SE2/BSE2 contribution only insignificantly varies from pixel to pixel whereas the SE1/BSE1 contribution depends sensitively on local features as small as the beam diameter. With a further increase of magnification the field of view becomes significantly smaller than the lateral size of the excitation volume, consequently the SE2/BSE2 contribution is almost constant over the image. The changes in the total SE/BSE signal are almost exclusively due to the SE1/BSE1 component and correspond to the changes in the very tiny volume where SE1/BSE1 are generated. Figure 5.38 shows an example of a high-resolution SE micrograph recorded from a test sample at a magnification of $500000\times$. The distinct changes in image intensity reflect the variation of the SE1 component, which is due to the large dif-

ferences in the atomic number between the carbon and the Au–Pd particles. This type of test sample is usually used to demonstrate the performance of SEMs.

The low SE yield of low atomic number specimens (Fig. 5.17) such as soft biological objects and polymers limits the resolution because of the poor SNR. However, the SNR can be improved significantly by coating the specimen surface with an ultrathin very fine-grain metal film [5.317] by Penning sputtering or by evaporation in oil-free high vacuum (Sect. 5.1.4). The thickness of such films can be as small as 1 nm and, as we shall see later, such ultrathin films do not mask fine surface structures. In addition to improving the SNR the ultrathin coating plays an important role in contrast formation and the image resolution obtainable. As mentioned earlier, the SE1 arise from the area directly irradiated by the electron beam and its immediate vicinity caused by the delocalization of the inelastic scattering in the order of a very few nanometers (Sect. 5.1.2). In the case of the specimen coated with an ultrathin metal film the SE1 generation is confined almost exclusively to the film. Figure 5.39a shows schematically the cross section of an object coated with a continuous metal film of constant thickness. As the electron beam is scanned across the object the projected film thickness will vary between the nominal film thickness and the maximum, which is several times greater than the nominal thickness. As shown by Monte Carlo calculations the SE1 yield increases very quickly with the thickness of the metal film [5.318]. For example, the Monte Carlo calculations by Joy [5.318] reveal for chromium and 20-keV electrons that half of the maximum SE1 yield is reached for a thickness of 1–1.5 nm only. The dependence of

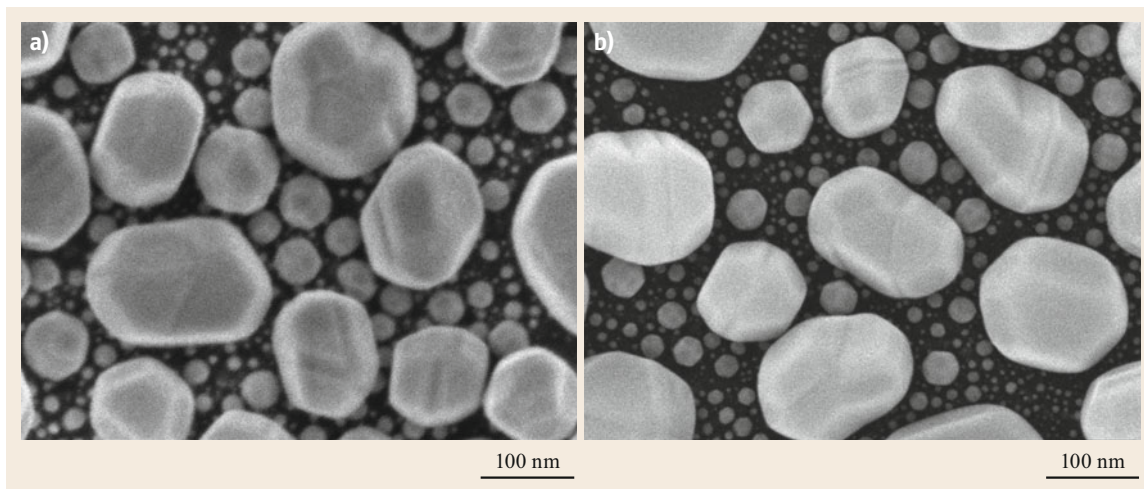


Fig. 5.38a,b Secondary electron micrographs of Au nanoparticles on Carbon support resolution standard recorded at 1 kV (a) and 15 kV (b) using a Schottky FESEM, JEOL JSM-7200F. The micrographs were recorded using a through-the-lens electron detector. Note the minimal change in resolution while changing accelerating voltage

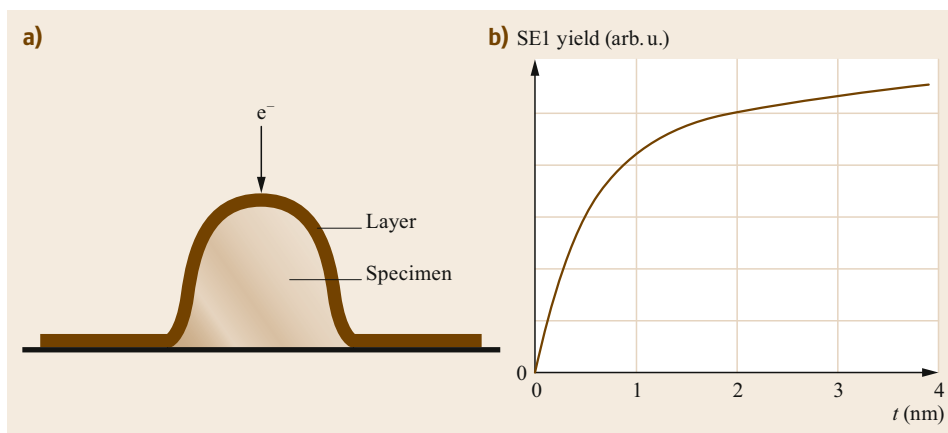


Fig. 5.39a,b Schematic cross section of a specimen coated with an ultrathin continuous metal layer of constant thickness (a). The projected mass thickness of the metal layer varies as the electron beam is scanned across the specimen. (b) Graph of the SEI yield versus the thickness of the coating film

the SEI yield versus the thickness of a coating film is shown schematically in Fig. 5.39b. It indicates that the increase of the SEI yield with the thickness slows down at twice the thickness at half of the maximum SEI yield, i. e., the continuous film should be as thin as possible. Monte Carlo calculations of the SEI yield for some of the metals suitable for preparing ultrathin very fine-grain metal films show a monotonic increase with the atomic number [5.155]; thus some further improvement of the SNR may be expected with high atomic number metals.

The ultrathin very fine-grain metal film on the sample surface also improves the BSE1 component significantly, thus improving the SNR in high-magnification BSE micrographs. The BSE1 are very important for high-resolution SEM because the elastic electron scattering is strongly localized. The intensity of the BSE1 component increases with the projected film thickness, i. e., increases with the number of atomic scattering centers. Since the BSE coefficient strongly increases with the atomic number (Fig. 5.17), the BSE1 component of the metal film is significantly larger than the contribution from the coated low-atomic number specimen. The same is also true for small metal clusters or small particles at the specimen surface, e. g., such as colloidal gold down to a minimum diameter of 0.8 nm [5.319], which can be identified unambiguously in the high-resolution BSE micrograph.

Selected Applications

Since the achievable resolution is the main difference between the high-resolution field-emission SEM and the conventional SEM, it is obvious that the high-resolution SEM (HRSEM) can readily handle almost all of the applications mentioned in Sect. 5.1.6. Because vacuum conditions in FESEMs are more strict concerning the pressure in the specimen chamber (at least one order of magnitude less than in conventional

high-vacuum scanning electron microscopy (CSEM)) as well as the content of gaseous hydrocarbons and hydrocarbons at the specimen, some specimens may not meet the requirements for cleanness and very low partial pressure. However, if high-resolution FESEM is applied instead of CSEM, more information about the specimen will be obtained due to the higher resolution as soon as the magnification used exceeds approximately $10\,000\times$ to $20\,000\times$. That means that lateral resolutions requiring magnifications clearly beyond about $20\,000\times$ belong to the dedicated domain of high-resolution SEM.

The following few applications selected from an almost unlimited quantity should demonstrate the strength of HRSEM in several fields of research. It is clearly beyond the scope of this section to discuss in this context specific details about the specimens and imaging techniques.

Figure 5.40a shows the secondary electron micrograph of a regular protein surface layer of a bacterial cell envelope. The specimen was unidirectional shadowed with an ultrathin tungsten layer leaving an uncoated region behind the latex bead. Comparison of the regular structure of the HPI layer in the coated and the uncoated region shows that the contrast in the uncoated area is significantly lower than in the coated region, though the resolution of structural details is very similar as verified by the related power spectra. This example also demonstrates that coating with the ultrathin very fine-grain metal film does not mask fine structural features. In principle, a similar resolution can also be obtained with nonregular organic specimens, however, it remains more difficult to quantify unambiguously the resolution obtained.

An extremely important application of HRSEM, as yet unrivaled by other surface imaging techniques, is the localization of molecules on surfaces by immunolabeling techniques (for reviews see [5.234, 322–325]).

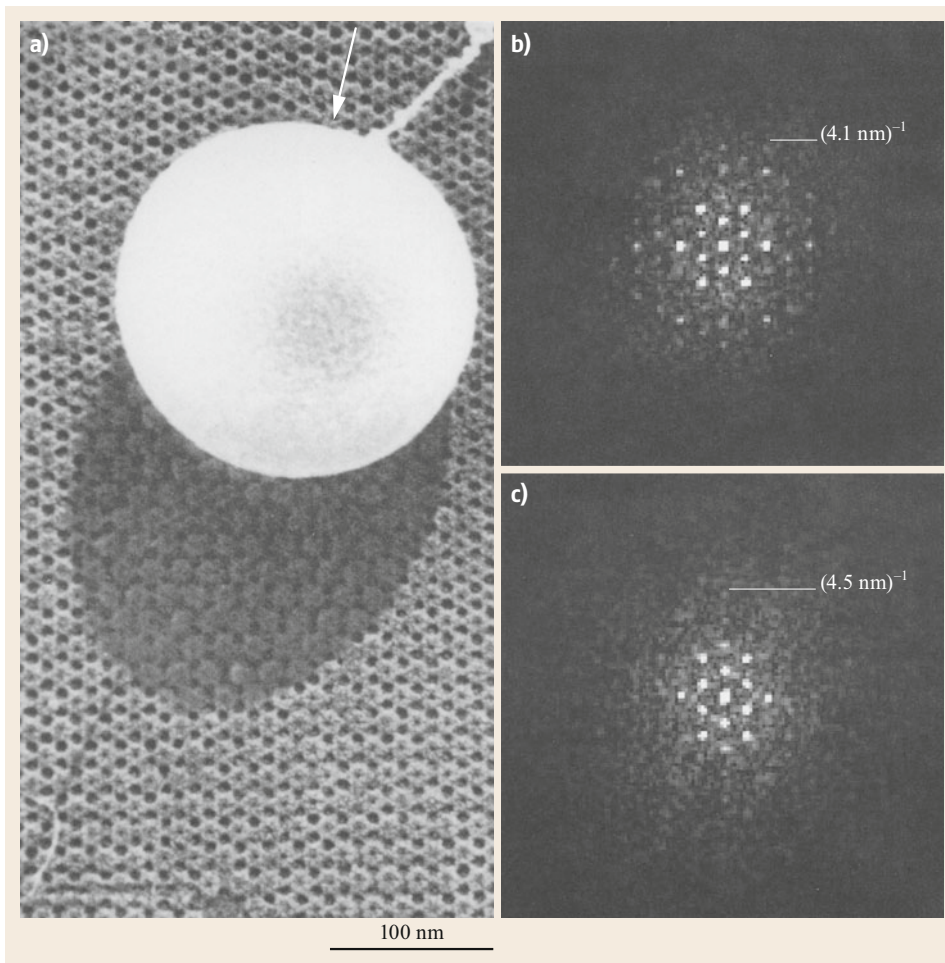


Fig. 5.40a-c Secondary electron micrograph of a regular protein surface layer (hexagonally packed intermediate (HPI) layer [5.320]) of *Deinococcus radiodurans* recorded with an *in-lens* FESEM at 30 kV (a). The specimen was unidirectional shadowed (see *arrow*) at an elevation angle of 45° with a 0.7 nm-thick tungsten layer leaving an uncoated region behind the latex bead. The power spectra of a coated (b) and an uncoated (c) region of the HPI layer reveal the resolution obtained (outermost diffraction spots are indicated and the corresponding reciprocal values of resolution are given). The contrast in the uncoated region is about 15–20% of that from the coated region. Reprinted with permission from [5.321], micrographs kindly provided by R. Wepf

The use of HRSEM for immunoelectron microscopy started more than 20 years ago [5.326–332]. Since then efforts have been made to optimize the technique of immunoscanning electron microscopy in terms of localization precision, contrast, and SNR [5.319, 333–335]. While the colloidal gold can be localized directly in the BSE image, the precision of the indirect localization of the antigen depends on the type of labeling and the size of the colloidal gold and ranges from less than 5 to about 10 nm [5.336, 337]. Figure 5.41b demonstrates the unambiguous detection of immunogold-labeled proteins on cells (specimen was coated with a thin layer of carbon prior to imaging). However, for more than

a decade immunoscanning electron microscopy has been established as a trusted technique and, with the commercial availability of high-quality gold probes (available in sizes ranging from 1 to 40 nm), is used in many electron microscopic laboratories for various studies [5.338–343].

The interior structure of biological specimens is accessible by HRSEM, if samples are rapidly frozen and opened by cryofracturing or cryoultramicrotomy. After partial freeze-drying and double-layer coating of the block face, the specimen can be directly analyzed in the cryo-SEM [5.286, 287, 344]. Figure 5.42 shows for comparison a cross section of yeast cells prepared via

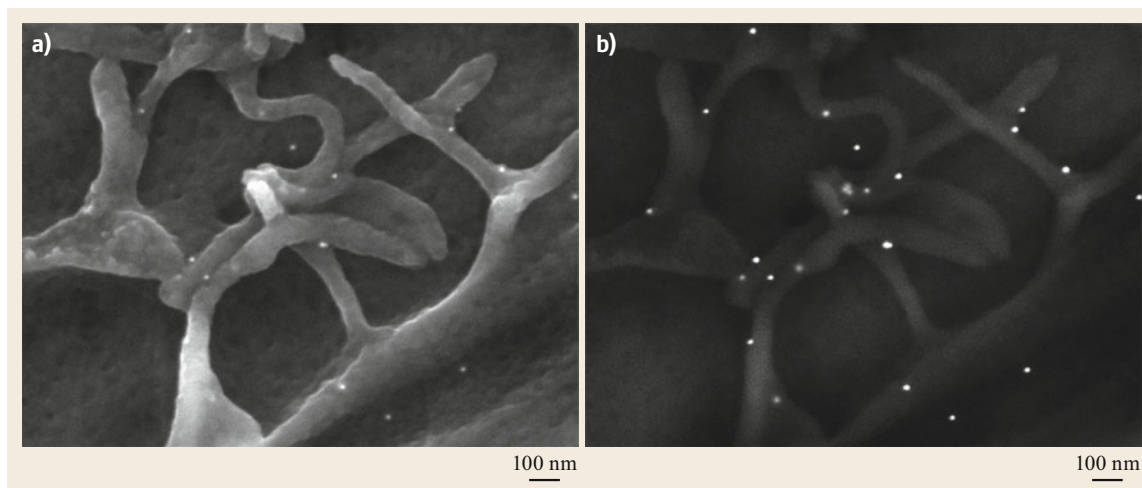


Fig. 5.41a,b Secondary electron (a) and backscatter electron (b) micrographs of immunogold-labeled cells

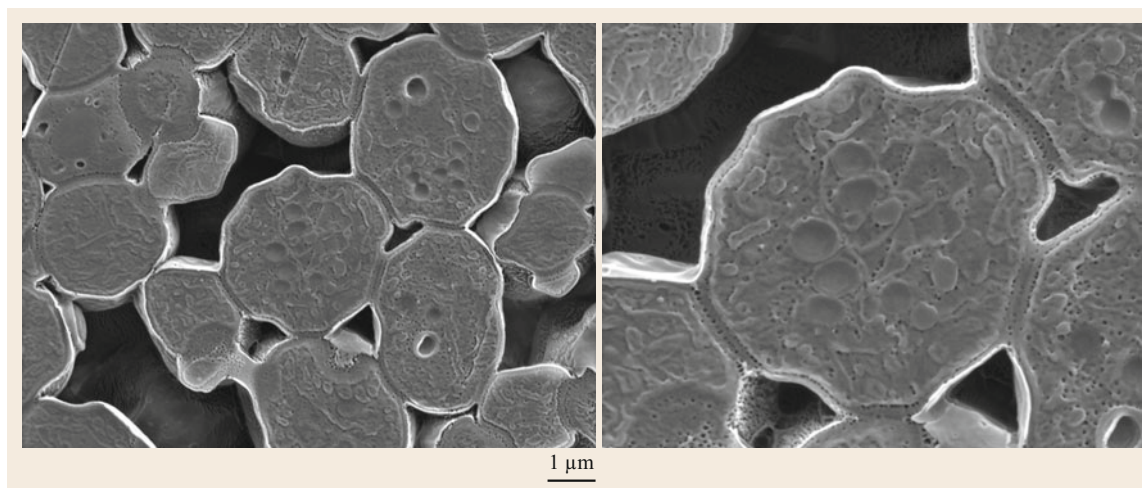


Fig. 5.42 Secondary electron images of yeast cell cross sections taken with an ET detector at 3 kV. The sample was prepared from a freeze-dried specimen using a broad-beam argon ion polisher (IB-19530 CP, JEOL Ltd)

argon ion polishing with subsequent etching by a low-voltage ion beam. Particles and structures as small as 25 nm can be visualized clearly.

Both strengths of the HRSEM, namely the high resolution and the high depth of focus, are required to resolve surface structures at the nanometer scale on randomly oriented tilted surfaces. One typical example are submicrometer-sized crystalline zeolite particles as shown in Fig. 5.43. The HRSEM is the tool most suited to characterize the habit of the individual particles as well as to visualize the fine surface structure such as growth steps of terraces [5.345]. The current resolution of the FESEM allows observation of nanopore arrangement in zeolites, and make a determination about zeolite reactivity and functionality in

catalytic processes (blocked pores, surface step structure, etc.).

HRSEM is also a very valuable tool for the evaluation of mechanical properties of structural materials. For example, most structural materials are strengthened by fine particles of second phases usually having diameters less than 500 nm. The strengthening effect is primarily governed by the mean size, the size distribution, and the volume fraction of the particles. Both HRSEM and AFM allow for the precise determination of the mean size, size distribution, and volume fraction of the particles as demonstrated by *Fruhstorfer et al.* [5.346]. Figure 5.44 shows the SEM micrograph (Fig. 5.44a) and the AFM topograph (Fig. 5.44c) of the electrolytically polished surface of the superal-

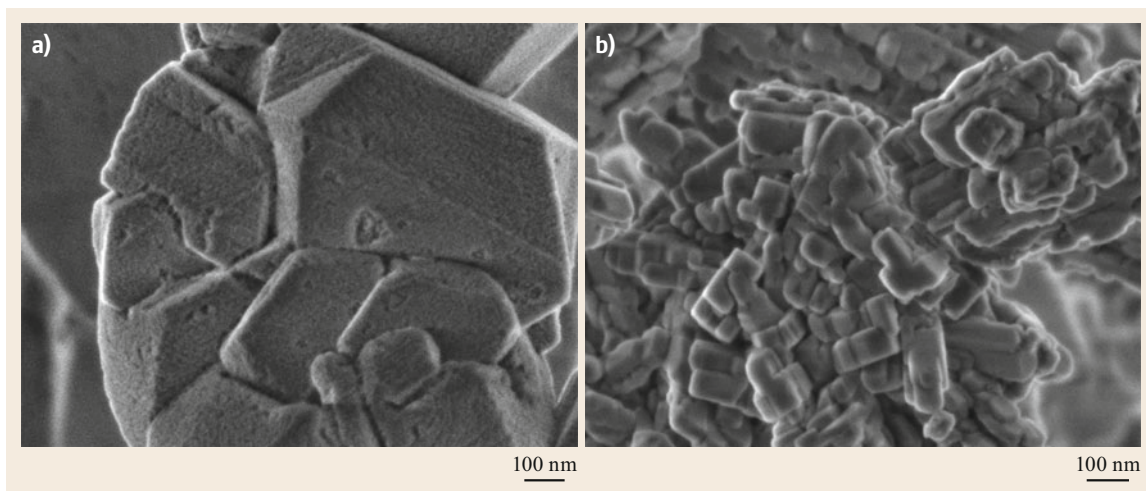


Fig. 5.43a,b Secondary electron micrographs of zeolites Y (a) and ZSM-5 (b) imaged with a through-the-lens detector in Schottky FESEM using a 0.8 kV landing voltage, uncoated

loy NIMONIC PE16 with the protruding caps of the second-phase particles. In contrast to AFM, where corrections were necessary to take into account the exact tip radius, corrections for the very small electron probe diameter are not urgently required in HRSEM. The size distribution function and mean radius of the second-phase particles calculated from HRSEM (Fig. 5.44b) and AFM (Fig. 5.44d) data are in excellent agreement with those gained earlier by TEM [5.347]. The distinct advantages of HRSEM in this application are that micrographs are readily recorded and the data can be processed without additional correction procedures.

The characterization of porous materials such as porous silicon or porous aluminum oxide gains increasing attention because of important potential applications [5.348–353]. Among others, HRSEM is an indispensable tool for structural characterization of porous materials taking advantage of the large depth of focus and the high resolution obtainable. Figure 5.45 shows high-resolution SE and BSE micrographs of the surface and cross section of porous aluminum oxide, which exhibits a network with randomly distributed, but almost perfectly aligned cylindrical pores perpendicular to the substrate. The simultaneous imaging of the surface and the cross section reveals information about the three-dimensional specimen structure. Under the conditions given the SE mode yields higher resolution than the BSE mode.

However, the BSE mode is of significant importance if greater information depth and material differentiation are required. Figure 5.46 shows SE and BSE micrographs of temperature-sensitive hydrogels, based on poly(vinylmethyl ether) (PVME), with ferromagnetic

properties due to incorporated nickel particles used as a ferromagnetic filler. The contrast in the SE micrograph (Fig. 5.46a) is mainly caused by the very thin membrane-like PVME, which envelops the nickel particles, whereas the BSE image (Fig. 5.46b) has a strong material contrast component due to the nickel particles underneath the PVME membrane. This new class of hydrogels is of great interest for delivery of materials at the micro- and nanometer scale.

As mentioned in Sect. 5.1.2, *Transmitted Electrons*, the high-resolution *in-lens* FESEM equipped with an annular dark-field detector is capable of mass measurements on thin specimens [5.354, 355] at a resolution approaching that of a dedicated STEM [5.134, 356, 357]. Mass measurement of molecules and molecular assemblies are of great importance in biophysics and structural biology (for a review see [5.358]).

Finally, nanotechnology and *nanoelectromechanical systems* (NEMSs) are additional fields in which HRSEM is used as a tool for monitoring processes, detecting defects, or measuring sizes and distances, e. g., in nanodevices, which will contain nanotubes, nanoparticles, nanowires, and other particles [5.309, 359, 360].

5.2.2 Low- and Very-Low-Voltage Scanning Electron Microscopy

Scanning electron microscopy with electron energies below 5 keV is usually designated as scanning low-energy electron microscopy (SLEEM) or, related to the acceleration voltage, LVSEM. The energy of 5 keV can be considered as a threshold energy because the monotonic dependence of the BSE coefficient on the atomic

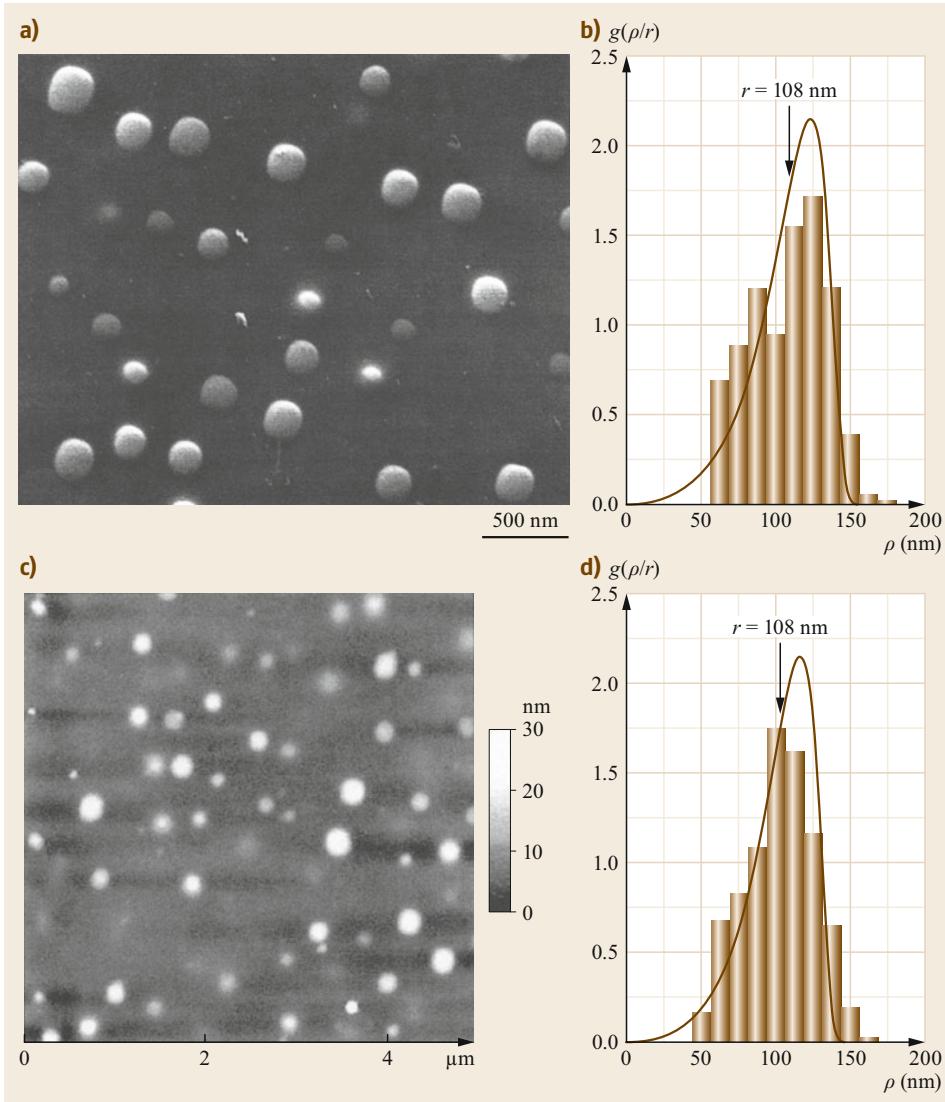


Fig. 5.44a–d Surface of electrolytically polished superalloy NIMONIC PE16. Secondary electron micrograph recorded with an *in-lens* FESEM at 10 kV (a) and AFM topograph (c). The related distribution functions g of the true radii ρ are shown for the HRSEM in (b) and for the AFM in (d). Reprinted with permission from Taylor Francis Ltd from [5.346], www.tandfonline.com

number breaks below this (Sect. 5.1.2, *Backscattered Electrons*). A second prominent energy threshold is at about 50 eV, which corresponds to the electron energy with minimum inelastic mean free path of electrons in matter [5.182]. Therefore, scanning microscopy with electron energies below 50 eV is designated as scanning very low-energy electron microscopy [5.33] or, related to the acceleration voltage in the scanning mode, very low-voltage scanning electron microscopy (VLVSEM). An excellent review on the latest developments in low-voltage electron microscopy was presented by Bell and Erdman [5.34].

What is the motivation for low electron energy operation in SEM? What are the advantages expected at low energies and what are the inherent disadvantages?

Clearly, almost all of the advantages for working at low energy derive directly from the energy dependence of the electron–specimen interaction (Sect. 5.1.2). The advantages include the following:

1. The penetration depth of the impinging electrons decreases with decreasing energy due to the reduced electron range R (5.29), i.e., the excitation volume in the specimen shrinks (Fig. 5.13) and the volume emitting SE2 and BSE2 approaches the volume emitting SE1 and BSE1 (Fig. 5.14). As a result the edge effect, i.e., overbrightening of edges, is strongly reduced or even suppressed completely.
2. The SE yield δ increases because of the reduced electron range and the SE are generated near the sur-

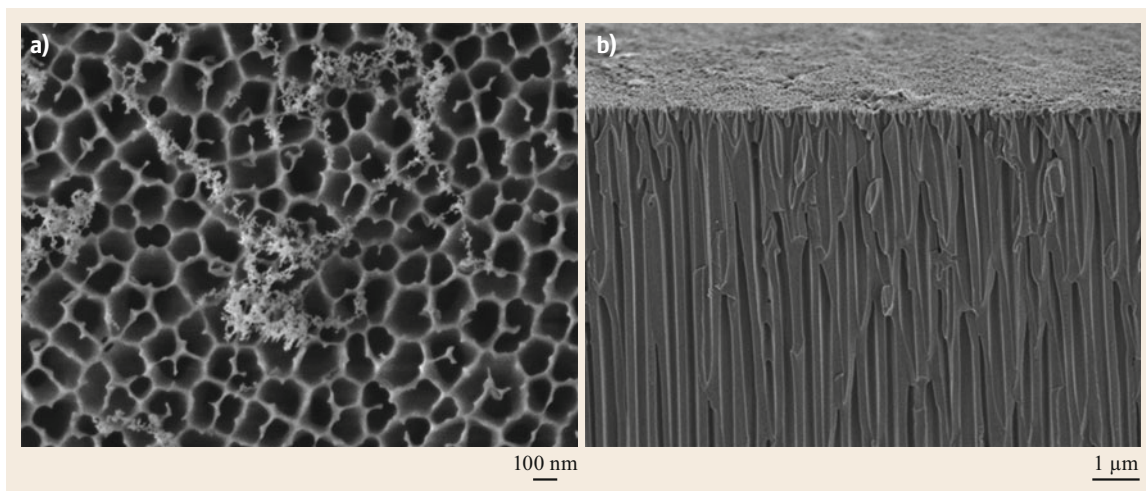


Fig. 5.45a,b High-resolution micrograph of the surface (a) and cross section (b) of porous aluminum oxide membrane recorded using FESEM. The images were acquired at 0.2 and 1.2 kV, respectively, the specimen was imaged uncoated

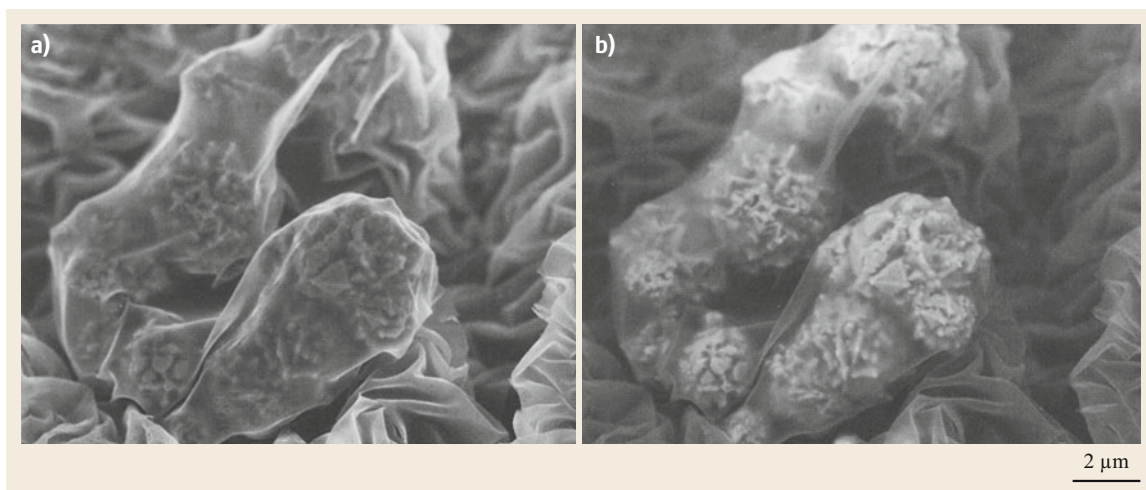


Fig. 5.46a,b High-resolution micrographs of poly(vinylmethyl ether) (PVME) hydrogel with ferromagnetic properties filled with submicrometer nickel particles in the swollen state. The hydrogel was rapidly frozen, freeze dried, and rotary shadowed with an ultrathin layer of platinum/carbon. The SE (a) and BSE (b) micrograph were recorded with an *in-lens* FESEM at 10 kV, (specimen kindly provided by Dr. K.-F. Arndt, Institut für Physikalische Chemie und Elektrochemie, Technische Universität Dresden, Dresden, Germany)

face, where they can escape (Fig. 5.15). As a result, the SNR of the SE signal increases with decreasing energy as low as $E_{0,m}$.

3. As the SE yield increases, the total amount of emitted electrons approaches unity (Fig. 5.16). Because of the conservation of electric charge (5.40) the amount of incoming and emitted charges is balanced and, consequently, the specimen current equals zero. That means that at this particular electron energy E_2 no electric conductivity of the specimen is required. Ideally, imaging of electric

insulators without conductive coating becomes possible. For normal incidence, E_2 is within the range 0.5–5 keV for most of the materials. E_2 increases with the increasing angle of beam incidence θ according to

$$E_2(\theta) = \frac{E_2(0)}{\cos^2 \theta}, \quad (5.43)$$

where $E_2(0) = E_2(\theta = 0)$ [5.361], i. e., increases as θ increases.

4. As mentioned above, the monotonic dependence of the BSE coefficient on the atomic number breaks below 5 keV [5.152, 362]. This behavior enables the material contrast in the BSE image to be fine-tuned by choosing the most suitable electron energy [5.363].
5. There is a reduced depth of specimen radiation damage (Sect. 5.1.5). At very low electron energies, say less than 30 eV, the elastic scattering dominates and radiation damage becomes negligible [5.33].

The problems and disadvantages inherent to microscopy at low electron energy concern both the instrumentation and the specimen and include the following:

1. Reduced resolution due to chromatic aberration and diffraction ((5.8)–(5.10)).
2. Stronger sensitivity of the electron beam to electromagnetic stray fields.
3. Special detector strategies required for SE and BSE.
4. Enhanced contamination rate, which can be counteracted by ultrahigh vacuum or an anticontamination device.
5. Reduced topographic contrast in SE and BSE micrographs. For electron energies below 5 keV, the increase of SE yield $\delta(\theta)$ with increasing θ (5.31) drops way down to 0.5 keV as shown for different metals experimentally and by Monte Carlo simulation [5.364, 365]. Similarly, the backscattering coefficient $\eta(\theta)$ shows less increase with θ than given by (5.34), which is more pronounced at low electron energies [5.305].
6. Reduced material contrast, because the differences of the backscattering coefficient between low and high atomic number material become smaller [5.152, 366, 367].

Electron Lenses

Modern commercial field-emission scanning electron microscopes can operate usually from 30 down to 0.5 keV or even 0.01 keV, i.e., an energy range that covers conventional electron energies and most of the low-energy region. Improved computer-aided methods enable electron optical systems to be designed such that they have high performance within the whole energy range mentioned above. Compared with the old-fashioned thermionic gun scanning electron microscopes the aberration coefficients of the objective lens were improved dramatically for modern field-emission instruments commercially available: C_s was reduced by a factor of about 30 down to $C_s = 1.6$ mm [5.368], and C_c was reduced by a factor of about 10. With the ultrahigh-resolution objective lens, the CFEG, improved electrical and mechanical stability, as well as

strongly reduced specimen contamination rate, the resolution obtained with test specimens amounts presently to 0.5 nm (at 30 keV) and 0.7 nm (at 1 keV). Those values are exemplary for the high performance of commercial FESEM over an energy range from 1 to 30 keV, though obtained with special test specimens. More recently, a commercial FESEM equipped with a spherical and chromatic aberration corrector has been developed, consisting of four sets of a 12-pole component that corrects the spherical and chromatic aberrations simultaneously [5.369]. Another development has been the development of a monochromator for FESEM [5.370].

Electrostatic as well as combined magnetic and electrostatic lenses in LVSEM are a very interesting alternative to the magnetic lenses mentioned above. Microscopes equipped with this type of objective lens permit nonconstant beam energy along the column, i.e., the beam electrons pass the column with high energy and are decelerated to low energy in the immersion electrostatic lens. First, the magnitude of the aberrations of immersion electrostatic lenses corresponds to the high energy at the entrance side. A more detailed treatment of the estimation of electrostatic lenses is beyond the scope of this section [5.371, 372]. Second, the high electron energy in the column is advantageous because the gun brightness increases with electron energy ((5.4) and (5.42)) and electromagnetic stray fields result in less deterioration of the electron beam at high energy. The combined magnetic–electrostatic objective lens [5.81] has aberration coefficients as low as $C_s = 3.7$ mm and $C_c = 1.8$ mm.

Very low landing energies of the electrons can be realized with a retarding-field SEM. There are several retarding-field configurations described in the literature but basically in all of them the specimen is connected to the adjustable bias supply U_{sp} [5.5, 79, 80, 373–375]. The landing energy of the beam electrons is simply given by the difference $E_0 - eU_{sp}$. Using retarding-field SEM, landing energies of a few electronvolts are achievable and recently micrographs with reflected electrons even at 0.5 eV were obtained [5.363].

With the availability of magnetic materials having high coercive force permanent rare-earth-metal magnets have attracted attention as replacements for magnetic lens coils [5.376]. Khurshheed et al. [5.377] proposed a portable SEM column design, which makes use of permanent magnets. The column of this miniature SEM amounts to a height of less than 12 cm and is designed to be modular, so that it can fit onto different specimen chamber types, and can also be readily replaced. Focusing of the electron beam onto the specimen can be achieved by varying the specimen height or by an outer magnetic slip ring on the objective lens,

which controls the strength of the magnetic field on the axis. Scanning of the beam is performed by deflection coils, which are located above and within the permanent magnet objective lens. A high-resolution miniature SEM with a total height of less than 5.5 cm, proposed by *Khurshed* [5.378], uses a permanent magnet objective lens that lies outside the vacuum with spherical and chromatic aberration coefficients (parameters: $E_0 = 1$ keV, $WD = 7.5$ mm) of 0.36 and 0.6 mm, respectively. These aberration coefficients are about an order of magnitude smaller than those for conventional SEMs with comparable working distance conditions.

Miniaturization of the SEM column has advantages such as microlenses with small aberration coefficients, reducing the influence of electromagnetic stray fields and of the electron–electron interaction, improving the mechanical stability, and reducing the demands on space for the microscope. *Chang* et al. [5.379] proposed a miniaturized electron optical system consisting of a field-emission microsource and an electrostatic microlens for probe forming with performance exceeding that of a conventional system over a wide range of potentials (0.1–10 kV) and working distances (up to 10 mm). *Liu* et al. [5.380] proposed another design that has a column length of only 3.5 mm and can be operated over a wide retarding range of potentials (0.1–10 kV). The instrument has an optimized design (microinzel lens followed by a retarding region) to minimize the primary beam diameter and to maximize secondary electron collection (approximately 50% of SE are collected).

Detectors and Detection Strategies

As mentioned previously, modern commercial FESEMs can operate usually from 30 down to 0.1 keV or even 0.01 keV; the commonly used detectors and detection strategies of these instruments were discussed in Sects. 5.1.1 and 5.2.1, *Detectors and Detection Geometries*. It is clear from Fig. 5.12 that the lower the energy E_0 of the beam electrons the lower the energy difference between the secondary and backscattered electrons. The lower the difference of the different signal electrons the more difficult is their separation. At very low electron landing energies SE and BSE are almost indistinguishable, thus the total emission is detected. The majority of FESEMs nowadays feature some form of in-lens or through-the-lens detection system that has an ability to separate and collect SE, BSE, or a mixture of both types of signals. The instruments are also typically equipped with a dedicated BSE detector (retractable type). The BSE detectors are often multisegmented solid-state-type detectors that are highly sensitive and work at essentially any accelerating voltage, from ultralow to

high kV. For an in-depth review of the current detector technology on FESEM, please see [5.34].

Contrast Formation

The contrast formation in LVSEM and VLVSEM is controlled by the electron–specimen interaction at the electron energy used, the specific signal considered, the detector, and the detection geometry. However, the contrast formation at low energies is much more complex than for electron energies ranging from 5 to 30 keV. A variety of reasons accounts for this complexity. For example, the BSE coefficient is for a given material almost constant and the SE yield depends just weakly on the electron energy for $E_0 \geq 5$ keV. In contrast to this, the monotonic increase of the BSE coefficient with rising atomic number breaks below 5 keV as previously mentioned and, additionally, the BSE coefficient becomes dependent on the electron energy for many chemical elements. Furthermore, the signals obtained at low electron energies are affected more strongly on electron beam-induced contamination or other thin layers on the surface, which is caused by the strongly reduced electron range.

Nevertheless, the main types of contrast, such as topographic, compositional, voltage, electron channeling, crystal orientation, and type-1 and type-2 magnetic and mass-thickness contrast, are also observed in LVSEM, although it is in many respects different from that obtained at conventional energies. There are also several observations that evidently show some *chemical* or *electronic* contrast, i.e., contrast that does not result from an increase in the mean atomic number of the specimen [5.381–383]. Although these effects may also be visible at conventional energies they are most readily observed at low energies where the SE yield is higher.

The thickness contrast described in Sect. 5.2.1, *Contrast Formation and Resolution*, also plays an important role in LVSEM of electric insulators. Though direct imaging of electrical insulators without electric charge-up should be feasible at electron energy E_2 , where incoming and emitted charges are balanced, in practice it often does not work for various reasons. Therefore, coating the specimen surface with an ultrathin very fine-grain metal film [5.317] by Penning sputtering or by evaporation in oil-free high vacuum is often done. As in high-resolution SEM with conventional beam energies, the film plays an important role in contrast formation, in image resolution obtainable, and in the improvement of the SNR. The image contrast of coated specimens essentially depends on the projected film thickness, which will vary between the nominal film thickness and the maximum film thickness, which is several times greater than the nominal thickness in tilted regions (Fig. 5.39a). Monte Carlo calculations of

the SE yield of a film of chromium at 2 keV also prove for low electron energy a monotonic increase with film thickness [5.364].

Selected Applications

The application of LVSEM and VLVSEM logically seems likely in cases in which SEM at conventional acceleration voltages obviously would fail, e. g., the investigation of uncoated insulating materials and radiation-sensitive semiconductors. Another compelling reason is the necessity of a reduced electron range, e. g., with specimens having one or more very thin surface layers and samples possessing a spongy- or foam-like fine structure. SEM studies of these types of specimens aim at information restricted to the surface-near zone. With ever-decreasing device dimension and film thickness this issue becomes more and more crucial. There are also not compelling, but still justifiable reasons, which may aim at optimum imaging conditions at low electron energy, or LVSEM may be part of a series of increasing or decreasing electron energies over a wide energy range as used for depth profiling. Finally, there are also applications of LVSEM that may also work at conventional energies but are most readily obtained at low energies.

The LVSEM is widely applied to semiconductor structures relating to an examination of their geometry, critical dimensions, and local voltages or currents, which may be either biased or induced by the electron beam. One example of an integrated circuit was previously shown in Fig. 5.30. Figure 5.47 shows the cross-fractured semiconductor structure with Schottky barrier on tungsten contacts. A nanostructured two-

dimensional lattice of 100-nm-spaced inverted square pyramids in silicon used as standard for scanning probe microscopy is shown in Fig. 5.48. Imaging of the uncoated lattice is necessary to avoid modifications of the standard by thin film coating, thus LVSEM is most appropriate.

Another challenging application for LVSEM is the quantitative characterization of the geometry and radius of very sharp tips for atomic force microscopy, which are necessary for many quantitative measurements with the AFM [5.346, 384, 385]. Figure 5.49 shows two extremely sharp commercial tips. The tip radius at the very end amounts typically to 2–3 nm, thus only SE1 contribute to the signal. An optimum quality of SE imaging in terms of sharpness, contrast, and SNR can be obtained with electron energies ranging from about 3 to 10 keV. It seems worth mentioning that very sharp tips are interesting samples with which to study experimentally the delocalization of the secondary electrons.

The characterization of organic mono- and multilayers on solids is especially valuable in technology development, such as bio- and chemosensors, since detailed information on the film surface and its morphology is obtained. Figures 5.50–5.53 demonstrate with different mono- and multilayered ultrathin uncoated and coated organic films how direct information about the film thickness, step heights of the film, and differences in the *chemistry* and molecular packing density can be obtained. As shown by Fig. 5.50a, upward and downward steps with height differences of a few nanometers can be readily identified on a tilted sample coated with an ultrathin conductive film. Whereas the step of constant height reveals in an *in-lens* SEM a constant inten-

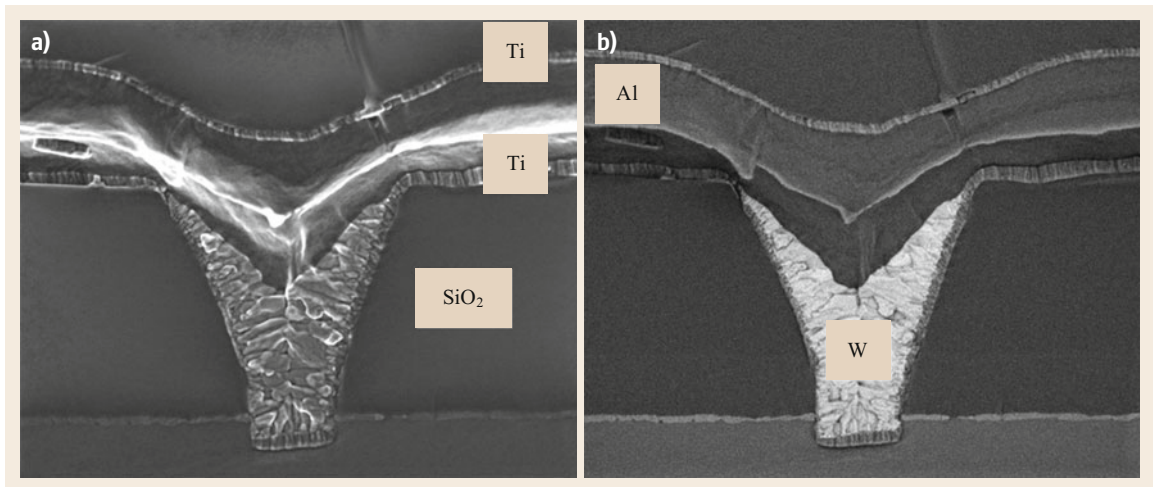


Fig. 5.47a,b Secondary (a) and backscatter (b) electron images of a cross section of an IC semiconductor device. The image was recorded using an in-lens detector with energy filtering grid in Schottky FESEM. The image was taken using 5 kV accelerating voltage

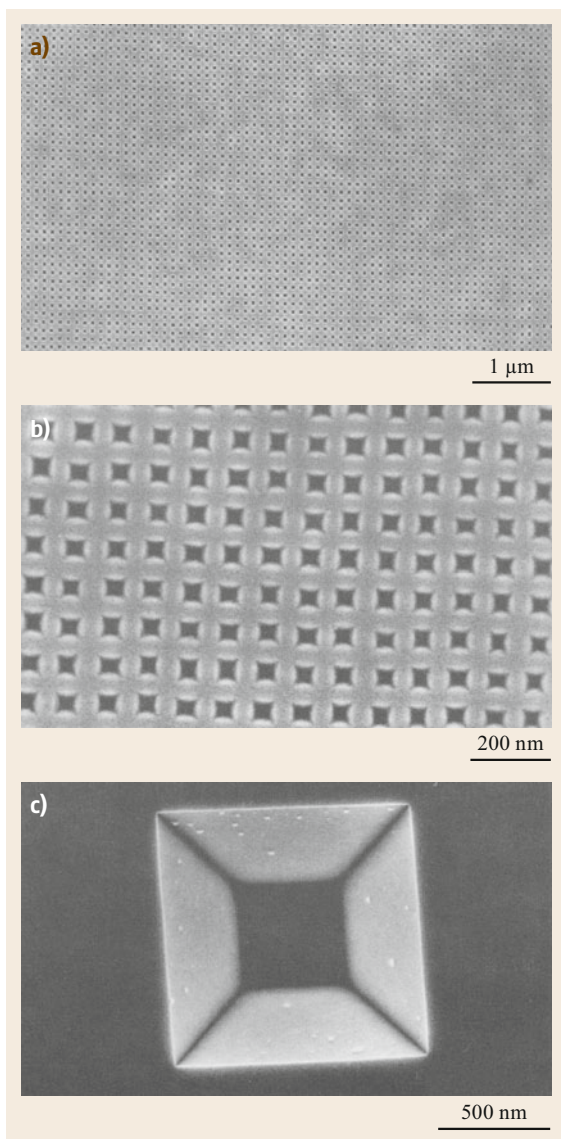


Fig. 5.48a–c Secondary electron micrographs of an uncoated 100-nm calibration standard made from silicon for scanning probe microscopy (NANO WORLD, Neuchatel, Switzerland) recorded with an *in-lens* field-emission SEM at 3 kV. The calibration standard consists of a two-dimensional lattice (lattice constant = 100 nm) of inverted pyramids shown at different magnifications (**a**, **b**). (**c**) Structural details of a large pyramidal pit

sity at normal electron-beam incidence, tilting causes an asymmetry such that steps can face upward or downward, which leads to an increase or decrease of their image intensities, respectively. Uncoated organic layers on solids usually reduce the SE yield as shown in Fig. 5.50b. As demonstrated in Fig. 5.51 by a compari-

son of an SE micrograph with an AFM topograph of the same area, the SE intensity decreases with increasing thickness of the organic layer [5.386]. The monotonic dependence of SE intensity and the thickness of the organic film enables its thickness to be mapped without destruction of the film. The influence of organic film thickness on the SE yield vanishes after ultrathin coating of the organic film as proven by Fig. 5.50a.

Figure 5.52a demonstrates that the SE yield also depends on the chemical nature of the molecules assembling an organic film. For example, differences in the terminal group of molecules obviously cause a significant difference in the SE yield, which creates a sufficient chemical contrast in the micrograph. This chemical contrast vanishes after ultrathin coating of the organic film (Fig. 5.52b). Finally, Fig. 5.53 shows that the SE yield is sensitive to the molecular packing density of the organic film, i. e., the number of organic molecules per area [5.388].

It is easy to understand that the BSE signal is not sensitive to the film thickness and differences in the *chemistry* and molecular packing density, because the backscattering of thin low atomic number films is negligible compared with those of the substrate having a significantly higher atomic number.

Figures 5.54 and 5.55 show secondary electron micrographs of an uncoated glass micropipette and a microtome glass knife, which are almost free of electric charging. However, at higher magnifications the typical signs of charging occur.

The characterization of sponge-like microstructures, such as hydrogels and microgels, is a further challenging application of LVSEM, where a large depth of focus, high resolution, and low penetration power (i. e., small electron range) of the electron beam are required. Figure 5.56 shows a stereopair of highly magnified SE micrographs of a hydrogel. The optimum imaging quality of fine structural details well below 10 nm was obtained with electron energies around 2 keV.

Figures 5.57 and 5.58 show a set of secondary electron micrographs recorded from biological samples at low magnification with different electron energies. The micrographs demonstrate to what extent the contrast and information depth vary with the electron energy in a range from 0.4 to 30 keV, which corresponds to about the accessible energy range of commercial FESEMs. As yet, not all of the contributing contrast mechanisms are fully understood, thus the interpretation of micrographs recorded at a specific selected energy requires great care.

Finally, LVSEM is also a promising and efficient alternative to conventional approaches for micromorphological and microstructural characterization of polymers [5.32, 389–391].

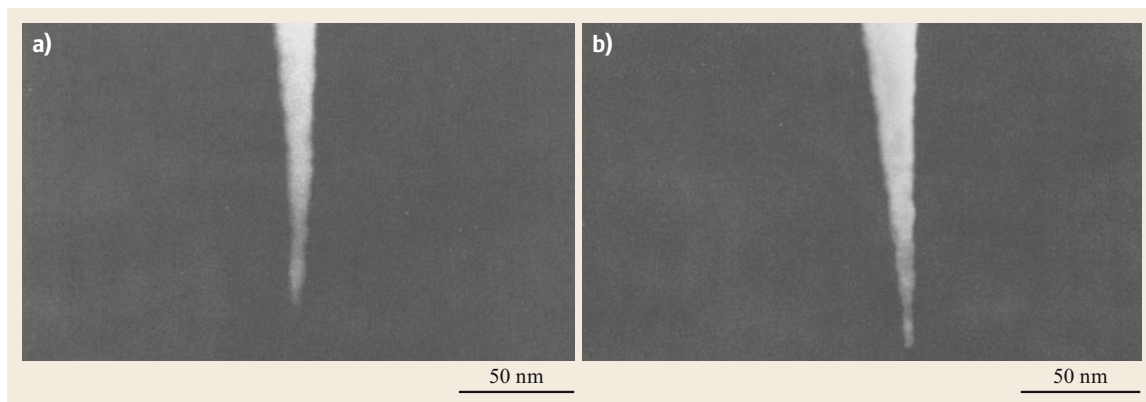


Fig. 5.49a,b Secondary electron micrographs of uncoated SuperSharpSilicon AFM Probe silicon cantilevers for non-contact/tapping mode (NANOWORLD, Neuchatel/Switzerland) in atomic force microscopy recorded with an *in-lens* field-emission SEM at 3 kV (a) and at 10 kV (b). The tip radius of both tips amounts to about 2–3 nm

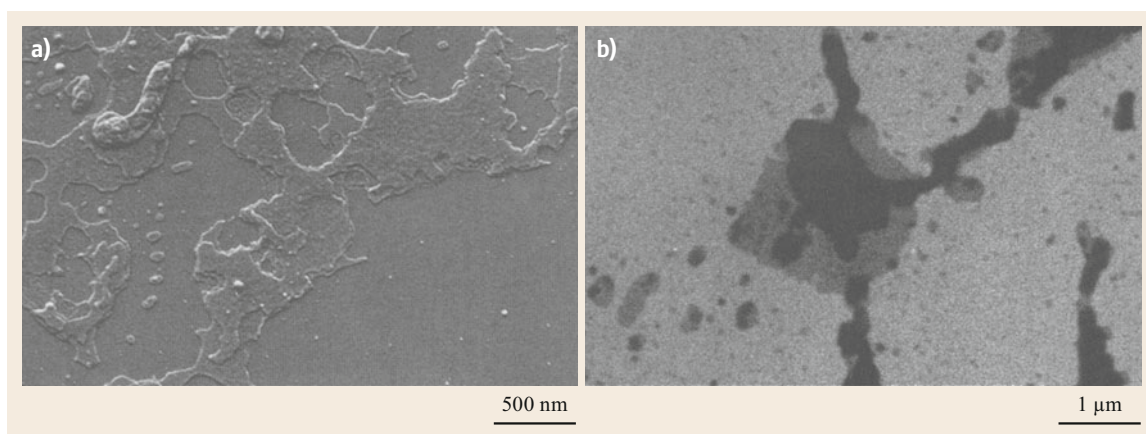


Fig. 5.50a,b Secondary electron micrographs of a phospholipid/protein film (dipalmitoylphosphatidylcholine (DPPC):dipalmitoylphosphatidylglycerol (DPPG) (ratio = 4 : 1)/pulmonary surfactant protein C (SP-C; 0.4 mol%)) supported by a silicon wafer. The organic film has terrace-like regions of different thickness (height differences between terraces are between 5.5 and 6.5 nm [5.387]). Micrographs were recorded with an *in-lens* FESEM at 2 keV from the ultrathin platinum/carbon-coated film (tilted 40° around the horizontal axis) (a) and at 1.8 keV from the uncoated film (b). (Specimens kindly provided by Dr. H.-J. Galla and Dr. M. Siebert, Institut für Biochemie, University of Münster, Münster, Germany)

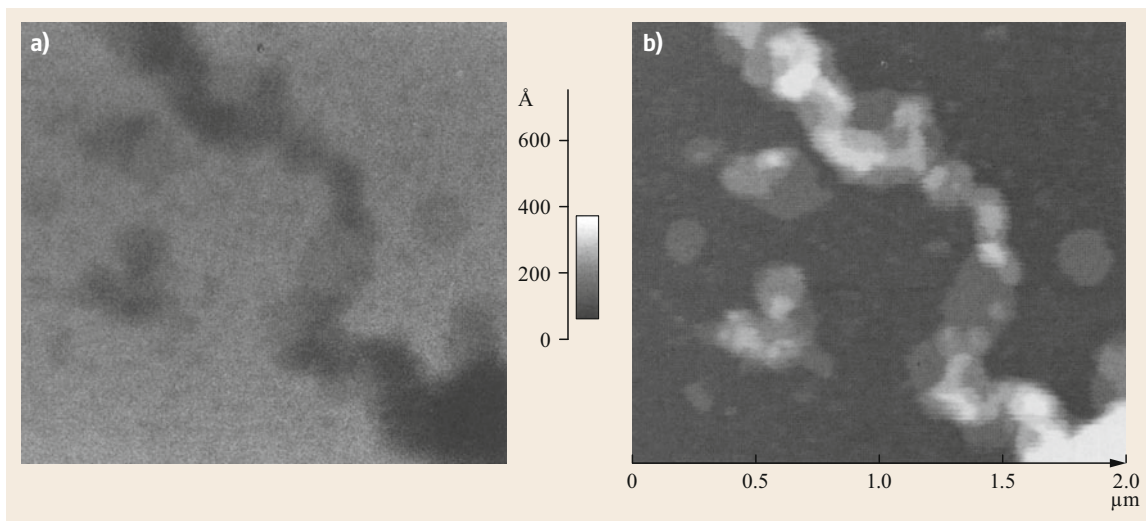


Fig. 5.51a,b Secondary electron micrograph (a) and AFM topography (b) of the same area of an uncoated phospholipid/protein film (dipalmitoylphosphatidylcholine (DPPC):dipalmitoylphosphatidylglycerol (DPPG) (ratio = 4 : 1)/pulmonary surfactant protein C (SP-C; 0.4 mol%) supported by a silicon wafer. The organic film has terrace-like regions of different thickness (height differences between terraces are between 5.5 and 6.5 nm [5.387]). The micrograph was recorded with an *in-lens* FESEM at 2 keV. The scale in between (a) and (b) represents the coding of brightness relative to the height used in the topograph (b). (Specimens kindly provided by Dr. H.-J. Galla and Dr. M. Siebert, Institut für Biochemie, University of Münster, Münster, Germany)

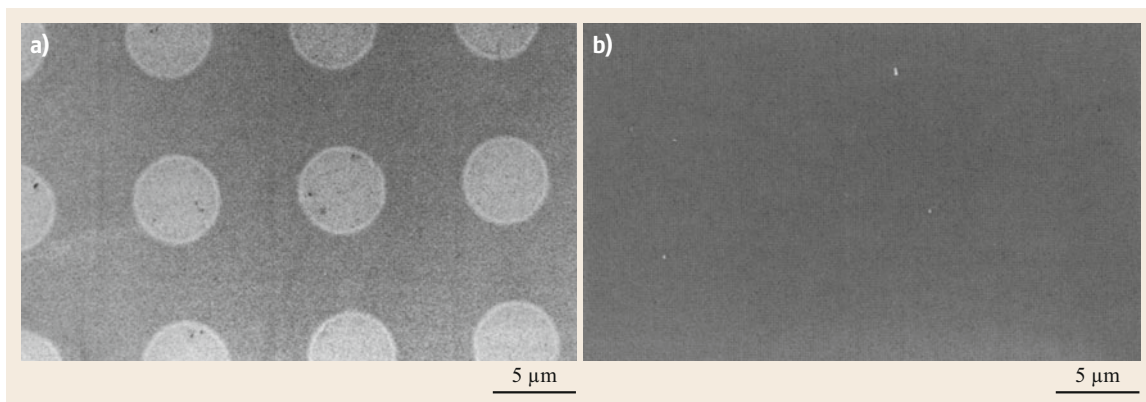


Fig. 5.52a,b Secondary electron micrographs of a patterned self-assembled thiol monolayer on polycrystalline gold recorded at 2 keV with the *in-lens* FESEM. (a) Uncoated monolayer. The circular domains consist of $-(\text{CH}_2)_{15}\text{CH}_3$ molecules (hydrophobic), which are surrounded by $-\text{S}(\text{CH}_2)_{12}\text{OH}$ molecules (hydrophilic). The contrast is due to the different end groups rather than to the small difference in chain length. (b) Monolayer coated with an ultrathin platinum/carbon film. (Specimen kindly provided by Dr. G. Bar, Freiburger Materialforschungszentrum, Freiburg, Germany)

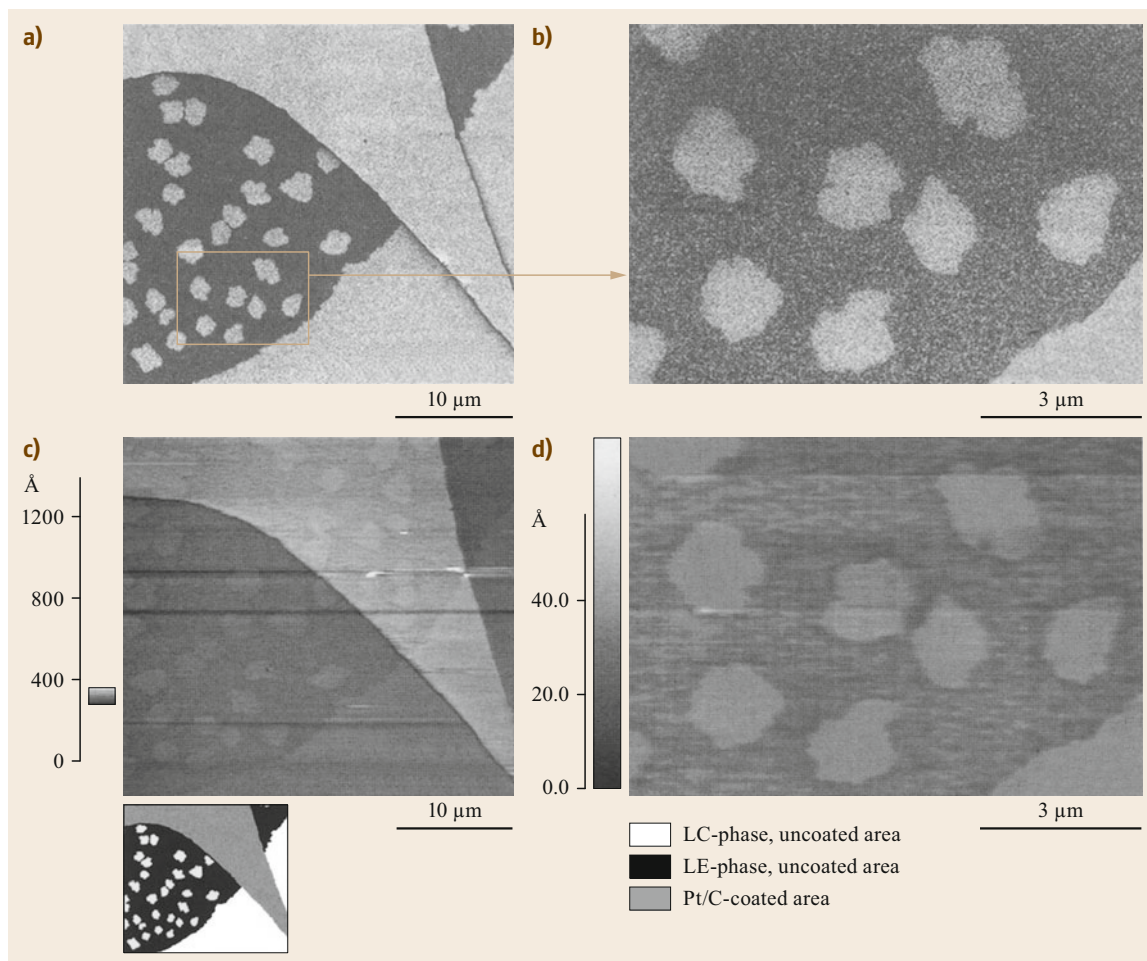


Fig. 5.53a–d Secondary electron micrographs (a,b) and AFM topographs (c,d) of the same area of a 1,2-dipalmitoyl-*sn*-glycero-3-phosphothioethanol (DPPTE) monolayer on a silicon wafer having domains with densely (liquid condensed (LC) phase) and loosely (liquid expanded (LE) phase) packed molecules. The specimen was masked by a TEM finder grid and then coated with an ultrathin platinum/carbon film to obtain neighboring coated and uncoated areas on the specimen (for details see [5.388]). The SE micrographs were recorded with an *in-lens* FESEM at 5 keV. The *brighter regions* of the SE micrograph (b) correlate with the elevated domains (LC phase) in the AFM topograph (d), whereas the *darker regions* correlate with the LE phase. In contrast to the SE micrograph (a) the height differences in coated areas of the film, which are related to its molecular packing density, are still visible in the AFM topograph (c). Reprinted with permission from [5.388]. Copyright 2001 American Chemical Society

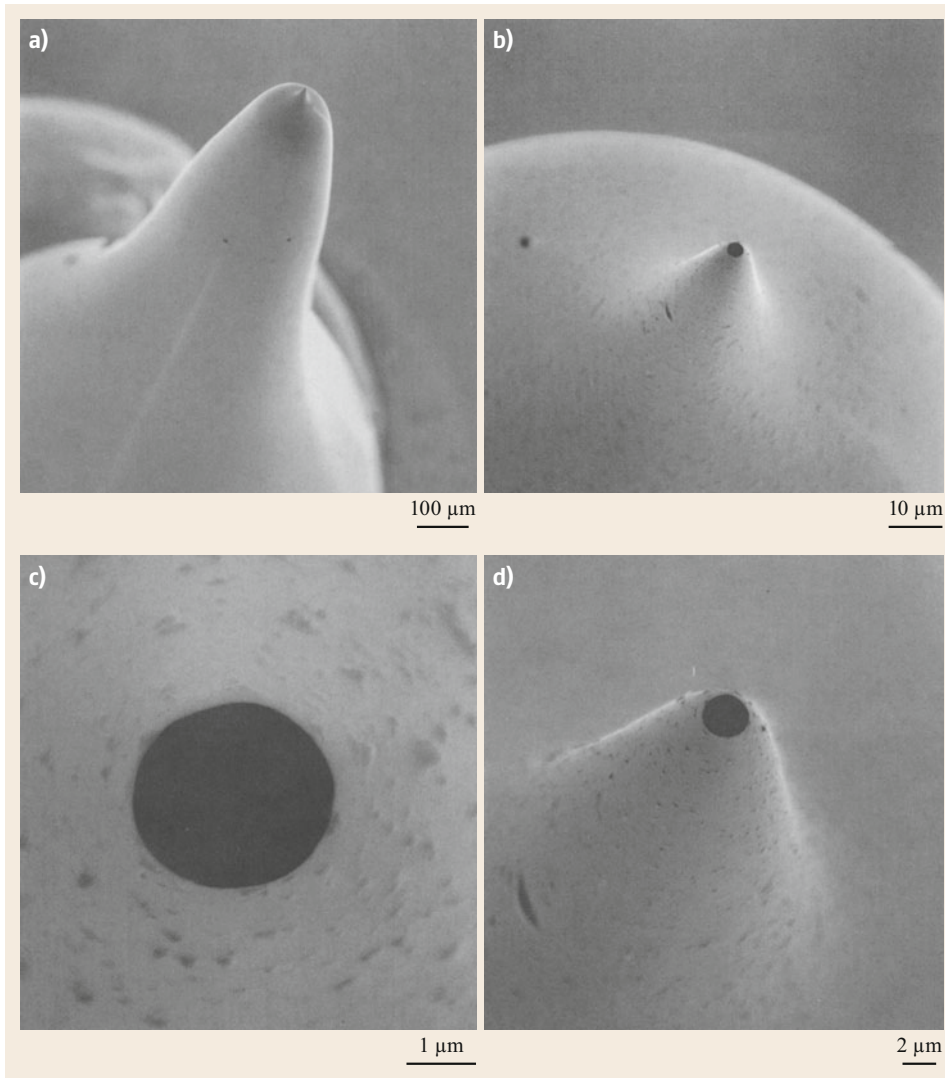


Fig. 5.54a–d Secondary electron micrograph series of increasing magnification of an uncoated glass micropipette recorded at 2 kV with an *out-lens* FESEM. The uppermost part of the tip of the micropipette is within the depth of focus. The lower part is out of focus

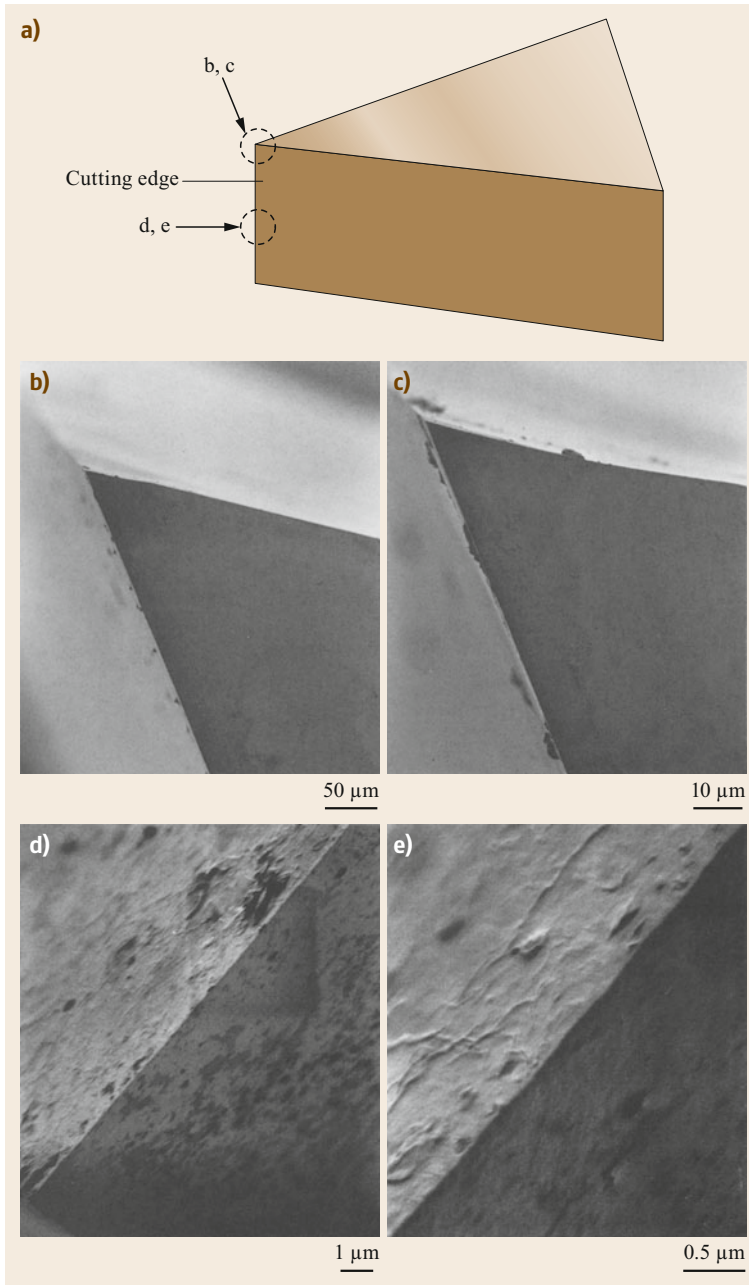


Fig. 5.55a–e Scheme and SE micrographs of an uncoated microtome glass knife recorded at 1 kV with an *out-lens* FESEM. The *arrows* in (a) indicate the two directions of the electron beam related to the glass knife, which were used for imaging. (b,c) The electron beam has a shallow angle against the cutting edge. Only the uppermost part of the cutting edge is within the depth of focus. (d,e) The electron beam impinges perpendicularly onto the cutting edge. The different mean brightness of the clearance angle side and backside of the knife is due to the effect of the detection geometry of the ET detector.

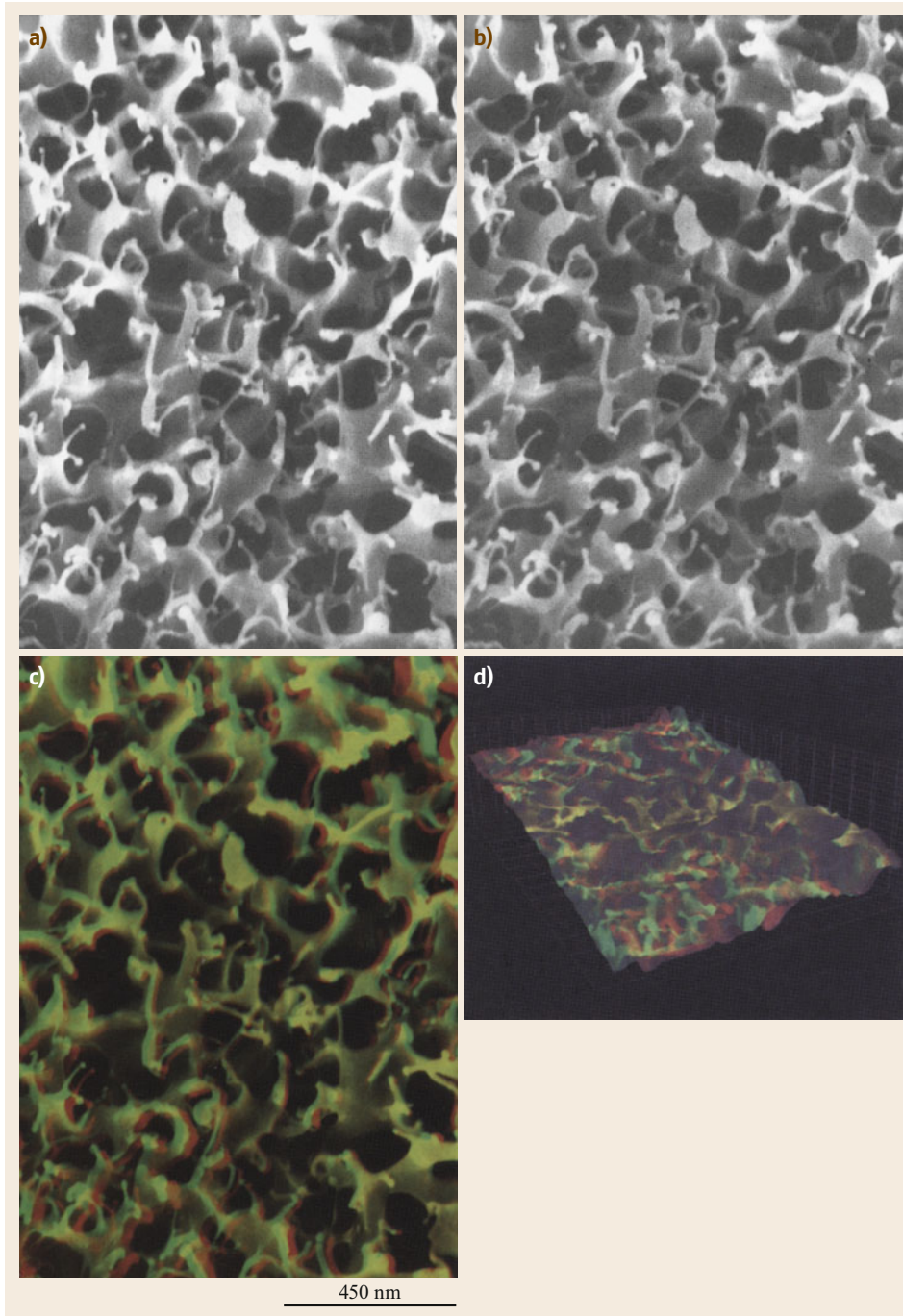


Fig. 5.56a–d Stereo pair of SE micrographs (a,b) of the hydrogel poly-(N-isopropylacrylamide) (PNIPAAm) in the swollen state recorded at 2 keV with the *in-lens* FESEM. The specimen was rapidly frozen, freeze dried, and ultrathin rotary shadowed with platinum/carbon. (c) Red–green stereo anaglyph prepared from (a,b). The tilt axis has a vertical direction. (d) Red–green stereo anaglyph in a *bird's-eye view*

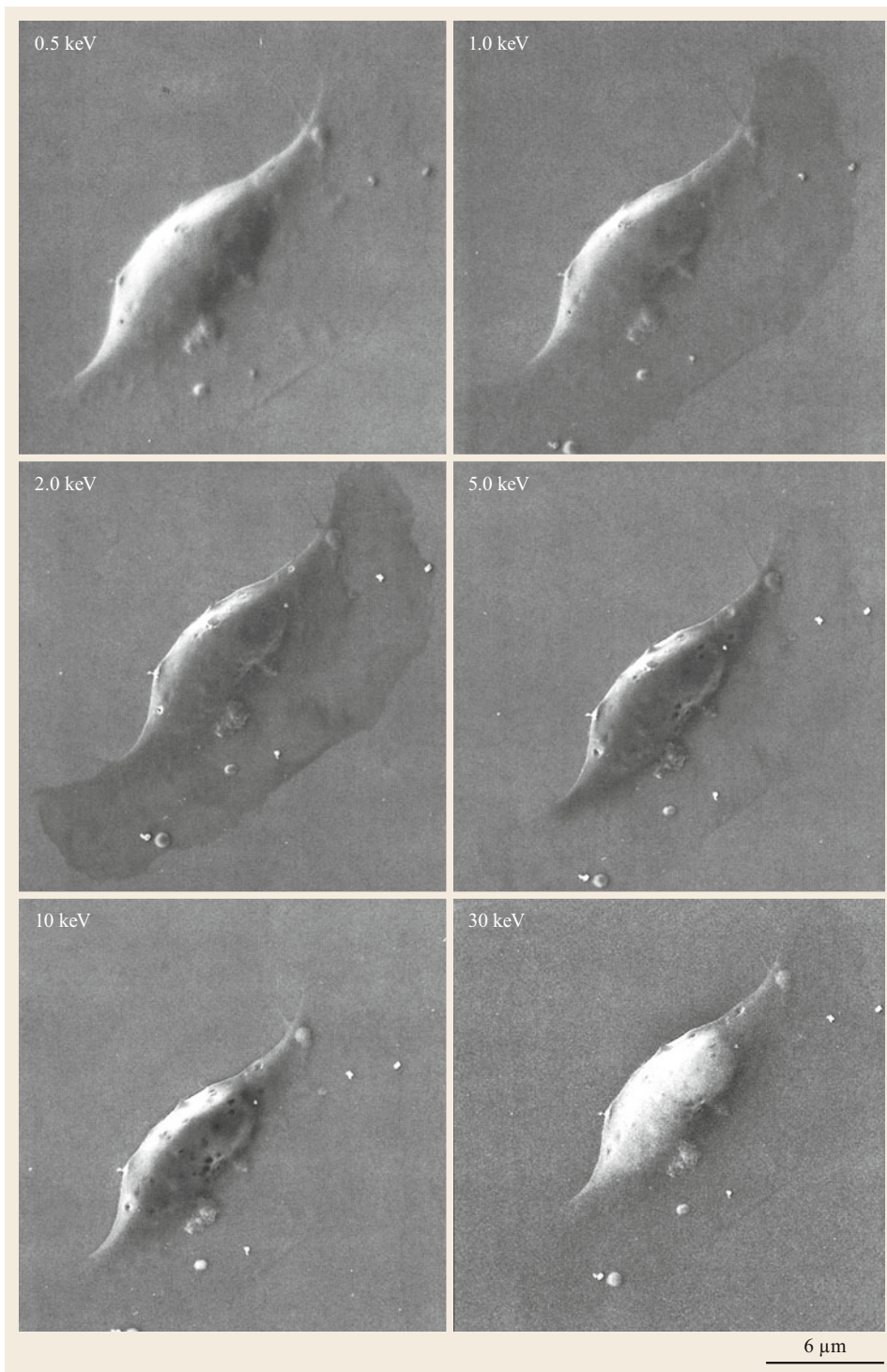


Fig. 5.57 Secondary electron micrograph series of increasing electron energies from 0.5 to 30 keV from a keratinocyte. The micrographs are recorded with an *in-lens* FESEM. The image contrast varies significantly with the electron energy. Inhomogeneities in the *leading edge* of the keratinocyte, which has a thickness of about 200–400 nm, are most clearly visible at 2 keV. (Micrographs kindly provided by Dr. R. Wepf, Beiersdorf AG, Hamburg, Germany)

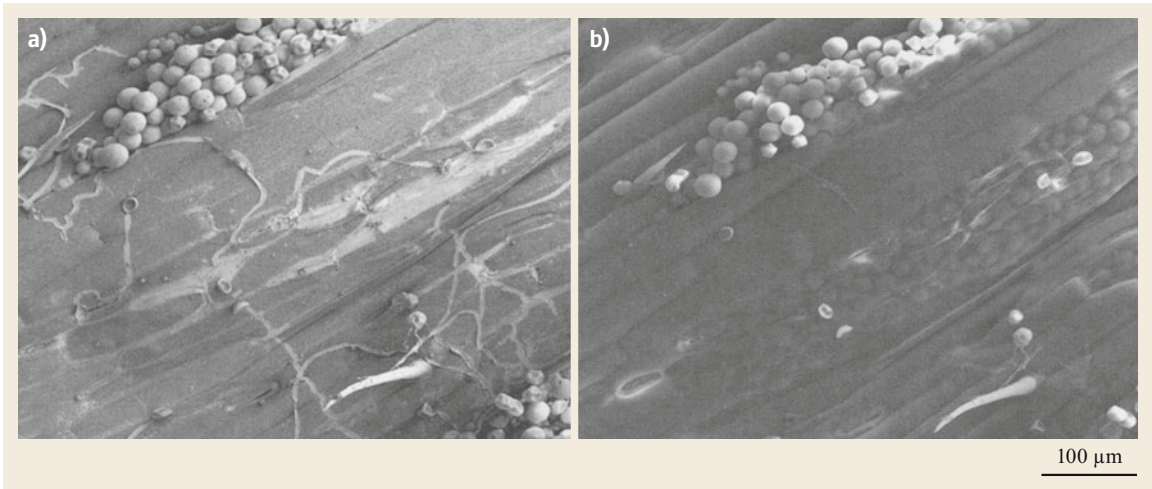


Fig. 5.58a,b Secondary electron micrograph pair of the cuticula of a leaf recorded at electron energies of 0.4 (a) and 30 keV (b) with an *in-lens* SEM. The low-energy image contains information only from the surface whereas the 30-keV image also reveals information about structural features below the surface, e. g., new spores, which are not visible in (a). Courtesy of R. Wepf

5.3 Scanning Electron Microscopy at Elevated Pressure

The scanning electron microscopic investigation of specimens must meet several requirements, which were mentioned in previous sections. To sum it up, it can be said that specimens:

1. Have to be compatible with the low pressure in the specimen chamber ($\approx 10^{-3}$ Pa in conventional SEM and 10^{-5} – 10^{-4} Pa in field-emission SEM)
2. Have to be clean, i. e., the region of interest has to give free access to the primary beam
3. Need sufficient electrical conductivity
4. Need to be resistant to some extent to electron radiation
5. Have to provide a sufficient contrast.

In a narrower sense, only metals, alloys, and metallic compounds fulfill those requirements. Numerous preparation procedures mentioned in Sect. 5.1.4 were developed in the past and are still in the process of improvement, to provide a sufficient electrical conductivity to nonconductive specimens, to remove the water in samples, and to replace it or to rapidly freeze it in a structure-conserving manner. Nevertheless, there was and still is enormous interest in investigating specimens in their genuine state.

Thirty years ago *Robinson* [5.392] proposed examining any uncoated insulating specimen in the SEM at high accelerating voltages in the specimen chamber,

which had been modified to contain a small residual water vapor environment. It appeared that the presence of the water vapor sufficiently reduced the resistance of the insulator so that no charging effects were detected in backscattered electron micrographs. *Danilatos* [5.393] developed an *atmospheric scanning electron microscope* (ASEM), which later was called an *environmental scanning electron microscope* (ESEM®) [5.394] and is now a registered trademark. To enable the investigation of water and water-containing specimens in their native state at stationary conditions a minimum pressure of water vapor of about 612 Pa is required at 0 °C (Fig. 5.59). Stationary conditions in the specimen chamber of the SEM can be accomplished by controlling the water vapor pressure p in close vicinity of the specimen as well as the specimen temperature T such that the p – T values always correspond to points on the solid p – T graph in Fig. 5.59. For example, at 20 °C a water vapor pressure as large as about 2330 Pa is required for stationary conditions. p – T values below the solid graph, e. g., 300 Pa at 0 °C (Fig. 5.59), correspond to a relative humidity of less than 100%, thus representing nonstationary conditions.

How can stationary conditions be reached during imaging of a wet sample in the specimen chamber of an SEM? Figure 5.60 shows the cross section of the ESEM, which permits investigations at pressures sufficient for stationary conditions. Basically, the electron

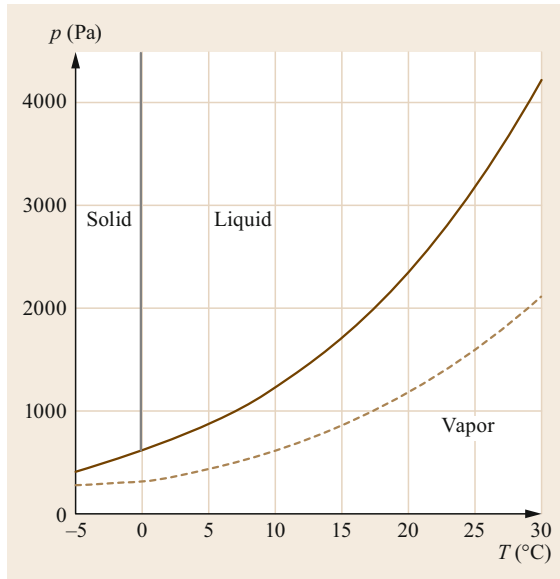


Fig. 5.59 Phase diagram of water. *Solid line*: 100% relative humidity (saturated vapor conditions); *dashed line*: 50% relative humidity. (Data from [5.395])

beam propagates in the column as in a conventional SEM until it reaches the final aperture. Then, since the pressure increases gradually as the electrons proceed toward the specimen, the electrons undergo significant scattering on gas molecules until they reach the specimen surface.

The electron–gas interaction is discussed in detail by Danilatos [5.35]. According to this study the average number of scattering events per electron n can be approximated by

$$n = \frac{\sigma_g p_g L}{k_B T}, \quad (5.44)$$

where σ_g represents the total scattering cross section of the gas molecule for electrons, L is the electron path length in gas, and k_B is the Boltzmann constant. These approximations hold for $\Lambda \gg L$, where Λ represents the mean free path of a beam electron in the gas. According to (5.44) the average number of collisions increases linearly with the gas pressure p_g and the path length in the specimen chamber. Furthermore, n depends via the scattering cross section on the type of gas molecules and on the temperature. When the beam electrons start to be scattered by the gas molecules, the fraction of scattered electrons is removed from the focused beam and hit the specimen somewhere in a large area around the point of incidence of the focused beam. The scattered electrons form a *skirt* around the focused beam, which has a radius of 100 μm for a pathlength of

5 mm (conditions: $E_0 = 10 \text{ keV}$, water vapor pressure = 10^3 Pa) [5.35]. Using a phosphor imaging plate, the distribution of unscattered beam electrons and the scattered *skirt* electrons was directly imaged by exposure to the electron beam for a specified time [5.397]. Related to the electron-beam intensity within 25 μm , the *skirt* intensity as a function of the distance from the center drops to 15% at 100 μm , 5% at 200 μm , and 1% at 500 μm (conditions: $E_0 = 20 \text{ keV}$, water vapor pressure = 266 Pa, $l = 10 \text{ mm}$) [5.397]. The signals generated by the electrons of the skirt originate from a large area, which contributes to the background, whereas the unscattered beam remains focused to a small spot on the specimen surface, although its intensity is reduced by the fraction of electrons removed by scattering. The resolution obtainable depends on the beam diameter and the size of the interaction volume in the specimen, which is analogous to the situation in conventional and high-resolution SEM, i. e., the resolving power of ESEM can be maintained in the presence of gas.

The detection of BSE, CL, and x-rays is to a great extent analogous to the detection in a conventional SEM, because these signals can penetrate the gas sufficiently [5.37, 398, 399]. However, the situation is completely different for the detection of SE. The conventional Everhart–Thornley detector would break down at elevated pressure in the specimen chamber. However, the gas itself can be used as an amplifier in a fashion similar to that used in ionization chambers and gas proportional counters. An attractive positive voltage on a detector will make all the secondary electrons drift toward it. If the attractive field is sufficiently large, each drifting electron will be accelerated, thus gaining enough energy to cause ionization of gas molecules, which can create more than one electron. This process repeating itself results in a significant avalanche amplification of the secondary electron current, which arrives at the central electrode of the environmental secondary electron detector (ESD) [5.35]. The avalanche amplification works best only in a limited pressure range and can amplify the SE signal up to three orders of magnitude [5.400]. Too high pressure in the specimen chamber makes the mean free path of the electrons very small and a high electric field between specimen and detector is required to accelerate them sufficiently. Too low pressure in the chamber results in a large mean free electron path, i. e., only a few ionization events take place along the electron path from the specimen to the detector, thus the avalanche amplification factor is low. The new generation of ESD, the gaseous secondary electron detector (GSED), which consists of a 3 mm diameter metallic ring placed above the specimen, provides better discrimination against parasitic

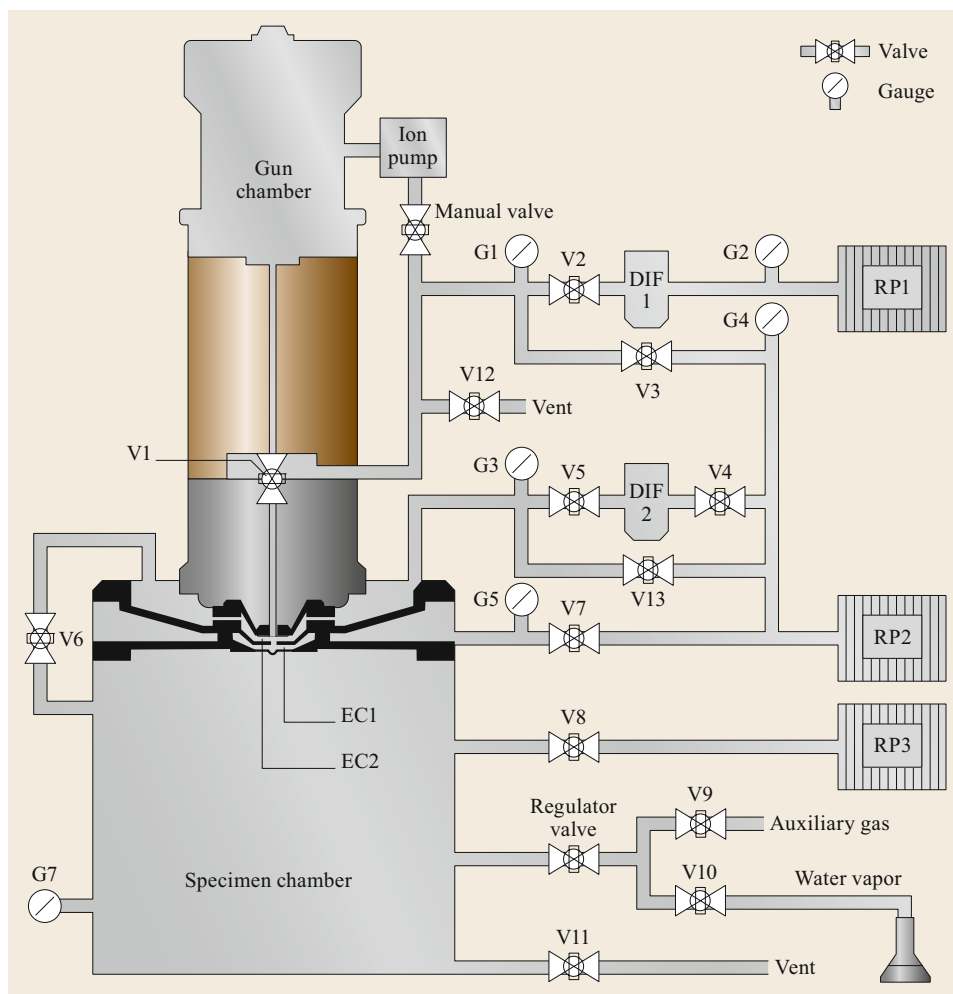


Fig. 5.60 Schematic cross section of the first commercial electroscan environmental SEM (ESEM[®]) showing the vacuum and pumping system. Two pressure-limiting apertures separate the electron optical column from the specimen chamber. Differential pumping of the stage above and between the two pressure-limiting apertures ensures the separation of high vacuum in the column from low vacuum in the specimen chamber. The differential pumping of two stages and optimum arrangement of the pressure-limiting apertures can work successfully to achieve pressures up to 10^5 Pa in the specimen chamber. After [5.396]

electron signals. Both the ESD and GSED are patented and are available only in the ESEM [5.37].

However, the ionization of gas molecules creates not only electrons but also ions and gaseous scintillation. The latter can be used to make images [5.399], i. e., in that case the imaging gas acts as a detector. This principle is used in the patented variable pressure secondary electron (VPSE) detector. Nonconductive samples attract positive gas ions to their surface as negative charge accumulates from the electron beam, thus effectively suppressing or at least strongly reducing charging artifacts [5.37, 401–405]. The gas ions can affect or even reverse the contrast in the GSED image under spe-

cific conditions, e. g., at specimen regions of enhanced electron emission, where the rate of electron-ion pairs increases [5.400]. The highly mobile electrons generated by electron-gas interaction are removed from the gas by rapid sweeping to the GSED, which in turn causes an increased concentration of positive ions during image acquisition due to different electric field-induced drift velocities of negative and positive charge carriers in the imaging gas [5.406].

However, imaging of wet, soft specimens can be hampered by the effect of surface tension [5.279], which may flatten and hereby deform the specimen. Obviously, this is a misleading situation demonstrating that

Fig. 5.61a–e Time-resolved sequence of secondary electron images recorded with an ESEM[®]-E3 (ElectroScan Corp., Wilmington, MA). The water meniscus between the hydrophilic tungsten tip (normal electron-beam incidence) and the Pt/C-coated mica (incidence angle of 85°) is clearly visible (**a–d**). Because of locally decreasing relative humidity the meniscus becomes gradually smaller until it snaps off (**e**). The absence of the meniscus leads to a significant change of shape of the water bead below the tip (**d,e**). Some water drops are located on the sample in front of and behind the tip. The sequence was recorded within 11 s and each image was acquired within about 2 s. Experimental conditions: $E_0 = 30$ keV, $I_p = 200$ pA, $p_g = 1.2$ kPa. Reprinted from [5.407], with the permission of AIP Publishing ►

environmental conditions do not necessarily guarantee structural preservation.

As mentioned above, about 612 Pa is the crucial minimum pressure for wet specimens. In addition to the ESEM, which enables imaging with SE at pressures up to about 6500 Pa, numerous variable pressure scanning electron microscopy (VPSEM), high-pressure SEM, and low vacuum scanning electron microscopy (sometimes the abbreviation LVSEM is used, which cannot be distinguished from the low-voltage SEM) became commercially available. The water vapor pressure in the specimen chamber of those SEM is typically at maximum 300 Pa, i.e., below the crucial value of 612 Pa, which is not sufficient for imaging of wet specimens at stationary conditions. To separate the specimen pressure of maximum 300 Pa from the high vacuum in the column only one pressure-limiting aperture is sufficient. For imaging at pressures in the range from 250 to 300 Pa backscattered electrons are utilized.

The workaround has been demonstrated by *Thiberge et al.* [5.408] for scanning electron microscopy of cells and tissues under fully hydrated atmospheric conditions utilizing a small chamber with a polyimide membrane (145 nm in thickness) that is transparent to beam and backscattered electrons. The membrane protects the fully hydrated sample from the vacuum. BSE imaging at acceleration voltages in the range of 12–30 kV revealed structures inside cultured cells and colloidal gold particles having diameters of 20 and 40 nm, respectively. Another interesting experimental setup is the habitat chamber designed to keep living cells under fully hydrated atmospheric conditions as long as possible and to reduce the exposure time to the lower pressure in the ESEM below 2 min [5.409].

Scanning electron microscopy at elevated pressure is increasingly used in very different fields. Apart from variations in the pressure and chamber gas a heating stage (maximum temperature about 1500°C) allows changes in the specimen temperature. For example, chemical reactions such as corrosion of metals, electrolyte–solid interactions, alloy formation, and the degradation of the space shuttle ceramic shields by increasing oxygen partial pressures at high temperatures are possible with micrometer resolution. The onset of chemical reactions that depend on various parameters

can be studied in detail. Insulators, including oil and oily specimens, can be directly imaged. Water can also be imaged directly in the ESEM, which allows studies of wetting and drying surfaces [5.410–412] and direct visualization of the dynamic behavior of a water meniscus [5.407, 413].

Figure 5.61 shows an example of dynamic studies of a water meniscus between the scanning tunneling tip and a support when the tip is moved across the sample. The wetting of the tip indicates a hydrophilic surface, whereas Fig. 5.62 clearly indicates a hydrophobic tip surface.

ESEM studies of the wettability alteration due to aging in crude oil/brine/rock systems that are initially water wet are of significant importance in the petroleum industry in understanding the water condensation behavior on freshly exposed core chips. Surface active compounds are rapidly removed from the migrating petroleum, thus changing the wettability and subsequently allowing larger hydrophobic molecules to sorb [5.414–416]. Furthermore, the ESEM is a power-

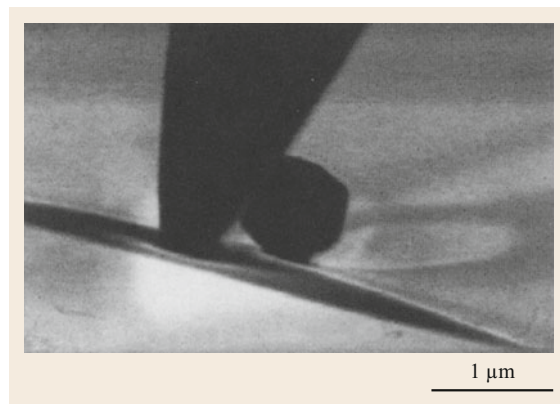
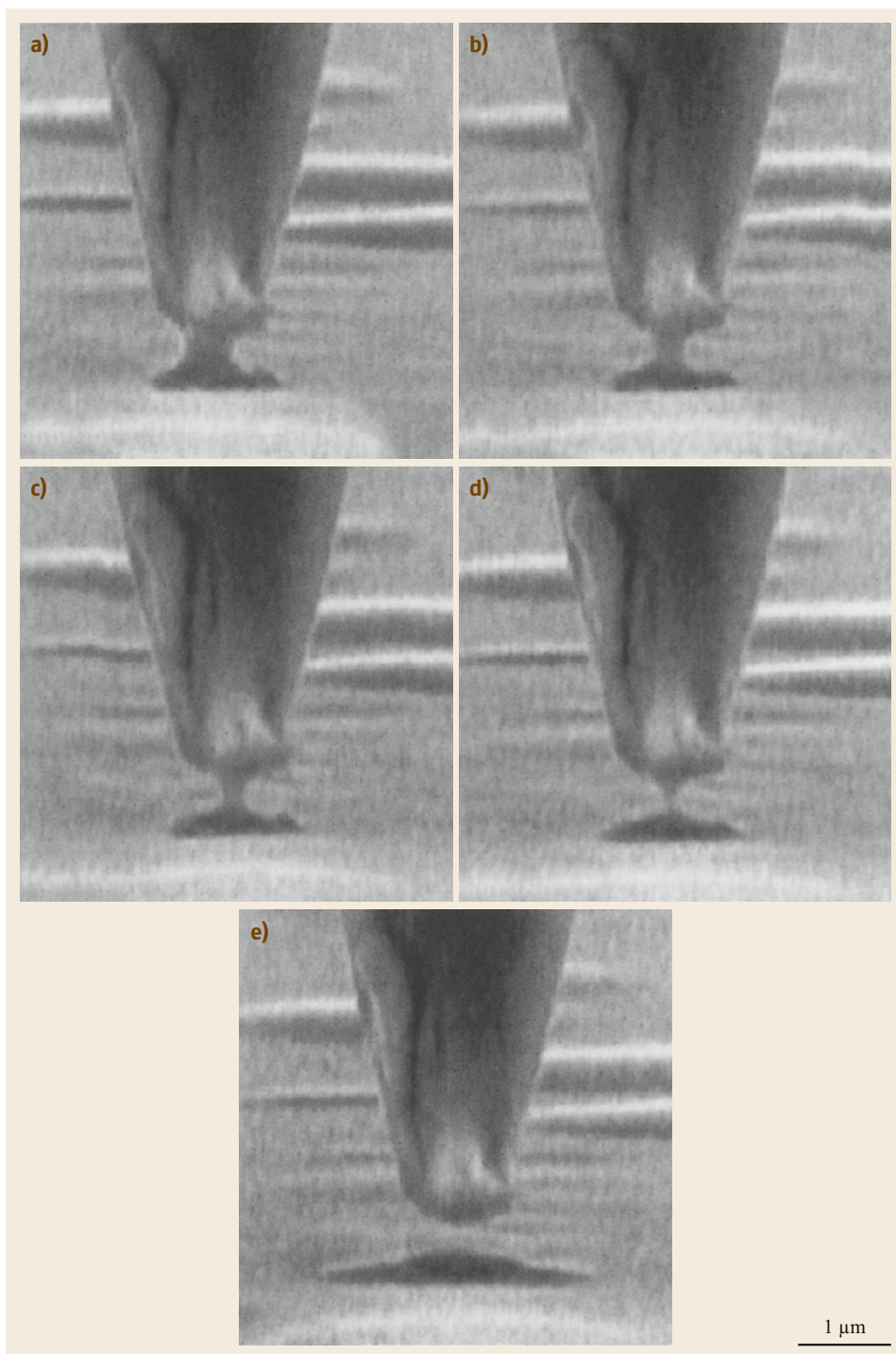


Fig. 5.62 Secondary electron image recorded with an ESEM-E3 (ElectroScan Corp., Wilmington, MA) from a hydrophobic tungsten tip (normal electron-beam incidence) and a water bead on Pt/C-coated mica (incidence angle of 85°). The shape of the deformed water surface in the submicrometer vicinity of the tip clearly indicates its hydrophobic surface. The spherical object (*black*) at the right of the tip in the back is probably a polystyrene sphere and any resemblance is purely coincidental. Reprinted from [5.407], with the permission of AIP Publishing



ful tool with which study the influence of salt, alcohol, and alkali on the interfacial activity of novel polymeric surfactants that exhibit excellent surface activity due to their unique structure [5.417].

Environmental scanning electron microscopy has disseminated rapidly among scientific and engineering disciplines. Applications range widely over diverse technologies such as pharmaceutical formulations, per-

sonal care and household products, paper fibers and coatings, cement-based materials, boron particle combustion, hydrogen sulfide corrosion of Ni-Fe, micromechanical fabrication, stone preservation, and biodeterioration. In spite of the broad applications, numerous contrast phenomena are not fully understood as yet. In

addition, ESEM investigations of polymeric and biological specimens, which are known from conventional electron microscopy to be highly irradiation sensitive, are more difficult because water acts as a source of small, highly mobile free radicals, which accelerate specimen degradation [5.418, 419].

5.4 Microanalysis in Scanning Electron Microscopy

The generation of x-rays due to electron–specimen interactions was discussed in Sect. 5.1.2, *X-Rays*. The characteristic x-rays emitted from the specimen carry information about its local element composition, which is utilized as a powerful microanalytical tool combining SEM with EDX and WDX spectrometers. X-ray microanalysis is by far the most widely used method combined with SEM, which enables in various modes qualitative and quantitative element analysis from a point or area of interest as well as mapping of the distribution of various elements simultaneously with SE and BSE imaging. The size of the interaction volume emitting x-rays is significantly larger than the ones for AE, SE, and BSE because of the weaker absorption of x-rays inside the specimen (Fig. 5.14) and the secondary emission by x-ray fluorescence outside the electron interaction volume. The secondary x-ray emission volume is much larger than that for primary x-ray emission since x-rays are more penetrating than electrons having the same energy. For electron-excited x-ray spectrometry performed on thick specimens in the SEM, the range $R_{\Delta 1}$ for x-ray excitation in μm is given according to Kanaya and Kayama [5.420] by

$$R = \left(\frac{0.0276A}{\rho Z^{0.89}} \right) (E_0^{1.67} - E_X^{1.67}), \quad (5.45)$$

where A is the atomic weight (g mol^{-1}), ρ is the density (g cm^{-3}), Z is the atomic number, E_0 is the incident electron energy (keV), and E_X is the x-ray energy (keV).

For reliable quantitative x-ray microanalytical studies, x-ray absorption, x-ray fluorescence, and the fraction of backscattered electrons, all of which depend on the composition of the specimen, have to be taken into account and are performed by the so-called ZAF correction. Z stands for atomic number, which affects the penetration of incident electrons into the material, A for absorption of x-rays in the specimen on the path to the detector, and F for fluorescence caused by other x-rays generated in the specimen.

Three different types of detectors can be used to measure the emitted x-ray intensity as a function of

the energy or wavelength. In an EDX system, as described there are now two different types of detectors available, an SiLi detector and a silicon drift detector (SDD) (Fig. 5.63a,b). The x-rays enter the detector and create electron–hole pairs that cause a pulse of current to flow through the detector circuit. The number of pairs produced by each x-ray photon is proportional to its energy (Sect. 5.1.1, *Detectors and Detection Strategies*).

SDDs have a small-sized anode with respect to their active area. The x-ray generates charged carriers (i. e., holes and electrons) that are directed along these electric field lines to the dramatically smaller anode at the center of the detector. Since the capacitance of the device is proportional to the anode size, a very small anode leads to a drastically lower device capacitance. Having a very small anode helps achieve better resolution at shorter shaping times (higher count rates) owing to the fact that the electronic noise at short shaping times varies in proportion to capacitance squared, especially at low energies where the SNR is much less. If the noise is small enough, it is possible to operate the device at temperatures ($\approx -20^\circ\text{C}$) that are readily achievable with a Peltier device. This avoids the use of LN2 cooling as in SiLi detectors.

In a WDX spectrometer (Fig. 5.64) the x-rays fall on a bent crystal and are reflected only if they satisfy Bragg's law. The crystal bending is such that it focuses x-rays of one specific wavelength onto a proportional counter and rotates to scan the wavelength detected. Some important features of both types of x-ray spectrometer are listed in Table 5.9. However, since instrumentation and analysis of data in x-ray microanalysis are usually considered a separate discipline, no further details are discussed in this section [5.27, 28, 43, 421–423].

A selected application of the very powerful combination of SEM imaging, x-ray microanalysis, and element mapping—the latter was invented almost exactly 50 years ago by *Cosslett and Duncumb* [5.424]—is illustrated in Fig. 5.65. The selected specimen is a Cr-Fe alloy with an Si phase, which has a locally varying composition as clearly indicated by the energy-dispersive

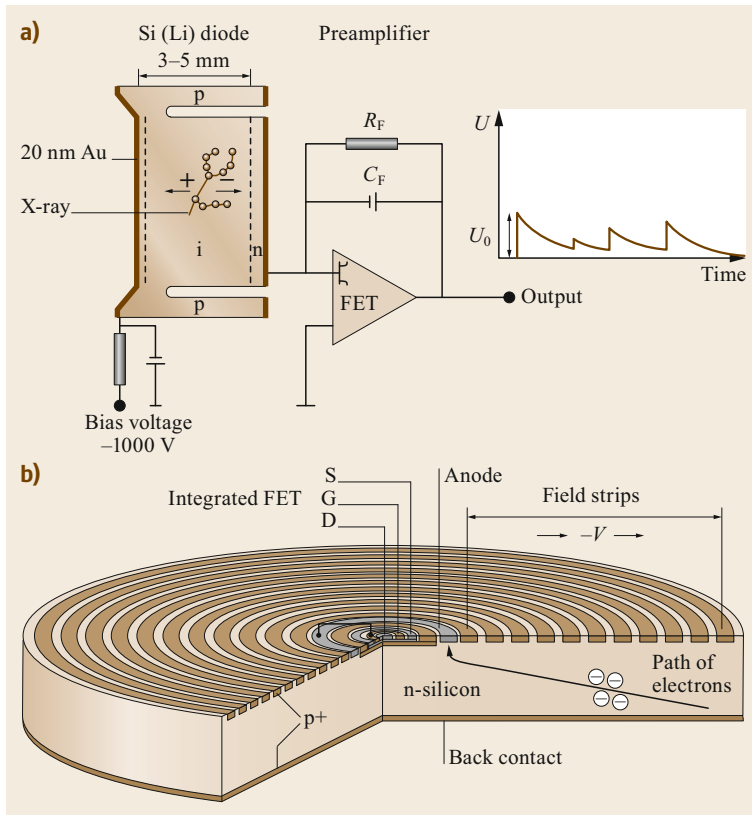
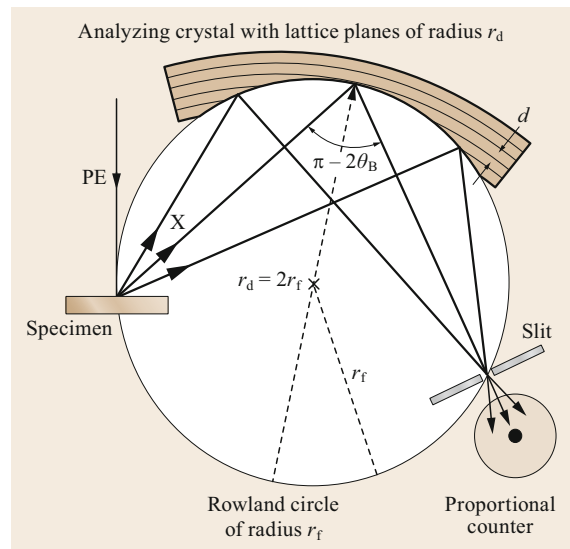


Fig. 5.63 (a) Scheme of Si(Li) x-ray diode coupled to a field-effect transistor (FET) with a resistive feedback loop (R_F , C_F). The shape of the output signal is shown in the output voltage versus time diagram. Typically, this principle is used in energy-dispersive x-ray (EDX) detectors. (b) Silicon drift detector, showing small anode size. Courtesy of PNSensor

Fig. 5.64 Principle of a wavelength-dispersive x-ray (WDX) spectrometer. Generated x-rays that hit the analyzing crystal are focused and because of Bragg reflection directed to a slit in front of the proportional counter lying on a Rowland circle with radius r_f . The lattice planes of the crystal are bent to a radius of $2r_f$ ▶

spectra in Fig. 5.65a,b recorded at different locations (Fig. 5.65c).

The area under each characteristic peak represents the amount of x-ray counts, which is—after subtraction of the Bremsstrahlung background below the peak and ZAF correction—a direct quantitative measure of the number of atoms of the specific element belonging to that peak. However, a simple visual inspection of the spectra shows, e. g., that the location 1 (Fig. 5.65a) contains significantly more chromium and less iron than location 2 (Fig. 5.65b). In addition, a strong silicon peak emerges in the spectrum of location 2 not present in the spectrum of 1 (Fig. 5.65a). The element distribution maps of four important chemical elements in the specimen, namely iron, chromium, silicon, and titanium, are shown in Fig. 5.65d–g. Comparing the information given by the four element distribution maps on the one hand and the two spectra on the other hand immediately



makes clear why the titanium peak does not emerge in the spectra and the chromium peak is dominant at location 1 but not at 2. By means of simple image-processing procedures the SE micrograph (Fig. 5.65c) and the element distribution maps (Fig. 5.65d–g) can

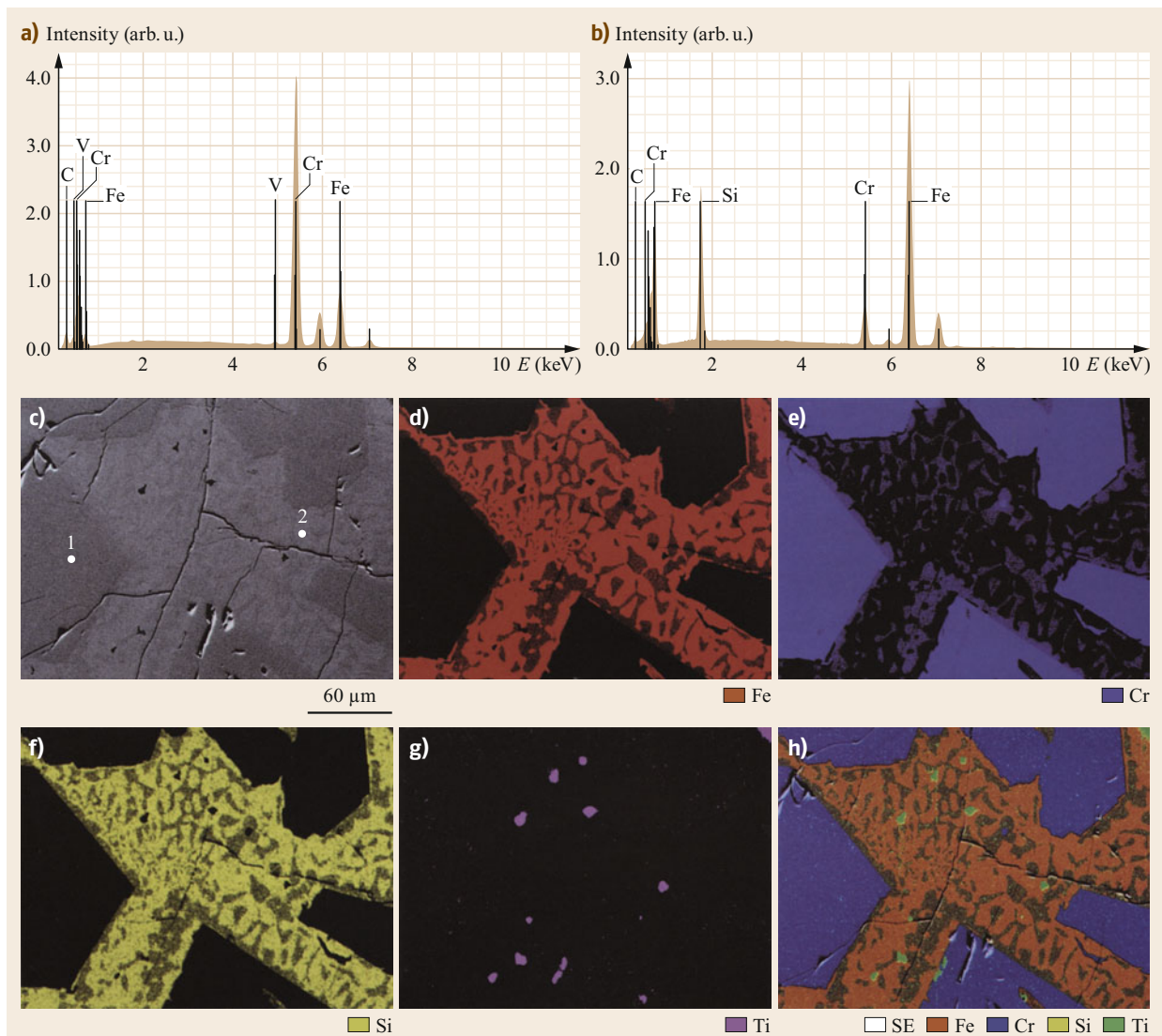


Fig. 5.65a-h X-ray microanalysis of a Cr-Fe-alloy with an Si phase. The EDX spectra (a,b) were recorded with the Bruker Flash[®] 3001 from locations 1 and 2 marked in the SE micrograph of the specimen (c). The positions of the characteristic x-ray energies for the various elements emerging in the spectra are indicated by thin lines, which are labeled with the chemical symbol of the corresponding chemical element. The elements iron, chromium, and vanadium occur with one K_{α} peak each in the energy range from 4.95 to 6.40 keV and with one less intense L_{α} peak each in the energy range from 0.51 to 0.71 keV. Elemental distribution maps of Fe (d), Cr (e), Si (f), and Ti (g) were recorded using the K_{α} lines. (h) Mixed micrograph obtained by superimposition of the SE image and the maps of the distribution of Fe, Cr, Si, and Ti within the field of view. Experimental conditions: SEM, LEO 438VP. For recording spectra: $E_0 = 20$ keV; count rate, $\approx 3 \times 10^3$ cps; acquisition time, 300 s. For recording maps: $E_0 = 25$ keV; count rate $\approx 1.5 \times 10^5$ cps; acquisition time 600 s. Kindly provided by Bruker Nano GmbH (formerly Röntec GmbH), Berlin, Germany

Table 5.9 Characteristic features of energy-dispersive x-ray (EDX) and wavelength-dispersive x-ray (WDX) detectors^a. Modern SDD EDS is capable of an energy resolution of down to 121 eV at Mn K_α and a maximum output count rate of 400 cps per detector, amounting to 1.6 Mcps for a BrukerFlatQUAD detector^{b,c}

Features	Energy-dispersive Si(Li) x-ray detector ^d	Energy-dispersive Si drift (SD) x-ray detector ^{e,f,g}	Wavelength-dispersive x-ray detector ^d
Geometric collection efficiency	< 2%	< 2%	< 0.2%
Quantum efficiency	≈ 100%	> 90%	≤ 30%
Element detection	Z ≥ 11 (Be window) Z ≥ 4 (windowless)	Z ≥ 5	Z ≥ 4
Energy resolution (eV)	150 (at 5.9 keV)	150 (at 10 ⁵ cps) 230 (at 6 × 10 ⁵ cps)	≈ 5
Maximum counting rate (cps)	3 × 10 ³	≈ 6 × 10 ⁵	10 ⁵
Spectrum acquisition	All energies simultaneously	All energies simultaneously	One wavelength at a time
Probe current (nA)	0.1–20	0.1–10	1–100

^a Si(Li): lithium-drifted silicon; cps: counts per second,

^b Friel et al. [5.425],

^c Goldstein et al. [5.426],

^d Reichelt [5.321],

^e Strüder et al. [5.427],

^f Strüder et al. [5.428],

^g Lechner et al. [5.429]

be superimposed in one image (Fig. 5.65h) presenting information for five individual images.

The most powerful tool in electron-beam microanalysis is the ability to depict the elemental compositional heterogeneity of matter with micrometer to nanometer lateral resolution. Many developments have occurred over the intervening years to advance this critical method (see detector performance comparison in Table 5.9). Further, computer-controlled SEM in connection with image processing and EDX spectrometry enables the unattended and automated determination of both the geometric parameters and the chemical composition of thousands of individual particles down to a size of 50–100 nm [5.34, 430]. Consequently, correlations between particle size, chemical composition, the number of different compounds, and their contribution to the overall concentration can be established. Problems may arise in connection with specimen preparation, optimization of the image contrast, the sometimes non-homogeneous composition of particles, shadowing of the x-rays in the case of large particles, and the lack

of a rigorous ZAF correction procedure for particles of arbitrary shape.

Another increasingly important application is multilayer analysis, i. e., the nondestructive measurement of the thickness and composition of thin films both unsupported and on substrates, which can be performed with high accuracy down to a thickness of 2 nm by a combination SEM and EDX [5.431–433]. For this purpose the ratio between the x-ray intensity of the film and the intensity of the same element of a bulk standard is used.

Low-voltage scanning electron microscopy ($E_0 < 5$ keV) offers both high spatial resolution and a significantly reduced x-ray generation depth. This enables the composition of thin layers on substrates to be determined without the need to use a dedicated thin film analysis program. The analysis of small phases down to a size of 50 nm is also possible [5.434, 435]. In principle elements of higher atomic number can be identified using L- and M-shell x-rays, but these are somewhat more complicated than the rather simple K-shell x-ray emissions.

5.5 Crystal Structure Analysis by Electron Backscatter Diffraction

In crystalline specimens electrons are diffracted at lattice planes according to Bragg's law given as

$$2d \sin \vartheta = n\lambda, \quad (5.46)$$

where d is the lattice-plane spacing, ϑ is Bragg's angle, and λ is the electron wavelength. Bragg's law requires that the incident and emergent angles should be equal ϑ . As previously mentioned, the backscattering coefficient sensitively depends on the tilt of the incident electron beam relative to the lattice and Bragg position. Changing the tilt of the incident beam relative to the lattice, e. g., by rocking the electron beam or tilting the specimen, affects the backscattering coefficient, which results in an electron channeling pattern (ECP). To obtain from an ECP information about the crystal structure, e. g., the crystal orientation and the lattice-plane spacings, a so-called panorama diagram recorded by successively tilting the specimen over a large angular range is required [5.43, 436, 437]. However, establishing a panorama diagram is a somewhat difficult task.

Another way of obtaining information about the crystal structure of the specimen is the use of electron diffraction effects associated with the scattered electrons. As described in Sect. 5.1.2, the beam electrons are scattered elastically and inelastically due to the electron-specimen interaction, thus scattered beam electrons travel within the excitation volume in all directions (Fig. 5.13). This scattering process can be considered as a small electron source inside the crystalline specimen emitting electrons in all directions as shown in Fig. 5.66. These electrons may be diffracted at sets of parallel lattice planes according to Bragg's law (5.46) as first observed by *Venables and Harland* [5.438]. Figure 5.66 illustrates that the electrons emitted from one point and diffracted at lattice planes will form pairs of cones centered with respect to the normal vector of these lattice planes. The opening angle of the cones is $180^\circ - 2\vartheta$ and the angle between them is 2ϑ . Since the Bragg angle is in the order of 1° for 15–30 keV electrons and lattice-plane spacings of 0.2–0.3 nm, the intersections of the cones with a flat observation screen positioned at a distance much larger than d (usually 2–4 cm from the point of beam-specimen intersection) and tangential to the propagation sphere of the scattered electrons are almost straight and parallel pairs of lines. They are called Kikuchi lines. The angle between parallel pairs of Kikuchi lines is 2ϑ . The whole EBSD pattern with the Kikuchi lines reveals local information about the crystalline structure within the individual excitation volume. A detailed treatment of EBSD, which is beyond the scope of this section, is

given by *Wilkinson and Hirsch* [5.439]. Nevertheless, it is worth mentioning that the relationship between EBSD and the previously introduced ECP is characterized by the reciprocity of their ray diagrams [5.38].

The recording of the EBSD pattern, which originally was performed by exposure of a photographic film, is now done by position-sensitive detectors such as a scintillation window with a CCD camera attached. To allow the diffracted electrons to escape from the specimen its surface is usually tilted approximately 60° or 70° toward the screen. The EBSD patterns are digitally acquired by computer, which also controls the positioning of the beam. In the case of automated crystal orientation mapping, the computer scans the electron beam stepwise across the specimen and controls the dynamic focusing of the beam (Fig. 5.9e and Sect. 5.1.1, *Specimen Tilting and Stereo Imaging*).

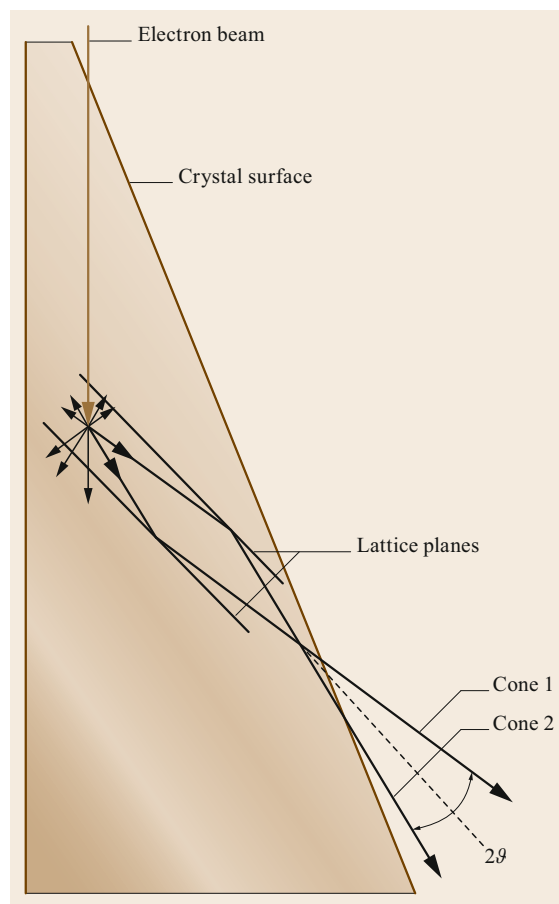


Fig. 5.66 Scheme of the formation of one pair of cones from diffraction of scattered electrons at one set of parallel lattice planes

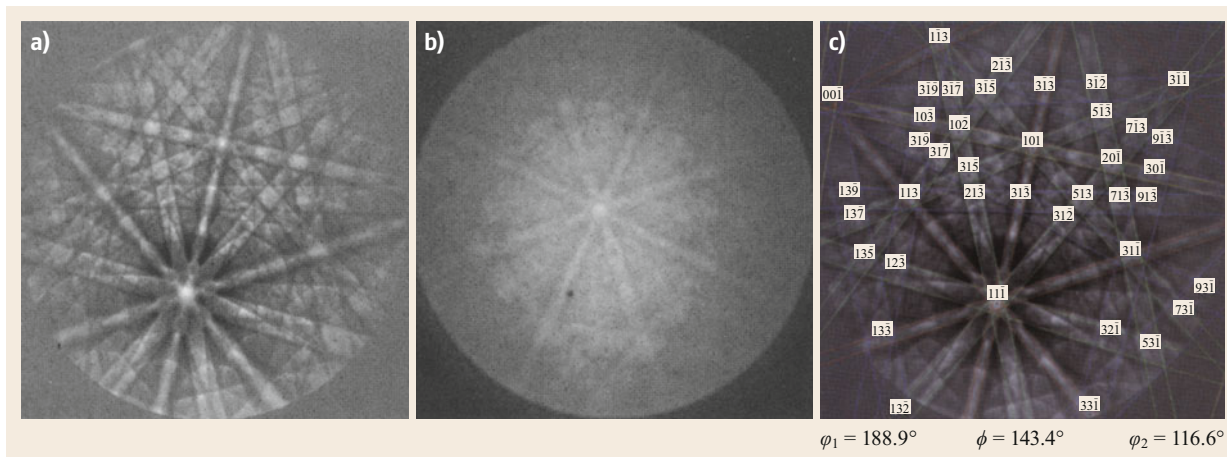


Fig. 5.67a–c EBSD patterns from an as-cast niobium specimen. **(a)** High-resolution EBSD pattern with background subtraction. Exposure time, 7 s. **(b)** Raw data EBSD pattern for high-speed mapping. Exposure time, 15 ms. EBSD patterns are recorded with a JSM-6500F thermal FESEM. **(c)** EBSD pattern from **(a)** with pairs of Kikuchi lines generated by automatic indexing. Images courtesy of JEOL USA

Since special software algorithms for the automated detection and indexing of Kikuchi lines in EBSD patterns were introduced by *Krieger-Lassen et al.* [5.440], *Adams et al.* [5.441] developed a new scanning technique called *orientation imaging microscopy* (OIM). In OIM, which is also called automated crystal orientation mapping, the EBSD pattern from each individual point at the specimen surface radiated by the electron beam is recorded and analyzed.

In the past decade, EBSD has become a powerful tool for crystallographic analysis such as the determination of the orientation of individual crystallites of polycrystalline materials in the SEM, phase identification, and characterization of grain boundaries, which is illustrated by the following examples. Figure 5.67 shows two different EBSD patterns from an as-cast niobium sample recorded with high (Fig. 5.67a) and low resolution (Fig. 5.67b), respectively [5.442], at a stationary beam position. Figure 5.67c shows the colored pairs of Kikuchi lines generated by automatic indexing and overlaid to the EBSD monitored in Fig. 5.67a.

Figure 5.68a shows an SE micrograph of polycrystalline austenite with the related color-coded orientation map of polycrystalline austenite monitored in Fig. 5.68b [5.443]. The spatial resolution obtained amounts to about 50 nm (at $E_0 = 15$ keV), i. e., smaller grains or precipitates cannot be detected in the orientation map. The map shown in Fig. 5.68c provides information about the grain boundary character and the orientation variations inside of each grain. The latter is shown for an individual grain in more detail in Fig. 5.69.

The OIM developed into a powerful technique providing a wealth of information about the type and distribution of different phases, the size, shape, and defects of grains, the type of grain boundaries, the local crystal orientation, and the preferential orientation (texture). To take full advantage of this new imaging technique in terms of spatial and orientation accuracy the thermal field-emission SEM providing a high beam current is most suitable. Furthermore, the SEM needs a very high mechanical and electronic stability because EBSD measurements require very long recording time, e. g., up to 12 h for very large orientation maps [5.442]. Finally, the preparation of specimens is a very delicate task since EBSD is a very surface-sensitive technique with an information depth of less than 10 nm up to a few tens of nanometers. Thus, the surface-near zone must be free of any deformation and, in addition, the surface has to be rather smooth because any surface relief may affect data acquisition.

The application of OIM is not restricted to metals and alloys. Crystalline materials such as semiconductors [5.444], ceramics [5.445, 446], and minerals [5.447, 448] can be investigated. A new avenue for EBSD introduced in the last few years is called TKD, or transmission Kikuchi diffraction [5.449]. The technique effectively used ultrathin, TEM-like specimens to achieve on the order of 10–20 nm resolution crystallographic analysis inside the SEM. TKD requires a slightly different holder to accommodate an ultrathin specimen imaged and analyzed using transmitted electrons in SEM.

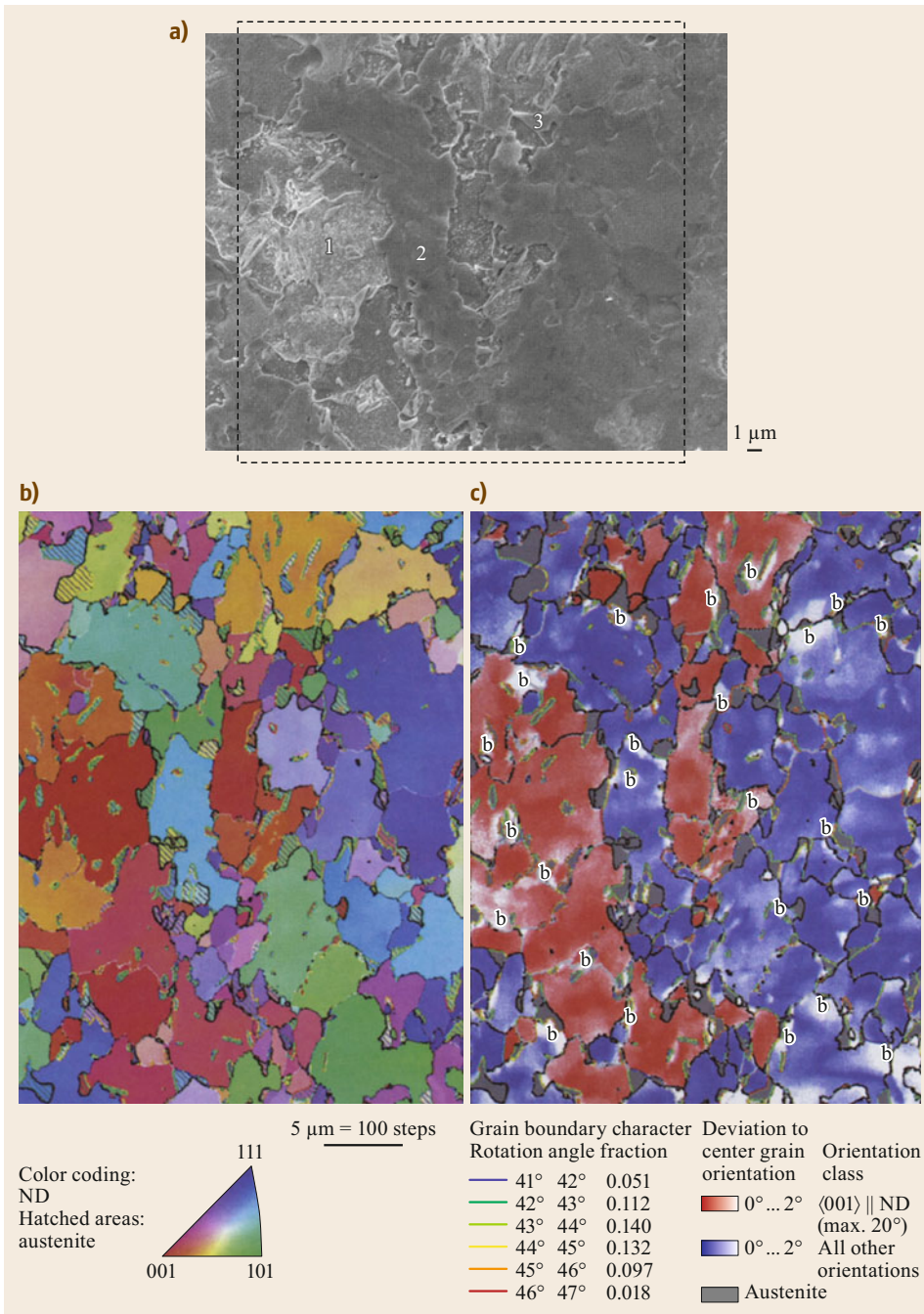
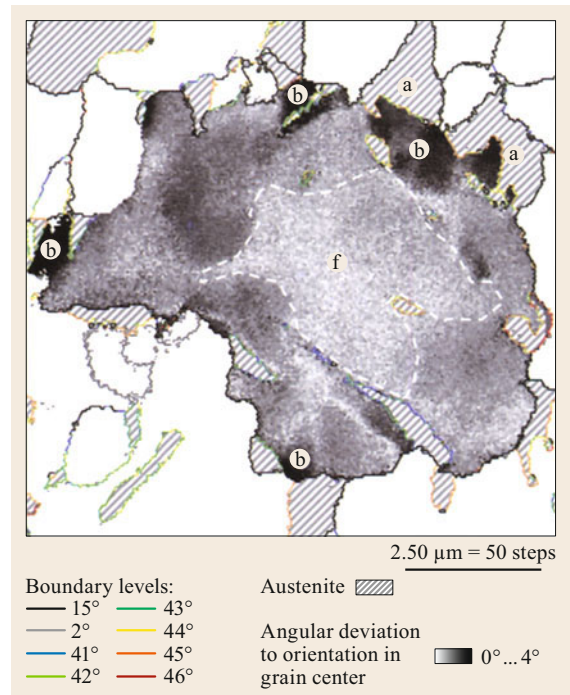


Fig. 5.68a–c Secondary electron micrograph of austenite **(a)** with rough (1), relatively smooth (2), and smooth (3) surface areas. **(b)** Orientation map of **(a)** measured by automated crystal orientation mapping and grayscale coded for the crystal direction parallel to the normal direction (ND) of the sheet. *Hatched areas* correspond to austenite grains. **(c)** The boundary character between γ - and α -grains, different orientation components ($(001) \parallel ND$, red; all others blue) and the orientation variations inside of each grain (*color shading*; b: bainite). The micrograph and the maps are recorded with a JSM-6500F thermal FESEM. Note: the extension toward the top and bottom of the measured area in **(b,c)** is larger than the area marked in **(a)**. (Reprinted from [5.443], with permission from Elsevier)

Fig. 5.69 Orientation map of one grain from the microstructure in Fig. 5.68a. Grayscale code: angular deviation of every mapping point to one orientation in the center of the grain. Bainite appears in conjunction with a steep orientation gradient in ferrite. The white line marks the maximum extension of austenite at the austenization temperature. f: ferrite; a: austenite (hatched); b: bainite. Reprinted from [5.443], with permission from Elsevier ►

Acknowledgments. In the contribution in *Science of Microscopy*, on which this chapter is based, the late Professor Reichelt thanked Dipl.-Ing. Harald Nüsse (artwork), Dr. Vladislav Kryzaneck (Monte Carlo simulations of scattering in thin and bulk specimens), Mrs. Ulrike Keller (scanning electron microscope expertise) and Mrs. Gudrun Kiefermann (photography), all of the Institut für Medizinische Physik und Biophysik of the University of Münster, for very welcome help. The chapter was dedicated to his wife Doris and his daughter Hanna.

D.C.B. and N.E., who have undertaken the revision of the earlier text, would like to thank Mr. Masateru Shibata (JEOL USA) for his kind help with some of the illustrations in this chapter. D.C.B. and N.E. would like to dedicate it to Campbell, Angus, and Gideon.



References

- 5.1 H. Stintzing: Verfahren und Einrichtung zum automatischen Nachweis, Messung und Zählung von Einzelteilchen beliebiger Art, Form und Größe, German Patent 485155 (1927)
- 5.2 M. Knoll: Aufladepotential und Sekundäremission elektronenbestrahlter Körper, Z. Tech. Phys. **116**, 467 (1935)
- 5.3 M. von Ardenne: Das Elektronen-Rastermikroskop. Praktische Ausführung, Z. Tech. Phys. **19**, 407 (1938)
- 5.4 E. Ruska: *Die frühe Entwicklung der Elektronenlinsen und der Elektronenmikroskopie* (Deutsche Akademie der Naturforscher Leopoldina, Halle 1979)
- 5.5 V.K. Zworykin, J. Hillier, R.L. Snyder: A scanning electron microscope, ASTM Bulletin **117**, 15 (1942)
- 5.6 C.W. Oatley: *The Scanning Electron Microscope. Part 1: The Instrument* (Cambridge Univ. Press, Cambridge 1972)
- 5.7 J. Ohnsorge, R. Holm: *Rasterelektronenmikroskopie—Eine Einführung für Mediziner und Biologen* (Thieme, Stuttgart 1973)
- 5.8 D.B. Holt, M.D. Muir, P.R. Grant, I.M. Boswarva (Eds.): *Quantitative Scanning Electron Microscopy* (Academic Press, London 1974)
- 5.9 O.C. Wells: *Scanning Electron Microscopy* (McGraw-Hill, New York 1974)
- 5.10 M.A. Hayat (Ed.): *Principles and Techniques of Scanning Electron Microscopy*, Vol. 1–6 (Van Nostrand Reinhold, New York 1974)
- 5.11 J. Goldstein, H. Yakowitz: *Practical Scanning Electron Microscopy* (Plenum, New York 1975)
- 5.12 L. Reimer, G. Pfefferkorn: *Raster-Elektronenmikroskopie* (Springer, Berlin 1973)
- 5.13 L. Reimer, G. Pfefferkorn: *Raster-Elektronenmikroskopie*, 2nd edn. (Springer, Berlin 1977)
- 5.14 G. Pfefferkorn (Ed.): *Beiträge zur elektronenmikroskopischen Direktabbildung und Analyse von Oberflächen (BEDO)*, Vol. 1 (R.A. Remy, Münster 1968)
- 5.15 O. Johari (Ed.): *Proceedings of the Annual Scanning Electron Microscopy Symposium* (IIT Research Institute, Chicago 1987)
- 5.16 L. Reimer: Scanning electron microscopy—Present state and trends, Scanning **1**, 3 (1978)
- 5.17 V.H. Heywood: *Scanning Electron Microscopy. Systematic and Evolutionary Applications* (Academic Press, London 1971)
- 5.18 T. Fujita, M.D.J. Tokunaga, H. Inoue: *Atlas of Scanning Electron Microscopy in Medicine* (Elsevier, Amsterdam 1971)
- 5.19 P.R. Thornton: *Scanning Electron Microscopy. Application to Materials and Device Science* (Chapman Hall, London 1972)
- 5.20 P.R. Troughton, L.A. Donaldson: *Probing Plant Structure* (Chapman Hall, London 1972)
- 5.21 B.M. Siegel, D.R. Beaman: *Physical Aspects of Electron Microscopy and Microbeam Analysis* (Wiley, New York 1975)
- 5.22 J.A. Chandler: *X-Ray Microanalysis in the Electron Microscope* (North-Holland, Amsterdam 1978)
- 5.23 J.-P. Revel, G.H. Haggis, T. Barnard (Eds.): *The Science of Biological Specimen Preparation for Microscopy and Microanalysis* (Scanning Electron Microscopy, Chicago 1983)

- 5.24 D.E. Newbury, D.C. Joy, P. Echlin, C.E. Fiori, J.I. Goldstein: *Advanced Scanning Electron Microscopy and X-Ray Microanalysis* (Plenum, New York 1987)
- 5.25 K. Wetzig, D. Schulze (Eds.): *In Situ Scanning Electron Microscopy in Materials Research* (Akademie, Berlin 1995)
- 5.26 S.J.B. Reed: *Electron Microprobe Analysis and Scanning Electron Microscopy in Geology* (Cambridge Univ. Press, Cambridge 1996)
- 5.27 J.J. Goldstein, D.E. Newbury, P. Echlin, D.C. Joy, C. Fiori, E. Lifshin: *Scanning Electron Microscopy and X-Ray Microanalysis* (Plenum, New York 1984)
- 5.28 J.J. Goldstein, D.E. Newbury, D.C. Joy, C.E. Lyman, P. Echlin, E. Lifshin, L.C. Sawyer, J.R. Michael: *Scanning Electron Microscopy and X-Ray Microanalysis*, 3rd edn. (Kluwer Academic/Plenum, New York 2003)
- 5.29 C.E. Lyman, D.E. Newbury, J.I. Goldstein, D.B. Williams, A.D. Romig, J.T. Armstrong, P. Echlin, C.E. Fiori, D.C. Joy, E. Lifshin, K.-R. Peters: *Scanning Electron Microscopy, X-Ray Microanalysis and Analytical Electron Microscopy* (Plenum, New York 1990)
- 5.30 L. Reimer: *Image Formation in Low-Voltage Scanning Electron Microscopy* (SPIE, Bellingham/Washington 1993)
- 5.31 D.C. Joy: *Monte Carlo Modeling for Electron Microscopy and Microanalysis* (Oxford Univ. Press, New York 1995)
- 5.32 L.C. Sawyer, D.T. Grubb: *Polymer Microscopy* (Chapman Hall, London 1996)
- 5.33 I. Müllerová, L. Frank: Scanning low-energy electron microscopy, *Adv. Imaging Electron Phys.* **128**, 310–443 (2003)
- 5.34 D.C. Bell, N. Erdman: *Low Voltage Electron Microscopy: Principles and Applications* (Wiley, New York 2013)
- 5.35 G.D. Danilatos: Foundations of environmental scanning electron microscopy, *Adv. Electron. Electron Phys.* **71**, 109–250 (1988)
- 5.36 G.D. Danilatos: Theory of the gaseous detector device in the ESEM, *Adv. Electron. Electron Phys.* **78**, 1–102 (1990)
- 5.37 D. Stokes: *Principles and Practice of Variable Pressure: Environmental Scanning Electron Microscopy (VP-ESEM)* (Wiley, New York 2008)
- 5.38 L. Reimer: *Scanning Electron Microscopy* (Springer, Berlin 1985)
- 5.39 W. DeVore, S.D. Berger: High emittance electron gun for projection lithography, *J. Vac. Sci. Technol. B* **14**, 3764 (1996)
- 5.40 W. Glaser: *Grundlagen der Elektronenoptik* (Springer, Wien 1952)
- 5.41 P. Grivet: *Electron Optics* (Pergamon, Oxford 1972)
- 5.42 O. Klemperer: *Electron Optics* (Cambridge Univ. Press, Cambridge 1971)
- 5.43 L. Reimer: *Scanning Electron Microscopy*, 2nd edn. (Springer, Berlin 1998)
- 5.44 V.E. Cosslett: Probe size and probe current in the STEM, *Optik* **36**, 85 (1972)
- 5.45 J.E. Barth, P. Kruit: Absorption of additional photons in the multiphoton ionisation continuum of xenon at 1064, 532 and 440 nm, *Optik* **101**, 101 (1996)
- 5.46 R. Kolarik, M. Lenc: An expression for the resolving power of a simple optical system, *Optik* **106**, 135 (1997)
- 5.47 T.E. Everhart, R.F.M. Thornley: Wide-band detector for micro-microampere low-energy electron currents, *J. Sci. Instrum.* **37**, 246 (1960)
- 5.48 A.V. Crewe, M. Isaacson, P. Johnson: Secondary electron detection in a field emission scanning microscope, *Rev. Sci. Instrum.* **41**, 20 (1970)
- 5.49 M.T. Postek, W.J. Keery: Low profile high-efficiency microchannel-plate detector system for scanning electron microscopy applications, *Rev. Sci. Instrum.* **61**, 1648 (1990)
- 5.50 R. Aufrata, R. Hermann, M. Müller: An efficient BSE single crystal detector for SEM, *Scanning* **14**, 127 (1992)
- 5.51 R. Aufrata, J. Jiráč, J. Spinka, O. Hutar: Integrated single crystal detector for simultaneous detection of cathodoluminescence and backscattered electrons in scanning electron microscopy, *Scanning Microsc.* **6**, 69 (1992)
- 5.52 V.N.E. Robinson: BSE imaging at low accelerating voltages, *Hitachi Instrum. News* **19**, 32 (1990)
- 5.53 J. Stephen, B.J. Smith, D.C. Marshall, E.M. Wit-tam: Applications of a semiconductor backscattered electron detector in a scanning electron microscope, *J. Phys. E* **8**, 607 (1975)
- 5.54 E.F. Bond, D. Beresford, H.H. Haggis: Improved cathodoluminescence 'microscopy', *J. Microsc.* **100**, 271 (1974)
- 5.55 A. Rasul, S.M. Davidson: Applications of a high performance SEM-based CL analysis system to compound semiconductor devices, *Scanning Electron Microsc.* **1**, 233 (1977)
- 5.56 R. Aufrata: A modification of the ET secondary electron detector with a single crystal scintillator, *Scanning* **12**, 119 (1990)
- 5.57 R. Aufrata, J. Hejna: Detectors for low voltage scanning electron microscopy, *Scanning* **13**, 275 (1991)
- 5.58 R. Aufrata, P. Schauer: Cathodoluminescence of Polysilanes. In: *13th Eur. Congr. Microsc.*, ed. by D. Schryvers, J.-P. Timmermans, D. van Dyck, P. van Oostveldt (Belgian Society for Microscopy, Liège 2004) pp. 75–76
- 5.59 C.H. Wu, D.B. Wittry: Investigation of minority-carrier diffusion lengths by electron bombardment of Schottky barriers, *J. Appl. Phys.* **49**, 2827 (1974)
- 5.60 P.E. Russel, J.F. Mancuso: Microchannel plate detector for low voltage scanning electron microscopes, *J. Microsc.* **140**, 323 (1985)
- 5.61 F.J. Judge, J.M. Stubbs, J. Philp: A concave mirror, light pipe photon collecting system for cathodoluminescence studies on biological specimens in the JSM 2 scanning electron microscope, *J. Phys. E* **7**, 173 (1974)
- 5.62 A. Boyde, S.A. Reid: New methods for cathodoluminescence in the SEM, *Scanning Electron Microsc.* **4**, 1803 (1983)
- 5.63 W.R. McKinney, P.V.C. Hough: A new detector system for cathodoluminescence 'microscopy', *Scanning Electron Microsc.* **1**, 251 (1977)

- 5.64 E.M. Hörl: SEM of biological material using cathodoluminescence, *Micron* **3**, 540 (1972)
- 5.65 E.M. Hörl: Rasterelektronenmikroskopie unter Verwendung eines Farbmonitors, *Beitr. Elektronenmikr. Direktabb. Anal. Oberfl.* **8**, 233 (1975)
- 5.66 E.I. Rau, R.A. Sennov, D.S.H. Chan, J.C.H. Phang: The main principles of improved spatial resolution cathodoluminescence microscopy and microtomography using elliptical mirror optics. In: *Proc. 13th Eur. Congr. Microsc.*, ed. by J.-P. Timmermans, D. Schryvers, D. van Dyck, P. van Oostveldt (Belgian Society for Microscopy, Liège 2004) pp. 411–412
- 5.67 A. Ishikawa, F. Mizuno, Y. Uchikawa, S. Maruse: High resolution and spectroscopic cathodoluminescent images in SEM, *Jpn. J. Appl. Phys.* **12**, 286 (1973)
- 5.68 L. Reimer: Electron signal and detector strategy. In: *Electron Beam Interactions with Solids for Microscopy, Microanalysis & Microlithography*, ed. by D.F. Kyser, H. Niedrig, D.E. Newbury, R. Shimizu (Scanning Electron Microscopy, Chicago 1984) pp. 299–310
- 5.69 S. Kimoto, H. Hashimoto, T. Suganama: Stereoscopic observation in SEM using multiple detectors. In: *The Electron Microprobe*, ed. by T.D. McKinley, K.F.J. Heinrich, D.B. Wittrey (Wiley, New York 1966) pp. 480–489
- 5.70 J. Hejna, L. Reimer: Backscattered electron multi-detector systems for improved quantitative topographic contrast, *Scanning* **9**, 162 (1987)
- 5.71 J. Lebedzik: An automatic topographical surface reconstruction in the SEM, *Scanning* **2**, 230 (1979)
- 5.72 D. Kaczmarek: The method of increasing COMPO contrast by linearization of backscattering characteristic $\eta = f(Z)$, *Scanning* **19**, 310 (1997)
- 5.73 D. Kaczmarek, J. Domaradzki: The method for the reconstruction of complex images of specimens using backscattered electrons, *Scanning* **24**, 65 (2002)
- 5.74 I. Müllerová, M. Lenc, M. Florián: Collection of backscattered electrons with a single polepiece lens and a multiple detector, *Scanning Microsc.* **3**, 419 (1989)
- 5.75 P. Kruit: Magnetic through-the-lens detection in electron microscopy and spectroscopy, Part 1. In: *Advances in Optical and Electron Microscopy*, Vol. 12, ed. by T. Mulvey, C.J.R. Sheppard (Academic Press, London 1991) pp. 93–137
- 5.76 A.E. Lukianov, G.V. Spivak, E.I. Rau, D.D. Gorodsky: The secondary electron SEM-collector with magnetic field. In: *Proc. 5th Eur. Congr. Electron Microsc.*, ed. by V.E. Cosslett (The Institute of Physics, London 1972) pp. 186–187
- 5.77 H. Koike, K. Ueno, M. Suzuki: Scanning device combined with conventional electron microscope. In: *Proc. EMSA* (Clayton's Publishing Division, Baton Rouge 1971) p. 28
- 5.78 J. Zach: Design of a high-resolution low-voltage scanning electron microscope, *Optik* **83**, 30 (1989)
- 5.79 J. Zach, H. Rose: High-resolution low-voltage electron microprobe with large SE detection efficiency. In: *Inst. of Phys. Conf. Ser. No. 93* (IOP, Bristol 1988) pp. 81–82
- 5.80 J. Zach, H. Rose: Efficient detection of secondary electrons in low-voltage SEM, *Scanning* **8**, 285 (1988)
- 5.81 J. Frosien, E. Plies, K. Anger: Compound magnetic and electrostatic lenses for low-voltage applications, *J. Vac. Sci. Technol. B* **7**, 1874 (1989)
- 5.82 S. Menzel, K. Wetzig: In situ production and defect characterization of laser PVD layers from YBaCuO HTSC targets inside a scanning electron microscope, *J. Mater. Sci.* **3**, 5 (1992)
- 5.83 A.J. Craven, J.M. Gibons, A. Howie, D.R. Spalding: Study of single-electron excitations by electron microscopy I. Image contrast from delocalized excitations, *Philos. Mag. A* **38**, 519 (1978)
- 5.84 M.S. Isaacson: Specimen damage in the electron microscopy. In: *Principles and Techniques of Electron Microscopy*, Vol. 7, ed. by M.A. Hayat (Van-Nostrand Reinhold, New York 1977) pp. 1–78
- 5.85 M. Isaacson: Electron beam induced damage of organic solids: Implications for analytical electron microscopy, *Ultramicroscopy* **4**, 193 (1979)
- 5.86 L. Reimer, A. Schmidt: The shrinkage of bulk polymers by radiation damage in an SEM, *Scanning* **7**, 47 (1985)
- 5.87 R.F. Egerton, P. Li, M. Malac: Radiation damage in the TEM and SEM, *Micron* **35**, 399 (2004)
- 5.88 J. Bastacky, C. Wodley, R. Labrie, C. Backhus: Addendum to: A bibliography of low-temperature scanning electron microscopy (LTSEM, Cryo SEM) and scanning electron microscopy of frozen hydrated biological systems, *Scanning* **10**, 37 (1988)
- 5.89 C.E. Jeffree, N.D. Read: Ambient- and low-temperature scanning electron microscopy. In: *Electron Microscopy of Plant Cells*, ed. by J.L. Hall, C. Hawes (Academic Press, London 1991) pp. 313–413
- 5.90 P. Walther, J. Hentschel, P. Herter, T. Müller, K. Zierold: Imaging of intramembranous particles in frozen-hydrated cells (*Saccharomyces cerevisiae*) by high-resolution cryo SEM, *Scanning* **12**, 300 (1990)
- 5.91 R.P. Huebener: Scanning electron microscopy at very low temperatures, *Adv. Electron. Electron Phys.* **70**, 1–78 (1988)
- 5.92 L. Lawson: Fatigue stage for quantitative acoustic emission measurements, *Scanning* **17**, 322 (1995)
- 5.93 E. Oho, M. Miyamoto: Mechanical scanning of the specimen in the scanning electron microscope, *Scanning* **26**, 250 (2004)
- 5.94 C. Gerber, G. Binnig, H. Fuchs, O. Marti, H. Rohrer: Scanning tunneling microscope combined with a scanning electron microscope, *Rev. Sci. Instrum.* **57**, 221 (1986)
- 5.95 A. Stemmer, R. Reichelt, R. Wyss, A. Engel: Biological structures imaged in a hybrid scanning transmission electron microscope and scanning tunneling microscope, *Ultramicroscopy* **35**, 255 (1991)
- 5.96 M. Troyon, H.N. Lei, A. Bourhettar: Integration of an STM in an SEM, *Ultramicroscopy* **1564**, 42–44 (1992)
- 5.97 I. Joachimsthaler, R. Heiderhoff, L.J. Balk: A universal scanning-probe-microscope-based hybrid system, *Meas. Sci. Technol.* **14**, 87 (2003)

- 5.98 R. Heiderhoff, O.V. Sergeev, Y.Y. Liu, J.C.H. Phang, L.J. Balk: Comparison between standard and near-field cathodoluminescence, *J. Cryst. Growth* **210**, 303 (2000)
- 5.99 M.T. Postek, A.E. Vladár: Digital imaging for scanning electron microscopy, *Scanning* **18**, 1 (1996)
- 5.100 N.C. Yew: Dynamic focusing technique for tilted samples in SEM. In: *Proc. 4th Annu. Scanning Electron Microsc. Symp.* (IIT Research Institute, Chicago 1971) pp. 33–40
- 5.101 A.W. Judge: *Stereographic Photography* (Chapman Hall, London 1950)
- 5.102 W. Malkusch, M.A. Konerding, B. Klaphor, J. Bruch: A simple and accurate method for 3-D measurements in microcorrosion casts illustrated with tumour vascularization, *Anal. Cell Pathol.* **9**, 69 (1995)
- 5.103 B. Minnich, H. Leeb, E.W.N. Bernroder, A. Lametschwandtner: A 3-dimensional morphometry in scanning electron 'microscopy': A technique for accurate dimensional and angular measurements of microstructures using stereopaired digitized images and digital image analysis, *J. Microsc.* **195**, 23 (1999)
- 5.104 B. Minnich, W.-D. Krautgartner, A. Lametschwandtner: Quantitative 3-D analysis in SEM: A review, *Microsc. Microanal.* **9**(S3), 118 (2003)
- 5.105 L. Reimer, E.-R. Krefting: The effect of scattering models on the results of Monte Carlo calculations. In: *Use of Monte Carlo Calculations in Electron Probe Microanalysis and Scanning Electron Microscopy*, NBS Special Publication, Vol. 460, ed. by K.F.J. Heinrich, D.E. Newbury, H. Yakowitz (U.S. Dept. of Commerce, Washington 1976) pp. 45–60
- 5.106 P. Rez: Elastic scattering of electrons by atoms. In: *Electron Beam Interactions with Solids for Microscopy, Microanalysis & Microlithography*, ed. by D.F. Kyser, H. Niedrig, D.E. Newbury, R. Shimizu (Scattering Electron Microscopy, Chicago 1984) pp. 43–49
- 5.107 L. Reimer, B. Lödding: Theory of secondary electron emission II, *Scanning* **6**, 128 (1984)
- 5.108 Z. Czyżewski, D. O'Neill MacCallum, A. Romig, D.C. Joy: Calculations of Mott scattering cross-sections, *J. Appl. Phys.* **68**, 3066 (1990)
- 5.109 A. Jablonski, F. Salvat, C.J. Powell: *NIST Electron Elastic-Scattering Cross Section Database #64 Version 3.1* (NIST, Gaithersburg 2003)
- 5.110 H. Raether: *Excitation of Plasmons and Interband Transitions by Electrons*, Springer Tracts in Modern Physics, Vol. 88 (Springer, Berlin 1980)
- 5.111 C.J. Powell: Inelastic scattering of electrons in solids. In: *Electron Beam Interactions with Solids for Microscopy, Microanalysis & Microlithography*, ed. by D.F. Kyser, H. Niedrig, D.E. Newbury, R. Shimizu (Scanning Electron Microscopy, Chicago 1984) pp. 19–31
- 5.112 M. Isaacson, J.P. Langmore: Determination of the non-localization of the inelastic scattering of electrons by electron microscopy, *Optik* **41**, 92 (1974)
- 5.113 E. Zeitler: Utilization of inelastic scatter in the STEM mode, *Ann. N.Y. Acad. Sci.* **306**, 62 (1978)
- 5.114 R. Reichelt, A. Engel: Contrast and resolution of scanning transmission electron microscope imaging modes, *Ultramicroscopy* **19**, 43 (1986)
- 5.115 D.A. Müller, J. Silcox: Delocalization in inelastic electron scattering. In: *13th Int. Congr. Electron Microsc.*, Vol. 1, ed. by B. Jouffrey, C. Colliex (Les Editions de Physique, Les Ulis 1994) pp. 741–742
- 5.116 D.A. Müller, J. Silcox: Delocalization in inelastic scattering, *Ultramicroscopy* **59**, 195 (1995)
- 5.117 R.D. Leapman, P. Rez, D.F. Mayers: K, L, and M shell generalized oscillator strengths and ionization cross sections for fast electron collisions, *J. Chem. Phys.* **72**, 1232 (1980)
- 5.118 M. Inokuti, S.T. Manson: Cross sections for inelastic scattering of electrons by atoms—Selected topics related to electron microscopy. In: *Electron Beam Interactions with Solids for Microscopy, Microanalysis & Microlithography*, ed. by D.F. Kyser, H. Niedrig, D.E. Newbury, R. Shimizu (Scanning Electron Microscopy, Chicago 1984) pp. 1–17
- 5.119 R.F. Egerton: *Electron-Energy-Loss Spectroscopy in the Electron Microscope* (Plenum, New York 1986)
- 5.120 C.J. Powell, A. Jablonski: *Electron Inelastic-Mean-Free-Path Database Version 1.1*, NIST Standard Reference Database 71 (National Institute of Standards and Technology, Gaithersburg 2000)
- 5.121 S.A. Goudsmit, J.L. Saunderson: Multiple scattering of electrons II, *Phys. Rev.* **58**, 36 (1940)
- 5.122 D.F. Kyser: Monte Carlo calculations for electron microscopy, microanalysis, and microlithography. In: *Electron Beam Interactions with Solids for Microscopy, Microanalysis & Microlithography*, ed. by D.F. Kyser, H. Niedrig, D.E. Newbury, R. Shimizu (Scanning Electron Microscopy, Chicago 1984) pp. 119–135
- 5.123 L. Reimer, D. Stelter: FORTRAN 77 Monte-Carlo program for minicomputers using Mott cross-sections, *Scanning* **8**, 265 (1986)
- 5.124 D.C. Joy: A model for calculating secondary and backscattered electron yields, *J. Microsc.* **147**, 51 (1987)
- 5.125 L. Reimer: Monte-Carlo-Rechnungen zur Elektrendiffusion, *Optik* **27**, 86 (1968)
- 5.126 L. Reimer: MOCASIM – Ein Monte Carlo Programm für Forschung und Lehre, *Beitr. Elektronenmikr. Direktabb. Anal. Oberfl.* **29**, 1–10 (1996)
- 5.127 D. Drouin, P. Hovington, R. Gauvin: CASINO: A new Monte Carlo code in C language for the electron beam interactions—Part II: Tabulated values of the Mott cross section, *Scanning* **19**, 20 (1997)
- 5.128 P. Hovington, D. Drouin, R. Gauvin: CASINO: A new Monte Carlo code in C language for electron beam interaction—Part I: Description of the program, *Scanning* **19**, 1 (1997)
- 5.129 P. Hovington, D. Drouin, R. Gauvin, D.C. Joy, N. Evans: CASINO: A new Monte Carlo code in C language for electron beam interactions—Part III: Stopping power at low energies, *Scanning* **19**, 29 (1997)
- 5.130 H. Bethe: Zur Theorie des Durchgangs schneller Korpuskularstrahlen durch Materie, *Ann. Phys.* **5**, 325 (1930)

- 5.131 M.J. Berger, S.M. Seltzer: Tables of energy losses and ranges of electrons and positrons. In: *Studies in Penetration of Charged Particles in Matter*, ed. by U. Fano (National Academies Press, Washington 1964) pp. 205–268
- 5.132 D.C. Joy, S. Luo: An empirical stopping power relationship for low-energy electrons, *Scanning* **11**, 176 (1989)
- 5.133 R. Reichelt, A. Engel: Monte Carlo calculations of elastic and inelastic electron scattering in biological and plastic materials, *Ultramicroscopy* **13**, 279 (1984)
- 5.134 V. Krzyzanek, R. Reichelt: MONCA: A new MATLAB package for Monte Carlo simulation of electron scattering in thin specimens in the energy range 10–200 keV, *Microsc. Microanal.* **9**(S3), 110 (2003)
- 5.135 R. Kollath: Sekundärelektronen-Emission fester Körper bei Bestrahlung mit Elektronen. In: *Electron-Emission Gas Discharges I/Elektronen-Emission Gasentladungen I*, Handbuch der Physik, Vol. 4/21 (Springer, Berlin 1956) pp. 232–302
- 5.136 A.J. Dekker: Secondary electron emission, *Solid State Phys.* **6**, 251 (1958)
- 5.137 K. Kanaya, S. Ono: Interaction of electron beam with the target in scanning electron microscope. In: *Electron Beam Interactions with Solids for Microscopy, Microanalysis & Microlithography*, ed. by D.F. Kyser, H. Niedrig, D.E. Newbury, R. Shimizu (Scanning Electron Microscopy, Chicago 1984) pp. 69–98
- 5.138 H. Seiler: Einige aktuelle Probleme der Sekundärelektronen-Emission, *Z. Angew. Phys.* **22**, 249 (1967)
- 5.139 H. Seiler: Secondary electron emission. In: *Electron Beam Interactions with Solids for Microscopy, Microanalysis & Microlithography*, ed. by D.F. Kyser, H. Niedrig, D.E. Newbury, R. Shimizu (Scanning Electron Microscopy, Chicago 1984) pp. 33–42
- 5.140 J.L.H. Jonker: On the theory of secondary emission of metals, *Philips Res. Rep.* **12**, 249 (1957)
- 5.141 W. Oppel, H. Jahrreiss: Messungen der Winkelverteilung von Sekundärelektronen an dünnen freitragenden Al- und Au-Schichten, *Z. Phys.* **252**, 107 (1972)
- 5.142 H. Drescher, L. Reimer, H. Seidel: Rückstreuoeffizient und Sekundärelektronenausbeute von 10–100 keV-Elektronen und Beziehungen zur Raster-Elektronenmikroskopie, *Z. Angew. Phys.* **29**, 331 (1970)
- 5.143 S. Ono, K. Kanaya: The energy dependence of secondary emission based on the range-energy retardation power formula, *J. Phys. D* **12**, 619 (1979)
- 5.144 H.E. Bauer, H. Seiler: Determination of the non-charging electron beam energies of electrically floating metal samples. In: *Scanning Electron Microscopy*, Vol. 3, ed. by O. Johari (Scanning Electron Microscopy, Chicago 1984) pp. 1081–1088
- 5.145 D.C. Joy: A data base on electron–solid interactions, <http://extras.springer.com/2003/978-0-306-47292-3/Database/Joy%20Electron%20Database.doc> (2001)
- 5.146 K.F.J. Heinrich: Optiques de rayons X et micro-analyse. In: *Fourth International Congress on X-Ray Optics and Microanalysis*, ed. by R. Castaing, P. Deschamps, J. Philibert (Hermann, Paris 1966) pp. 159–167
- 5.147 D.B. Wittry: Secondary electron emission in the electron probe. In: *4th Int. Congr. X-ray Opt. Microanal.*, ed. by R. Castaing, P. Deschamps, J. Philibert (Hermann, Paris 1966) pp. 168–180
- 5.148 H. Seiler: Die physikalischen Aspekte der Sekundärelektronenemission für die Elektronen-Raster-Mikroskopie, *Beitr. Elektronenmikr. Direktabb. Anal. Oberfl.* **1**, 27 (1968)
- 5.149 K. Murata: Monte Carlo simulation of electron scattering in resist film/substrate targets. In: *Electron Beam Interactions with Solids for Microscopy, Microanalysis & Microlithography*, ed. by D.F. Kyser, H. Niedrig, D.E. Newbury, R. Shimizu (Scanning Electron Microscopy, Chicago 1984) pp. 311–329
- 5.150 K. Murata: Spatial distribution of backscattered electrons in the SEM and electron microprobe, *J. Appl. Phys.* **45**, 4110 (1974)
- 5.151 H. Seiler: Determination of the information depth in the SEM, *Scanning Electron Microsc.* **1**, 9 (1976)
- 5.152 L. Reimer, C. Tollkamp: Measuring the backscattering coefficient and secondary electron yield inside a scanning electron microscope, *Scanning* **3**, 35 (1980)
- 5.153 W. Reuter: The ionization function and its application to the electron probe analysis of thin films. In: *6th Int. Congr. X-ray Opt. Microanal.*, ed. by G. Shinoda, K. Kohra, T. Ichinokawa (Tokyo Univ. Press, Tokyo 1972) pp. 121–130
- 5.154 H.-J. Hunger, L. Küchler: Measurements of the electron backscattering coefficient for quantitative EPMA in the energy range of 4 to 40 keV, *Phys. Status Solidi (a)* **56**, K45 (1979)
- 5.155 D.C. Joy: Contrast in high-resolution scanning electron microscope images, *J. Microsc.* **161**, 343 (1991)
- 5.156 M. Zadrazil, M.M. El-Gomati, A. Walker: Measurements of very low energy secondary and backscattered electron coefficients, *J. Comput. Assist. Microsc.* **9**, 123 (1997)
- 5.157 F. Arnal, P. Verdier, P.-D. Vincensini: Coefficient de retrodiffusion dans le cas d' électrons monocinétiques arrivant sur la cible sous une incidence oblique, *C. R. Acad. Sci.* **268**, 1526 (1969)
- 5.158 L. Reimer, H.G. Badde, H. Seidel: Orientierungsanisotropie des Rückstreuoeffizienten und der Sekundärelektronenausbeute von 10–100 keV Elektronen, *Z. Angew. Phys.* **31**, 145 (1971)
- 5.159 E. Oho, T. Sasaki, K. Adachi, Y. Muranaka, K. Kanaya: An inexpensive and highly efficient device for observing a STEM image in a SEM. In: *11th Int. Congr. Electron Microsc.*, ed. by T. Imura, S. Maruse, T. Suzuki (Japanese Society of Electron Microscopy, Kyoto 1986) pp. 421–422
- 5.160 R. Reichelt, A. Engel: Quantitative scanning transmission 'electron microscopy' in biology, *J. Microsc. Spectrosc. Electron.* **10**, 491 (1985)
- 5.161 J. Frank, P. Bussler, R. Langer, W. Hoppe: Einige Erfahrungen mit der rechnerischen Analyse und

- Synthese von elektronenmikroskopischen Bildern hoher Auflösung, Ber. Bunsenges. Phys. Chem. **74**, 1105 (1970)
- 5.162 D.C. Joy: SMART—A program to measure SEM resolution and imaging performance, *J. Microsc.* **208**, 24 (2002)
- 5.163 J. Frank: The role of correlation techniques in computer image processing. In: *Computer Processing of Electron Microscope Images*, ed. by P.W. Hawkes (Springer, New York 1980) pp. 187–222
- 5.164 M.D. Muir, P.R. Grant: Cathodoluminescence. In: *Quantitative Scanning Electron Microscopy*, ed. by D.B. Holt, M.D. Muir, P.R. Grant, I.M. Boswarva (Academic Press, London 1974) pp. 287–334
- 5.165 D.B. Holt, B.G. Yacobi: Cathodoluminescence characterization of semiconductors. In: *SEM Microcharacterization of Semiconductors*, ed. by D.B. Holt, D.C. Joy (Academic Press, London 1989) pp. 373–423
- 5.166 B.G. Yakobi, D.B. Holt (Eds.): *Cathodoluminescence Microscopy of Inorganic Solids* (Plenum, New York 1990)
- 5.167 D.B. Holt, F.M. Saba: The cathodoluminescence mode of the SEM: A powerful microcharacterization technique, *Scanning Electron Microsc.* **3**, 1023 (1985)
- 5.168 M. DeMets: Relationship between cathodoluminescence and molecular structure of organic compounds, *Microsc. Acta* **76**, 405 (1975)
- 5.169 M. DeMets, K.J. Howlett, A.O. Yoffe: Cathodoluminescent spectra of organic compounds, *J. Microsc.* **102**, 125 (1974)
- 5.170 W. Bröcker, E.-R. Krefting, L. Reimer: Abhängigkeit des Kathodolumineszenzsignals vom Kippwinkel der Probe im Raster-Elektronenmikroskop, *Beitr. Elektronenmikr. Direktabb. Anal. Oberfl.* **10**, 647 (1977)
- 5.171 H.A. Kramers: On the theory of x-ray absorption and of the continuous x-ray spectrum, *Philos. Mag.* **46**, 836 (1923)
- 5.172 S.T. Stephenson: The continuous x-ray spectrum. In: *Handbuch der Physik*, Vol. 30 (Springer, Berlin 1957) pp. 337–370
- 5.173 W. Bambynek, B. Crasemann, R.W. Fink, H.U. Freund, H. Mark, C.D. Swift, R.E. Price, P.V. Rao: X-ray fluorescent yields, Auger, and Coster–Kronig transition probabilities, *Rev. Mod. Phys.* **44**, 716 (1972)
- 5.174 J.A. Bearden: X-ray wavelengths, *Rev. Mod. Phys.* **39**, 78 (1967)
- 5.175 J.A. Bearden: Reevaluation of x-ray atomic energy levels, *Rev. Mod. Phys.* **39**, 125 (1967)
- 5.176 W.L. Baun: Changes in x-ray emission spectra observed between pure elements in combination with others to form compounds or alloys, *Adv. Electron. Electron Phys.* **6**, 155 (1969)
- 5.177 E.H.S. Burhop: *The Auger Effect* (Cambridge Univ. Press, Cambridge 1952)
- 5.178 T. Åberg, G. Howat: Theory of the Auger effect. In: *Handbuch der Physik*, Vol. 31, ed. by W. Mehlhorn, S. Flügge (Springer, Berlin 1982) pp. 469–619
- 5.179 H.H. Madden: Chemical information from Auger electron spectroscopy, *J. Vac. Sci. Technol.* **18**, 677 (1981)
- 5.180 H.E. Bishop: The role of the background in Auger spectroscopy. In: *Electron Beam Interactions with Solids for Microscopy, Microanalysis & Microlithography*, ed. by D.F. Kyser, H. Niedrig, D.E. Newbury, R. Shimizu (Scanning Electron Microscopy, Chicago 1984) pp. 259–269
- 5.181 P.W. Palmberg: Quantitative analysis of solid surfaces by Auger electron spectroscopy, *Anal. Chem.* **45**, 549A (1973)
- 5.182 M.P. Seah, W.A. Dench: Quantitative electron spectroscopy of surfaces: A standard data base for electron inelastic mean free paths in solids, *Surf. Interface Anal.* **1**, 2 (1979)
- 5.183 E. Bauer, W. Telieps: Emission and low energy reflection 'electron' microscopy. In: *Surface and Interface Characterization by Electron Optical Methods*, ed. by A. Howie, A. Valdre (Plenum, New York 1988) pp. 195–233
- 5.184 H.E. Bishop, J.C. Riviere: Surface segregation in boron doped iron observed by Auger, *J. Appl. Phys.* **40**, 1740 (1969)
- 5.185 J. Kirschner: The role of backscattered electrons in scanning Auger microscopy. In: *Scanning Electron Microscopy*, Vol. 1, ed. by O. Johari (Scanning Electron Microscopy, Chicago 1976) pp. 215–220
- 5.186 M. Jacka: Scanning Auger microscopy: Recent progress in data analysis and instrumentation, *J. Electron Spectrosc. Relat. Phenom.* **277**, 114–116 (2001)
- 5.187 D.E. Newbury: The utility of specimen current imaging in the SEM, *Scanning Electron Microsc.* **1**, 111 (1976)
- 5.188 D.K. Hindermann, R.H. Davis: SEM techniques for the examination of blind and through holes, *Scanning Electron Microsc.* **1**, 183 (1974)
- 5.189 K.-R. Peters: Generation, collection and properties of an SE-I enriched signal suitable for high resolution SEM on bulk specimens. In: *Electron Beam Interactions with Solids for Microscopy, Microanalysis & Microlithography*, ed. by D.F. Kyser, H. Niedrig, D.E. Newbury, R. Shimizu (Scanning Electron Microscopy, Chicago 1984) pp. 363–372
- 5.190 H. Seiler, G. Kuhnle: Zur Anisotropie der Elektronenausbeute in Abhängigkeit von der Energie der auslösenden Primärelektronen von 5 bis 50 keV, *Z. Angew. Phys.* **29**, 254 (1970)
- 5.191 L. Reimer: Methods of detection of radiation damage in electron microscopy, *Ultramicroscopy* **14**, 291 (1984)
- 5.192 B. Volbert, L. Reimer: Advantages of two opposite Everhart–Thornley detectors in SEM, *Scanning Electron Microsc.* **4**, 1 (1980)
- 5.193 P. Rappaport: The electron-voltaic effect in p-n junctions induced by beta-particle bombardment, *Phys. Rev.* **93**, 246 (1954)
- 5.194 C.W. Oatley, T.E. Everhart: The examination of p-n junctions with the scanning electron microscope, *J. Electron. Control* **2**, 568 (1957)
- 5.195 T.E. Everhart, O.C. Wells, C.W. Oatley: Factors affecting contrast and resolution in the scanning electron microscope, *J. Electron. Control* **7**, 97 (1959)

- 5.196 W.S.M. Werner, H. Lakatha, H.E. Smith, L. LeTarte, V. Ambrose, J. Baker: Auger voltage contrast imaging for the delineation of two-dimensional junctions in cross-sectioned metal-oxide-semiconductor devices, *J. Vac. Sci. Technol. B* **16**, 420 (1998)
- 5.197 J. Edelmann, K. Wetzig: Low-temperature microscopy and analysis. In: *In Situ Scanning Electron Microscopy in Materials Research*, ed. by K. Wetzig, D. Schulze (Akademie, Berlin 1995) pp. 109–125
- 5.198 Y. Uchikawa, S. Ikeda: Application of scanning electron microscopy (SEM) to analysis of surface domain structure of ferroelectrics, *Scanning Electron Microsc.* **1**, 209 (1981)
- 5.199 D. Hesse, K.-P. Meyer: Domänenstruktur ferroelektrischer und ferromagnetischer Festkörper. In: *Elektronenmikroskopie in der Festkörperphysik*, ed. by H. Bethge, J. Heydenreich (D VW, Berlin 1982) pp. 473–507
- 5.200 D.V. Roshchupkin, M. Brunel: SEM observation of the voltage contrast image of the ferroelectric domain structure in the LiNbO₃ crystal, *Scanning Microsc.* **7**, 543 (1993)
- 5.201 H. Bahadur, R. Parshad: SEM of vibrating quartz crystals—A review, *Scanning Electron Microsc.* **1**, 509 (1980)
- 5.202 A.E. Lukianov, G.V. Spivak: Electron mirror microscopy of transient phenomena in semiconductor diodes. In: *Electron Microscopy*, Vol. 2, ed. by R. Uyeda (Maruzen, Tokyo 1966) p. 611
- 5.203 G.S. Plows, W.C. Nixon: Stroboscopic electron microscopy, *J. Phys. E* **1**, 595 (1968)
- 5.204 T. Hosokawa, H. Fujioka, K. Ura: Generation and measurement of subpicosecond electron beam pulses, *Rev. Sci. Instrum.* **49**, 624 (1978)
- 5.205 H. Fujioka, K. Ura: Waveform measurements on gigahertz semiconductor devices by scanning electron microscope stroboscopy, *Appl. Phys. Lett.* **39**, 81 (1981)
- 5.206 S.M. Davidson: Voltage contrast and stroboscopy. In: *SEM Microcharacterization of Semiconductors*, Techniques in Physics, Vol. 12, ed. by D.B. Holt, D.C. Joy (Academic Press, New York 1989) pp. 153–240
- 5.207 P. Girard: Voltage contrast, *J. Phys. IV* **01**, C6–259 (1991)
- 5.208 L. Dubbeldam: Advances in voltage-contrast detectors in scanning electron microscopes. In: *Advances in Optical and Electron Microscopy*, Vol. 12, ed. by T. Mulvey, C.J.R. Sheppard (Academic Press, London 1991) pp. 139–242
- 5.209 J.M. McKenzie, D.A. Bromely: Observation of charged-particle reaction products, *Phys. Rev. Lett.* **2**, 303 (1959)
- 5.210 D.B. Holt: Quantitative scanning electron microscope studies of cathodoluminescence in adamantin semiconductors. In: *Quantitative Scanning Electron Microscopy*, ed. by D.B. Holt, M.D. Muir, P.R. Grant, I.M. Boswarva (Academic Press, London 1974) pp. 213–286
- 5.211 D.B. Holt: The conductive mode. In: *SEM Microcharacterization of Semiconductors*, ed. by D.B. Holt, D.C. Joy (Academic Press, London 1989) pp. 241–338
- 5.212 H.J. Deamy: Charge collection scanning electron microscopy, *J. Appl. Phys.* **53**, R51 (1982)
- 5.213 S.P. Shea, L.D. Partain, P.J. Warter: Resolution limits of the EBIC technique in the determination of diffusion lengths in semiconductors, *Scanning Electron Microsc.* **1**, 435 (1978)
- 5.214 H. Alexander: What information on extended defects do we obtain from beam-injection methods?, *Mater. Sci. Eng. B* **24**, 1 (1994)
- 5.215 E.B. Yakimov: Electron-beam-induced-current study of defects in GaN; experiments and simulation, *J. Phys. Condens. Matter* **14**, 13069 (2002)
- 5.216 A.E. Grün: Lumineszenz-photometrische Messungen der Energieabsorption im Strahlungsfeld von Elektronenquellen. Eindimensionaler Fall in Luft, *Z. Naturforsch. A* **12**, 89 (1957)
- 5.217 T.E. Everhart, P.H. Hoff: Determination of kilovolt electron energy dissipation vs. penetration distance in solid materials, *J. Appl. Phys.* **42**, 5837 (1971)
- 5.218 H.E. Bishop: Electron-Solid interactions and energy dissipation. In: *Quantitative Scanning Electron Microscopy*, ed. by D.B. Holt, M.D. Muir, P.R. Grant, I.M. Boswarva (Academic Press, London 1974) pp. 41–64
- 5.219 H.J. Leamy: Charge collection scanning electron microscopy, *J. Appl. Phys.* **53**, R51 (1982)
- 5.220 A. Georges, J.M. Fournier, D. Bois: Time resolved EBIC: A non destructive method technique for an accurate determination of p-n junction depth, *Scanning Electron Microsc.* **1**, 147 (1982)
- 5.221 T. Sekiguchi, K. Sumino: Quantitative electron-beam tester for defects in semiconductors (CL/EBIC/SDLTS system), *Rev. Sci. Instrum.* **66**, 4277 (1995)
- 5.222 D.S.H. Chan, J.C.H. Phang, J.M. Chin, S. Kolachina: Single contact beam induced current phenomena—A review, *Solid State Phenom.* **78–79**, 11–18 (2000)
- 5.223 H. Drescher, E.-R. Krefting, L. Reimer, H. Seidel: The orientation dependence of the electron backscattering coefficient of gold single crystal films, *Z. Naturforsch. A* **29**, 833 (1974)
- 5.224 J.R. Dorsey: Scanning electron probe measurements of magnetic fields. In: *Electron Probe Microanalysis*, ed. by A.J. Tousimis, L. Marton (Academic Press, New York 1969) pp. 291–321
- 5.225 G.A. Wardly: Magnetic contrast in the scanning electron microscope, *J. Appl. Phys.* **42**, 376 (1971)
- 5.226 V. Szmaja: Improvements and actual problems in domain imaging by type-I magnetic contrast in SEM, *Czechoslov. J. Phys.* **52(S1)**, A145 (2002)
- 5.227 W. Szmaja: Digitally enhanced type-I magnetic contrast in SEM as a method of domain investigation, *J. Magn. Magn. Mater.* **219**, 281 (2000)
- 5.228 J. Philibert, R. Tixier: Effets de contraste cristallin en microscopie électronique à balayage, *Micron* **1**, 174 (1969)
- 5.229 D.J. Fathers, J.P. Jacobovics, D.C. Joy, D.E. Newbury, H. Yakowitz: A new method of observing magnetic domains by scanning electron microscopy. I. Theory of the image contrast, *Phys. Status Solidi (a)* **20**, 535 (1973)

- 5.230 T. Yamamoto, H. Nishizawa, K. Tsuno: Magnetic domain contrast in backscattered electron images obtained with a scanning electron microscope, *Philos. Mag.* **34**, 311 (1976)
- 5.231 O.C. Wells: Isolation of type-2 magnetic contrast in the SEM by a lock-in technique, *Appl. Phys. Lett.* **35**, 644 (1979)
- 5.232 L. Reimer: *Elektronenmikroskopische Untersuchungs- und Präparationsmethoden*, 2nd edn. (Springer, Berlin 1967)
- 5.233 M.A. Hayat (Ed.): *Principles and Techniques of Biological Scanning Electron Microscopy* (Univ. Park Press, Baltimore 1978)
- 5.234 J.M. Polak, J.M. Varndell (Eds.): *Immunolabelling for Electron Microscopy* (Elsevier, Amsterdam 1984)
- 5.235 M. Müller (Ed.): *The Science of Biological Specimen Preparations for Microscopy and Microanalysis* (Scanning Microscopy International, Chicago 1985)
- 5.236 R.A. Steinbrecht, K. Zierold (Eds.): *Cryotechniques in Biological Electron Microscopy* (Springer, Berlin 1987)
- 5.237 R.M. Albrecht, R.L. Ornberg (Eds.): *The Science of Biological Specimen Preparations for Microscopy and Microanalysis* (Scanning Microscopy International, Chicago 1988)
- 5.238 L. Edelmann, G.M. Roomans (Eds.): *The Science of Biological Specimen Preparations for Microscopy and Microanalysis* (Scanning Microscopy International, Chicago 1990)
- 5.239 F. Grasenick, A. Aldrian, R. Bauer, H. Bangert, R. Essl, R.H. Haefer, P. Hagemann, K.-H. Hermann, E.M. Hörl, P. Karthaler, E. Knapke, R. Nobiling, K.-R. Peters, G. Weber: *Elektronenmikroskopie. Erweiterte Einsatzmöglichkeiten und spezielle Abbildungs- und Präparationsmethoden* (Expert, Ehningen 1991)
- 5.240 P. Echlin: *Low-Temperature Microscopy and Analysis* (Plenum, New York 1992)
- 5.241 M. Malecki, G.M. Roomans (Eds.): *The Science of Biological Specimen Preparations for Microscopy* (Scanning Microscopy International, Chicago 1996)
- 5.242 G. Schimmel, W. Vogell: *Methodensammlung der Elektronenmikroskopie* (Wissenschaftliche Verlagsgesellschaft, Stuttgart 1970)
- 5.243 A.W. Robards, A.J. Wilson (Eds.): *Procedures in Electron Microscopy* (Wiley, Chichester 1993)
- 5.244 T.C. Isabell, P.E. Fischione, C. O'Keefe, M.U. Guruz, V.P. Dravid: Plasma cleaning and its applications for electron microscopy, *Microsc. Microanal.* **5**, 126 (1999)
- 5.245 J.H.M. Willison, A.J. Rowe: *Replica, Shadowing and Freeze-Etching Techniques* (North-Holland, Amsterdam 1980)
- 5.246 Y. Shibata, T. Arima, T. Yamamoto: Double-axis rotary replication for deep-etching, *J. Microsc.* **136**, 121 (1984)
- 5.247 R. Hermann, J. Pawley, T. Nagatani, M. Müller: Double-axis rotary shadowing for high resolution scanning electron microscopy, *Scanning Microsc.* **2**, 1215 (1988)
- 5.248 R.P. Apkarian, J.C. Curtis: Hormonal regulation of capillary fenestrae in the rat adrenal cortex: Quantitative studies using objective lens staging scanning electron microscopy, *Scanning Electron Microsc.* **4**, 1381 (1986)
- 5.249 T. Nagatani, S. Saito: Development of a high resolution SEM and comparative TEM/SEM observation of fine metal particles and thin films, *Inst. Phys. Conf. Ser.* **98**, 519–522 (1989)
- 5.250 T. Müller, P. Walther, C. Scheidegger, R. Reichelt, S. Müller, R. Guggenheim: Cryo-preparation and planar magnetron sputtering for low temperature 'scanning' electron microscopy, *Scanning Microsc.* **4**, 863 (1990)
- 5.251 H. Gross, T. Müller, I. Wildhaber, H. Winkler: High resolution metal replication, quantified by image processing of periodic test specimens, *Ultramicroscopy* **16**, 287 (1985)
- 5.252 R. Wepf, H. Gross: Pt/Ir/C: a powerful coating material for high resolution SEM. In: *12th Int. Congr. Electron Microsc.*, ed. by L.D. Peachy, D.B. Williams (San Francisco Press, Seattle 1990) pp. 6–7
- 5.253 R. Wepf, M. Amrein, U. Bürkli, H. Gross: Platinum/iridium/carbon: A high-resolution shadowing material for TEM, STM and SEM of biological macromolecular structures, *J. Microsc.* **163**, 51–64 (1991)
- 5.254 K.-R. Peters: Penning sputtering of ultra thin metal films for high resolution electron microscopy, *Scanning Electron Microsc.* **1**, 143 (1980)
- 5.255 A.M. Glauert (Ed.): *Practical Methods in Electron Microscopy* (North-Holland, Amsterdam 1973)
- 5.256 W. Hauffe: Development of the surface topography on polycrystalline metals by ion bombardment investigated by scanning electron microscopy, *Phys. Status Solidi (a)* **4**, 111 (1971)
- 5.257 W. Hauffe: Ion bombardment experiments. In: *In Situ Scanning Electron Microscopy in Materials Research*, ed. by K. Wetzig, D. Schulze (Akademie, Berlin 1995) pp. 195–218
- 5.258 N. Reid, J.E. Beesely: *Sectioning and Cryosectioning for Electron Microscopy*, Practical Methods in Electron Microscopy, Vol. 13 (Elsevier, Amsterdam 1991)
- 5.259 H. Sitte: Process of ultrathin sectioning. In: *The Science of Biological Specimen Preparation for Microscopy and Microanalysis* (Scanning Electron Microscopy, Chicago 1984) pp. 97–104
- 5.260 H. Sitte: Advanced instrumentation and methodology related to cryoultramicrotomy: a review. In: *The Science of Biological Specimen Preparation for Microscopy and Microanalysis*, ed. by M. Malecki, G.M. Roomans (Scanning Microscopy International, Chicago 1996) pp. 387–466
- 5.261 W. Hauffe: Das Ionenstrahl-Böschungsschnitt-Verfahren, *Beitr. Elektronenmikr. Direktabb. Anal. Oberfl.* **23**, 305–310 (1990)
- 5.262 W. Hauffe, S. Pannicke, S. Däbritz, P. Schade: Combined application of ion beam slope cutting and SEM/EDX for investigation of the surface layer system on tungsten microwires after tribological treatment, *Surf. Interface Anal.* **34**, 768 (2002)
- 5.263 N. Erdman, R. Campbell, S. Asahina: Precise SEM cross section polishing via argon beam milling, *Microsc. Today* **14**(3), 22 (2006)

- 5.264 E.C.G. Kirk, R.A. McMahon, J.R.A. Cleaver, H. Ahmed: Scanning ion microscopy and microsectioning of electron beam recrystallized silicon on insulator devices, *J. Vac. Sci. Technol. B* **6**, 1940 (1988)
- 5.265 K. Madl, A.L. Toth, A. Barna: p/n junction localization in integrated-circuits with scanning electron-microscope, *Inst. Phys. Conf. Ser.* **93**, 65 (1988)
- 5.266 T. Ishitani, T. Yaguchi: Cross-sectional sample preparation by focused ion beam: A review of ion-sample interaction, *Microsc. Res. Tech.* **35**, 320 (1996)
- 5.267 M. Shibata: Cross section specimen preparation device using argon ion beam for SEM—Cross section polisher (CP) SM-09010, *JEOL News* **39**(1), 28 (2004)
- 5.268 L.A. Giannuzzi, F.A. Stevie: *Introduction to Focused Ion Beams: Instrumentation, Theory, Techniques and Practice* (Springer, New York 2005)
- 5.269 P. Sudraud, P. Ballongue, E. Varoquaux, O. Avenel: Focused ion-beam milling of a submicrometer aperture for a hydrodynamic Josephson-effect experiment, *J. Appl. Phys.* **62**, 2163 (1987)
- 5.270 P. Gnauck, P. Hoffrogge, J. Greiser: New crossbeam inspection tool combining ultrahigh resolution FE-SEM and FIB, *Microsc. Anal.* **9**(3), 11–13 (2003)
- 5.271 P. Gnauck, U. Zeile, W. Rau, M. Schuhmann: Real time SEM imaging of FIB milling processes for extended accuracy in cross-sectioning and TEM preparation, *Microsc. Microanal.* **9**(S3), 524 (2003)
- 5.272 P.E. McGuinness: DualBeam focused ion beam technology, *Scanning* **25**, 221 (2003)
- 5.273 L. Holzer, F. Indutnyi, P.H. Gasser, B. Munch, M. Wegmann: Three-dimensional analysis of porous BaTiO₃ ceramics using FIB nanotomography, *J. Microsc.* **216**, 84 (2004)
- 5.274 U. Sennhauser, P. Jacob, P. Gasser: Anwendung der FIB für Materialwissenschaft und Fehleranalyse, *Prakt. Metallogr.* **41**, 199 (2004)
- 5.275 R. Flindt: *Biologie in Zahlen*, 5th edn. (Spektrum, Berlin 2000)
- 5.276 M. Milani, F.P. Pucillo, M. Ballerini, M. Camatini, M. Gualtieri, S. Martino: First evidence of tire debris characterization at the nanoscale by focused ion beam, *Mater. Charact.* **52**, 283 (2004)
- 5.277 N. Feder, R.L. Sidman: Methods and principles of fixation by freeze-substitution, *J. Biophys. Biochem. Cytol.* **4**, 593 (1958)
- 5.278 M.W. Hess: Of plants and other pets: Practical aspects of freeze-substitution and resin embedding, *J. Microsc.* **212**, 44 (2003)
- 5.279 E. Kellenberger, J. Kistler: The physics of specimen preparation. In: *Unconventional Electron Microscopy for Molecular Structure Determination*, Advances in Structure Research by Diffraction Methods, Vol. 3, ed. by W. Hoppe, R. Mason (Vieweg, Wiesbaden 1979) pp. 49–79
- 5.280 E. Kellenberger, M. Häner, M. Wurtz: The wrapping phenomenon in air-dried and negatively stained preparations, *Ultramicroscopy* **9**, 139 (1982)
- 5.281 A.W. Robards, U.B. Sleytr: *Low Temperature Methods in Biological Electron Microscopy*, Vol. 10 (North-Holland, Amsterdam 1985)
- 5.282 M.J. Dykstra: *Biological Electron Microscopy* (Plenum, New York 1992)
- 5.283 E. Kellenberger, R. Johansen, M. Maeder, B. Bohrmann, E. Stauffer, W. Villiger: Artefacts and morphological changes during chemical fixation, *J. Microsc.* **168**, 181 (1992)
- 5.284 N.J. Severs, D.M. Shotton (Eds.): *Rapid Freezing, Freeze Fracture and Deep Etching* (Wiley, Chichester 1995)
- 5.285 P. Walther: Recent progress in freeze-fracturing of high-pressure frozen samples, *J. Microsc.* **212**, 34 (2003)
- 5.286 P. Echlin: The examination of biological material at low temperatures, *Scanning Electron Microsc.* **1**, 225 (1971)
- 5.287 R. Hermann, M. Müller: Progress in scanning electron microscopy of frozen-hydrated biological specimens, *Scanning Microsc.* **7**, 343 (1993)
- 5.288 P. Walther, M. Müller: Biological ultrastructure as revealed by high resolution cryo-SEM of block faces after cryo-sectioning, *J. Microsc.* **196**, 279 (1999)
- 5.289 S.P. Shea: Energy and atomic number dependence of electron depth-dose and lateral-dose functions. In: *Electron Beam Interactions with Solids for Microscopy, Microanalysis & Microlithography*, ed. by D.F. Kyser, H. Niedrig, D.E. Newbury, R. Shimizu (Scanning Electron Microscopy, Chicago 1984) pp. 145–151
- 5.290 R.O. Bolt, J.G. Carroll (Eds.): *Radiation Effects on Organic Materials* (Academic Press, New York 1963)
- 5.291 M. Dole (Ed.): *The Radiation Chemistry of Macromolecules* (Academic Press, New York 1973)
- 5.292 W. Baumeister, M. Hahn, J. Seredynski, L.M. Herbertz: Radiation damage of proteins in the solid state: Changes of amino acid composition in catalase, *Ultramicroscopy* **1**, 377 (1976)
- 5.293 R.F. Egerton: *Electron-Energy-Loss Spectroscopy in the Electron Microscope*, 2nd edn. (Plenum, New York 1989)
- 5.294 R.F. Egerton: Dose-rate dependence of electron-induced mass loss from organic specimens, *Ultramicroscopy* **80**, 247 (1999)
- 5.295 R.F. Egerton, P.A. Crozier, P. Rice: Electron energy-loss spectroscopy and chemical change, *Ultramicroscopy* **23**, 305 (1987)
- 5.296 A. Engel: Beam damage, contamination and etching. In: *Microsc. Électron. Sci. Matér., Bombannes*, ed. by B. Jouffrey, A. Bourret, C. Colliex (CNRS, Toulouse 1983) pp. 185–192
- 5.297 K. Siangchaew, M. Libera: The influence of fast secondary electrons on the aromatic structure of polystyrene, *Philos. Mag. A* **80**, 1001 (2000)
- 5.298 J. Strane, L.D. Marks, D.E. Luzzi, M.I. Buckett, J.P. Zhang, B.W. Wessels: Encapsulation, diffusion and DIET in the electron microscope, *Ultramicroscopy* **25**, 253 (1988)
- 5.299 S.M. Salih, V.E. Cosslett: Reduction in electron irradiation damage to organic compounds by conducting coatings, *Philos. Mag.: J. Theor. Exp. Appl. Phys.* **30**(1), 225–228 (1974)

- 5.300 J.T. Fourie: A theory of surface origination contamination and a method for its elimination, *Scanning Electron Microsc.* **2**, 87 (1979)
- 5.301 J.S. Wall: Contamination in the STEM at ultra high vacuum, *Scanning Electron Microsc.* **1**, 99 (1980)
- 5.302 M.T. Postek: Immunolabelling for electron microscopy, *Scanning* **18**, 269 (1996)
- 5.303 M. Isaacson, D. Kopf, M. Ohtsuki, M. Utlaut: Contamination as a psychological problem, *Ultramicroscopy* **4**, 97 (1979)
- 5.304 L.-M. Peng, Q. Chen, X.L. Liang, S. Gao, J.Y. Wang, S. Kleindiek, S.W. Tai: Performing probe experiments in the SEM, *Micron* **35**, 495 (2004)
- 5.305 A. Boyde: Improved depth of field in the 'scanning' electron microscope derived from through-focus image stacks, *Scanning* **26**, 265 (2004)
- 5.306 G. Pfefferkorn, M. Pfautsch: Präparation biologischer Objekte für die Raster-Elektronenmikroskopie, *Beitr. Elektronenmikr. Direktabb. Anal. Oberfl.* **4**, 137–157 (1971)
- 5.307 A. Rukosujew, R. Reichelt, A.M. Fabricius, G. Drees, T.T.D. Tjan, M. Rothen-Burger, A. Hoffmeier, H.H. Scheld, C. Schmid: Skeletonization versus pedicle preparation of the radial artery with and without the ultrasonic scalpel, *Ann. Thorac. Surg.* **77**, 120 (2004)
- 5.308 H. Ishikawa, H. Dobashi, T. Kodama, T. Furuhashi, Y. Uchikawa: Investigation of micro mechanical vibration of piezoelectric actuators. Using a stroboscopic SEM, *J. Electron Microsc.* **42**, 35 (1993)
- 5.309 S. Aoyagi: JEOL's challenge to nanotechnology, *JEOL News* **37**, 70 (2002)
- 5.310 J.L. Hernandez-Lopez, R.E. Bauer, W.S. Chang, G. Glasser, D. Grebel-Koehler, M. Klapper, M. Kreiter, J. Leclair, J.P. Majoral, S. Mittler, K. Mullen, K. Vasilev, T. Weil, J. Wu, T. Zhu, W. Knoll: Functional polymers as nanoscopic building blocks, *Mater. Sci. Eng. C* **23**, 267 (2003)
- 5.311 B. Khamsehpour, S.T. Davies: Micromachining of semi-conductor materials by focused ion beams, *Vacuum* **45**, 1169 (2004)
- 5.312 K.D. Micheva, S.J. Smith: Array tomography: A new tool for imaging the molecular architecture and ultrastructure of neural circuits, *Neuron* **55**, 25 (2007)
- 5.313 W. Denk, H. Horstmann: Serial block-face scanning electron microscopy to reconstruct three-dimensional tissue nanostructure, *PLoS Biol.* **2**, e329 (2004)
- 5.314 D.W. Tuggle, L.W. Swanson: Emission characteristics of the ZrO/W thermal field electron source, *J. Vac. Sci. Technol. B* **3**, 220 (1985)
- 5.315 T. Mulvey: Electron lenses, *Scanning Electron Microsc.* **1**, 43 (1974)
- 5.316 Hitachi: *The S-5200 Ultra-High Resolution Field Emission SEM: Features and Some Applications*, Technical Data Sheet No. 98, HTD-E050-01 2001.11 (Hitachi, Tokyo 2001)
- 5.317 K.-R. Peters: Conditions required for high quality high magnification images in secondary electron, *Scanning Electron Microsc.* **4**, 1359 (1982)
- 5.318 D.C. Joy: Monte Carlo studies of high-resolution secondary imaging. In: *Microbeam Analysis*, ed. by A.D. Romig Jr., J.I. Goldstein (San Francisco Press, San Francisco 1984) pp. 81–86
- 5.319 R. Hermann, H. Schwarz, M. Müller: High precision immunoscanning electron microscopy using Fab fragments coupled to ultra-small colloidal gold, *J. Struct. Biol.* **107**, 38 (1991)
- 5.320 W. Baumeister, F. Karrenberg, R. Rachel, A. Engel, B. ten Heggeler, W.O. Saxton: The major cell envelope protein of *Micrococcus radiodurans* (R1): Structural and chemical characterization, *Eur. J. Biochem.* **125**, 535 (1982)
- 5.321 R. Reichelt: Rasterelektronenmikroskopie und Röntgenmikroanalyse. In: *Mikroskopie in Forschung und Praxis*, ed. by H. Robenek (GIT, Darmstadt 1995) pp. 185–217
- 5.322 G. Griffith: *Fine Structure Immunocytochemistry* (Springer, Berlin 1993)
- 5.323 M.A. Hayat (Ed.): *Colloidal Gold. Principles, Methods, and Applications*, Vol. 1 (Academic Press, London 1989)
- 5.324 M.A. Hayat (Ed.): *Microscopy, Immunohistochemistry, and Antigen Retrieval Methods: For Light and Electron Microscopy* (Kluwer Academic/Plenum, New York 2002)
- 5.325 A. Verkleij, J. Leunissen: *Immunogold Labelling in Cell Biology* (CRC, Boca Raton 1989)
- 5.326 E. de Harven, R. Leung, H. Christensen: A novel approach for scanning electron microscopy of colloidal gold-labeled cell surfaces, *J. Cell Biol.* **99**, 53 (1984)
- 5.327 H. Gamliel, A. Polliack: The use of scanning immuno-electron microscopy to detect surface membrane immunoglobulins and antigens on normal and leukemic human leukocytes: Current status, *Scanning Electron Microsc.* **2**, 929 (1983)
- 5.328 D. Hicks, R.S. Molday: Analysis of cell labelling for scanning and transmission electron microscopy. In: *The Science of Biological Specimen Preparation for Microscopy and Microanalysis*, ed. by J.-P. Revel, T. Barnard, C.H. Haggis (Scanning Electron Microscopy, Chicago 1984) pp. 203–220
- 5.329 R.S. Molday, P. Maher: A review of cell surface markers and labelling techniques for scanning electron microscopy, *Histochem. J.* **12**, 273 (1980)
- 5.330 P. Walther, M. Müller: Detection of small (5–15 nm) gold-labelled surface antigens by back-scattered electrons. In: *43rd Annu. Meet. Electron Microsc. Soc. Am.*, ed. by G.W. Bailey (San Francisco Press, San Francisco 1985) pp. 538–541
- 5.331 P. Walther, M. Müller: Detection of small (5–15 nm) gold-labelled surface antigens by back-scattered electrons. In: *Science of Biological Specimen Preparation*, ed. by M. Müller, R.P. Becker, A. Boyde, J.J. Wolosewick (Scanning Electron Microscopy, Chicago 1986) pp. 195–201
- 5.332 T. Ushiki, R. Yui, T. Fujita: Immunohistochemical localization of serotonin in the third ventricular wall of the lamprey, using backscattered electron imaging, *J. Electron Microsc.* **35**, 157 (1986)
- 5.333 R.M. Albrecht, S.R. Simmons, J.R. Prudent, C.M. Erickson: High resolution SEM of colloidal gold labels. In: *Proc. 46th Annu. Meet. Electron Microsc. Soc.*

- Am*, ed. by G.W. Bailey (San Francisco Press, San Francisco 1988) pp. 214–217
- 5.334 P. Hirsch, M. Kässens, L. Reimer, R. Senkel, M. Spranck: Contrast of colloidal gold particles and thin films on a silicon substrate observed by backscattered electrons in a low-voltage scanning electron microscope, *Ultramicroscopy* **50**, 263 (1993)
- 5.335 S.R. Simmons, J.B. Pawley, R.M. Albrecht: Optimizing parameters for correlative immunogold localization by video-enhanced light microscopy, high-voltage transmission electron microscopy, and field emission scanning electron microscopy, *J. Histochem. Cytochem.* **38**, 1781 (1990)
- 5.336 W. Baschong, N.G. Wrigley: Colloidal gold conjugated to Fab fragments or to immunoglobulin G as high resolution labels for immunoelectron microscopy, *J. Electron Microsc. Tech.* **14**, 313 (1990)
- 5.337 M. Müller, R. Hermann: Towards high resolution SEM of biological objects, *Hitachi Instrum. News* **19**, 50 (1990)
- 5.338 R.P. Apkarian, D.C. Joy: Analysis of metal films suitable for high-resolution SE-I microscopy. In: *Microbeam Analysis*, ed. by D.E. Newbury (San Francisco Press, San Francisco 1988) pp. 459–462
- 5.339 S.L. Erlandsen, R.D. Nelson, S.R. Hasslen, G.M. Dunney, S.B. Olmsted, C. Frethem, C.L. Wells: High resolution. FESEM: Application of backscatter electron (BSE) imaging for biological samples, *Hitachi Instrum. News* **27**, 10 (1995)
- 5.340 M. Grote, V. Mahler, S. Spitzauer, T. Fuchs, R. Valenta, R. Reichelt: In situ localization of latex allergens in 3 different brands of latex gloves by means of immunogold field emission scanning and transmission electron microscopy, *J. Allergy Clin. Immunol.* **105**, 561 (2000)
- 5.341 M. Müller, R. Hermann: High resolution SEM-immunocytochemistry. In: *10th Eur. Congr. Electron Microsc.*, Vol. 3, ed. by L. Megías-Megías, M.I. Rodríguez-García, A. Ríos, J.M. Arias (Secretariado de Publicaciones de la Universidad de Granada, Granada 1992) pp. 741–742
- 5.342 H. Ris, M. Malecki: High-resolution field emission scanning electron microscope imaging of internal cell structures after Epon extraction from sections: A new approach to correlative ultrastructural and immunocytochemical studies, *J. Struct. Biol.* **111**, 148 (1993)
- 5.343 J. Yamaguchi, M. Shibano, T. Saito: Immuno-scanning electron microscopic study of cytoskeletons and actin-binding proteins on phagocytosis of zymosans in mouse macrophages by using double marking method. In: *13th Int. Congr. Electron Microsc.*, Vol. 3A, ed. by B. Jouffrey, C. Colliex (Les Editions de Physique, Les Ulis 1994) pp. 43–44
- 5.344 P. Walther, E. Wehrli, R. Hermann, M. Müller: Double-layer coating for high-resolution low-temperature scanning electron 'microscopy', *J. Microsc.* **179**, 229 (1995)
- 5.345 M. Suga, S. Asahina, Y. Sakuda, H. Kazumori, H. Nishiyama, T. Nokuo, V. Alfredsson, T. Kjellman, S.M. Stevens, H.S. Cho, M. Cho, L. Han, S. Che, M.W. Anderson, F. Schüth, H. Deng, O.M. Yaghi, Z. Liu, H.Y. Jeong, A. Stein, K. Sakamoto, R. Ryoo, O. Terasaki: Recent 'progress' in scanning electron microscopy for the characterization of fine structural details of nano materials, *Prog. Solid State Chem.* **42**, 1 (2014)
- 5.346 B. Fruhstorfer, V. Mohles, R. Reichelt, E. Nembach: Quantitative characterisation of second phase particles by atomic force microscopy (AFM) and scanning electron microscopy (SEM), *Philos. Mag. A* **82**, 2575 (2002)
- 5.347 E. Nembach: *Particle Strengthening of Metals and Alloys* (Wiley, New York 1996)
- 5.348 E.J. Anglin, M.P. Schwartz, V.P. Ng, L.A. Perelman, M.J. Sailor: Engineering the chemistry and nanostructure of porous silicon Fabry-Pérot films for loading and release of a steroid, *Langmuir* **20**, 11264 (2004)
- 5.349 A.C. Galca, E.S. Kooij, H. Wormeester, C. Salm, V. Leca, J.H. Rector, B. Poelsema: Structural and optical characterization of porous anodic aluminum oxide, *J. Appl. Phys.* **94**, 4296 (2003)
- 5.350 H. Pan, H. Gao, S.H. Lim, Y.P. Feng, J. Lin: Highly ordered carbon nanotubes based on porous aluminum oxide, *J. Nanosci. Nanotechnol.* **4**, 1014 (2004)
- 5.351 Y. Yamazaki: Application of MEMS technology to micro fuel cells, *Electrochim. Acta* **50**, 663 (2004)
- 5.352 Y.C. Zhao, M. Chen, Y.N. Zhang, T. Xu, W.M. Liu: A facile approach to formation of through-hole porous anodic aluminum oxide film, *Mater. Lett.* **59**, 40 (2005)
- 5.353 Z.X. Zhao, R.Q. Cui, F.Y. Meng, Z.B. Zhou, H.C. Yu, T.T. Sun: Nanocrystalline silicon thin films deposited by high-frequency sputtering at low temperature, *Solar Energy Mater. Solar Cells* **86**, 135–144 (2005)
- 5.354 A. Engel: Molecular weight determination by scanning transmission electron microscopy, *Ultramicroscopy* **3**, 273 (1978)
- 5.355 J.S. Wall: Mass measurement in electron microscope, *Scanning Electron Microsc.* **2**, 291 (1979)
- 5.356 R. Reichelt, A. Engel, U. Aebi: Adaptation of an annular dark field detector capable of single-electron counting to a high resolution field emission scanning electron microscopy. In: *Proc. 9th Eur. Congr. Electron Microsc.*, ed. by H.G. Dickinson, P.J. Goodhew (IOP, York 1988) pp. 33–34
- 5.357 D.C. Bell, M. Mankin, R.W. Day, N. Erdman: Successful application of low voltage electron microscopy to practical materials problems, *Ultramicroscopy* **145**, 56–65 (2014)
- 5.358 S.A. Müller, A. Engel: Structure and mass analysis by scanning transmission electron microscopy, *Micron* **32**, 21 (2001)
- 5.359 M. Nagase, K. Kurihara: Imaging of Si nano-patterns embedded in SiO₂ using scanning electron microscopy, *Microelectron. Eng.* **53**, 57 (2000)
- 5.360 M. Nagase, H. Namatsu: A method for assembling nano-electromechanical devices on microcantilevers using focused ion beam technology, *Jpn. J. Appl. Phys.* **43**, 4624 (2004)

- 5.361 D.C. Joy: Control of charging in low-voltage SEM, *Scanning* **11**, 1 (1989)
- 5.362 R. Schmid, K.H. Gaukler, H. Seiler: Measurement of elastically reflected electrons ($E < 2.5$ keV) for imaging of surfaces in a simple ultra high vacuum 'scanning electron microscope', *Scanning Electron Microsc.* **2**, 501 (1983)
- 5.363 I. Müllerová, L. Frank, O. Hutar: Visualization of the energy band contrast in SEM through low-energy electron reflectance, *Scanning* **23**, 115 (2001)
- 5.364 D.C. Joy: Low voltage scanning electron microscopy. In: *Electron Microscopy Microanalysis*, Institute of Physics Conference Series, Vol. 90, ed. by J.N. Chapman, A.J. Craven (Institute of Physics, Bristol 1987) pp. 175–180
- 5.365 R. Böngeler, U. Golla, M. Kässens, L. Reimer, B. Schindler, R. Senkel, M. Spranck: Electron-specimen interactions in LVSEM, *Scanning* **15**, 1 (1993)
- 5.366 E.H. Darlington, V.E. Cosslett: Backscattering of 0.5–10 keV electrons from solid targets, *J. Phys. D* **5**, 1969 (1972)
- 5.367 B. Lödding, L. Reimer: Monte Carlo Rechnungen im Energiebereich 1–20 keV, *Beitr. Elektronenmikr. Direktabb. Anal. Oberfl.* **14**, 315 (1981)
- 5.368 S. Uno, K. Honda, N. Nakamura, M. Matsuya, J. Zach: Probe shape extraction and automatic aberration correction in scanning electron microscopes. In: *8th Asia-Pac. Conf. Electron Microsc.* (Yoshida, Kanazawa 2004) pp. 46–47
- 5.369 H. Kazumori, K. Honda, M. Matsuya, M. Date, C. Nielsen: Field emission SEM with a spherical and chromatic aberration corrector, *Microsc. Microanal.* **10**(S02), 1370–1371 (2004)
- 5.370 R.J. Young, G.N. van Veen, A. Henstra, L. Tuma: Extreme high-resolution (XHR) SEM using S beam monochromator. In: *Low Voltage Electron Microscopy: Principles and Applications*, ed. by D.C. Bell, N. Erdman (Wiley, Chichester 2013) pp. 57–71
- 5.371 B. Lencová, M. Lenc: Computation of properties of electrostatic lenses, *Optik* **97**, 121 (1994)
- 5.372 B. Lencová: Electrostatic lenses. In: *Handbook of Charged Particle Optics*, ed. by J. Orloff (CRC, New York 1997) pp. 177–221
- 5.373 R.S. Paden, W.C. Nixon: Retarding field scanning electron microscopy, *J. Phys. E* **2**, 1073 (1968)
- 5.374 E. Munro, J. Orloff, R. Rutherford, J. Wallmark: High-resolution, low-energy beams by means of mirror optics, *J. Vac. Sci. Technol. B* **6**, 1971 (1988)
- 5.375 I. Müllerová, M. Lenc: The scanning very low-energy electron microscope, *Mikrochim. Acta* **12**, 173 (1992)
- 5.376 P. Adamec, A. Delong, B. Lencova: Miniature magnetic electron lenses with permanent magnets, *J. Microsc.* **179**, 129 (1995)
- 5.377 A. Khursheed, J.C. Phang, J.T.L. Thong: A portable scanning electron microscope column design based on the use of permanent magnets, *Scanning* **20**, 87 (1998)
- 5.378 A. Khursheed: Recent developments in scanning electron microscope design, *Rev. Sci. Instrum.* **71**, 1712 (2000)
- 5.379 T.H.P. Chang, D.P. Kern, L.P. Muray: Microminaturization of electron optical systems, *J. Vac. Sci. Technol. B* **8**, 1698 (1990)
- 5.380 W. Liu, T. Ambe, R.F. Pease: Micro objective lens with compact secondary electron detector for miniature low voltage electron beam systems, *J. Vac. Sci. Technol. B* **14**, 3738 (1996)
- 5.381 E.W. Wollman, C.D. Frisbie, M.S. Wrighton: Scanning electron microscopy for imaging photopatterned, self-assembled monolayers on gold, *Langmuir* **9**, 1517 (1993)
- 5.382 A.L. Bleloch, M.R. Castell, A. Howie, C.A. Walsh: Atomic and electronic Z-contrast effects in high-resolution imaging, *Ultramicroscopy* **54**, 107 (1994)
- 5.383 D.D. Perovic, M.R. Castell, A. Howie, C. Lavoie, T. Tiedje, J.S.W. Cole: Doping layer imaging in the field emission scanning electron microscope. In: *13th Int. Congr. Electron Microsc.*, ed. by B. Jouffrey, C. Colliex (Les Editions de Physique, Les Ulis 1994) pp. 91–92
- 5.384 T.R. Matzelle, N. Kruse, R. Reichelt: Characterization of the cutting edge of glass knives for ultramicrotomy by scanning force 'microscopy' using cantilevers with a defined tip geometry, *J. Microsc.* **199**, 239 (2000)
- 5.385 T.R. Matzelle, H. Gnaegi, A. Ricker, R. Reichelt: Characterization of the cutting edge of glass and diamond knives for ultramicrotomy by scanning force 'microscopy' using cantilevers with a defined tip geometry, *J. Microsc.* **209**, 113 (2003)
- 5.386 R. Reichelt: Unpublished results (1997)
- 5.387 A. von Nahmen, M. Schenk, M. Sieber, M. Amrein: The structure of a model pulmonary surfactant as revealed by scanning force microscopy, *Biophys. J.* **72**, 463 (1997)
- 5.388 A.G. Bittermann, S. Jacobi, L.F. Chi, H. Fuchs, R. Reichelt: Contrast studies on organic monolayers of different molecular packing in FESEM and their correlation with SFM data, *Langmuir* **17**, 1872 (2001)
- 5.389 V.K. Berry: Characterization of polymer blends by low voltage scanning electron microscopy, *Scanning* **10**, 19 (1988)
- 5.390 J.H. Butler, D.C. Joy, G.F. Bradley, S.J. Krause: Low-voltage scanning electron microscopy of polymers, *Polymer* **36**, 1781 (1995)
- 5.391 G.M. Brown, J.H. Butler: New method for the characterization of domain morphology of polymer blends using ruthenium tetroxide staining and low voltage scanning electron microscopy (LVSEM), *Polymer* **38**, 3937 (1997)
- 5.392 V.N.E. Robinson: The elimination of charging artefacts in the scanning electron microscope, *J. Phys. E* **8**, 638 (1975)
- 5.393 G.D. Danilatos: An atmospheric scanning electron microscope (ASEM), *Scanning* **3**, 215 (1980)
- 5.394 G.D. Danilatos: The examination of fresh or living plant material in an environmental scanning electron 'microscope', *J. Microsc.* **121**, 235 (1981)
- 5.395 E. Lax (Ed.): *D'Ans-Lax Taschenbuch für Chemiker und Physiker* (Springer, Berlin 1967)
- 5.396 G.D. Danilatos: Review and outline of environmental SEM at present, *J. Microsc.* **162**, 391 (1991)

- 5.397 S.A. Wight, C.J. Zeissler: Direct measurement of electron beam scattering in the environmental scanning electron microscope using phosphor imaging plates, *Scanning* **22**, 167 (2000)
- 5.398 G.D. Danilatos: Design and construction of an atmospheric or environmental SEM (Part 3), *Scanning* **7**, 26 (1985)
- 5.399 G.D. Danilatos: Cathodoluminescence and gaseous scintillation in the environmental SEM, *Scanning* **8**, 279 (1986)
- 5.400 B.L. Thiel, I.C. Bache, A.L. Fletcher, P. Meredith, A.M. Donald: An improved model for gaseous amplification in the environmental SEM, *J. Microsc.* **187**, 143 (1997)
- 5.401 J. Cazaux: About the mechanisms of charging in EPMA, SEM, and ESEM with their time evolution, *Microsc. Microanal.* **10**, 670 (2004)
- 5.402 Y. Ji, H.S. Guo, T.X. Zhong, H. Zhang, X.L. Quan, Y.Q. Zhang, X.D. Xu: Charge and charging compensation on oxides and hydroxides in oxygen environmental SEM, *Ultramicroscopy* **103**, 191 (2005)
- 5.403 X. Tang, D.C. Joy: Quantitative measurements of charging in a gaseous environment, *Scanning* **25**, 194 (2003)
- 5.404 B.L. Thiel, M. Toth, J.P. Craven: Charging processes in low vacuum scanning electron microscopy, *Microsc. Microanal.* **10**, 711 (2004)
- 5.405 K. Robertson, R. Gauvin, J. Finch: Charge contrast imaging of gibbsite using the variable pressure SEM, *Microsc. Microanal.* **10**, 721 (2004)
- 5.406 M. Toth, M.R. Phillips: The role of induced contrast in images obtained using the environmental scanning electron microscope, *Scanning* **22**, 370 (2000)
- 5.407 M. Schenk, M. Fütting, R. Reichelt: Direct visualization of the dynamic behavior of a water meniscus by scanning electron microscopy, *J. Appl. Phys.* **84**, 4880 (1998)
- 5.408 S. Thiberge, A. Nechushtan, D. Sprinzak, O. Gileadi, V. Behar, O. Zik, Y. Chowders, S. Michaeli, J. Schlesinger, E. Moses: Scanning electron microscopy of cells and tissues under fully hydrated conditions, *Proc. Natl. Acad. Sci. U.S.A.* **101**, 3346 (2004)
- 5.409 A. Cismak, M. Schwanecke, M. Fütting, A. Heilmann: Environmental scanning electron microscopy of living mammalian cell cultures, *Microsc. Microanal.* **9**(S3), 480 (2003)
- 5.410 R.E. de la Parra: A method to detect variations in the wetting properties of microporous polymer membranes, *Microsc. Res. Tech.* **25**, 362 (1993)
- 5.411 N.A. Stelmashenko, J.P. Craven, A.M. Donald, E.M. Terentjev, B.L. Thiel: Topographic contrast of partially wetting water droplets in environmental scanning electron microscopy, *J. Microsc.* **204**, 172 (2001)
- 5.412 A. Liukkonen: Contact angle of water on paper components: Sessile drops versus environmental scanning electron microscope measurements, *Scanning* **19**, 411 (1997)
- 5.413 M.P. Rossi, H.H. Ye, Y. Gogotsi, S. Babu, P. Ndungu, J.C. Bradley: Environmental scanning electron microscopy study of water in carbon nanopipes, *Nano Lett.* **4**, 989 (2004)
- 5.414 B. Bennett, J.O. Buckman, B.F. Bowler, S.R. Larter: Wettability alteration in petroleum systems: The role of polar non-hydrocarbons, *Petroleum Geosci.* **10**, 271 (2004)
- 5.415 E. Kowalewski, T. Boassen, O. Torsaeter: Wettability alterations due to aging in crude oil; wettability and cryo-ESEM analyses, *J. Petrol. Sci. Eng.* **39**, 377 (2003)
- 5.416 M. Robin: Interfacial phenomena: Reservoir wettability in oil recovery, *Oil Gas Sci. Technol.* **56**, 55 (2001)
- 5.417 Y. Cao, H.L. Li: Interfacial activity of a novel family of polymeric surfactants, *Eur. Polym. J.* **38**, 1457 (2002)
- 5.418 S. Kitching, A.M. Donald: Beam damage in the ESEM: an FTIR study of polypropylene. In: *11th Europ. Conf. Electron Microsc., Dublin*, Vol. 1 (1996) pp. 138–139
- 5.419 C.P. Royall, B.L. Thiel, A.M. Donald: Radiation damage of water in environmental scanning electron 'microscopy', *J. Microsc.* **204**, 185 (2001)
- 5.420 K. Kanaya, S.O. Kayama: Penetration and energy-loss theory of electrons in solid targets, *J. Appl. Phys. D* **5**, 43 (1972)
- 5.421 K.F.J. Heinrich: *Microbeam Analysis* (San Francisco Press, San Francisco 1982)
- 5.422 K.F.J. Heinrich, D.E. Newbury (Eds.): *Electron Probe Quantification* (Plenum, New York 1991)
- 5.423 D.E. Newbury, D.S. Bright: "Derived spectra" software tools for detecting spatial and spectral features in spectrum images, *Scanning* **27**, 15 (2005)
- 5.424 V.E. Cosslett, P. Duncumb: Micro-analysis by a flying-spot x-ray method, *Nature* **177**, 1172 (1956)
- 5.425 J.J. Friel, R. Terborg, S. Langner, T. Salge, M. Rohde, J. Berlin: *X-Ray and Image Analysis in Electron Microscopy*, 3rd edn. (Pro Business, Berlin 2017)
- 5.426 J. Goldstein, D.E. Newbury, D.C. Joy, C.E. Lyman, P. Echlin, E. Lifshin, L. Sawyer, J.R. Michael: *Scanning Electron Microscopy and X-Ray Microanalysis*, 3rd edn. (Springer, New York 2003)
- 5.427 L. Strüder, P. Lechner, P. Leutenegger: Silicon drift detector—The key to new experiments, *Naturwissenschaften* **85**, 539 (1998)
- 5.428 L. Strüder, N. Meidinger, D. Stotter, J. Kemmer, P. Lechner, P. Leutenegger, H. Soltau, F. Eggert, M. Rohde, T. Schulein: High-resolution x-ray spectroscopy close to room temperature, *Microsc. Microanal.* **4**, 622 (1998)
- 5.429 P. Lechner, C. Fiorini, R. Hartmann, J. Kemmer, N. Krause, P. Leutenegger, A. Longoni, H. Soltau, D. Stotter, R. Stotter, L. Strüder, U. Weber: Silicon drift detectors for high count rate x-ray spectroscopy at room temperature, *Nucl. Instrum. Methods Phys. Res. A* **458**, 281 (2001)
- 5.430 P. Poelt, M. Schmied, I. Obernberger, T. Brunner, J. Dahl: Automated analysis of submicron particles by computer-controlled scanning electron microscopy, *Scanning* **24**, 92 (2002)
- 5.431 Y. Hu, Y. Pan: Method for the calculation of the chemical composition of a thin film by Monte Carlo simulation and electron probe microanalysis, *X-Ray Spectrom.* **30**, 110 (2001)

- 5.432 D.G. Rickerby, N. Wächter, R. Reichelt: Quantitative EDX analysis of $\text{SiO}_2/\text{Al}_2\text{O}_3/\text{TiO}_2$ multilayer films, *Mikrochim. Acta Suppl.* **15**, 149 (1998)
- 5.433 G.C. Smith, D. Park, O. Cochonneau: Maximum entropy reconstruction of compositional depth profiles from electron probe microanalysis data, *J. Microsc.* **178**, 48 (1995)
- 5.434 P. Poelt: Low voltage EDXS and elements of the first transition series, *Mikrochim. Acta* **132**, 129 (2000)
- 5.435 R. Wurster: EDX measurements on nanoparticles in a high resolution scanning electron microscope, *J. Trace Microprobe Tech.* **15**, 467 (1997)
- 5.436 D.C. Joy, D.E. Newbury, D.L. Davidson: Electron channeling patterns in scanning electron microscope, *J. Appl. Phys.* **53**, R81 (1982)
- 5.437 C.G. van Essen, E.M. Schulson, R.H. Donaghy: The generation and identification of SEM channeling patterns from 10 μm selected areas, *J. Mater. Sci.* **6**, 213 (1971)
- 5.438 J.A. Venables, C.J. Harland: Electron back-scattering patterns—A new technique for obtaining crystallographic information in the scanning electron microscope, *Philos. Mag.* **27**, 74 (1973)
- 5.439 A.J. Wilkinson, P.B. Hirsch: Electron diffraction based techniques in scanning electron microscopy of bulk materials, *Micron* **28**, 279 (1997)
- 5.440 N.C. Krieger-Lassen, D. Juul-Jensen, K. Conradsen: Image processing procedures for analysis of electron back scattering patterns, *Scanning Microsc.* **6**, 115 (1992)
- 5.441 B.L. Adams, S.I. Wright, K. Kunze: Orientation imaging: The emergence of a new microscopy, *Metall. Trans. A* **24**, 819 (1993)
- 5.442 S. Zaefferer: The electron backscatter diffraction technique—A powerful tool to study microstructures by SEM, *JEOL News* **39**, 10 (2004)
- 5.443 S. Zaefferer, J. Ohlert, W. Bleck: A study of microstructure, transformation mechanisms and correlation between microstructure and mechanical properties of a low alloyed TRIP steel, *Acta Mater.* **52**, 2765 (2004)
- 5.444 A.J. Wilkinson: Advances in SEM-based diffraction studies of defects and strains in semiconductors, *J. Electron Microsc.* **49**, 299 (2000)
- 5.445 D. Katrakova, F. Mücklich: Specimen preparation for electron backscatter diffraction (EBSD)—Part II: Ceramics, *Prakt. Metallogr.* **39**, 644 (2002)
- 5.446 M.R. Koblischka, A. Koblischka-Veneva: Characterization of bulk superconductors through EBSD methods, *Physica C* **392**, 545 (2003)
- 5.447 A. Mauler, G. Godard, K. Kunze: Crystallographic fabrics of omphacite, rutile and quartz in vendee eclogites (Armorican Massif, France): Consequences for deformation mechanisms and regimes, *Tectonophysics* **342**, 81 (2001)
- 5.448 D.J. Prior, A.P. Boyle, F. Brenker, M.C. Cheadle, A. Day, G. Lopez, L. Peruzzo, G.J. Potts, S. Reddy, R. Spiess, N.E. Timms, P. Trimby, J. Wheeler, L. Zeterstrom: The application of electron backscatter diffraction and orientation contrast imaging in the SEM to textural problems in rocks, *Am. Mineral.* **84**, 1741 (1999)
- 5.449 P.W. Trimby: Orientation mapping of nanostructured materials using transmission Kikuchi diffraction in the scanning electron microscope, *Ultramicroscopy* **120**, 16 (2012)



Natasha Erdman

JEOL USA Inc.
Peabody, MA, USA
erdman@jeol.com

Natasha Erdman received her PhD in Materials Science from Northwestern University, IL in 2002. She has worked at JEOL USA since 2004, specializing in scanning electron microscopy and ion beam instrumentation and applications. Her research interests include low-voltage electron microscopy and correlative microscopy applications in materials science and biology.

David C. Bell

Center for Nanoscale Systems
Harvard University
Cambridge, MA, USA
dcb@seas.harvard.edu



David C. Bell received his PhD in Physics from the University of Melbourne, and did his postdoctoral study at the Massachusetts Institute of Technology. He is the Gordon McKay Professor of the Practice of Electron Microscopy at Harvard University, and also Associate Director of the Center for Nanoscale Systems. His research focuses on nanoscale materials' properties and applications and theory and applications of aberration-corrected electron microscopy.

Rudolf Reichelt (deceased)

Rudolf Reichelt (1947–2010) studied Physics at the Technical University Dresden and acquired his PhD in 1973. He accomplished his postdoctoral training in the *Zentralinstitut für Molekularbiologie* in Berlin. In 1982, he joined the Biozentrum of the University of Basel, Switzerland, where he developed a fully corrected electron spectrometer for a scanning transmission electron microscope used for biological applications. The *Westfälische Wilhelms-Universität* in Münster appointed Dr. Reichelt as successor of Dr. Ludwig Reimer in 1990. Rudolf Reichelt established an active team that developed and applied techniques to image and analyze biological as well as solid materials using high-resolution microscopes. SEM, STEM, and TEM were the primary tools, but scanning probe microscopes were used as well. Dr. Reichelt was engaged in the application of STEM for mass-determination of biomolecules. His open mind and creativity resulted in a rich variety of publications, many in excellent journals.